PROBING THE AFFINITY, SELECTIVITY AND INHIBITION OF UBIQUITIN–UBIQUITIN BINDING DOMAIN COMPLEXES BY ELECTROSPRAY IONIZATION MASS SPECTROMETRY

Kleitos Sokratous, M.Sc.

Thesis submitted to the University of Nottingham
for the degree of Doctor of Philosophy

June 2013

ABSTRACT

This thesis describes the development and application of a rapid and sensitive electrospray ionization-mass spectrometry (ESI-MS) method to study the weak hydrophobic interactions seen in many Ub•Ub-binding domain (UBD) complexes. A range of UBDs has been screened against mono-Ub, di-Ub (Ub_2) and tetra-Ub (Ub_4). Affinities in the 2-200 μM range were found to be in excellent agreement with data obtained from other biophysical techniques. Insights into the UBD's preference for poly-Ub chain linkage and length are also provided by this methodology. Detection of a ternary complex involving Ub interacting simultaneously with two different UBDs demonstrated the co-existence of multi-site interactions. A simple, clean and effective method for reducing charge states observed in ESI-MS without the use of any solution additives or instrumental modifications is also reported; with the charge reduction method ultimately promoting the investigation of the Ub•UBD interactions.

Moreover, the development and application of a top-down proteomics approach to characterize the topology of an unanchored Ub dimer purified from rat skeletal muscle is also described in this thesis. This study has identified the topology of the Ub_2 to be Lys48-linked. In addition, ESI-MS of endogenous Ub_2 species has revealed the presence of cyclic Lys48-linked Ub_2 and demonstrates for the first time that cyclisation of poly-Ub can also occur *in vivo*.

Further to these studies, the inhibitory activity of small peptides against the complex formed by Ub with the ZnF domain of isopeptidase T (IsoT) is also investigated. Finally, the unusual effects of cation adduction upon the gas-phase conformation of three-helix bundle UBDs are revealed by ESI-IMS-MS and reported in this thesis.

PUBLICATIONS

The effects of cation adduction upon the conformation of three-helix bundle proteins Kleitos Sokratous, Robert Layfield, Neil J Oldham, *International Journal for Ion Mobility Spectrometry* **2013**, *16*, 19-27

Cyclisation of Lys48-linked diubiquitin *in vitro* and *in vivo*. Kleitos Sokratous, Joanna Strachan, Lucy V Roach, Robert Layfield and Neil J Oldham, *FEBS letters* **2012**, *586*, 4144-4147

Probing affinity and ubiquitin linkage selectivity of ubiquitin-binding domains using mass spectrometry Kleitos Sokratous, Lucy V Roach, Debora Channing, Joanna Strachan, Jed E Long, Mark S Searle, Robert Layfield and Neil J Oldham, *Journal of the American Chemical Society* **2012**, *134*, 6414 - 6424

Insights into the molecular composition of endogenous unanchored polyubiquitin chains Joanna Strachan, Lucy Roach, Kleitos Sokratous, David Tooth, Jed Long, Thomas P Garner, Mark S Searle, Neil J Oldham and Robert Layfield, *Journal of Proteome Research* **2012**, *11*, 969 - 1980

Charge state and adduct reduction in electrospray ionization-mass spectrometry using solvent vapor exposure Jonathan T S Hopper[1], Kleitos Sokratous[1] and Neil J Oldham, *Analytical Biochemistry* **2012**, *421*, 788 - 790

Book Chapter: **"Protein-Protein Interactions Studied By Mass Spectrometry"** Kleitos Sokratous and Jose P. Afonso *Encyclopedia of Biophysics, Gordon Roberts, Springer,* **2013** *(In Press).*

ACKNOWLEDGEMENTS

First and foremost, I would like to express my deepest gratitude to my supervisor Dr. Neil Oldham, for giving me the opportunity to work in such an interesting area of research, and also for his advice, guidance and support throughout my studies.

I am particularly thankful to Dr. Lucy Roach for the productive and exciting collaboration, and for sharing her thoughts in countless valuable discussions. I am also very grateful to Dr. Robert Layfield and Dr. Joanna Strachan for their collaboration throughout the past three years and for their help in the expression and purification of the UBD proteins, and to Prof. Mark Searle and Dr. Jed Long for providing the protein mutants. I would also like to thank Dr. David Tooth for always being willing to help and for sharing resources and his knowledge in peptide synthesis and purification. Special thanks to Nicky Herbert for his contribution in the peptide synthesis and purification experiments.

I am particularly thankful to Jonathan Hopper, for many fruitful discussions and for the exciting collaboration over the charge reduction experiments.

I am indebted to all the current and past members of the Oldham group, in particular to Lucy Roach, Jonathan Hopper, Jose Afonso, Matt Jenner and Richard Elms, for providing an inspiring and fun environment in which to learn. I am especially grateful to Matt Jenner for being an invaluable colleague, a good housemate and a great friend.

Finally and most importantly, I would like to dedicate this thesis to my parents, as a small symbol of my gratitude for their encouragement and support, without which, this work would not be carried out.

ABBREVIATIONS

CCS	Collision cross section
CD	Circular dicroism
CI	Chemical ionization
CID	Collision induced dissociation
CRM	Charge residue model
DTT	Dithiothreitol
ECD	Electron capture dissociation
ESI	Electrospray ionization
ESSI	Electrosonic spray ionization
EHSS	Exact hard-spheres scattering
EI	Electron ionization
FAB	Fast atom bombardment
FD	Field desorption
FI	Field ionization
FT-ICR	Fourier Transform -Ion Cyclotron Resonance
K_d	Dissociation constant
KE	Kinetic energy

IEM	Ion evaporation model
IMS	Ion mobility spectrometry
IM-MS	Ion mobility-Mass spectrometry
IPTG	Isopropylthio-β-galactoside
ITC	Isothermal titration calorimetry
LB	Luria broth
MALDI	Matrix assisted laser desorption ionization
MD	Molecular dynamics
MS	Mass spectrometry
MS/MS	Tandem mass spectrometry
m/z	Mass to charge ratio
nESI	Nano-electrospray ionization
NMR	Nuclear magnetic resonance
PA	Projection approximation
PDB	Protein databank
PPI	Protein-protein interaction
PTM	Post-translational modification
SPR	Surface plasmon resonance
t_D	Drift time

TOF	Time-of-flight
TM	Trajectory method
TTR	Transthyretin
TWIMS	Travelling wave ion mobility spectrometry
Ub	Ubiquitin
UBA	Ubiquitin associated domain
UBD	Ubiquitin binding domain
ZnF	Zinc finger

TABLE OF CONTENTS

CHAPTER 1

INTRODUCTION

1.1 MASS SPECTROMETRY

Mass spectrometry (MS) has evolved into a powerful analytical tool that is used for measuring the molecular mass of a sample molecule, for the determination of elemental composition, for protein sequencing, and many other applications. The fundamental basis of MS is the generation of gas-phase ions and their separation driven by differences in their mass-to-charge ratio (m/z).

The development of MS can be mainly attributed to the work of J.J. Thomson and of his student, Fransis Aston. Thomson discovered the electron and determined its mass-to-charge ratio (m/z) in 1897 (Nobel Prize in physics, 1906) and then he constructed the first mass spectrometer in 1912 [1] with which he managed to obtain mass spectra of various gases. A few years later, in 1919, Aston designed a significantly improved apparatus and used it to discover isotopes of the non-radioactive elements [2]. In 1922, Aston received the Nobel Prize in chemistry for his pioneering work. Today, more than 70 years after the launch of the first commercial instrument, several improvements including development of revolutionary mass analysers and ionization techniques, have extended the use of MS in a very broad scientific field; from the analysis of single elements up to the analysis of complex biomolecular assemblies.

Several types of MS instruments are currently available; however, all of them consist of three basic components, which are the ion source, the mass analyser(s)

and the detector. Figure 1.1.1 illustrates a typical configuration of a mass spectrometer composed of these three units together with a controlling/data system. While the mass analyser(s) and detector are held under vacuum, ion source, depending on the ionization process, may be held either under vacuum or at atmospheric pressure.

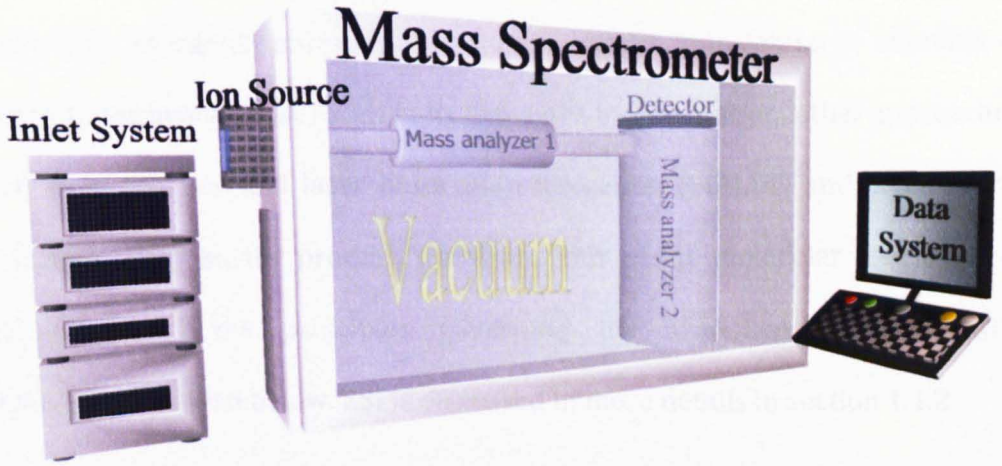

Figure 1.1.1 A typical configuration of a mass spectrometry platform, consist of an inlet system, the mass spectrometer and the data system.

An inlet system, such as a gas chromatograph (GC), liquid chromatograph (LC) or a solids probe, or simple syringe pump, is frequently used to subject sample to MS analysis. Sample ionization followed by ion separation according to their *m/z* ratio and finally ion detection, are the three key steps that are followed in every MS experiment. Finally, a data processing system such as a computer, also frequently used to control the whole instrument, will produce a mass spectrum.

1.1.1 Ion Source

Ionization of the analyte can be achieved using several different techniques. Ions can be generated thermally, by electric fields or by collisions between analyte molecules and other "particles", such as energetic electrons, ions, photons and energetic neutral atoms. Choice of the appropriate ionization technique depends

on the nature of the analyte, principally its physical and chemical properties. For example, thermally labile compounds are very challenging, and usually not feasible, for some ionization techniques such as electron ionization (EI), chemical ionization (CI) and field ionization (FI), largely due to the need to vaporize them by heating. Another factor that has to be taken into account, when selecting an ion source, is the amount of internal energy that is transferred during ionization. While high energetic ionization techniques, like EI, transfer large amounts of energy to the analyte that result in its extensive fragmentation, other approaches, such as matrix assisted laser desorption ionization (MALDI) and electrospray ionization (ESI) usually produce dominant ions of the molecular species. Brief descriptions of the principles governing the aforementioned ionization techniques are given below. ESI is discussed in more details in section 1.1.2.

1.1.1.1 Electron Ionization (EI)

In an EI source, a heated filament produces highly energetic electrons (a procedure known as *thermionic* emission), which are accelerated towards an anode. When neutral gaseous analytes are injected into the source, they collide with these energetic electrons. The collision results in energy transfer to the neutral molecules, and if this energy is sufficient to expel an electron it leads to the formation of a radical cation ($M^{+\cdot}$). The energy of the electrons and the chemistry of the analyte regulate the ionization efficiency (i.e. the ratio of the number of formed ions to the number of electrons used) and its fragmentation level.

When an electron is accelerated, it behaves as a wave. Therefore, each electron has a characteristic wavelength λ, known as *de Broglie wavelength* (eq. 1.1), and its value is determined by its mass (m), its velocity (v) and the Planck (h) constant.

$$\lambda = \frac{h}{mv}$$ Equation 1.1

The wavelength is inversely proportional to the kinetic energy of electrons. For example, when the kinetic energy of the electrons is increased from 20 eV to 70 eV, the wavelength is decreased from 2.7 Å to 1.4 Å, respectively. The ionization efficiency of a given sample at a constant temperature depends on the kinetic energy of the electrons. While the energy transferred to the analyte molecules by "slow" electrons it can be insufficient to cause their ionization, electrons with very high kinetic energy exhibit very small wavelengths and as a consequence the analyte molecules become "transparent" to them. In case of organic molecules, maximum ionization efficiency is achieved when electrons are accelerated around 70 eV. Under these conditions, between 10 and 20 eV is transferred to the analyte molecule resulting in its ionization. However, since 10 eV or less is usually sufficient to cause ionization, the excess energy is used to fragment the molecular ion [3].

1.1.1.2 Chemical Ionization (CI)

In the CI technique, in contrast to EI, sample ionization is achieved via ion-molecule collisions instead of energetic electron-molecule collisions. CI is a lower energy process, compared to EI, therefore it induces less analyte fragmentation. During a CI experiment, a reagent gas present in the CI chamber is ionised via EI, which leads to the formation of ionization plasma through a series of ion-molecule reactions. Subsequent reactions between analyte molecules and this plasma leads to the ionization of the former [3]. Ionization occurs via different chemical reactions, including proton transfer from the reagent ion to the analyte molecule, hydride abstraction with the transfer of a hydride ion from the analyte molecule to the reagent gas, charge transfer from the reagent ion to the analyte molecule and adduct formation [3].

1.1.1.3 Field Ionization and Field Desorption (FI and FD)

FI uses strong electric fields to ionize gas-phase molecules. The electric field is created by a filament called the emitter and a counter-electrode held at a potential difference of 8–12 kV. As sample molecules approach the surface of the emitter, an electron is transferred to the emitter by quantum tunnelling resulting in the formation of a radical cation, which is then repelled by the emitter. Ions travel towards the negative counter-electrode and pass into the mass analyser through a hole located on counter-electrode's surface. Similar to EI and CI processes, FI can be used for the ionization of sufficiently volatile and thermally stable compounds. Due to the very low energy that is transferred to the analyte molecules, FI is a much softer ionization method compared to EI and CI. In reality, the energy is so low that only the molecular ion is generated. The main drawbacks for the FI are its very low ionization efficiency and that thermal decomposition of the analyte can occur prior its ionization [3].

Field desorption (FD) is an ionization method that is basically governed by the same principles as FI; in FD ionization is driven by the application of high electric fields [4]. However, in contrast to FI, in FD, evaporation of the analyte prior to ionization is not required. Instead, the analyte is deposited on a tungsten or rhenium filament covered with carbon microneedles. Contrary to FI, FD can be used in the analysis of thermally labile compounds. While the filament is kept under the influence of a high electric field of approximately 10^8 V cm^{-1}, is simultaneously heated by the application of a high current, causing the melting of the sample. At the tip of the microneedles, the ions are desorbed, carrying along molecules of the sample. The analyte molecules interact with the high electric field and they are ionised in a similar to FI mechanism being described above.

1.1.1.4 Fast Atom Bombardment (FAB)

FAB was introduce in 1981 by Barber *et al.* [5] and it became a popular technique mainly for its capability to ionise polar and higher molecular weight compounds such as peptides and nucleotides. In FAB the sample is mixed with a low volatility liquid matrix; the most often used liquid matrix is glycerol. Subsequently, the dissolved sample is "bombarded" under vacuum with a high energy beam of neutral atoms which is produced by the ionization of an inert gas, usually argon. A similar approach is used in liquid secondary-ion mass spectrometry (LSIMS) with the difference that the beam of neutral atoms is replaced by a beam of caesium (Cs^+) ions [6]. In both ionization methods the energetic particles (neutral atoms or ions) collide with analyte molecules in solution. Such a collision results in the formation of a shock wave which ejects ions and molecules present in solution. The resultant ions are accelerated towards the mass analyser by means of a potential difference.

1.1.1.5 Matrix Assisted Laser Desorption Ionization (MALDI)

Although the MALDI technique was introduced in 1988 [7, 8], the use of laser beams in the ionization of organic molecules, dates back to 1978, when Posthumus *et al* introduced the laser desorption ionization (LDI) technique [9]. In LDI method, ionization occurs by directly irradiating the sample with a laser beam. However, the levels of energy transferred to the analyte molecules is usually very high and result in extensive fragmentation. In contrast to LDI, during the MALDI process the analyte is deposited in a matrix containing small organic molecules. The mixture is then irradiated with intense short duration laser pulses. The exact mechanism of this desorption-ionization procedure is not fully understood [10-13]. Regarding desorption process, however, it is thought that the energy transferred by the laser beam to the matrix, results in the excitation of

matrix molecules. In turn, the excited molecules cause the rapid heating of the crystals, which leads to localized sublimation of the matrix crystals, ablation of the crystal surface and transfer of matrix particles containing the analyte to the gas-phase [14]. Moreover, the most widely accepted ionization mechanism involves proton transfer reactions either in the solid phase prior desorption or in the gas-phase [3]. The MALDI desorption ionization process is illustrated in Figure 1.1.2.

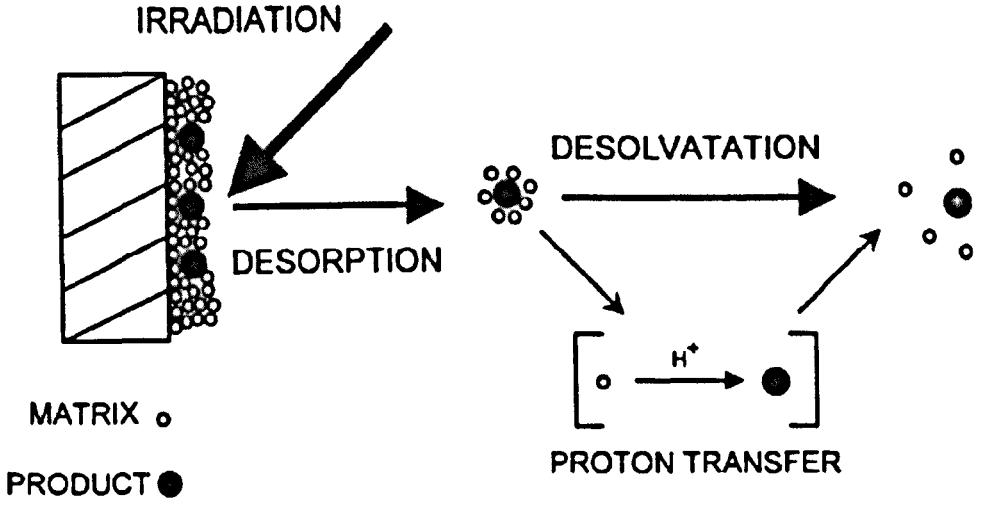

Figure 1.1.2 A diagram of the MALDI desorption ionization process. Adapted from reference [3].

1.1.2 Electrospray Ionization

Electrospray is the consequence of the application of electricity to an ion-containing liquid, which lead to its dispersion into a fine aerosol. ESI in turn, is a soft ionization technique that is very well known for its use in the analysis of large, non-volatile molecules such as biomolecules. The work of a number of researchers has successfully demonstrated the ability of ESI-MS to measure non-covalently bound protein assemblies, like the ribosome, a 2 MDa protein-RNA complex [15], the tetradecameric GroEL [16] and the 20S proteasome, a 690 kDa 28-mer [17]. The development of ESI in combination with instrumental

improvements (better sensitivity, resolving power and mass accuracy) has led to a revolution in biological mass spectrometry.

1.1.2.1 HISTORICAL ORIGINS

In 1882, Lord Rayleigh, published, *"On the Equilibrium of Liquid Conducting Masses charged with Electricity"*, which is the study that established the theories of charged droplets, balancing the forces of surface tension and coulomb repulsion to determine charged droplet stability [18]. The first experimental demonstrations of electrospray process were reported by John Zeleny, in 1916-1917 [19, 20]. His research on the electrified liquid surfaces became the first study that investigated the effects of the application of electric field on a liquid, and revealed that the electric field can cause droplet instability-disintegration, when it is applied to a conductive liquid. Fifty years later, in 1968, Malcolm Dole, published, *"Molecular beams of Macroions"*, which is the first study that demonstrates the usage of electrospray as a potential ionization source, for the ionization of large nonvolatile molecules [21]. However the breakthrough and the establishment of electrospray ionization, as a potential ion source for the analysis of biomolecules by mass spectrometry, started in 1989, when John Fenn, published *"Electrospray Ionization for Mass-Spectrometry of Large Biomolecules"* [22]. It was the first study that reported a successful combination of ESI and MS that was used for the analysis of biological macromolecules (Figure 1.1.3). The importance of Fenn's work was recognised with the award of the Nobel Prize in Chemistry in 2002 [23].

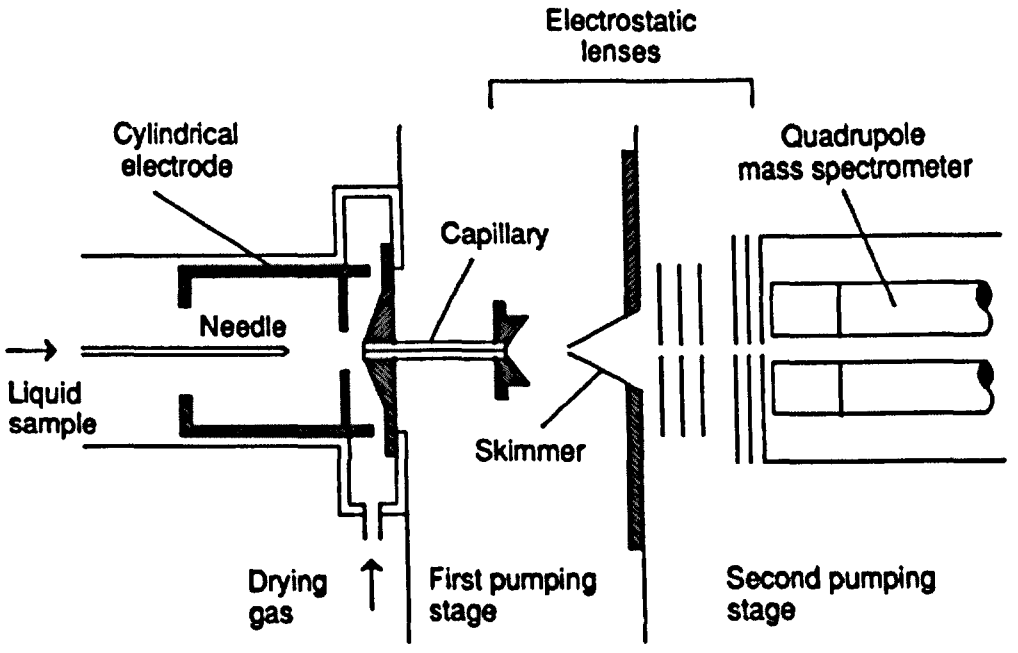

Figure 1.1.3 The electrospray ionization instrument used by Fenn, which was also coupled to liquid chromatography. Adapted from [22].

1.1.2.2 Formation of Gas-phase Ions in Electrospray Ionization

The sample liquid, which consists of the analyte of interest in a suitable solvent, passes through a needle at a rate of 1–20 $\mu l.min^{-1}$, which is held at a high potential of 3–4 kV. As the liquid reaches the open end of the needle it is exposed to a strong electric field ($\sim 10^6$ $V.m^{-1}$). This causes the expansion of the liquid into a Taylor cone [24] and the creation of a fine jet of liquid from its tip (Figure 1.1.4). The generated liquid jet is enriched in ions of a particular charge sign [25] (either positively or negatively charged, depending on the applied potential) (Figure 1.1.4). Two opposite forces govern the stability of these charged droplets forming the liquid jet. On one hand is the surface tension, which holds the droplets together and on the other hand is the coulomb repulsion (or electrostatic repulsion) due to like-charges at the surface. During the process, solvent evaporates from the droplets surface and as a result the charge density increases and thus the coulomb repulsion also increases.

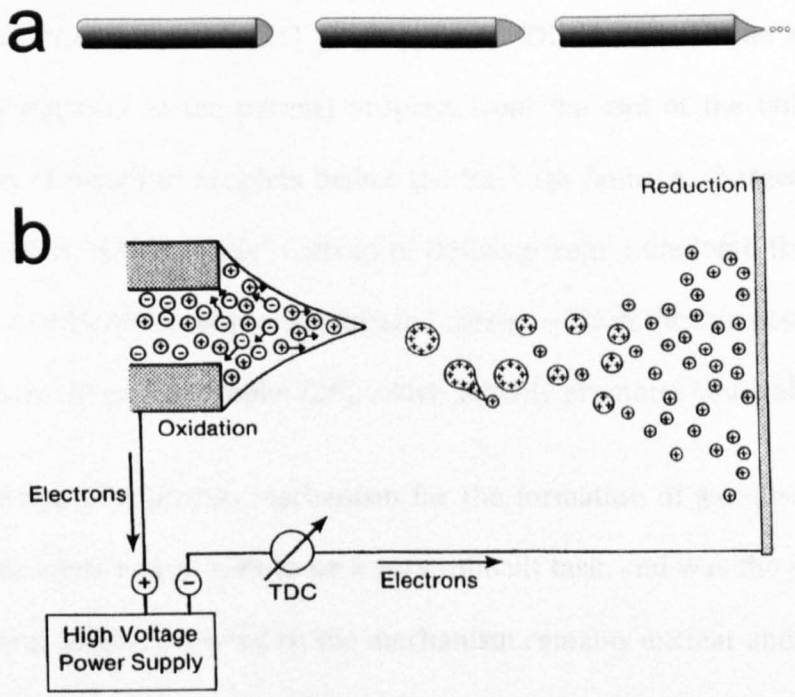

Figure 1.1.4 a) Effect of electrospray potential on the drop at the tip of the capillary as the voltage is increased from left to right. At the end the shape of the drop changes to a Taylor cone and small droplets are released. Adapted from reference [3]. b) Charge flow is maintained by an electrochemical oxidation reaction at the positive electrode in contact with the solution. Adapted from reference [25].

At the point, known as *Rayleigh limit,* where the coulomb repulsion overcomes surface tension, the fine liquid jet disperses into a fine spray of charged droplets, which are driven apart due to Coulomb repulsion.

The Rayleigh equation (Eq. 1.2) describes the relationship between the charge of the droplet (Q_{Ry}), droplet radius (R), surface tension (γ) and the electrical permittivity of the atmosphere (ε_0) under which the droplet is present.

$$Q_{Ry} = 8\pi(\varepsilon_0 \gamma R^3)^{1/2} \qquad \text{Equation 1.2}$$

Initially it was believed that at the Rayleigh limit, a Coulomb fission (or Coulomb explosion) was taking place, and the droplets were "exploding" continuously, until a fine spray of droplets was produced. Although this theory remains

partially correct, later work has revealed that the shape of the droplets is more like a "tail" than a sphere [26] (Figure 1.1.5). This results in the ejection of smaller (compared to the parent) droplets from the end of the tail, thus the generation of daughter droplets before the Rayleigh limit i.e. charged droplets, can also occur "mechanically" instead of deriving from a Coulomb fission. Each daughter droplet generated "mechanically" carries ~2% of the mass and ~15% of the charge of the parent droplet [26], which actually promotes coulomb fission.

The discovery of a precise mechanism for the formation of gas-phase ions by charged droplets had proven to be a very difficult task, and was the subject of a long-lasting debate. Even today, the mechanism remains unclear and the debate is still ongoing. Our current understanding is concentrated around two theories. The two prevailing models are the charged-residue model (CRM) and the ion evaporation model (IEM).

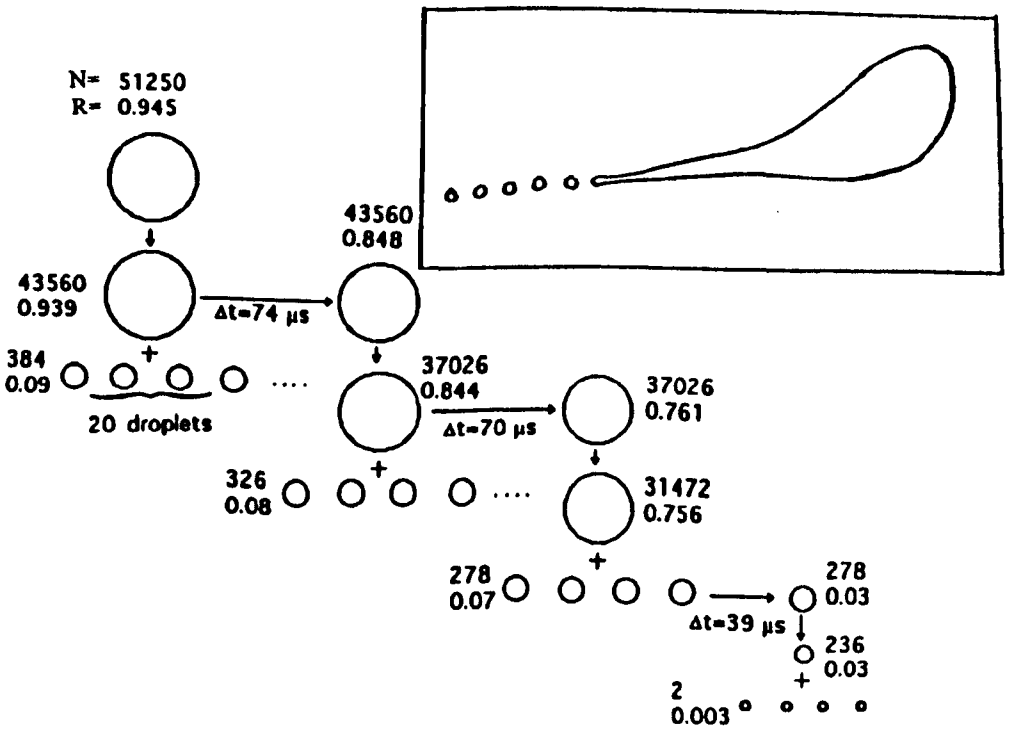

Figure 1.1.5 Droplet evolution scheme due to solvent evaporation at constant charge. Adapted from reference [25].

Charged-Residue Model (CRM) and Ion Evaporation Model (IEM)

The CRM theory was proposed by Dole during his work with electrospray. According to this theory, the charged droplets are entering in a Coulomb fission-reduction cycle until no further evaporation of the solvent can occur. At this point, each droplet contains only one analyte molecule, and the charges are transferred onto it [27]. Contrary, IEM theory [28, 29] suggests that charged analyte ions can directly evaporate from the charged droplets, when the size of the charged droplet reaches a certain radius R_E before reaching radius R_R (Figure 1.1.6).

The R_R is the radius at which the droplet becomes disrupted due to Rayleigh instability [18]. Figure 1.1.7 shows a simplistic diagram of CRM and IEM ion formation processes.

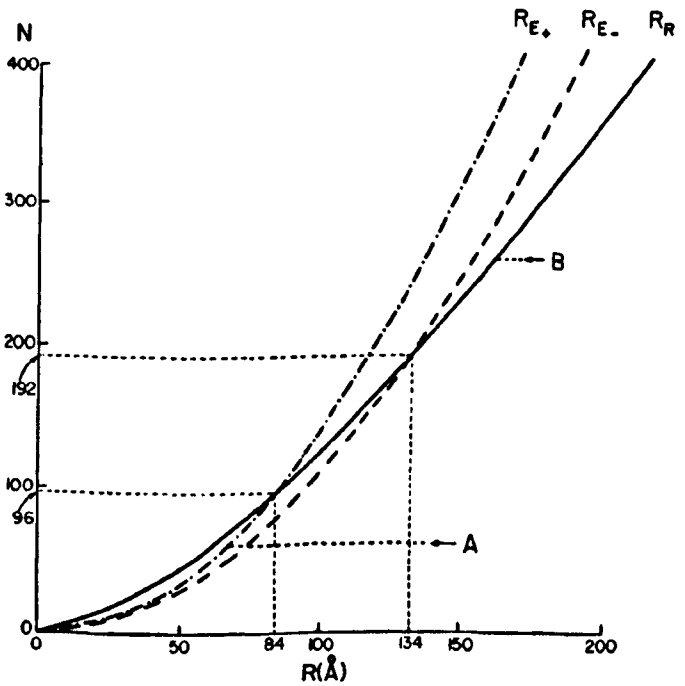

Figure 1.1.6 Critical droplet radius (R_{E+}; for large clusters, R_{E-}; for small clusters) and Rayleigh instability (R_R). N: the number of elementary charges in the drop; A: the evaporating drop reaches ion evaporation limit first; B: the evaporating drop reaches Rayleigh limit first and therefore is disrupted. Adapted from [28].

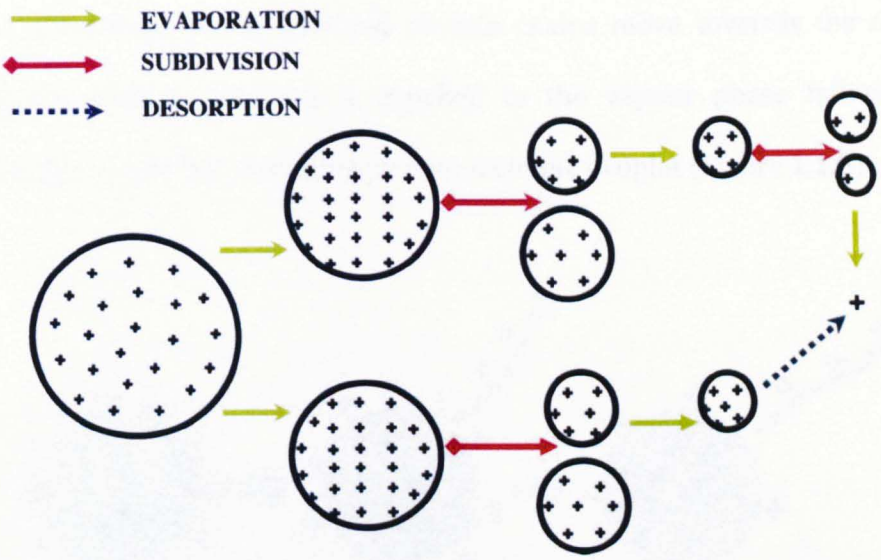

Figure 1.1.7 A simplistic diagram showing CRM (top) and IEM (bottom) ion formation processes. Adapted from reference [30].

Evidence for both, IEM [28, 30, 31] and CRM [32, 33] ion formation mechanisms, has been provided. These studies suggested that relatively small ions such as peptide ions are formed by ion evaporation, i.e. the IEM mechanism, whereas ionization of large molecules, such as proteins, most probably proceeds via the CRM pathway. A study from Fernadez de la Mora [33] has provided evidence that ionization of native globular proteins and naturally compact starburst dendrimers (with a mass greater than 3.3 kDa at least), follows the logic developed by Dole, i.e. CRM pathway. The same study has also suggested that relatively small ions, particularly small PEG (polyethylene glycols) ions, may be formed by ion evaporation.

Recently, Konermann and co-workers have suggested a different mechanism for the ESI process, referred to as the chain ejection model (CEM), which applies to unfolded proteins that are partially hydrophobic and also capable of accommodating excess charges [34]. According to the authors, when unfolded proteins are placed in a Rayleigh-charged nanodroplet, they immediately migrate to the droplet surface. This is attributed to the highly hydrophobic character of

disordered proteins, which makes it unfavourable to reside within the droplet interior. Therefore, as the unfolded protein chains move towards the droplet surface, the protein terminus is expelled to the vapour phase followed by stepwise ejection of the remaining protein from the droplet (Figure 1.1.8).

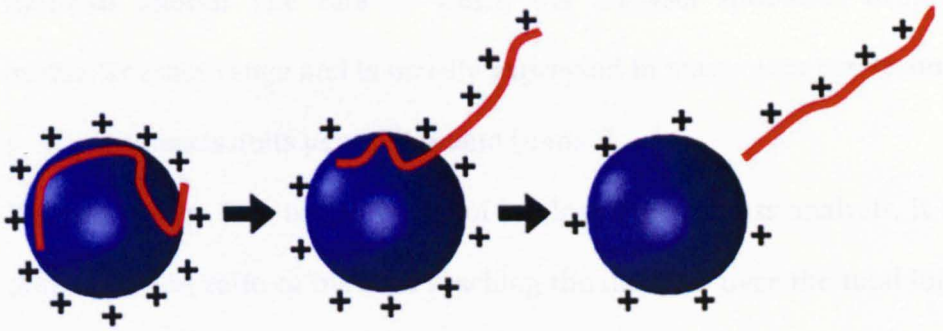

Figure 1.1.8 A simplistic diagram showing an unfolded protein (red) that separates from a charged nanodroplet (blue) during CEM. Reproduced (modified) from reference [34].

1.1.3 Mass analysers

The separation of the generated gas-phase analyte ions is based on their mass-to-charge ratio (m/z). The gas-phase ions can be analysed and separated using either fields (static, magnetic, dynamic or electric) or in a field free region as it is the case of Time-of-flight (TOF) mass spectrometer (although the reflectron—if used—provides a field). Several different types of mass analysers, which are based on different principles, have been developed (Table 1.1.1).

Table 1.1.1 Types of mass analysers

Type of analyser	Symbol	Principle of separation
Electric sector	E or ESA	Kinetic energy
Magnetic sector	B	Momentum
Quadrupole	Q	Trajectory stability
Ion Trap	IT	Resonance frequency
Time-of-flight	TOF	Velocity (flight time)
Fourier transform ion cyclotron resonance	FT-ICR	Resonance frequency
Fourier transform orbitrap	FT-OT	Resonance frequency

A mass analyser can be generally described by the following parameters, which are also used to demonstrate its performance.

a) **Mass range:** The *m/z* range over which the analyser can be used to separate and analyse gas-phase analyte ions.

b) **Analysis speed:** The rate at which the analyser measures over a particular mass range and is usually expressed in mass units per second ($u \cdot s^{-1}$) or in mass units per millisecond ($u \cdot ms^{-1}$).

c) **Transmission:** This is a measure of ion lose during mass analysis. It is defined as the ratio of the ions reaching the detector over the total ions entering the mass analyser.

d) **Mass accuracy:** It is given by the difference observed between the measured *m/z* ($m_{measured}$) and the theoretical mass *m/z* ($m_{theoretical}$) and it is often expressed in parts per million (ppm).

e) **Resolution/resolving power:** A parameter that is used to describe the ability of a mass analyser to differentiate signals deriving from two distinct ions with slightly different *m/z* values. The resolution R, of a mass analyser that is capable to resolve two peaks with masses *m* and $m+\Delta m$, is $R=m/\Delta m$. This definition requires the use of two peaks that are well resolved; for ICR and magnetic sector instruments, two peaks are considered to be resolved if the valley between them is 10 % of the weaker peak intensity; for other mass analysers the valley between two peaks has to be at least 50 %. Further to the above method, the estimation of resolution can be achieved by using the peak width Δm of an isolated peak with mass *m*. The peak width is measured at height *x* %, which is commonly be 50 %, which is known as FWHM (Full Width at Half Maximum).

1.1.3.1 QUADRUPOLE

The principles of quadrupole mass analyser was first described by Paul and Steinwedel in 1953 [35]. A quadrupole analyser consists of four cylindrically or ideally, hyperbolically shaped metal rod electrodes arranged parallel to each other, in a square configuration (Figure 1.1.9).

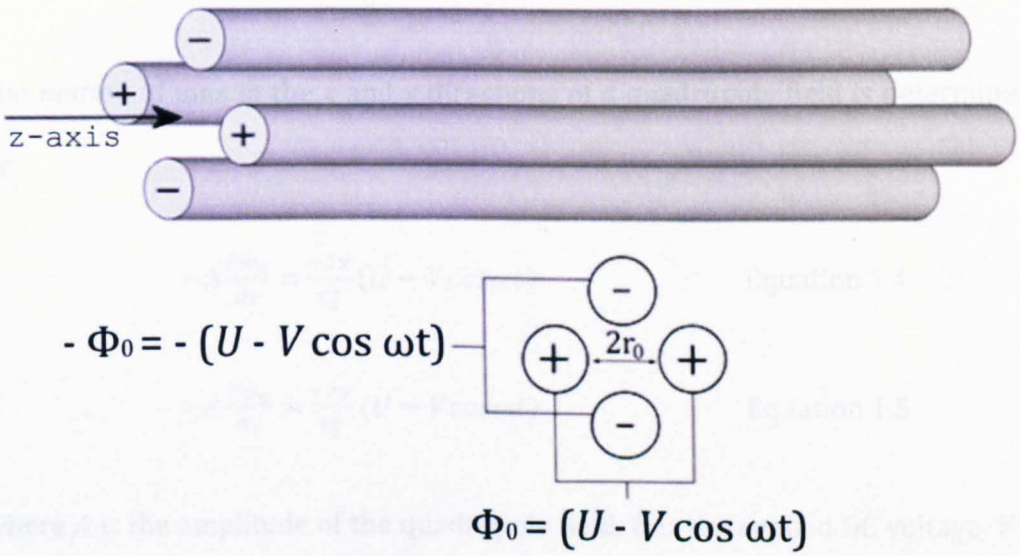

Figure 1.1.9 Top: Schematic representation of a quadrupole mass analyser. Bottom: Circuit diagram showing the four rods with alternative field applied by RF voltage ($V\ cos\ \omega t$), superposed on a constant field applied by DC voltage (U). Φ_0 represents the potential and ω is the angular frequency in radians per second $= 2\pi\nu$, where ν is the frequency of RF field.

Its operation is based upon the application of an oscillating electric field to the rods, which influences the stability of ion trajectories, resulting in separation of ions according to their m/z ratios. Ions are accelerated at the entrance of the quadrupole filter and travel along its z-axis. Their movement is influenced by an oscillating electric field which continuously forces ions towards the centre of the analyser.

The field is created by application of DC and RF voltages to the four electrodes and is applied along the x and y axes (2D field) of the mass analyzer (circuit diagram in Figure 1.1.9). Therefore, ions travel along a field free pathway (z-axis).

The 2D field quadrupole potential (Φ_0) is described by the following equation.

$$\Phi_0(x,y) = \frac{(x^2-y^2)}{r_0^2} \qquad \text{Equation 1.3}$$

The motion of ions in the x and y directions of a quadrupole field is determined by

$$-A\frac{\partial\Phi_0}{\partial x} = \frac{-2x}{r_0^2}(U - V cos\omega t) \qquad \text{Equation 1.4}$$

$$-A\frac{\partial\Phi_0}{\partial y} = \frac{+2y}{r_0^2}(U - V cos\omega t) \qquad \text{Equation 1.5}$$

where A is the amplitude of the quadrupole field, U is the applied DC voltage, V is the applied RF voltage and ω is the angular frequency of the RF ($\omega = 2\pi\nu$ where ν is frequency in Hz). Ions motion in quadrupole fields can be described by second-order Mathieu differential equations,

$$\frac{d^2x}{d\xi^2} + (a_x - 2q_x cos2\xi)x = 0 \qquad \text{Equation 1.6}$$

$$\frac{d^2y}{d\xi^2} + (a_y - 2q_y cos2\xi)y = 0 \qquad \text{Equation 1.7}$$

where the variables are a_x, a_y, q_x, q_y and ξ are given by:

$$a_x = -a_y = \frac{8zeU}{mr_0{}^2\omega^2} \qquad q_x = -q_y = \frac{4zeV}{mr_0{}^2\omega^2} \qquad \text{Equation 1.8 -1.9}$$

$$\xi = \frac{\omega t}{2} \qquad \text{Equation 1.10}$$

where e is the electronic charge, m is the mass, r_0 is the quadrupole radius [36]. Solutions of Mathieu equations can be classified as being either bounded solutions or unbounded solutions. A bounded solution corresponds to stable ion trajectory while unbounded solutions result in unstable ion trajectories. Figure 1.1.10 shows a stability diagram for a quadrupole mass analyser as a function of a_x and q_x variables.

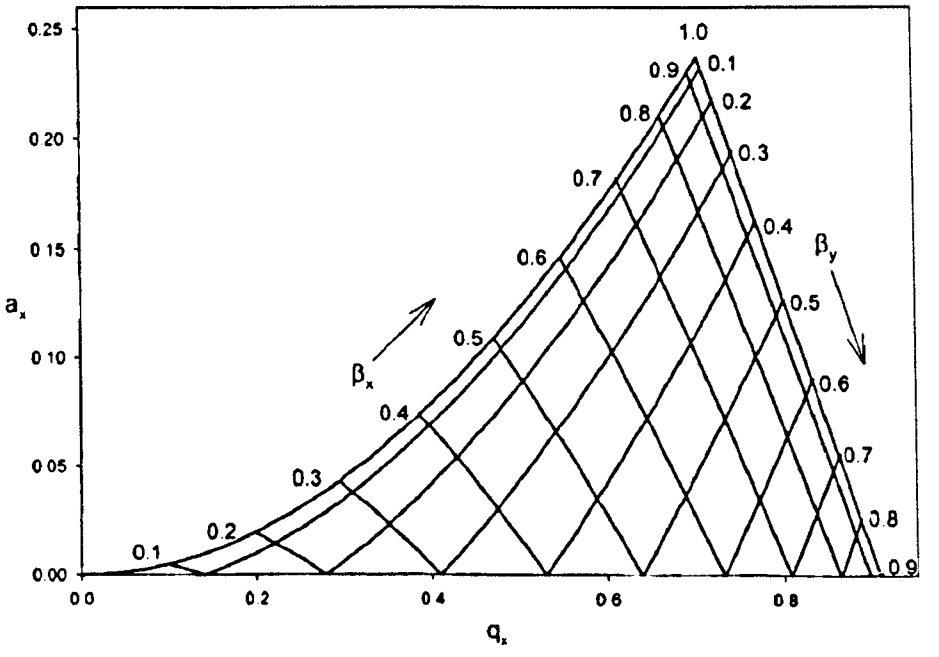

Figure 1.1.10 Stability region of a quadrupole mass filter as a function of a_x and q_x variables. β is a function of a and q. Taken from [36]

Considering the variables of Mathieu equation (a_x, a_y, q_x and q_y), we can deduce the following equations, where u is either x or y.

$$U = a_u \frac{m}{z} \frac{\omega^2 r_0^2}{8e} \qquad V = q_u \frac{m}{z} \frac{\omega^2 r_0^2}{4e} \qquad \text{Equations 1.11 - 1.12}$$

These equations describe the relationship of U and V parameters with m/z values. Figure 1.1.11 is a graphical representation of this relationship.

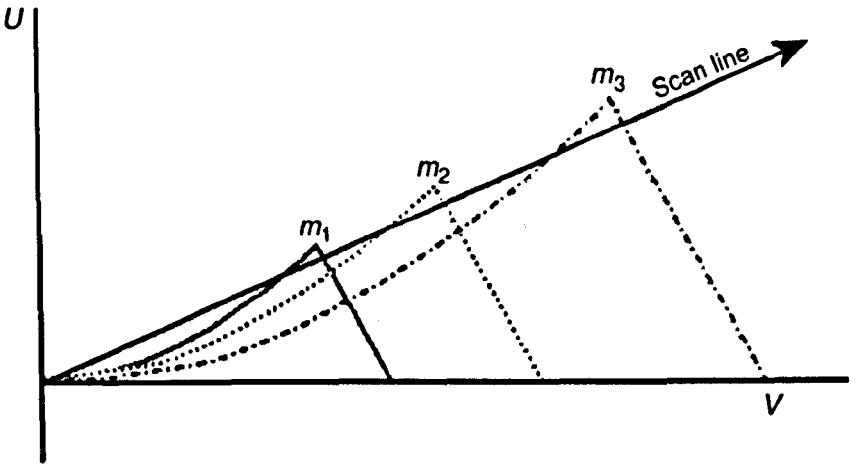

Figure 1.1.11 Stability diagram of a quadrupole mass filter as a function of *U* and *V* for ions with different masses ($m_1<m_2<m_3$). Reproduced (modified) from [3].

The scan line or operating line results from the linear change of *U* as a function of *V*. Ions of a given mass will possess a stable trajectory, as long as the scan line goes through their stability area (shaded). Therefore, a scan line with higher slope will result in higher resolution. Contrary, removal of DC voltage ($U = 0$), allows the transmission of all ions as long as the *V* value relies on their stability region.

1.1.3.2 Time Of Flight

The concept of an analyser that could discriminate ions based on their velocity in a field free environment, was first proposed by W. E. Stephens in 1946 [37]. Two years later, Cameron and Eggers published the design of a time-of-flight (TOF) mass spectrometer [38]. In 1955, Wiley and McLaren, have made significant improvements on the design of the TOF analyser [39]. Three years later, Bendix Corporation introduced the first commercial TOF mass spectrometer [40]. The principle that governs ion separation by a TOF analyser is quite simple; ions are separated on the basis of their velocity difference into a field free drift region (flight tube). Ions are accelerated by a source region that operates at high electric

field and all ions gain the same nominal kinetic energy, which is given by equation 1.16,

$$KE = zeV_{acc} = \frac{mv^2}{2} \qquad \text{Equation 1.16}$$

where z = the charge upon the ion, e = fundamental unit of charge (1.602×10^{-19} C), V_{acc} = accelerating voltage, m = mass of the ion and v = velocity of the ion. Consequently, the velocity of ions travel towards the detector, is given by

$$v = \left(\frac{2zeV_{acc}}{m}\right)^{1/2} \qquad \text{Equation 1.17}$$

It is clear from the above equations that the higher the mass of an ion the lower its velocity is within the field free drift region, and hence high mass ions will hit the detector later than low mass ions.

The time it takes for an ion to hit the detector plate that is located at the end of a flight tube of length L, is known as the flight time (t) and is given by

$$t = \frac{L}{v} \qquad \text{Equation 1.18}$$

Substituting v by equation 1.17, and rearranging, the following is obtained:

$$t^2 = \frac{m}{z}\left(\frac{L^2}{2eV_{acc}}\right) \qquad \text{Equation 1.19}$$

Solving the above equation for m/z, we obtain:

$$\frac{m}{z} = \left(\frac{2eV_{acc}}{L^2}\right)t^2 \qquad \text{Equation 1.20}$$

The above equation describes the operation principle of the linear TOF mass filters; m/z value of an ion can be determined by its flight time in a field free region.

When TOF analysers are compared to other mass filters, they demonstrate some key advantages, such as the theoretically unlimited mass range, high transmission efficiency, compatibility with pulsed ionization techniques and high sensitivity; detection limits of 100–200 amol quantities have been reported [41]. The performance of the early TOF designs, however, delivered very poor resolution. That was mainly attributed to variations of the initial kinetic energy of the ions of the same *m/z*, result in peak broadening and therefore poor resolution. The introduction of two main techniques, the delayed pulsed extraction [39] and the inclusion of an electrostatic reflector (reflectron), has substantially improved the resolving power of TOF analysers.

Delay pulse extraction

Delay pulse, originally known as time-lag focusing, is used to reduce kinetic energy spread of the ions. In delayed pulse extraction, the acceleration voltage is pulsed rather than continually applied. This introduces a delay between ion formation and ion extraction, which allows ions to expand into a field free region in the source. Ions of the same *m/z* ratio are distributed in the source region according to their kinetic energy; high energy ions move further towards the detector than lower energy ions which remain in the source for longer time. When the extraction pulse is applied, the less energetic ions, which have remained in the source for a longer time, receive more kinetic energy than the more energetic ions of the same *m/z* ratio. In this way, differences in initial kinetic energies are compensated and as a consequence ions of the same *m/z*, reach the detector in a narrow time distribution.

Reflectron

The electrostatic reflectror, known as reflectron, was originally proposed by Alikhanov, in 1957 [42] and was build a few years later, in 1973, by Mamyrin [43]. A reflectron is fundamentally an ion mirror, positioned after the field-free

region opposed to the ion source. It is usually consisted of a series of equally spaced, usually ring electrodes, which generate a retarding electric field that decelerates the ions and deflects them back into the flight tube. Ions with high kinetic energies penetrate further into the electrostatic field, thus they spend longer time in the reflectron than lower kinetic energy ions. Therefore, ions of the same *m/z* ratio with different kinetic energies, exhibit different flight paths–high energetic ions exhibit longer flight paths than low energetic ions–which compensates for any velocity differences between the ions (Figure 1.1.12). Thus, ions of the same *m/z* ratio, strike detector almost simultaneously, improving the resolving power of the analyser.

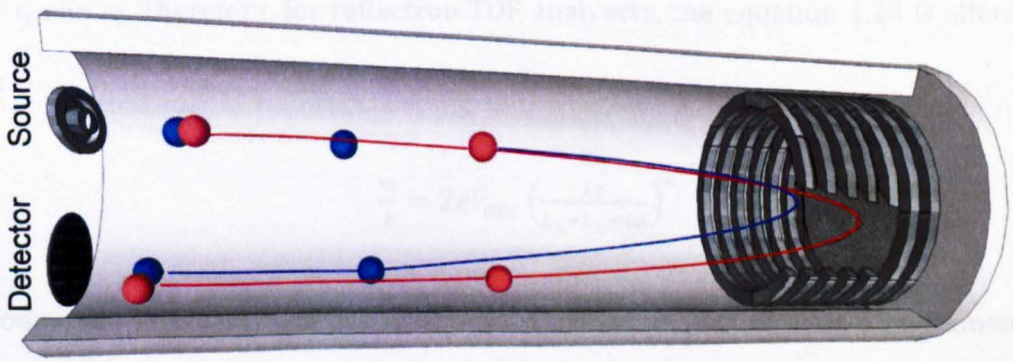

Figure 1.1.12 Schematic representation of a reflectron time-of-flight mass analyser; • = ions of a given mass with a given kinetic energy; • = ions of the same mass but with a lower kinetic energy. The former penetrate the field created by the reflectron more deeply and thereby have longer flight path than the slower (less energetic) ions. At the end both, fast and slow ions reach the detector at the same time.

Ions of a given *m/z* ratio and kinetic energy, will fly towards the reflectron with a constant velocity v_1 and will penetrate the electrostatic field at depth d before their velocity becomes zero (v_0). At this point the direction of movement will be reversed and the ions will be forced out of the reflectron towards the detector. Ions will enter the field free region with the same velocity (v_i). The mean velocity of ions within the reflectron is $v_i/2$, and total flight length inside the reflectron is

2d. Therefore, the total time inside the reflectron (t_R) is determined by equation 1.21.

$$t_R = \frac{4d}{v_i} \qquad \text{Equation 1.21}$$

If L_1 and L_2 are the distances from source to reflectron and reflectron to detector, respectively, then the total time in the field free region (t_F) is given by equation 1.22.

$$t_F = \frac{L_1+L_2}{v_i} \qquad \text{Equation 1.22}$$

The total flight time of ions in a reflectron TOF analyser (t_T), is given by the sum of t_F and t_R. Therefore, for reflectron TOF analysers, the equation 1.20 is altered to

$$\frac{m}{z} = 2eV_{acc}\left(\frac{t_T}{L_1+L_2+4d}\right)^2 \qquad \text{Equation 1.23}$$

Today, the TOF analysers are widely used, either as part of hybrid instruments (see section 1.1.3.4) or as single mass analysers, particularly in combination with MALDI or even ESI sources.

Orthogonal acceleration Time-of-Flight

Although the combination of a TOF analyser with a pulsed ionization technique, such as MALDI is directly compatible, their key advantages over the other mass analysers, has stimulated the development of techniques that allow the use of TOF analysers with continuous ion beam sources such as ESI. These involved the use of a narrow slit to sweep the ion beam and the use of pulsed ion extraction. Currently, the well established orthogonal acceleration technique is used with success to couple a TOF analyser with a continuous ionization source. A device, known as orthogonal accelerator is situated between the continuous ion beam

source and the TOF analyser. The ion accelerator operates in two phases; load stage at which the device is filled with ions and injection stage at which ions are transferred to the field-free region of the TOF analyser in a direction orthogonal to their original trajectory.

1.1.3.3 Fourier Transform Ion Cyclotron Resonance (FT-ICR)

The fundamental basis of the FT-ICR mass analyser relies on the circular motion of ions moving perpendicular to a homogeneous magnetic field [3]. The ions are injected into a cell, located in a magnetic field of 3 to 9.4 T that is produced by a superconducting magnet (Figure 1.1.13). Ions are trapped along the *z* axis, where the magnetic field is oriented, by a trapping voltage (typically 1 V) applied to the front and back plates. The ions are then excited by a RF pulse, which increases the radius of the ions spiral trajectories and induces an alternating current that can be detected and converted into a spectrum by the Fourier transform [44, 45].

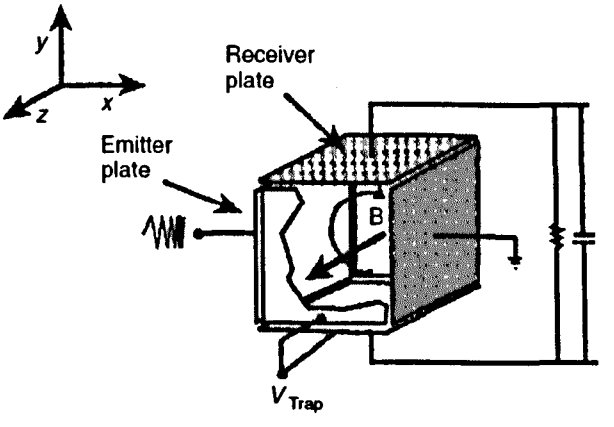

Figure 1.1.13 Diagram of an ICR cell.

1.1.3.4 Hybrid Instruments

Hybrid mass spectrometers have been developed, also. These instruments combine different types of mass analysers in a single configuration. One of the most common hybrid instruments is the quadrupole Time-of-flight (QTof), which consists of a quadrupole filter, a collision cell and a TOF analyser (Figure

1.1.14). The quadrupole can be operated in two modes; a) RF only mode allows all ions to pass through filter and analysed by the TOF analyser, thus full scan spectrum is recorder and b) resolving mode allows the selection of ions of a specific *m/z* ratio (precursor ions), which undergo fragmentation, usually due to collisional induced dissociation (CID), in the collision cell. Remaining precursor and its fragments are further separated and detected by the TOF analyser.

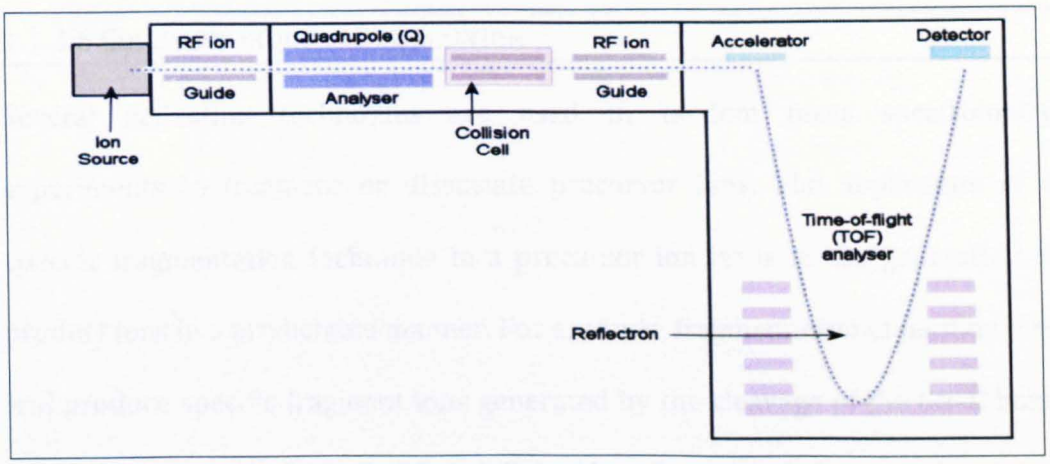

Figure 1.1.14 Diagram of a QTof instrument.

Another example of a hybrid instrument is the LTQ FT ULTRA by Thermo Scientific, which combines linear ion trap (LIT) analyser with fourier transfer–ion cyclotron resonance (FT–ICR) analyser.

1.1.3.5 Tandem Mass Spectrometry

Tandem mass spectrometry is a powerful technique used to gain structural information on a particular ionic species. The procedure involves at least two stages of mass analysis (MS/MS) that are linked by an intermediate stage which induces fragmentation of a preselected ion of a specific *m/z* ratio. When a tandem mass spectrometry experiment involves more than two stages it is usually referred as MS^n experiment, where *n* refers to the number of mass analysis steps been involved.

Tandem mass spectrometry experiments can be carried out in two ways: tandem analysis in space and tandem analysis in time. The former involves the coupling of two mass spectrometers, either of the same (e.g. triple quadrupole, QqQ) or different (e.g. QTof) type, in series. Tandem mass spectrometry in time can be performed using ion trap devices, such as LIT, quadrupole ion trap (QIT), orbitrap and ICR.

1.1.3.6 Collision-Induced Dissociation

Several activation techniques are used in tandem mass spectrometry experiments to fragment or dissociate precursor ions. The application of a specific fragmentation technique to a precursor ion leads to the generation of product ions in a predictable manner. For example, fragmentation of peptide ions will produce specific fragment ions generated by the cleavage of the Cα–C bond (a_n and x_n fragments), or C–N bond (b_n and y_n fragments) or N–Cα (c_n and z_n fragments) (Figure 1.1.15).

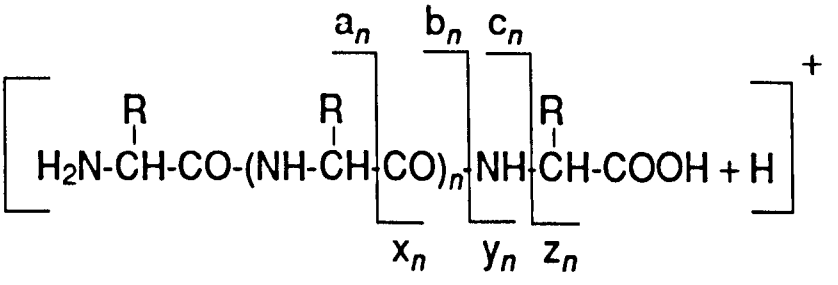

Figure 1.1.15 Main fragmentation paths of peptides in MS/MS

For example, electron transfer dissociation (ETD) and electron capture dissociation (ECD) generate c_n and z_n fragments, whereas collision-induced dissociation (CID) mainly creates b_n any y_n fragment ions.

The CID technique is based on the collisions of the precursor ion with neutral gas atoms (e.g N_2 or Ar) in a collision cell. During the collision, a part of the initial kinetic energy of ions, is converted into internal energy [46]. The maximum

amount of energy converted into internal energy from the collision in the centre of mass frame of reference (E_{cm}) is given in equation 1.24

$$E_{cm} = E_{lab}\frac{M_G}{M_I+M_G} \qquad \text{Equation 1.24}$$

where E_{lab} is the ion's kinetic energy, M_G is the mass of the buffer gas and M_I is the mass of the precursor ion [47]. CID experiments can be categorised as either low-energy or high-energy, with the barrier between these two categories defined as 100 eV. Generally, low energy CID favours facile bond cleavage resulting in a limited variety and quantity of product ions, whereas high energy CID induces significant fragmentation resulting to more complex spectra.

1.2 Ion Mobility – Mass Spectrometry

Ion mobility spectrometry (IMS) refers to the analytical technique that separates gas-phase ions based on their different mobility through a buffer gas at a (normally) uniformly applied electric field. In contrast to MS, IMS separates ions based on their charge and shape rather than their *m/z* ratio. The combination of IMS with MS, usually abbreviated as IM-MS, provides a platform capable of addressing a wide variety of analytical challenges. The complimentarily of these individual techniques affords 2D separation of analytes on the size-to-charge and mass-to-charge axes, respectively [48]. Relatively recent studies on highly complex mixtures have shown that IM-MS gives far greater resolution and information than is possible by either method alone [49, 50]. A particularly powerful application of IM-MS lies in its ability to size particles of defined *m/z* values through measurement of their collisional cross section (CCS) [48]. When it is combined with ESI, in particular, this technique may be utilised to study the

conformation of biomolecules in the gas-phase [51-56] with the potential to provide low resolution structural information [57, 58].

There is much debate on the structure of protein ions in gas-phase [59]. Whilst it appears probable that surface side-chain collapse occurs within picoseconds of dehydration, some elements of gross structural rearrangement may require milliseconds. Thus, there may be a window for the observation of species which are relatively similar to the solution structure.

1.2.1.1 Ion mobility

IMS is based on measurements of an ion's mobility in the gas-phase. The ions while passing through a 'drift tube', are accelerated by the applied static electric field and decelerated by the opposite flowing buffer gas (Figure 1.2.1).

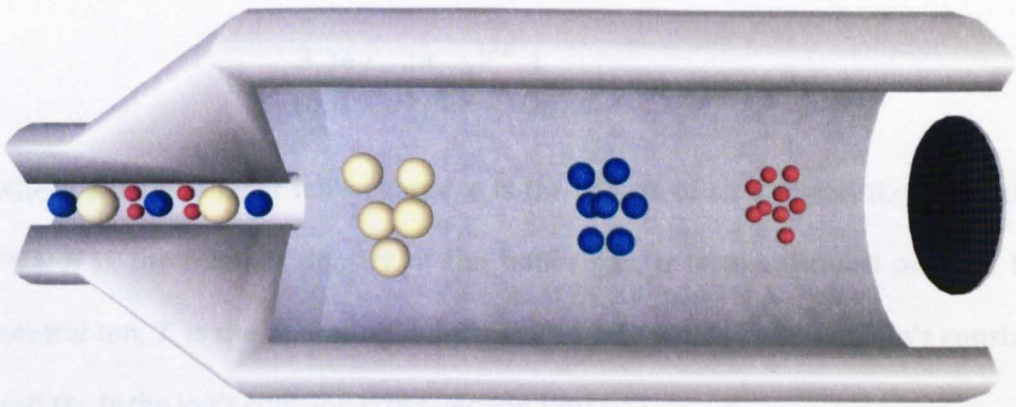

Figure 1.2.1 A simplistic image of an ion mobility spectrometer. Analytes with increased mobility move quicker through the drift tube.

Assuming the electric field is static and the pressure of the buffer gas is constant, the average 'drift velocity' (v_D) of an ion that travels through a 'drift tube', is dependent on the applied electric field (E) and its mobility (K) and it can be calculated by the following equation.

$$v_D = K.E \qquad \text{Equation 1.25}$$

In addition, the 'drift velocity' is given by:

$$v_D = \frac{L}{t_D} \qquad \text{Equation 1.26}$$

where L is length of the drift tube and t_D is the 'drift time' i.e. the time it takes an ion to pass through the 'drift tube'.

The ion's mobility at standard conditions (temperature and pressure) also known as reduced mobility, K_0, is given by the following equation:

$$K_0 = \frac{P}{760}\frac{273.2}{T}K \qquad \text{Equation 1.27}$$

where P is the operating pressure in Torr.

The mobility of an ion can also be calculated by following equation:

$$K_0 = \frac{3}{16}\frac{ze}{N}\left(\frac{2\pi}{\mu k_b T}\right)^{1/2}\frac{1}{\Omega_0} \qquad \text{Equation 1.28}$$

where z is the integer ion's charge, e is the charge of an electron (i.e. 1.602×10^{-19}C), N is the number density of the buffer gas, μ is the reduced mass of the neutral ion, T is the operating temperature in Kelvin, k_b is Boltzmann's constant and Ω_0 is the ion's collision cross-section [60].

The mobility of an ion depends on the number of collisions between that ion and the buffer gas. Larger collision cross-sections undergo more collisions with the buffer gas, thus their velocity is reduced and as a consequence the drift time is increased. For example, an unfolded protein ("open" form) has larger rotationally averaged collision cross-section compared to its folded form ("compact" form) and as a result higher drift time (assuming that both fold and unfold form, are equally charged).

Combining equations 1.27 and 1.28 and rearrange to solve for Ω:

$$\Omega = \frac{(18\pi)^{1/2}}{16}\frac{q}{(k_bT)^{1/2}}\left(\frac{1}{\mu}\right)^{1/2}\frac{1}{K}\frac{760}{P}\frac{T}{273.2}\frac{1}{N} \qquad \text{Equation 1.29}$$

But,

$$\left(\frac{1}{\mu}\right) = \left(\frac{1}{M_I} + \frac{1}{M_G}\right)$$

where, M_I and M_G are the masses of the neutral ion and buffer gas, respectively, and from equations 1.25 and 1.26,

$$K = \frac{L}{t_D E}$$

Thus, equation 1.29 can be re-written as,

$$\Omega = \frac{(18\pi)^{1/2}}{16}\frac{z\,e}{(k_bT)^{1/2}}\left(\frac{1}{M_I} + \frac{1}{M_G}\right)^{1/2}\frac{t_D E}{L}\frac{760}{P}\frac{T}{273.2}\frac{1}{N} \qquad \text{Equation 1.30}$$

Equation 1.30, gives the collision cross-section of an ion, which can be directly calculated from the measured drift times (t_D).

Clemmer's work [61], on the analysis of electrosprayed biomolecules by IM-MS in the late 90's, demonstrated that IM-MS can be applied to the analysis of biomolecules, and is especially beneficial for gas-phase conformational studies. Their studies played a central role in the development of the modern IM-MS instruments. For example, they showed that the usage of an ion trap in order to accumulate ions before entering the drift tubes, can increase the sensitive (in terms of *S/N* ratio) by factors of 10~30.

1.2.1.2 Travelling wave ion mobility spectrometry

A recently developed hybrid instrument, the Synapt HDMS by Waters (Figure 1.2.2), which is a quadrupole-IMS-TOF instrument, has introduced the use of a

travelling wave-enabled stacked ring ion guide [62] as an alternative to the classic drift tube IMS devices. In a TWIMS (travelling wave ion mobility spectrometry) device, the static gradient electric field (DC axial field) of the drift tube is replaced by high-speed travelling wave potential, which propagates along the drift tube at adjustable wave heights and velocities. The transmission of DC voltage in travelling waves is achieved with the application of RF voltage, of opposite phase, to the adjacent electrodes which produce a radial confinement for the transited DC voltage.

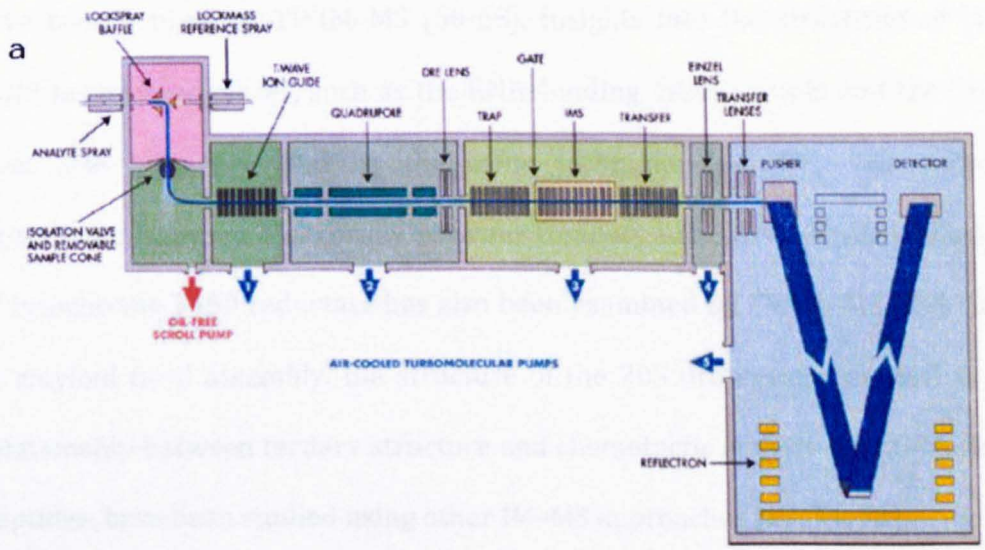

Figure 1.2.2 a) A schematic of the Waters Synapt HDMS. Adapted from reference [52].

A comparative study [63] has shown that the efficiency of mobility separation of protein ions by TWIMS is similar to that of static-field drift tube devices. In addition, as has been concluded from the same study, the usage of the TWIMS device, does not compromise mass spectrometers sensitivity when the instrument is running in mobility mode. However, the use of TWIMS device instead, of a conventional drift tube, comes at the cost that ion CCS cannot be directly measured from the arrival time of the ions. Instead it is necessary to calibrate the instrument using a series of protein or peptide calibrants [57, 64,

65] (see Chapter 2). A number of databases containing the CCSs of these calibrants are available; including those from the Clemmer group (http://www.indiana.edu/~clemmer) the Bush Lab (http://depts.washington.edu/bushlab) and the McLean group (http://www.vanderbilt.edu/AnS/Chemistry/groups/mcleanlab/ccs.html).

Several recent applications have successfully demonstrated the ability of IM-MS, including TWIM-MS, to study the conformation and stoichiometry of proteins and their complexes. For example, structural changes to amyloid and prion proteins, as well as the calcium-dependent conformational change in calmodulin have been probed by TWIM-MS [66-68]. Insights into the structures of large multi-protein complexes, such as the RNA-binding TRAP protein and the GroEL have also been provided by the same technique [64, 69]. The dynamic equilibrium between biologically-relevant compact and extended conformations of cytochrome P450 reductase has also been examined by TWIM-MS [70]. Steps in amyloid fibril assembly, the structure of the 20S proteasome as well as the relationship between tertiary structure and chemotactic activity in anti-bacterial peptides, have been studied using other IM-MS approaches [17, 71, 72].

1.2.1.3 Theoretical Collision Cross Section Calculation

Computational methods allowing the calculation of CCS from atomic coordinates derived from NMR spectroscopy, X-ray crystallography and molecular dynamics simulations are employed to evaluate the experimentally measured CCS obtained by IMS or IM-MS (including TWIM-MS) experiments. This can provide useful information about the maintenance or modification of the protein conformation upon transfer to the gas-phase [73]. In addition, in cases where the conformation of a protein or a protein assembly is unknown, combination of experimentally derived CCS data with those obtained by molecular modelling and/or molecular

dynamics simulations can provide a good prediction of the real structure or conformation.

Three different algorithms are commonly used to calculate the theoretical CCS of a molecule; the projection approximation (PA), the trajectory method (TM) and the exact hard sphere scattering (EHSS). The PA approach averages the geometric projection areas over all possible orientations and measures the CCS of this averaged shape. The EHSS method treats the protein and the buffer gas as hard spheres, and calculates the scattering angles of the buffer gas upon collision [74, 75]. The TM model is considered to be the most realistic model for the theoretical calculation of protein CCS values. This approach simulates the collisions between the analyte molecule and the gas particle as a Lenard-Jones potential; this also accounts the contribution of multiple collisions and long range interactions in the CCS calculation.

1.3 Concepts of Protein Structure and Function

1.3.1 Structure and Function of Proteins

Proteins or peptides are built by the assembly of small organic molecules, called amino acids. There are 20 proteinogenic amino acids, which are usually considered *natural* or *canonical*, since these correspond to 61 out of a total of 64 codons within the triplet code. Figure 1.3.1 shows a general amino acid structure. Amino acids are amphoteric organic molecules, therefore they can either be positively charged (protonated) or negatively charged (deprotonated), or they can exhibit a zwitterion structure (Figure 1.3.2). Each amino acid is characterized by a unique *R* functional group -hydrogen in case of glycine (Gly)- that is attached to the α-carbon, and it is commonly referred as the *side chain*. With the

exception of Gly, all the amino acids are optically activity, however, only the L-stereoisomer participates in the construction of polypeptide chains assembled by the ribosome. Moreover, the nature of the side chain, affects the electronic properties of the residue, which allows the classification of the 20 amino acids into four categories; basic residues, acidic residues, polar residues and non-polar residues (Table 1.3.1). The following subsections are dealing briefly with the important role of side chains in the construction of biologically functional protein structures.

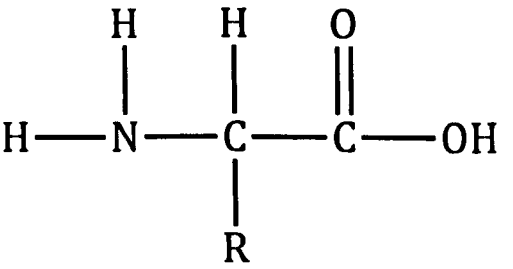

Figure 1.3.1 Generalised structure of amino acids. R represents the side chain.

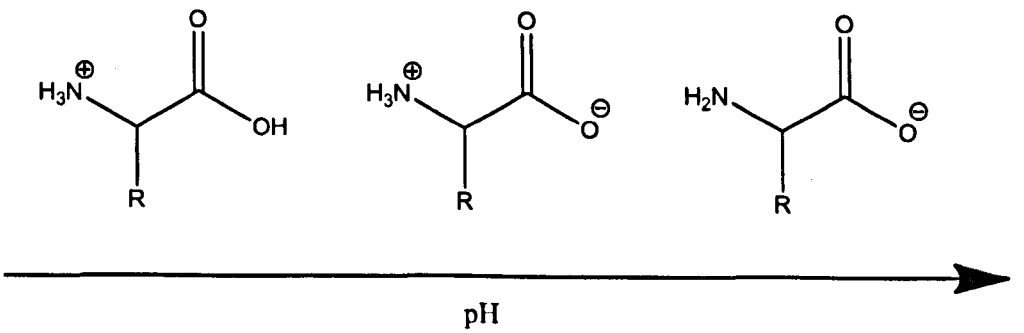

Figure 1.3.2 The amphoteric character of amino acids.

Table 1.3.1 The twenty amino acids

Special cases	Glycine Gly, G	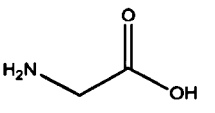	Special cases	Proline Pro, P	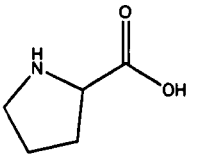
	Cysteine Cys, C	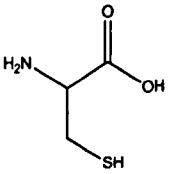			
	Residue name	Side chain		Residue name	Side chain
Basic	Arginine Arg, R	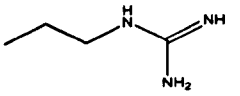	Non-polar	Alanine Ala, A	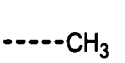
	Histidine His, H	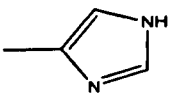		Valine Val, V	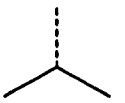
	Lysine Lys, K	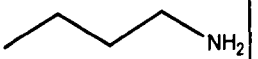		Isoleucine Ile, I	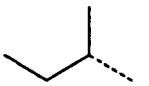
Acidic	Aspartic acid Asp, D	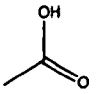		Leucine Leu, L	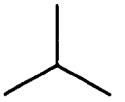
	Glutamic acid Glu, E	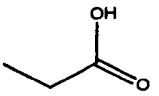		Methionine Met, M	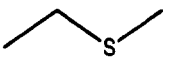
Polar	Serine Ser, S	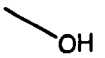		Phenylalanine Phe, F	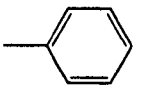
	Threonine Thr, T	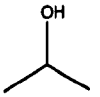		Tyrosine Tyr, Y	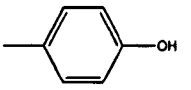
	Asparagine Asn, N	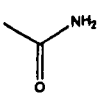		Tryptophan Trp, W	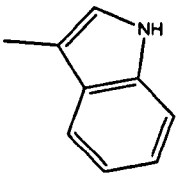
	Glutamine Gln,	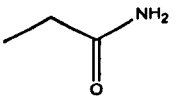			

1.3.1.1 LEVELS OF PROTEIN STRUCTURE

There are four structure levels involved in protein architecture:

a) The *primary structure* refers to the linear sequence of the covalently attached amino acids in a protein. Each protein is characterized by a unique amino acid sequence, which can also define its structure. In addition, PTMs as phosphorylation, glycosylation and formation of disulfide bonds are also considered a part of the primary structure.

b) The *secondary structure* refers to structural motifs occurring within the protein structure. These motifs are mediated by intermolecular and intramolecular hydrogen bonding of amide groups. For example, the α-helix is a common secondary structure motif that is stabilized by hydrogen bonds formed between the backbone N-H group of one residue with the backbone C=O group of the fourth residue away from it (Figure 1.3.3a). Another example, is the β-sheet which is stabilized by hydrogen bonds between N-H and C=O groups of adjacent antiparallel molecules (Figure 1.3.3b).

c) The *tertiary structure* is the three-dimensional arrangement of all the amino acids that are included in a single polypeptide chain. Its stability is determined by non-covalent interactions, including hydrogen bonding, dispersion forces and salt bridges as well as by the entropic driving force, known as the *hydrophobic effect.*

d) The *quaternary structure* refers to the three-dimensional structure of a biomolecular entity that consists of more than one polypeptide chain, and/or the addition of small molecule ligands. For example, the biologically active structure of haemoglobin, exhibits a quaternary structure since is consisted of 4 polypeptides chains and 4 iron-

containing heme groups (Figure 1.3.4). The establishment of quaternary structures is driven by non-covalent forces similar to those stated above for the determination of the tertiary structure.

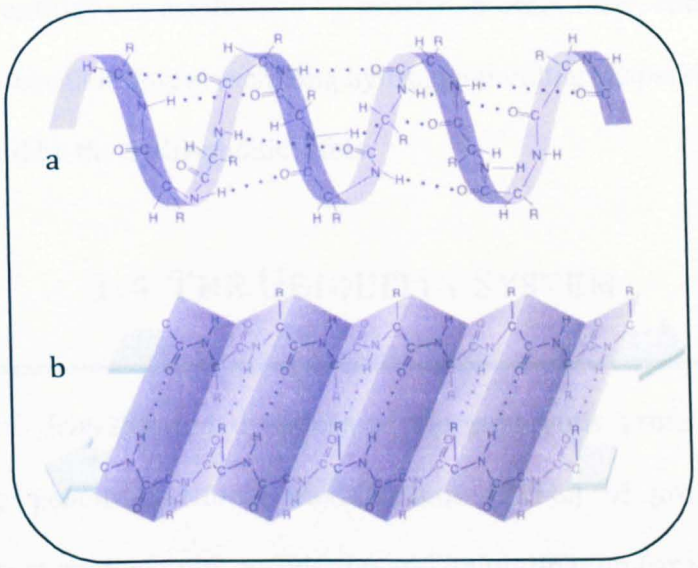

Figure 1.3.3 Two of the most commonly occurring secondary structures, (a) the a-helix and (b) the anti-parallel b-sheet. Hydrogen bonds are represented by the dotted lines. Figure adapted from *http://www.mun.ca/biology/scarr/MGA2_03-18b.html*

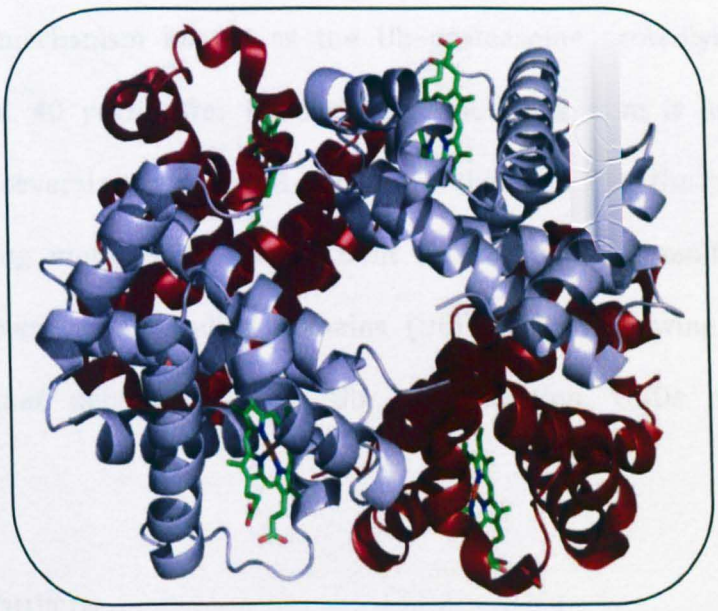

Figure 1.3.4 The quaternary structure of haemoglobin showing the two alpha (light blue) and two beta (red) chains as well as the four heme groups (green). From PDB ID: 1GZX.

1.3.2 Protein–Protein Interactions

Several vital cellular processes including, proteolysis, DNA repair, DNA replication and protein folding are carried out by large protein complexes. These biomolecular entities are established by protein-protein interactions, which are driven by non-covalent forces including hydrogen bonding, dispersion forces and salt bridges and by the hydrophobic effect.

1.4 The Ubiquitin System

The functional diversity and dynamics of the eukaryotic proteome is mainly attributed to post-translational modifications (PTMs) of proteins such as phosphorylation, methylation, acetylation and ubiquitination (or ubiquitylation). The first three modifications involve a small chemical group (phosphate, methyl and acetyl group, respectively) whereas the latter entails the conjugation of a small protein, namely Ub (Ub) to a target protein. This conjugation was initially recognized as the trigger for proteasomal protein degradation; a protein degradation mechanism known as the Ub–proteasome proteolytic pathway. Today, almost 40 years after its discovery, the Ub system is known to be implicated in several pathways. It is also known that, crucial to the function of Ub as a signalling motif is its non-covalent association with modular protein domains known as Ub-binding domains (UBDs). The following subsections provide further details regarding Ub, ubiquitination, UBDs and Ub•UBD interactions.

1.4.1 Ubiquitin

Ub is a 76-residue protein (~ 8.5 kDa) that is ubiquitously expressed in eukaryotic organisms and is highly conserved among the Eukaryota. Its

secondary structure is defined by a 3.5–turn α–helix, a 3_{10} helix and a 5–stranded β–sheet (Figure 1.4.1a). The human and yeast Ub share 96% sequence homology, with 73 out of 76 amino acids are located at the same position [76] leading to the conclusion that the primary structure and thus the secondary structure of Ub, is essential for its biological functionality. Key features of Ub include its C–terminal and the seven lysine (Lys) residues, located at positions 6, 11, 27, 29, 33, 48 and 63, which permit the formation of poly-Ub chains, both homotypic and heterotypic [77]. As we will see later on, Ub's ability to utilize any one of the seven Lys residues in order to form poly-Ub chains of specific topology and length is critical for its vital role as a signalling motif. Furthermore, three regions located on Ub's surface; the hydrophobic patch around Ile44, the polar patch Asp58 and the C-terminal Gly76 residue (Figure 1.4.1b), are known to promote the non-covalent interaction of Ub or ubiquitinated substrates with Ub receptor proteins i.e. biomolecular assemblies that recognize and process Ub signals.

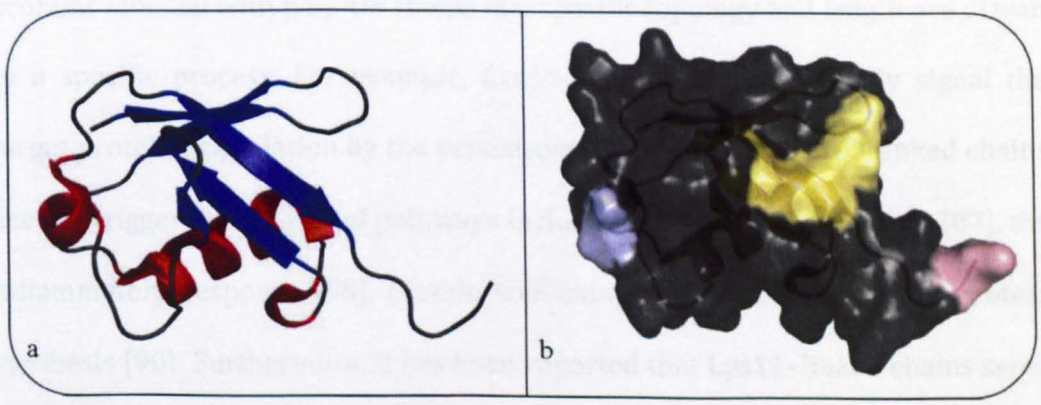

Figure 1.4.1 a) The secondary structure of Ub is defined by a 3.5-turn α-helix, a 3_{10} helix and a 5-stranded β-sheet, b) Surface representation of Ub showing the Ile44 hydrophobic patch (yellow), the polar patch Asp58 (light blue) and the C-terminal Gly76 residue (pink). PDB ID: 1D3Z

1.4.2 UBIQUITINATION

The Ub conjugation pathway—ubiquitination—is a fundamental regulatory mechanism involved in several eukaryotic cellular processes. Protein degradation [78], vesicular trafficking [79], DNA repair [80], endocytosis [81], transcription and gene silencing [82] are all regulated by this important PTM. It is catalysed by a triplet of enzymes,—E1, E2, E3—and leads to the formation of an isopeptide bond between the C-terminal glycine carboxyl group of Ub and, usually, a Lys residue in the target protein (more details regarding the mechanism are given below). The attachment of Ub to a target protein through substrate's N-terminus has been reported [83], as well as though the thiol group of cysteine (formation of thioester bond) [84] and the hydroxyl group of serine or threonine residues [85]. Repetition of the ubiquitination cycle leads to the formation of poly-Ub chains by utilizing any one of the seven Lys residues of the Ub monomer, as well as Ub's N-terminus. Clear evidence is emerging that proteins labelled with poly-Ub chains of a specific topology and length are driven to a specific process. For example, Lys48-linked chains classically signal the target protein degradation by the proteasome [86], whereas Lys63-linked chains act as a trigger in a variety of pathways including DNA damage tolerance [87], the inflammatory response [88], protein trafficking [89] and regulation of protein synthesis [90]. Furthermore, it has been reported that Lys11-linked chains serve as potent proteasomal degradation signals [91]. Studies on the BRCA1•BARD1 complex, have shown that Lys6-linked poly-Ub chains are likely to be involved in DNA repair [92, 93].

1.4.2.1 THE UBIQUITINATION CYCLE

The ubiquitination cycle starts with the activation of the C-terminus of Ub by E1 activating enzyme. This ATP dependent step forms a Ub-adenylate intermediate

i.e. a Ub–AMP adduct is bound to the E1 enzyme, which finally results in the formation of a thioester between a side chain of a cysteine (Cys) residue of E1 enzyme and the C–terminus of Ub. The activated Ub moiety is then attached to a Cys residue of an E2 conjugating enzyme, and finally transferred to an amino group (usually ε–amino group of a Lys residue) of the substrate through the E3 Ub protein ligase enzyme. Furthermore, the ligation of Ub to the target protein can be catalysed via two pathways, dependent on the type of the E3 enzyme that participates. There are two types of E3 ligases: The HECT-domain E3s form a thioester bond with Ub before substrate attachment. In contrast, the RING-domain E3s, instead of a straight interaction with Ub, they function as a bridge between an activated E2 and the substrate [94] (Figure 1.4.2).

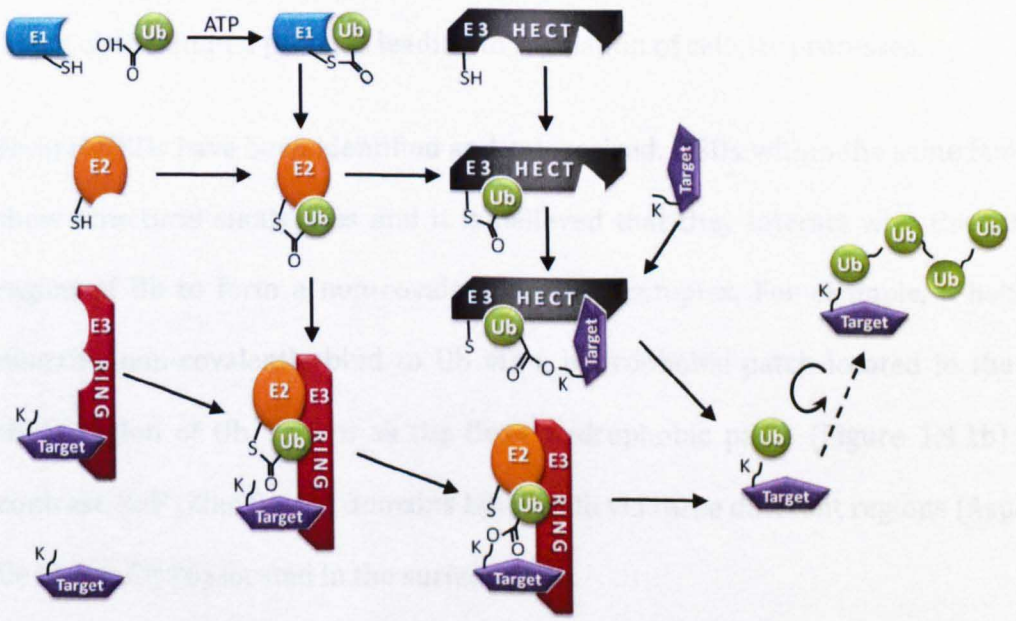

Figure 1.4.2 Major enzymatic pathways of protein ubiquitination

To date, only two E1 Ub activating enzymes have been discovered in the human proteome, in contrast to 50 E2 activating enzymes and 600 E3 ligase enzymes [95]. This hierarchical distribution of the Ubiquitination enzymes leads to the existence of a large number of possible enzyme combinations (E1/E2/E3) that

are able to carry out the ubiquitination mechanism, which results in high substrate specificity.

1.4.3 Ubiquitin Binding Domains

UBDs are modular protein domains that associate with Ub through non-covalent interactions. These motifs are found in proteins—Ub receptor proteins—which execute disparate biological functions, for example UBDs are present in the degradation machinery proteasome 26S and in the endocytic machinery EPS15. In addition, UBDs are present in ubiquitination enzymes, for example, in the E2 or Ub-conjugating enzyme (Ubc) [82, 96]. Therefore, this non-covalent interaction may promote covalent Ub attachment (ubiquitination) and thus the formation of poly-Ub chains of specific length and topology, as well as direct the fate of ubiquitinated proteins leading to regulation of cellular processes.

Several UBDs have been identified and categorized. UBDs within the same family show structural similarities and it is believed that they interact with the same region of Ub to form a non-covalent Ub•UBD complex. For example, α-helical domains non-covalently bind to Ub via a hydrophobic patch located in the β-sheet region of Ub, known as the Ile44 hydrophobic patch (Figure 1.4.1b). In contrast, ZnF (Zinc finger) domains bind to Ub via three different regions (Asp58, Ile44 and Gly76) located in the surface of Ub.

The binding affinities between Ub and UBDs are moderate to weak (Table 1.4.1). There is a range of binding affinities against mono-Ub and poly-Ub chains (in terms of length and topology) within the same family of UBDs (Table 1.4.1). However, the binding affinity and as a consequence the Ub-type preferred by an isolated UBD, might differ from that preferred by the UBD-containing protein due to steric interactions, for example.

Table 1.4.1 Binding affinities of monoUb•UBD complexes

UBD	Source Protein	Binding affinity		Function	Ref.
		K_d (μM)	Method*		
α-Helix					
MIU	Rabex-5	29±4.8	SPR	Endocytocis	[97]
		28.7	ITC		[98]
DUIM	Hrs	190	SPR	MVB biogenesis	[99]
UBA	HHR23A	400±100	NMR	Proteasome targeting, kinase regulation and autophagy	[100, 101]
UQ1	Ubiquilin-1	20±5	NMR		[102]]
Ub-conjugating (Ubc) domains					
UEV	Tsg101	510±35	SPR	DNA repair. MVB biogenesis and kinase regulation	[103]]
UBC	UBCH5C	300	NMR	Ub transfer	[104]]
Zinc finger (ZnF)					
NZF	Npl4	126±26	SPR	ERAD, MVB biogenesis and kinase regulation	[105]
A20 ZnF	Rabex-5	22±0.4	SPR	Endocytocis and kinase	[97]
		12	ITC	regulation	[98]
ZnF UBP	Isopeptidase T	2.8	ITC	Proteasome function, aggresome function and autophagy	[106]

* NMR: Nuclear Magnetic Resonance

SPR: Surface Plasmon Resonance

CD: Circular Dichroism

ITC: Isothermal Titration Calorimetry

1.4.3.1 Helical Domains

Most of the identified UBDs are members of the α-helical UBD family which interact with Ub via the Ile44 hydrophobic patch located on the surface of Ub. These domains can be further grouped into two subcategories, a) the single α-helix domains which bind Ub through a single α-helix and b) the three-helix

bundles which bind Ub through two of the three α-helices. For example, the UBA (Ub associated) domain of the human homologue Rad23A (hHR23A) is a three-helix bundle and binds to Ub through a conserved hydrophobic patch formed by α1 and α2 helices [107]. To date, only three single α-helix domains have been reported: UIM (Ub Interacting Motif), DUIM (Double-sided Ub Interacting Motif) and MIU (Motif Interacting Ub). In contrast, several three-helix bundles have been identified and some of the most common UBDs are listed in Table 1.4.1.

Single α-helix domains: UIM and its variants MIU and DUIM

UIM was the first single α-helix domain described[108]. It is found in many trafficking proteins such as the S5a subunit of the proteasome, the vacuolar protein sorting proteins including Hrs (yeast Vps27p) and the Stam1 (yeast Hse1), as well as the endocytic proteins Eps15 and Eps15R which are essential for endocytosis of receptors like the ligand complex of the epidermal growth factor (EGF) with its receptor (EGFR) [109].

MIU, a variant of UIM, it is presented only in the endosomal trafficking regulator Rab5 exchange factor Rabex-5, which contains another UBD, the A20 ZnF domain. Like UIM, MIU bind Ub via the Ile44 hydrophobic patch but with the single helix in inverted orientation against Ub's surface i.e. the C-terminus of UIM domain corresponds to the N-terminus of MIU domain. This inversion, however, allows MIU to interact with Ub more extensively compared to UIM, creating extra hydrogen bonds with the Lys63 region of Ub [97].

The last member of the single α-helix subfamily is DUIM which is found in the hepatocyte growth factor-regulated tyrosine kinase substrate (Hrs) protein that is essential for the endosomal sorting of ubiquitinated membrane proteins. For example, Hrs is needed for the sorting of the amino-terminal cytoplasmic domain of human transferin receptor (TfR) from endosomes to lysosomes for

degradation [99]. The DUIM domain is an alternative to a double repeat of UIM domain (Ub Interacting Motif) that is able to bind two Ub moieties simultaneously (one moiety in each side). It has been reported that this double-sided binding capability is essential for the degradation of the epidermal growth factor (EGF) receptor [81, 99].

Three-helix bundles

The Ub associated (UBA) domain was the first Ub binding domain described. It was discovered in a bioinformatic analysis of the enzymes involve in the ubiquitination pathway. It was found that a small motif about ~55 residues long, with a conserved number of nonpolar residues (which is stabilizing its structure) was present in E2 and E3 and UBPs (Ub carboxyl-terminal hydrolases) families as well as in Ub-like (UBL) domains[110]. The UBA-containing proteins as well as the UBA-UBL proteins are involved in the transfer of polyubiquitinated substrates (Lys48-linked) to proteasome[78, 111], in DNA excision-repair [107] and cell signalling via protein kinases.

An example of a UBA-containing protein is the human homologue of yeast Rad23A (hHR23A) which is involved in DNA-repair [107] and in proteasome proteolytic pathway [112], and contains two UBA domains, one internal (UBA1) and one at the C-terminus (UBA2). Both domains fold into similar three-helix bundles that are stabilised by hydrophobic interactions. In addition, both domains have a hydrophobic surface patch which is believed to mediate binding to Ub by interacting with Ub's hydrophobic surface patch Ile44 [113]. Studies reveal that the UBA2 domain shows strong binding preference for Lys48-linked poly-Ub chains [100].

The presenilin-interacting protein [114, 115], human ubiquillin-1 (UQ1 or hPLIC1), is an example of a UBL-UBA protein which is consisted of an N-terminal

UBL and a C-terminal UBA domain. The UBA domain of UQ1 (UQ1-UBA) forms a three-helix bundle and bind mono-Ub via the hydrophobic surface of Ub Ile44 with a relatively high affinity (K_d~20μM) compared to other UBA domains [102]. In addition, the same study showed that in contrast to the UBA2 domain of hHR23A, the UQ1-UBA domain has no selectivity against Lys48 and Lys63 chains, but in general it binds more strongly to poly-Ub chains than mono-Ub [102].

1.4.3.2 Zinc Finger Domains

Zinc finger (ZnF) domains represent the second largest family of UBDs. ZnFs are categorised in three classes; the NZF, the A20 ZnF and the ZnF UBP domains. In contrast to helical domains, ZnF bind to Ub via three different regions located on Ub's surface. For example, while the A20-type ZnF domain of RAB5 guanine nucleotide exchange factor (RABEX5) bind to Ub via the polar surface of Ub around Asp58, two other members of the ZnF family, the nuclear protein localization 4 ZnF (NZF) domain and the Ub-binding ZnF (UBZ) domain, bind to Ub via its hydrophobic surface around Ile44. The ZnF domain of IsoT, in contrast, interacts with Ub via the latter's C-terminal residue (Gly76) [82, 116].

1.4.3.3 Other UBDs

Ub-conjugating (Ubc) domains, also known as E2 conjugating enzymes, contain a common 150-amino-acid catalytic core with an α/β fold [94]. The role of E2 enzymes in protein ubiquitination has been previously discussed in this chapter. The UEV (Ubc E2 variant) domain, in contrast to Ubc domains, does not contain a catalytic cysteine residue. It has been shown that a UEV domain, Mms2, heterodimerizes with Ubc13 domain to facilitate the assembly of Lys63-linked poly-Ub chains [117].

1.5 AIMS AND OBJECTIVES

The intrinsic importance of the Ub•UBD interactions has been extensively discussed previously in this Chapter, and therefore their study accumulates high scientific interest. A number of biophysical methods, including NMR, SPR and ITC are currently employed to study Ub•UBD non-covalent complexes. These techniques have contributed significantly to our understanding of the often weak, non-covalent interactions of Ub. However, each technique has its limitations and drawbacks, which are discussed later in Chapter 4. The aim of Chapter 4 is to develop and apply a rapid and highly sensitive ESI-MS method to determine affinity and linkage-selectivity of Ub•UBD interactions.

The investigation of weak hydrophobic interactions seen in many Ub•UBD complexes, is expected to be very challenging for a gas-phase method such as ESI-MS. Indeed, as it will be shown in Chapter 4, a number of Ub•UBD complexes that are studied in this thesis, are readily dissociated and therefore their binding affinity cannot be determined. The aim of Chapter 3 is to develop a simple, clean and effective method for reducing charge state distributions and consequently prevent facile dissociation of the Ub•UBD complexes.

The role of unanchored poly-Ub chains has only recently begun to be understood and linked to Ub-mediated processes. In a similar manner to conjugated Ub chains, unanchored chains also exhibit linkage specificity and, therefore, their study is equally important. Chapter 5 aims to examine the development and employment of a top-down proteomics approach to reveal the topology of unanchored poly-Ub chains. Additionally, the presence of cyclic Ub_2 component in commercial samples of Lys48-Ub_2 and in samples of endogenous purified Ub_2 material is also investigated in Chapter 5.

In Chapter 6, the unusual effects of ammonium and alkali metal ion adducts upon the conformation of the three-helix bundle proteins UQ1-UBA and hHR23A-UBA2 are investigated. In the final Chapter 7, the synthesis of small peptides and the employment of ESI-MS to investigate their potential inhibitory activity against the Ub•IsoT-ZnF interaction, are examined.

CHAPTER 2

MATERIALS AND METHODS

2.1 MATERIALS

2.1.1 SAMPLES PURCHASED/PROVIDED

Ultrapure water (18.2 MΩ·cm), obtained from a Millipore water purification system (Epsom, UK), was used in the preparation of all sample solutions.

2.1.1.1 UBIQUITIN AND UBIQUITIN MUTANTS

Ammonium acetate was purchased from Thermo Fisher Scientific (Loughborough, UK). Lyophilized bovine red blood cell **ubiquitin** was obtained from Sigma-Aldrich (Poole, UK) and prepared as a 116 μM sample in 25 mM ammonium acetate solution. Lyophilized **diubiquitins** (Lys11-Ub_2, Lot# 32141210; Lys27-Ub_2, Lot# 34144710; Lys48-Ub_2, Lot# 3291529 and Lot# 11515211; Lys63-Ub_2, Lot# 1691689) and **tetraubiquitins** were obtained from Boston Biochem (Cambridge, USA) and prepared as a 58 μM and 29 μM samples, respectively, in 25 mM ammonium acetate solution. The **ubiquitin mutants** (double mutant Leu8/Ala, Ile44/Ala and Δ–Gly75/Gly76 deletion mutant) were designed and expressed by Dr. Jed Long (University of Nottingham). These samples were supplied as purified lyophilized stocks and were prepared as 116 μM samples in 25 mM ammonium acetate solution.

2.1.1.2 UBIQUITIN BINDING DOMAINS

The UBDs were expressed as GST fusion proteins in *E. coli* strain XL10-Gold, purified and thrombin cleaved. GST-fusion UBD plasmids were constructed and transformed into E. coli glycerol stocks by Dr. Debora Channing (University of Nottingham). More

details about the expression and purification of UBDs are given below (see Methods section).

Preparation of solutions for protein overexpression and purification

Luria Broth (LB) was obtained from Sigma-Alrich (Poole, UK). LB is consisted of 40% tryptone, 40% sodium chloride and 20% yeast extract. The solution was prepared by adding 25 g LB to 1 L deionised water and autoclaved at 121 °C, overnight.

Ampicillin stock: 100 mg/mL stock prepared by dissolving 1 mg in 10 mL of deionised water and was filter sterilised.

Isopropyl 1-thio-β-D-galactopyranoside (IPTG) obtained from Roche Diagnostics Ltd (Burgess Hill, UK) and prepared as a solution to a final concentration of 200 mM.

Tri-buffered Saline with 0.1% Triton (TBS-T): Solution consisted of 10 mM tris-HCl, 150 mM NaCl and 0.1% Triton X-100 at pH 7.5.

Throbin cleavage buffer (TCB): Solution consisted of 20 mM tris-HCl, 150 mM NaCl and 2.5 mM $CaCl_2$ [what do you mean dehydrated? Surely it was a solution] at pH 8.4.

Thrombin was obtained from Sigma-Aldrich (Poole, UK).

2.1.1.3 CHARGE REDUCTION BY SOLVENT EXPOSURE EXPERIMENTS

Acetonitrile, methanol, isopropanol and **dicloromethane** were purchased from Thermo Fisher (Loughborough, UK). Bovine pancreas **trypsin** (TPCK treated), **benzamidine hydrochloride, ubiquitin** and horse heart **myoglobin** were obtained from Sigma-Aldrich (Poole, UK). Human **transthyterin** (TTR) was obtained from AppliChem GmbH (Darmstadt, Germany). TTR was desalted using Vivaspin columns

(MWCO 10 kDa), (Sartorius, Goettingen, Germany), prior to use. Myoglobin and ubiquitin were prepared in 25 mM CH_3COONH_4 to a final protein concentration of 2μM and 1 μM, respectively. TTR (2.5 μM) and a mixture of trypsin (12 μM) and benzamidine hydrochloride (53 μM), were prepared in 10 mM CH_3COONH_4.

2.1.1.4 MOBILITY CALIBRATION STANDARDS

Lyophilised **myoglobin**, human heart **cytochrome c**, bovine red blood cell **ubiquitin** and **bradykinin** were purchased from Sigma-Aldrich (Poole, UK) and were prepared as a 1 μM samples in $CH_3OH/H_2O/CH_3COOH$ (50:50:1 (vol/vol)) solution. **Acetic acid** was obtained from Thermo Fisher Scientific (Loughborough, UK).

2.1.1.5 PEPTIDE SYNTHESIS

The N-α-Fmoc protected amino acids, **Fmoc-Gly-OH, Fmoc-Arg(Pbf)-OH, Fmoc-Leu-OH, Fmoc-Lys(Boc)-OH, Fmoc-His(Trt)-OH** and **Fmoc-Phe-OH**, and the preloaded Fmoc-amino acid resins, **Fmoc-Gly-Wang resin** and **Fmoc-Val-Wang resin,** as well as the phosphonium-based activating reagent **HCTU** (O-(1H-6-Chlorobenzotriazole-1-yl)-1,1,3,3-tetramethyluronium hexafluorophosphate) were obtained from Merck Bioscience Ltd (Nottingham, UK). Dimethylformamide **(DMF)**, dicholomethane **(DCM)** and **diethyl ether** were purchased from Thermo Fisher Scientific (Loughborough, UK). N,N-diisopropylethylamine/N-methylpyrrolidone **(DIPEA/NMP)** solution (2M), **piperidine** (99.5 %), trifluoroacetic acid **(TFA,** 99.5%) and triisoprolysilane **(TIPS)** were purchased from Sigma-Aldrich (Poole, UK).

2.1.2 INSTRUMENTS

2.1.2.1 MASS SPECTROMETERS

Synapt HDMS, Waters

Mass spectrometry (MS) and ion mobility–mass spectrometry (IM–MS) experiments were performed on a SYNAPT™ HDMS (Waters, Altrincham, UK), a hybrid quadrupole–ion mobility spectrometry–orthogonal acceleration time–of–flight (oa–TOF) MS instrument, with travelling–wave ion mobility spectrometry (TWIMS) capability, equipped with the standard z-spray source and a nanoESI source. A schematic representation of the instrument is shown below in Figure 2.1.1.

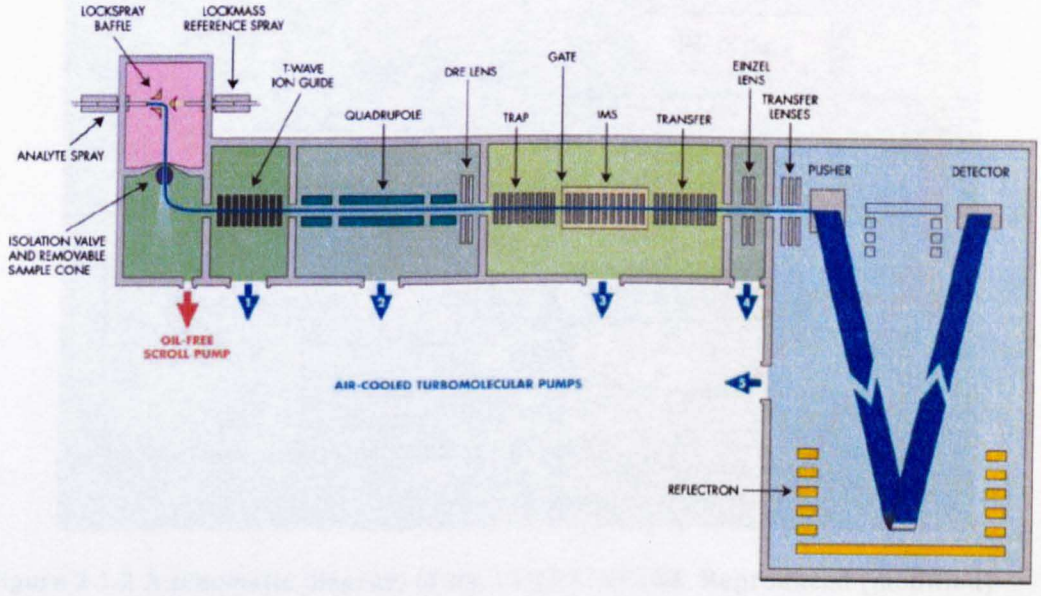

Figure 2.1.1 A schematic of the Waters Synapt HDMS (adapted from reference [63])

Instrument control as well as data processing was performed using the Waters MassLynx™ 4.1 data system. All spectra were acquired in ion positive mode and the TOF analyzer operated on V-mode. Minimum smoothing and background subtraction was applied to the obtained spectra prior to analysis. More details about the major instrument components and their operation are given in a separate section in this chapter.

LTQ FT-ULTRA, Thermo Scientific

Experiments of top-down proteomics to characterize *in vivo* polyubiquitin chains were performed of an LTQ FT-Ultra (Thermo Fisher, UK), a hybrid Linear Ion Trap-Fourier Transform Ion Cyclotron Resonance MS instrument, with CID, IRMPD (infrared multiphoton dissociation) and ECD capabilities. The instrument was equipped with the standard nanospray ion source (Thermo Scientific, UK). For continuous flow nanospray LC-MS operation, the fused-silica SilicaTip™ nanospray emitters (Cat.No FS360-75-30-CE5C10.5, NewObjective (Presearch Ltd, UK)) were used. A schematic representation of the instrument is shown in Figure 2.1.2.

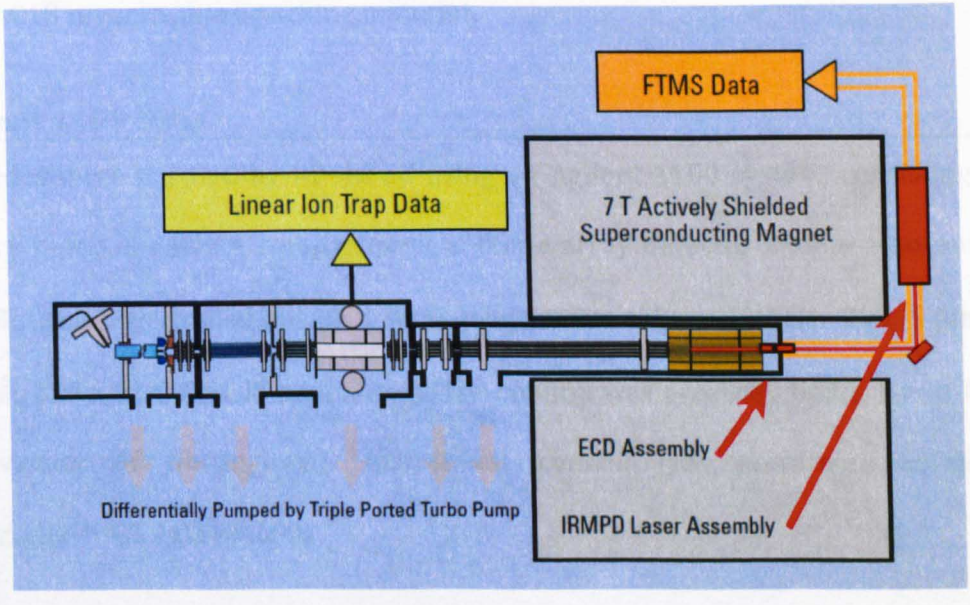

Figure 2.1.2 A schematic diagram of the LTQ FT-ULTRA. Reproduced (modified) from http://thomson.iqm.unicamp.br/instruments_details.php?cod_instrument=3

Instrument control as well as data processing was performed using the Xcalibur 2.0 SR2 data system. All spectra were acquired in ion positive mode.

2.1.2.2 Liquid Chromatography systems

Ultimate 3000 Nano-LC, Dionex

The eluted proteins that were subjected to top-down experiments were chromatographically separated and introduced to the LTQ FT Ultra MS system using

a Ultimate 3000 nano-LC system (Dionex, UK). Instrument control was performed either via the DCMSLink for Xcalibur 2.0, or via the Chromeleon 6.8 data system. The eluents from the column were directly driven to MS analysis. The sample manager compartment kept under the constant temperature of 8 °C. The injected samples were initially loaded to a trap column and then they were loaded to the analytical column by back-flushing the from the trap column. The trap columns (PepMap C4 or C18) were purchased from Dionex, UK. The analytical columns were manufactured *in house* using a pressure cell (Brechbuhler, Germany) to pack 75 μm i.d. capillary columns (Cat.No. IF360-75-50-N-5, NewObjective (Presearch Ltd, UK)) with either C4 or C18 reverse phase packing material.

Agilent 1100 HPLC

Peptides were purified by RP-HPLC using an Agilent 1100 system, consisting of a binary pump, a column compartment, a diode array detector and an autosampler. Purification was carried out on a semi-preparative column (Jupiter 300, 5 μm C18 300 Å, 250 x 10.0 mm, Phenomenex). The column was provided by Dr. David Tooth (University of Nottingham). Instrument control was performed using the MassLynx™ 4.1 data system.

2.1.2.3 Other Instruments

Protein expression and sample preparation

The centrifugations for cell collection were performed in an Avanti JA-25-50 centrifuge while protein concentrations were performed in a CS-15R (Beckman) centrifuge.

Protein samples were desalted and buffer exchanged for mass spectrometry analysis using ultracentrifugation spin filters with 3 kDa or 10 kDa molecular weight cut-off (Sartorius, Germany) and an Eppendorf 5417C centrifuge.

Peptide synthesis

1. A rotary evaporator, Stuart RE300, connected to a water jet vacuum pump was used to remove the excess cleavage mixture (see Methods).
2. A vacuum centrifuge, Jouan RC1022 (Thermo Scientific, UK) was used to re-concentrate the purified peptides.
3. The purified peptides were lyophilised using the Heto Powerdry® LL1500 freeze dryer (Thermo Scientific, UK).

2.2 METHODS

Some of the ESI mass spectra presented in this thesis have been truncated in the x axis for clarity, i.e. only the area of interest is shown.

2.2.1 CHARGE REDUCTION BY SOLVENT EXPOSURE

Charge reduction was obtained by simple exposure of the electrospray plume into acetonitrile vapour. The experiments were performed on a Synapt HDMS instrument. Reduction of charge states on the observed spectrum occurs instantly, while recovering to usual charge states takes less than a minute by simple removal of the solvent container from the source housing.

For solvent exposure experiments, a cap of a Falcon tube containing solvent was placed into the source housing and in the case of ESI the source was closed. The container was placed just inside the doorway to the source chamber (Figure 2.2.1).

Typical settings for ESI experiments: positive ion mode with the ESI capillary held between 2.5 and 3 kV; nitrogen desolvation gas, 200 L h^{-1}; source temperature, 50 °C; desolvation gas temperature, 50 °C; cone gas flow, 30 L h^{-1}.

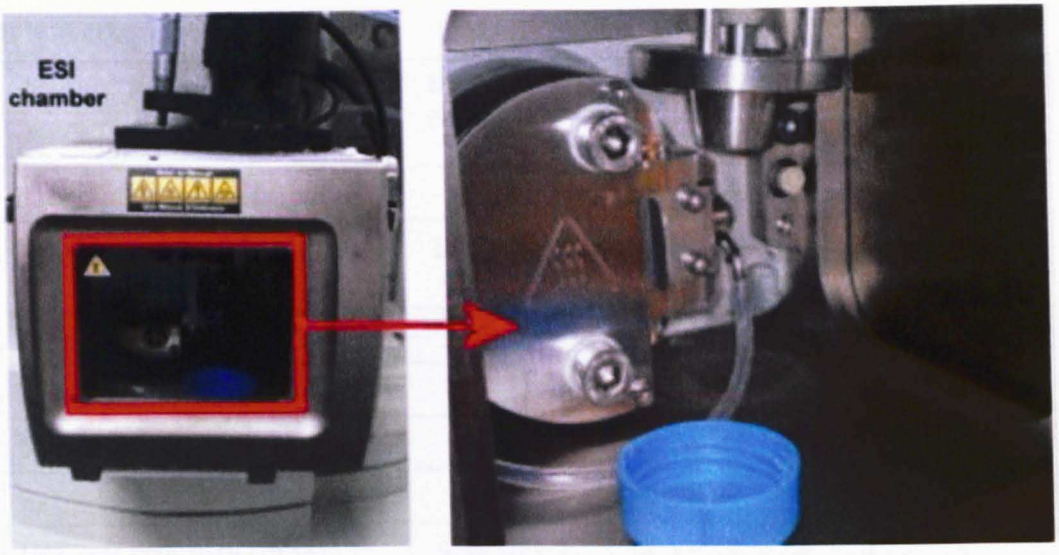

Figure 2.2.1 Photograph of the solvent container placed inside the doorway of the ESI source chamber.

In order to use the nanoESI source in a sealed environment, the front of the source was enclosed in a sealed polythene bag (Figure 2.2.2). A nitrogen rich atmosphere was achieved by flushing with nitrogen for approximately 2 minutes.

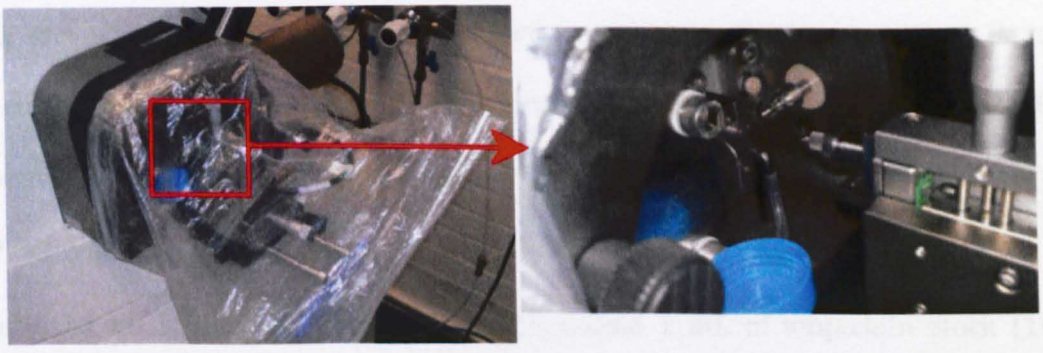

Figure 2.2.2 Photograph of the solvent container in a nanoESI source.

For nanoESI experiments, Waters nanoflow probe tips (Manchester,UK) were used. NanoESI experiments typical settings: capillary voltage, 0.95–1.4 kV; source temperature, 50 °C.

Instrument parameters

Four different protein complexes were used (Table 2.2.1).

Table 2.2.1

Parameter	Ub/UQ1 complex	Myoglobin	Human TTR	Trypsin/ Benzamidine
Backing pressure (mbar)	4.0	2.1	5.0	4.0
Trap pressure (mbar)	1.9×10^{-2}	8.6×10^{-3}	1.1×10^{-2}	1.0×10^{-2}
Trap collision voltage (V)	5	5	20–80	2
Transfer collision voltage (V)	5	5	5	5
Sampling cone voltage (V)	40	20	60	20
Extraction cone voltage (V)	5	5	5	5
IMS cell pressure (mbar)	4.5×10^{-1}	-	-	-
Traveling wave height (V)	8	-	-	-
Traveling wave velocity (m/s)	300	-	-	-

2.2.2 Studies of Ubiquitin–UBD Interactions

2.2.2.1 Expression and purification of UBDs

The UBDs were expressed as glutathione S-Transferase (GST) fusion proteins in *E. coli* strain XL10-Gold. All constructs were verified by DNA sequencing. *E. coli* bacterial cultures were prepared by inoculating glycerol stock cells in 10 mL LB solution containing 10 µL ampicillin stock (100 µg/mL) and incubating overnight at 37 °C with constant agitation (220 rpm). The solution was transferred to 1L of sterilised LB solution (25mg/mL) that contained 1 mL of ampicillin stock (100 µg/mL). Bacteria were grown at 37 °C for 4 h and then induced with 0.2 mM IPTG at OD_{600} ~ 0.6 and incubated overnight at 20 °C with agitation (200 rpm). Cells were pelleted by centrifugation (20 min at 4000 rpm) and were frozen for at least 2 h. Then cells were re-suspended with 10 mL of TBS-T solution and lysed by sonication (three times for 30 sec at 6–7 microns with 1 min relaxation between sonication cycles). Lysate was clarified by centrifugation (20 min at 15000 rpm) and the supernatant was applied to a 5 mL gravity polypropylene column (Qiagen Ltd, UK)

containing 130 µL glutathione beads (glutathione Sepharose™ 4B, GE Healthcare, UK) pre-equilibrated with TBS-T solution. The lysate–glutathione beads mixture was incubated for 1 h at 4 °C with continuous mixing by rotation. After the binding of GST-UBD fusion protein, the beads were washed with three column volumes of TBS-T solution followed by one washing cycle with TCB solution and finally incubation with 5 U of thrombin (diluted in 1 mL TCB) at 4 °C overnight. Released UBDs were eluted and the beads were washed with TCB (3 mL).

The amino acid sequence of each domain used in this study is shown in Table 2.2.2. The N-terminal Gly-Ser dipeptide is residual from thrombin cleavage.

Table 2.2.2 Sequences of UBDs used in this thesis

UBDs	Sequence of thrombin cleaved product
Rabex5-MIU	GSQKQIQEDW ELAERLQREE EEAFASSQS
UQ1 -UBA	GSVRFQQQLE QLSAMGFLNR EANLQALIAT GGDINAAIER LLGS
hHR23A-UBA2	GSQVTPQEKE AIERLKALGF PESLVIQAYF ACEKNENLAA NFLLSQNFDD E
IsoT-ZnF	GSKQEVQAWD GEVRQVSKHA FSLKQLDNPA RIPPCGWKCS KCDMRENLWL NLTDGSILCG RRYFDGSGGN NHAVEHYRET GYPLAVKLGT ITPDGADVYS YDEDDMVLDP SLAEHLSHFG IDMLKMQKTD K

2.2.2 Protein quantification by Lowry assay

The assay was carried out in a 96-well plate. BSA (bovine serum albumin) standard (1 mg/mL) was prepared in solution A (0.1 M NaOH / 0.3 KOH 9:1 (v/v)). A series of dilutions of BSA standard was performed to give eight BSA standards (200 µL each) with concentrations in a range of 0–80 µg. Standards were prepared in triplicates. Similarly, 10 µL of each sample was diluted in solution A to a final volume of 200 µL. 50 µL of Lowry reagent (sodium carbonate solution / sodium potassium tartrate solution / copper sulphate solution, 10:1:1 (v/v) were added to all standards and

samples and incubated for 10 min. Then, 50 μL of Folin reagent (10% (v/v) Folin and Ciocalteu's phenol reagent (Fisher Scientific, UK) in solution A) were added. The plate was incubated for 30 min at room temperature. Once colour had developed, the absorbance at 750 nm was measured using a plate reader (DYNEX technologies).

2.2.2.3 Sample Preparation for MS analysis

UBDs were desalted and buffer exchanged into 25 mM NH_4OAc buffer using Vivaspin 500 ultrafiltration spin filters with 3kDa (in the case of IsoT-ZnF 10kDa) molecular weight cut–off (Sartorius, Goettingen, Germany). The IsoT-ZnF domain, subsequent to buffer exchange in 25 mM NH_4OAc, was mixed with 0.5 mM dithiothreitol (DTT) at 4 °C, 24h prior the addition of Ub in order to reduce the disulfide-linked dimer to the monomeric domain. Samples were aliquoted (400 μL) and stored in -20 ^{0}C.

Titration MS experiments

Figure 2.2.3 illustrates the procedure flowchart of the method used in the titration MS experiments.

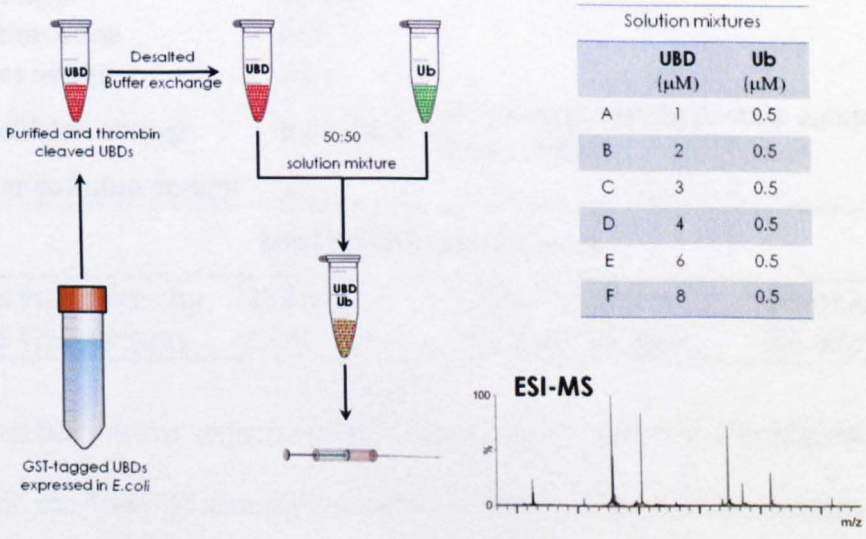

Solution mixtures

	UBD (μM)	Ub (μM)
A	1	0.5
B	2	0.5
C	3	0.5
D	4	0.5
E	6	0.5
F	8	0.5

Figure 2.2.3 Procedure flowchart of the titration MS experiments

Multiple replicates of six titration samples were prepared as 1:1 solution mixtures to final concentrations of Ub (0.5 μM (1 μM in the case of UQ1•tetra-Ub)) and UBD (1,

2, 3, 4, 6 and 8 μM). The samples were vortexed and subjected to MS analysis with no further preparation, using a syringe pump (Harvard syringe pump, model 55-2222 Holliston, MA, USA) and a 100 μL Hamilton syringe (Bonaduz, Switzerland), at a flow rate of 5 μL min^{-1}. Table 2.2.3 gives the instrument conditions.

Table 2.2.3 Instrument (Synapt HDMS) parameters used in Ub–UBD interactions

Pressures		
Region	**Value (mbar)**	**Comment**
Backing	3.8–4.4	Optimum pressure for optimum transmission of the protein complexes
Trap	2.1×10^{-2}	Argon collision gas
IMS	4.4×10^{-1}	Nitrogen buffer gas
TOF	1.5×10^{-6}	
Temperatures and gas flows		
Source temperature	50 °C	
Cone gas flow	30 L h^{-1}	Nitrogen gas
Desolvation temp.	50 °C	
Desolvation gas flow	200 L h^{-1}	Nitrogen gas
Voltages		
Region	**Value (V)**	**Comment**
Capillary voltage	2600	
Cone voltage	60–80	
Extraction Cone	5.0	
Transfer voltage	5.0	
Trap collision energy	8.0 – 60.0	Adjusted to induce protein complex dissociation
Transfer collision energy	5	
Ion Mobility parameters		
TWIMS Wave Velocity	280 m/s	IMS Gas (N_2) flow 26 mL/min
TWIMS Wave Height	8.0 V	Trap Gas (Ar) flow 2.5 mL/min

The parameters were experimentally optimized to provide the highest relative signals for the Ub•UQ1 complex sprayed from 25 mM ammonium acetate in the presence of acetonitrile vapour. The instrument operated on positive Mobility–TOF mode (V–mode). The quadrupole ion transmission profile (Quad profile) parameters: *Mass 1*, 1000 m/z; *Dwell 1*, 5%; *Ramp 1*, 0%; *Mass 2*, 2000 m/z; *Dwell 2*,

55%; *Ramp 2*, 40%; *Mass 3*, 4000 m/z. The instrument operated over the scanning range of 700-4000 *m/z*.

2.2.2.4 Determination of Ub•UBD binding affinity by ESI-MS

The equilibrium expression for the dissociation of a Ub•UBD complex is given by equation 2.2.1, where $[Ub]_{eq}$, $[UBD]_{eq}$, $[Ub•UBD]_{eq}$ are the equilibrium concentration of Ub, UBD and their complex, respectively.

$$K_d = \frac{[Ub]_{eq}[UBD]_{eq}}{[Ub \bullet UBD]_{eq}} \qquad \text{Equation 2.2.1}$$

The free and the bound Ub ions as measured by mass spectrometry in positive ion mode are Ub^{n+} and $Ub•UBD^{n+}$, respectively. Providing that electrospray response factors for Ub^{n+} and $Ub•UBD^{n+}$ are similar, it can be assumed that the ratio (R) of the ion intensity (I) of the bound and unbound protein ions represent solution equilibria (equation 2.2.2).

$$R = \frac{[Ub]_{eq}}{[Ub \bullet UBD]_{eq}} = \frac{\sum_n I(Ub^{n+})}{\sum_n I((Ub \bullet UBD)^{n+})} \qquad \text{Equation 2.2.2}$$

Assuming that Ub molecules can be either free or UBD-bound the mass conservation is given by equation 2.2.3, where $[Ub]_0$ is the initial concentration of Ub.

$$[Ub]_0 = [Ub]_{eq} + [Ub \bullet UBD]_{eq} \qquad \text{Equation 2.2.3}$$

Combining equations 2.2.2 and 2.2.3, the equilibrium concentration of Ub•UBD complex can be determined from the ratio R and the $[Ub]_0$ (equation 2.2.4).

$$[Ub \bullet UBD]_{eq} = \frac{[Ub]_0}{1 + R} \qquad \text{Equation 2.2.4}$$

Similarly, the mass conversion for UBD is given by equation 2.2.5, where $[UBD]_0$ is the initial concentration of UBD.

$$[UBD]_0 = [UBD]_{eq} + [Ub \bullet UBD]_{eq} \qquad \text{Equation 2.2.5}$$

Combining equations 2.2.2, 2.2.4 and 2.2.5 and replacing to equation 2.2.1, the K_d will be determined from the ratio (R) and the initial concentrations of Ub and UBD.

$$K_d = R\left([UBD]_0 - \frac{[Ub]_0}{1+R}\right) \qquad \text{Equation 2.2.6}$$

2.2.3 Top-down proteomics to characterize polyubiquitin chains and Cyclization of Lys-48 linked diubiquitin

2.2.3.1 Affinity Chromatography

The assays for the purification of ubiquitin dimmers, using either the IsoT-ZnF or ZnF A20 domains, from skeletal muscle or from cultured cell proteins extracted from HEK293T cells, were performed by Dr. Joanna Strachan (University of Nottingham). Briefly, proteins were captured from an *in vivo* source by affinity chromatography using a sepharose-immobilised recombinant ubiquitin-binding domain (ZnF A20 domain or ZnF UBP). Polyubiquitinated proteins were removed by treatment with the catalytic core of the USP2 deubiquitinating catalytic core (ENZO Life Science) [118].

2.2.3.2 Sample preparation for MS analysis

Samples were eluted from the beads using 0.1% formic acid, vortexed and incubated at room temperature (~20 °C) for 30 min followed by centrifugation (8000 rpm for 5 min). An aliquot of the supernatant was removed and diluted 5-fold with 0.1% formic acid in 95:5 water/acetonitrile (v/v) and transferred into polypropylene

vials (Dionex, UK). Monoubiquitin and diuiquitin (Ub_2) standards, were prepared as a 1 μM samples in 0.1% formic acid in 95:5 water/acetonitrile (v/v).

2.2.3.3 NanoLC – MS and MS/MS analyses

NanoLC separation and MS detection were performed using an Ultimate 3000 nanoLC system (Dionex, UK) coupled to an LTQ FT-Ultra MS (Thermo Scientific). MS/MS spectra were obtained and compared with those acquired for Lys11-, Lys27-, Lys48- and Lys63-linked Ub_2 standards (BostonBiochem, USA).

Liquid Chromatography

Reversed-phase liquid chromatography was performed using either on a C4 column (15 cm × 75 μm, 5 μm, 300 Å, packed in house) or a C18 column (15 cm × 75 μm, 3 μm, 100 Å, packed in house). A C4 PepMap300 (Dionex, UK) trapping column (300 μm × 5 mm) was used to concentrate the injected sample (1-3 μL sample injection). The trapping column was switched in-line with the analytical column after a 3 min loading time. A linear gradient of mobile phase B (acetonitrile/water (95:5, v/v) with 0.1% formic acid), in mobile phase A (water/acetonitrile (95:5, v/v) with 0.1% formic acid) was used to elute the samples from the hydrophobic stationary phase (C18 or C4). The gradient is given in Table 2.2.4

Table 2.2.4

Time (min)	A %	B %	Flow (μL/min)
0.00	100	0	0.200
30.00	30	70	0.200
30.01	10	90	0.200
35.00	10	90	0.200
35.01	100	0	0.200
50.00	100	0	0.200

Mass Spectrometry — LTQ FT-Ultra parameters

The instrumental conditions were optimised using Ub_2 standards. The heated capillary temperature was set at 200 °C; spray voltage, 1.6 kV; capillary voltage, 43 V.A full scan mode (300–2000 *m/z*) was used. MS/MS experiments were carried out by performing CID in the linear ion trap and subsequent transfer of the resulted fragments to the ICR cell for further measurement. An isolation widow width of 8 Da was used for selected protein charge states, which were subsequently activated for 30 ms using 18% normalised collision energy and an activation q of 0.25. A mass resolving power of 200,000 at 400 *m/z* was used and AGC (Automatic gain Control) was applied in all data acquisition modes.

2.2.4 Ion Mobility – Mass Spectrometry experiments

As has been mentioned in Chapter 1, the CCS of gas phase ions is directly related to its mobility through a gas under the influence of electric field. However, when TWIMS device is used instead of a conventional drift tube, it is necessary to calibrate the instrument is order to determine CCSs.

2.2.4.1 TWIMS calibration and CCS calculation

A calibration approach that has been well described in previous studies [57, 64, 65] was used in this thesis. The measurements of the calibrants and the analyte proteins were performed under the same instrument conditions; ESI capillary voltage, 2.6 kV; sampling cone voltage, 20 V; extraction cone voltage, 1 V; transfer voltage, 5 V; source temperature, 40 °C; desolvation temperature, 50 °C; cone flow gas, 30 $L \cdot h^{-1}$; desolvation flow gas, 200 $L \cdot h^{-1}$. The ion mobility cell contained N_2 gas and operated at a pressure of 5.0×10^{-1} mbar; travelling wave height and velocity, 6.2 V and 200 $m \cdot s^{-1}$, respectively; transfer wave height and velocity, 5.0 V and 300 $m \cdot s^{-1}$, respectively; trap and transfer collision voltage, 5 V and 4 V, respectively; trap DC

bias, 11 V; backing pressure, 3.8 mbar; trap pressure, 2×10^{-2} mbar; TOF region pressure, 1.3×10^{-6} mbar. Quad profile: *Mass 1, 700 m/z; Dwell 1, 5%; Ramp 1, 0%; Mass 2, 1000 m/z; Dwell 2, 55%; Ramp 2, 40%; Mass 3, 3000 m/z.*

Calibration was performed using the native-like ions from the following proteins: bradykinin [119], melitin and ubiquitin [120]. The measured drift time (t_D) of each charge state of the three calibrant proteins was recorded and it then converted to a corrected drift time (t_D'), using equation 2.2.7 [64]

$$tD' = tD - 33\left(\frac{\text{frequency}_{(\text{Pusher})}}{6}\right)\left(\frac{1}{1000}\right) - 1.3\sqrt{m/z}\left(\frac{1}{1000}\right) \quad \text{Equation 2.2.7}$$

where frequency $_{(\text{Pusher})}$ = 90μs (Experimental Mass Spectrometer Parameter). The CCS values (Ω) from the databases, they were converted to corrected CCS values (Ω') using equation 2.2.8

$$\Omega' = \frac{\Omega}{\left(z\sqrt{\frac{1}{\mu}}\right)} \quad \text{Equation 2.2.8}$$

where, Ω is the CCS value as given in the databases and μ is the reduced mass that is calculated by equation 2.2.9.

$$\left(\frac{1}{\mu}\right) = \left(\frac{1}{M_I} + \frac{1}{M_G}\right) \quad \text{Equation 2.2.9}$$

A plot of ln Ω' against ln t_D' is constructed and its slope, m, was used to obtain t_D'' (Equation 2.2.10) values that were further used to construct the linear plot Ω $=f(t_D'')$. The latter was used to calculate the experimental CCS values of protein ions.

$$tD'' = tD'^{m}\, z\sqrt{\frac{1}{\mu}} \quad \text{Equation 2.2.10}$$

Theoretical CCS values were obtained either by MOBCAL [74, 75] (TM) or by the CCS calculator (PA) as implemented in DriftScope 2.1 [121].

2.2.4.2 Molecular dynamics

The +3 species of UQ1-UBA domain was modelled, by replacing the negatively charged residues, glutamic acid (Glu) and aspartic acid (Asp) with the neutral residues glutamine (Gln) and asparagine (Asn), respectively. The construction of the modelled mutant was based on the available NMR structure of UQ1-UBA domain (PDB ID: 2JY5), which was modified using PyMOL (molecular visualization system) and MolProbity [122, 123]. The molecular dynamic (MD) simulations were carried out by Dr Neil Oldham using the AMPS-NMR (AMBER based Portal Server for NMR structures) suite of programs (http://www.enmr.eu/webportal/) [124]. Gas-phase MD simulations, for a total time period of 1 ns, were performed at 100 K, 300 K, 400 K, 600 K and 900 K, with a time step of 1 ps in each case, which resulted in 1000 candidate structures at each temperature. The AMBER99SB force field was employed for all calculations. The following sander [125] parameters were utilised: gas phase conditions (IGB = 0) without periodic boundary (NTB = 0), a non-bonded cut-off of 12 Å, constant temperature (as specified above for TEMP0 and TEMPI), with temperature scaling (NTT) = 3 and a collision frequency of 1 ps^{-1}. Following a similar approach the +4 charge state of hHR23A-UBA2 domain, was modelled, based on the available NMR structure (PDB ID: 1OQY).

Determination of TM-like CCS values

The TM method is generally believed to be the most realistic model for the theoretical calculation of protein CCS values, although it is computationally demanding. In contrast, the PA approach can calculate CCS values much faster, however, not as reliably as TM. Given that MD simulations under the conditions used generated 1000 structures per distinct temperature, the TM approach was

unfeasible. Instead a "hybrid" approach was employed to calculate theoretical CCS values for the modelled structures. By calculating the TM values for ten structures over the size-range of outputs from MD simulations of UQ1-UBA from 300 K to 900 K, a constant factor of 1.12 (± 0.01) for conversion between the rapidly-calculated PA CCS (using the Waters DriftScope PA CCS calculator) and the TM CCS for this protein was determined. Using this factor, TM-like CCS values for all 1000 output structures from each MD simulation were generated and plotted (Figure 2.2.4). Benesch and Ruotolo [126] have determined a similar ratio (1.14) for numerous proteins, over a wide range of CCSs, by comparison of theoretical PA CCSs with measured CCS values.

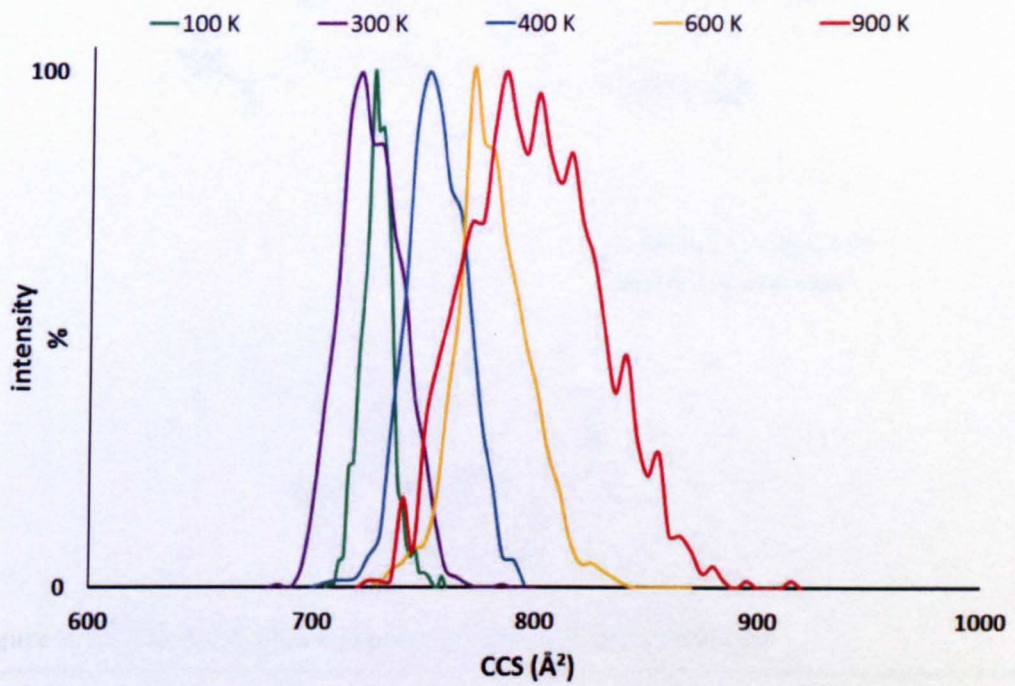

Figure 2.2.4 Ion mobility drift traces for UQ1-UBA showing modelled +3 charge state (consist of 1000 structures) at different temperatures

2.2.5 Preparation and Purification of Peptides

The peptide synthesis was performed using the solid-phase peptide synthesis (SPPS) approach Figure 2.2.5.

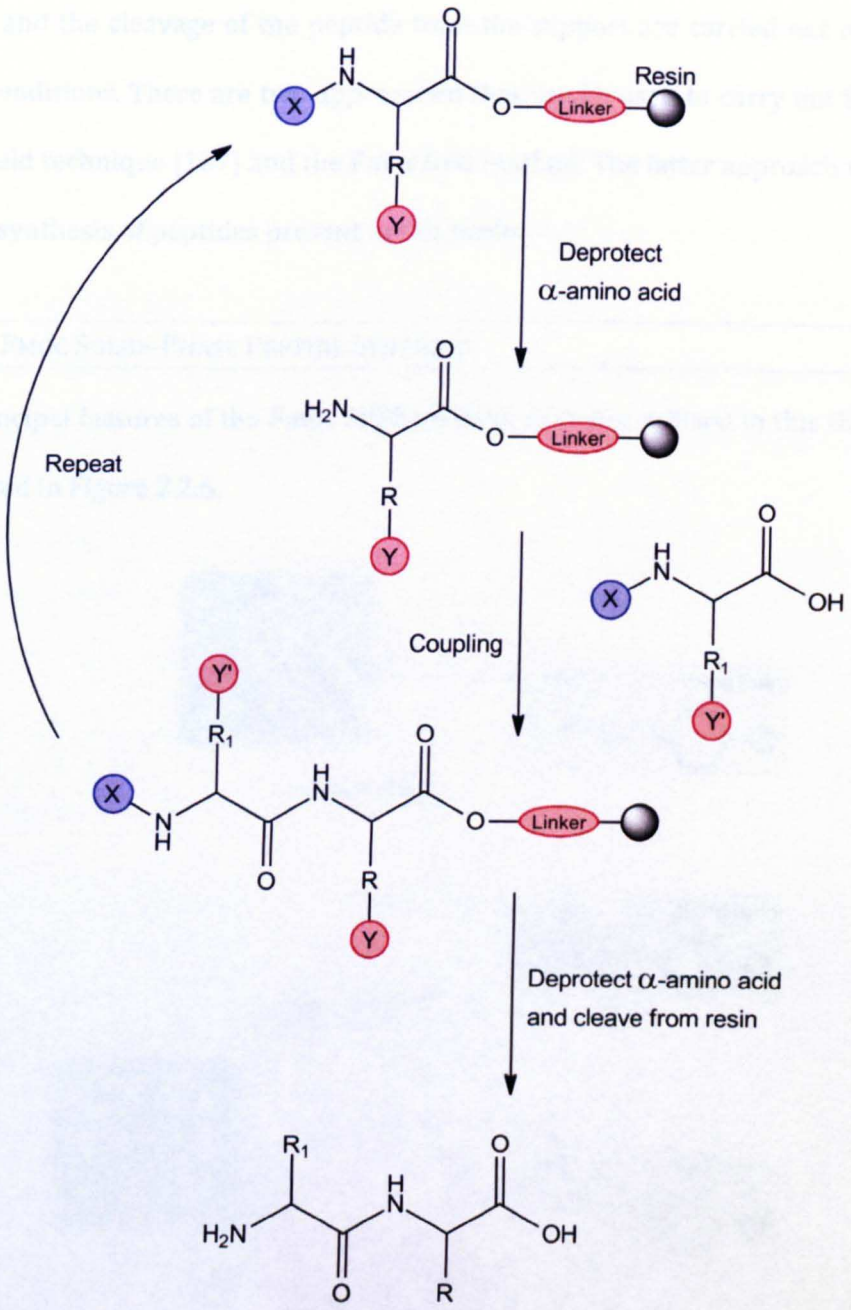

Figure 2.2.5 The solid-phase peptide synthesis (SPPS) principle

In contrast to the *in vivo* peptide synthesis, in SPPS method the peptide chain is assembled from C-terminus to N-terminus. Therefore, the C-terminus amino acid residue is immobilised to an insoluble support via its carboxyl group, while its α-amino group and any side chain ε-amino group are masked by protecting agents that can be selectively and individually removed. Usually, the ε-amino group protecting

agents and the cleavage of the peptide from the support are carried out under the same conditions. There are two approached that can be used to carry out SPPS; the Merrifield technique [127] and the Fmoc/*t*Bu method. The latter approach was used for the synthesis of peptides present in this thesis.

2.2.5.1 Fmoc Solid–Phase Peptide Synthesis

The principal features of the Fmoc SPPS method, as it was utilised in this thesis, are illustrated in Figure 2.2.6.

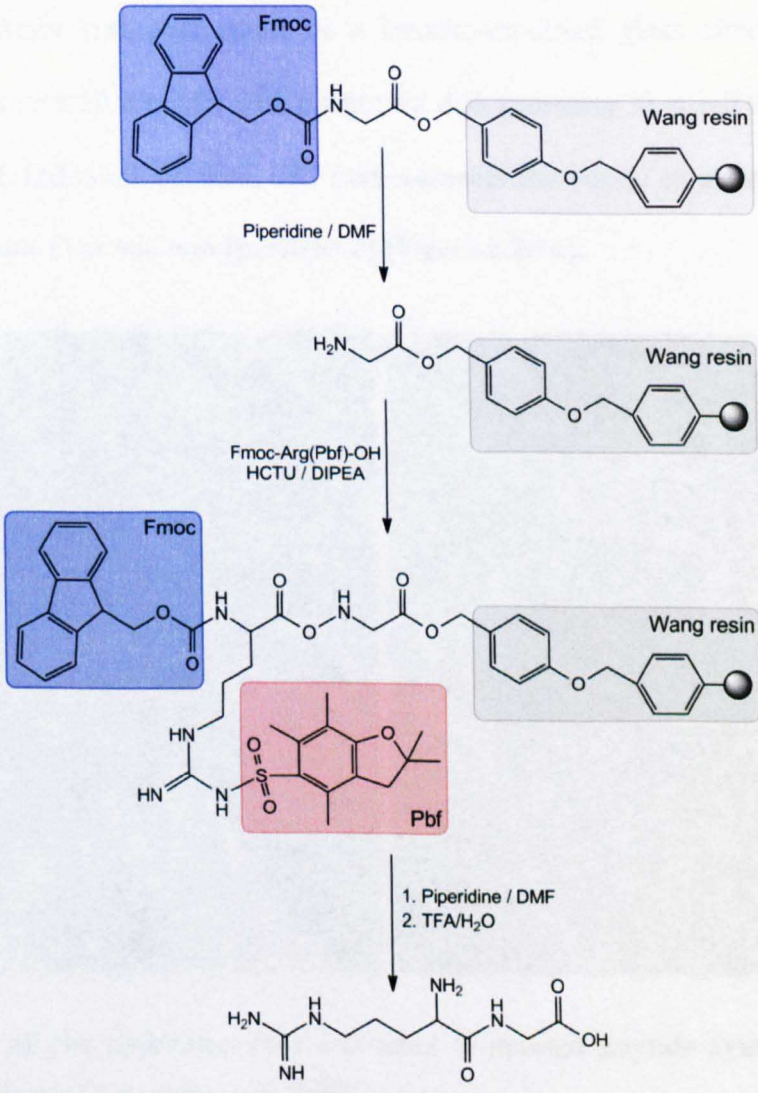

Figure 2.2.6 The Fmoc SPPS. Synthesis of the dipeptide Arg–Gly.

In brief, the C-terminal residue of a target peptide is anchored to the TFA-labile, Wang resin (p-hydroxylbenzyl alcohol (PHB) on polystyrene) via its carboxyl group, and carries a base-sensitive α-amino Fmoc (fluorenylmethyloxycarbonyl) protecting group. In contrast, any side chain ε-amino groups are masked by acid-labile protecting agents, which are not affected by the reactions conditions employed to deprotect α-amino group,, and to assemble the peptide chain. Preloaded Fmoc-amino acid-Wang resins and Fmoc protected residues were used in this thesis.

Manual synthesis

Peptide synthesis was performed in a custom-modified glass chromatography column (100 mm x 10 mm I.D) with a sintered disk (porosity 3), fitted with a 3–way stopcock (SGL Ltd, Staffordshire, UK) that connects the vessel to either a nitrogen source (position ***1***) or vacuum (position ***2***) (Figure 2.2.7a).

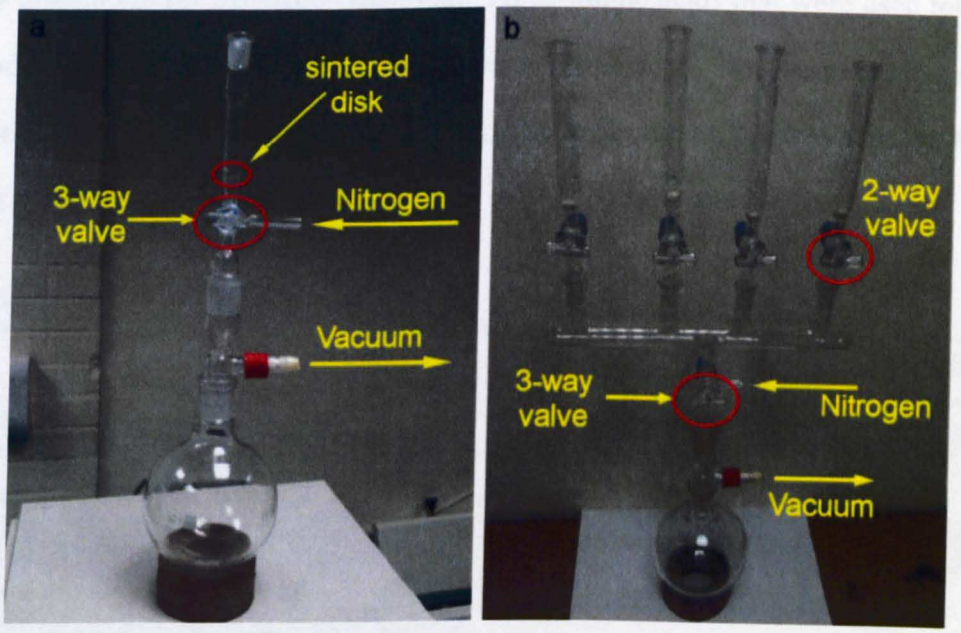

Figure 2.2.7 a) The apparatus that was used in manual peptide synthesis, b) the home–build 4–positions glass manifold.

Basic operation of the device is as follows: resin and all solvents are added from the top of the vessel; the reaction mixture is agitated by nitrogen–bubbling (tap position

1) and the solvents/reagents are removed by the application of vacuum (tap position ***2***). A home-built 4-position (socket size B14) glass manifold was also used for high throughput peptide synthesis. The manifold was fitted with a three-way stopcock, for the nitrogen and the vacuum inlets (Figure 2.2.75b). Figure 2.2.8 is a graphical description of the Fmoc SPPS methodology.

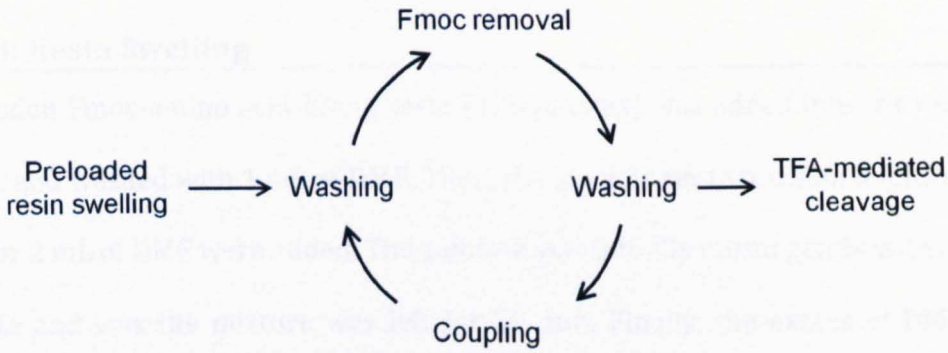

Figure 2.2.8 Diagram showing the Fmoc SPPS process

The quantity of the preloaded resins and Fmoc-amino acids that were used for the production of each hexapeptide, are given in Table 2.2.5. Ten hexapeptides were synthesised; ***LRLRGG, LRLRGV, LRLAGG, LALRGG, FRLRGG, LRFRGG, KRFRGG, KRLRGG, HRLRGG*** and ***FALRGG***.

Table 2.2.5

Amino acid	MW (g/mol)	Weight (mg) *
Fmoc-Gly-OH	297.3	149
Fmoc-Arg(Pbf)-OH	648.78	324
Fmoc-Leu-OH	353.41	176
Fmoc-Ala-OH	311.33	155
Fmoc-Phe-OH	387.43	193
Fmoc-Lys(Boc)-OH	468.54	235
Fmoc-His(Trt)-OH	619.71	310
*** This equals to 500 µmoles**		

Resin	mmol/g	Weight (mg) **
Fmoc-Gly-Wang	0.79	126
Fmoc-Val-Wang	0.61	164
** This equals to 100 µmoles		

PROCEDURE

Reagents

Deprotection reagent: 20% Piperidine in DMF (v/v).

Coupling reagent: HCTU was prepared as 0.45 M solution, typically by dissolving 1.86 g in 10 mL DMF.

Cleavage buffer: TFA/Water/TIPS (95:5:5 v/v)

Step I: Resin Swelling

Preloaded Fmoc-amino acid-Wang resin (100 μmoles) was added into the reaction vessel and washed with 1 mL of DMF. Then, the tap was set to position ***0*** (close) and further 2 mL of DMF were added. The solution was initially mixed gently with a glass pipette and was the mixture was left for 20 min. Finally, the excess of DMF was removed by the application of vacuum (tap position ***2***).

Step II: Fmoc removal

Deprotection reagent (1 mL) was added into the reaction vessel and the mixture was agitated gently for 10 min (tap position ***1***). Solvent was drained off and fresh deprotection reagent (1 mL) was added. After 10 min, the reagent was drained off and the resin was washed with 1 mL DMF (2 times). Then, further DMF (1 mL) was added and the mixture was agitated gently for 2 min and then disposed to waste. Finally, the resin was further washed with DMF (2 mL).

Step III: Coupling reaction

Fmoc-amino acid (500 μmoles, i.e. 5 eq. relative to resin) was dissolved in 1 mL of coupling reagent (*note:* 1 mL of coupling reagent equals to 450 μmoles). Then, 2M DIPEA/NMP (0.5 mL, i.e. 1000 μmoles) was added and the solution was mixed thoroughly. The solution was added to the N-deprotected resin and the mixture was agitated for 1 h by nitrogen bubbling (tap position ***1***). Reagents were drained off by applying vacuum (tap position ***2***) and the resin was washed with 1 mL DMF (2

times) followed by wash with 1 mL of DCM (2 times). After that, the resin was re-swelled by agitating it gently with DMF (2 mL) for 5 min. Finally, the solvents were drained off and steps II and III were repeated in order to elongate the peptide chain. Alternatively, Fmoc group was removed (step II) and the unprotected peptide was cleaved from the resin as is described below (step IV).

Step IV: TFA-mediated cleavage

It is crucial to completely remove all traces of DMF, to prevent formation of TFA-DMF complexes. Therefore, the resin was thoroughly washed with DCM (2 mL, 5 repeats) and diethyl ether (2 mL) and then, it was air-dried for 20 min by utilizing the vacuum line. Then, the resin left to dry overnight. After that, cleavage buffer (2 mL) was added into the reaction tube and the resin - cleavage buffer mixture was agitated very gently with nitrogen bubbling (tap position ***1***) for 1.5–2 h. The solution was collected into a small round-bottom flask (25 mL) and the resin was washed with 1 mL clean TFA (the wash was collected as well).

Step V: Peptide isolation

In order to remove the excess of the cleavage mixture, a rotary evaporator was utilized. The synthesised peptide was precipitated by the addition of cold diethyl ether (10 mL). Then, the ether solution was carefully rejected and the peptide was washed with further diethyl ether. After that, the peptide was left overnight to dry. The isolated peptides were re-solvated in a H_2O:CH_3CN (95:5) solution containing 0.1% TFA, and were further purified by RP-HPLC (see section 2.2.4.3). The purified peptides were concentrated by high speed vacuum centrifugation and freeze-dried.

CHAPTER 3

CHARGE STATE AND ADDUCT REDUCTION USING SOLVENT VAPOUR EXPOSURE

3.1 INTRODUCTION

The successful use of MS in studying proteins and their non-covalent interactions is mainly attributed to the ESI process and its capacity of producing multiply charged ions. The development of charge state manipulation techniques has expanded its capabilities. Several methods have been reported to either increase [128-131] or decrease [132, 133] the level of charging of protein ions electrosprayed from aqueous solutions. Increased charge states usually result in wider CSDs, and are commonly preferable in accurate mass measurements, or in certain tandem MS experiments. For example, the efficiency of ECD [134] is highly dependent upon ion's charge state. In the context of non-covalent interactions, this allows top-down analysis of protein complexes to be carried out [135]. The use of solution additives, known as supercharging agents, has been widely employed to increase charge states while preventing the non-covalent interactions [130, 131]. However, recent studies on the effects of supercharging agents on protein structure, using IM-MS, suggest that structural unfolding may be the origin of increased charge [136]. An alternative method involves the introduction of acid vapour in the curtain gas of the ESI source has also been reported [137].

The disruption of protein's higher structure has been related to increased charge states [138]. This leads to the assumption that lower charge states minimize

structure unfolding, leading to the formation of more native-like and stable species. This is mainly attributed to reduced intra- and intermolecular Coulomb repulsion within a protein ion complex. In a structural sense however, lower charge states can show significant collapse in the gas-phase [51], driven by the collapse of external side chain residues throughout the polypeptide [139].

Several approaches have been reported to reduce the charge states of protein ions produced by ESI. For example, studies have shown that the use of basic buffer salts such as triethylammonium bicarbonate (TEAB) result in significant charge state reduction [140, 141]. This is attributed to the high gas-phase basicity of the triethyllamonium cation in comparison to the ammonium cation and involves a proton competition mechanism. The Robinson group has recently used triethylammonium acetate buffer (TEAA) in combination with aza-18-crown-6 (A18C6) to investigate the dissociation pathways of the homtetrameric protein human transthyretin (hTTR) [142]. They have shown that at relatively high charge state, an unfolded monomer is released from the parent ion. In contrast, a compact monomer was produced at reduced charge states and a covalent peptide bond cleavage was preferred over dissociation of the non-covalent complex at the very lowest charge states. The use of very strong organic bases, including strained-systems referred to as 'proton sponges', has also been suggested [143]. Proton sponges have the ability to retain high proton affinities in the gas phase. The study revealed a linear relationship between the average charge state and the gas-phase basicities of the additives used. The use of the heterocyclic base imidazole either as a solution additive or when introduced as a separate spray in the source region, has also been reported [133, 144, 145]. It has been suggested that imidazole promotes the formation of multiple non-specific adducts around the protein ion, which

provide a cooling effect as they evaporate during transmission of the ions into the intermediate vacuum region of the MS.

Other methods involving the use of gas phase bases, include the addition of polar solvents to the nitrogen bath gas[30] and mixing ESI droplets and steam using a "Tee" interface [146]. Zenobi and co-workers have employed a charge state reduction technique to determine gas-phase basicities of proteins. In these studies, *totally desolvated* protein ions obtained by electrosonic spray ionization (ESSI) [147] were exposed to the vapour of various bases [148, 149]. Protein charge states can also be manipulated by gas-phase ion/ion reactions [150-153]. A very effective method of reducing charge states in a controllable way, was proposed by Scalf [132]. The method involves the use a ^{210}Po source, located immediately after the ESI source, to generate α-particles which interact with the gases originating from the ESI source. This leads to the production of a bipolar ionised gas that induces charge reduction in the droplets and ions produced by the electrospray process.

This chapter describes a simple, clean and effective method for reducing charge states observed in ESI-MS without the use of any solution additives or instrumental modifications. This approach is applicable to both ESI and nanoESI spray setups and has the additional benefit of reducing common adducts. Its utility is demonstrated using four systems: the weak Ub•UQ1 non-covalent complex, the weak trypsin-benzamidine protein-inhibitor complex [133, 154], holo-myoglobin, and the hTTR complex, which undergoes charge state-dependent dissociation pathways [142].

3.2 Results and Discussion

It has been noted previously that for a given protein the charge states obtained from ESI and nanoESI typically differ in their distribution. This is generally explained by

the significantly smaller droplet sizes obtained by nanoESI compared with conventional ESI [155, 156]. However, the design of the ESI and nanoESI chambers introduces another variable: the composition of the atmosphere under which the ionization process (either ESI or nanoESI) takes place. While in most commercial ESI sources the electrospray process is carried out under relatively dry nitrogen atmosphere, in nanoESI, it is performed in an open source design without a nebuliser gas. Figure 3.2.1 shows the mass spectrum of myoglobin, sprayed from 25 mM ammonium acetate, acquired by ESI (a, b) or nanoESI (c, d) under nitrogen rich atmosphere (a, c) or normal laboratory atmosphere conditions (b, d). Compared the spectra obtained under the same conditions (a, c or b, d), it is clear that they bear a notable similarity to each other.

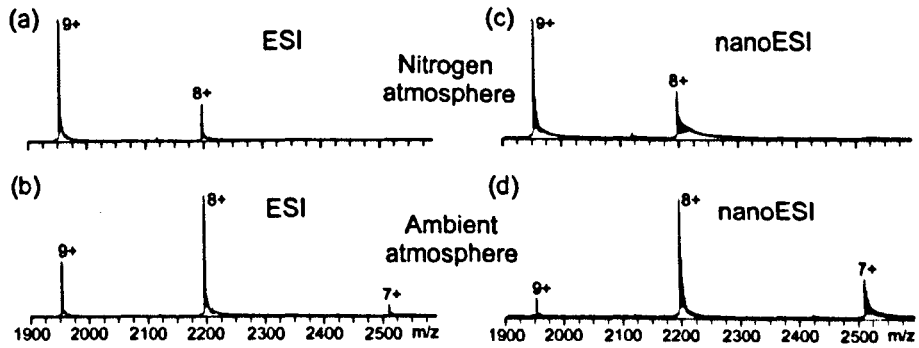

Figure 3.2.1 ESI mass spectra of myoglobin (2μM) sprayed from 25mM ammonium acetate solution. (a) and (c) were acquired using ESI and nanoESI respectively under an enclosed nitrogen atmosphere. ESI and nanoESI spectra obtained under atmospheric conditions (open source) are presented in (b) and (d).

Therefore, a limited manipulation of charge states can be achieved by simple control over the conditions under which the electrospray process takes place. An apparent difference between nitrogen rich atmosphere and normal laboratory atmosphere is the amount of oxygen that is present in each case. To investigate the effects of oxygen upon CSD, oxygen was either introduced into the closed chamber of a commercial Waters ESI source or it was used as a nebuliser gas instead of nitrogen. No change in CSD was observed.

Another atmosphere-related parameter that varies significantly, is the water vapour content (relative humidity). To investigate this, a small reservoir (see Chapter 2) of water (~ 5 mL) was introduced into the closed source housing. Figure 3.2.2b shows the CSD of myoglobin achieved when water was introduced to the closed environment of the ESI source compared to when no water was present (Figure 3.2.2a). A shift to lower charge state was observed, similar to the shift observed in case of ESI operation under laboratory atmosphere conditions (Figures 3.2.1a and 3.2.1b). An ion-molecule mechanism that involves a gas-phase charge transfer between protein ions present in the charged droplet and neutral water vapour in the atmosphere, can be used to explain this phenomenon. Such a charge state reduction mechanism should be highly dependent on the gas-phase basicity of the neutral solvent vapour. Figure 3.2.2 shows the ESI mass spectra of myoglobin sprayed from 25 mM ammonium acetate in the presence of five common laboratory solvents (water, isopropanol, methanol acetonitrile and triethylammine) in comparison to a solvent free environment. With the exception of isopropanol, a strong relationship was observed between the gas-phase basicity of the solvents used and the amount of charge reduction. Although isopropanol possesses a gas-phase basicity (763 $kJ \cdot mol^{-1}$) greater than that of acetonitrile (748 $kJ \cdot mol^{-1}$), it provokes less charge-shift compared to methanol (725 $kJ\ mol^{-1}$). Isopropanol, however, exhibits roughly half the vapour pressure of acetonitrile (Figure 3.2.2) and approximately one third that of methanol, which will clearly affect gas-phase presence of this solvent. To investigate the effects of solvent volatility upon the reduction of charge states of protein ions, two experiments were performed. Firstly, the rate of solvent evaporation was increased by simply increasing the number of isopropanol containers (and thus solvent surface area) in the source. Figure 3.2.3 shows the ESI mass spectrum of myoglobin sprayed from 25 mM ammonium acetate in the presence of multiple isopropanol reservoirs.

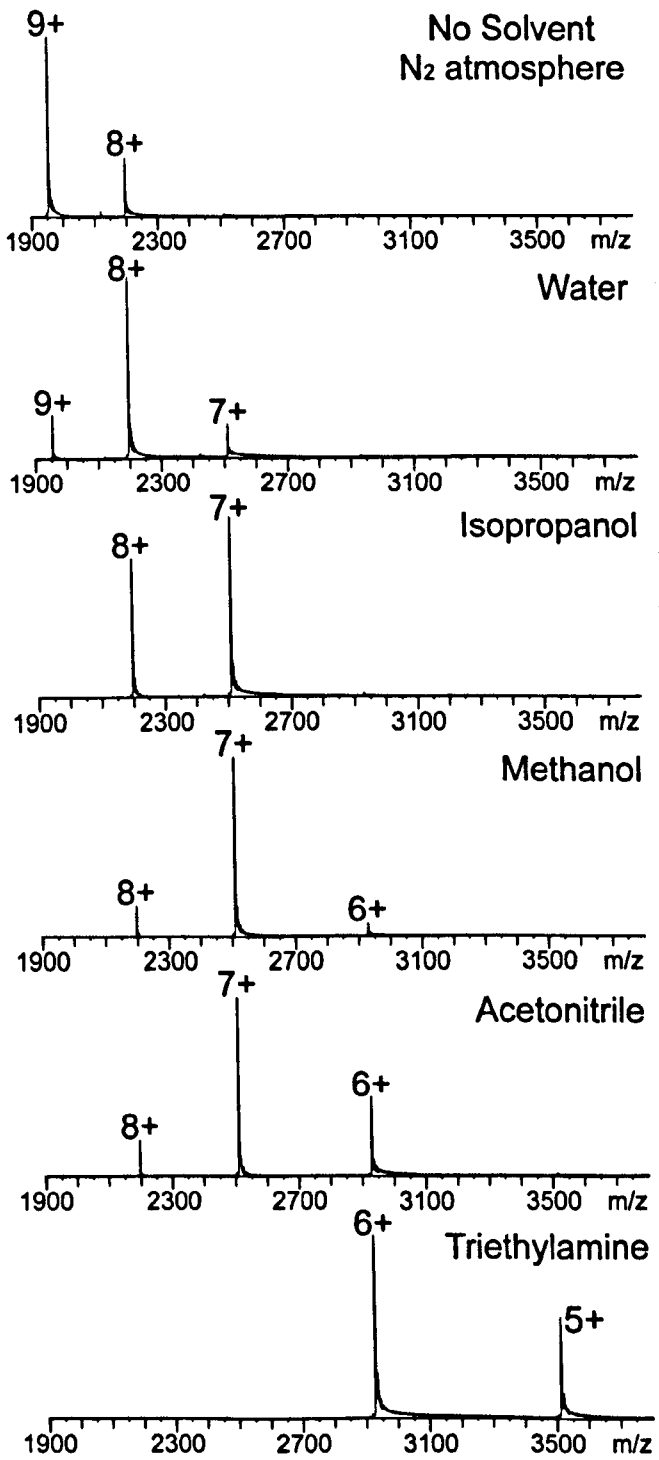

Figure 3.2.2 ESI spectra of myoglobin (2μM) sprayed from 25mM ammonium acetate in a closed source. Each spectrum was recorded with a different solvent (approximately 5ml) present within the source in an open top container. The values were obtained from reference [157]

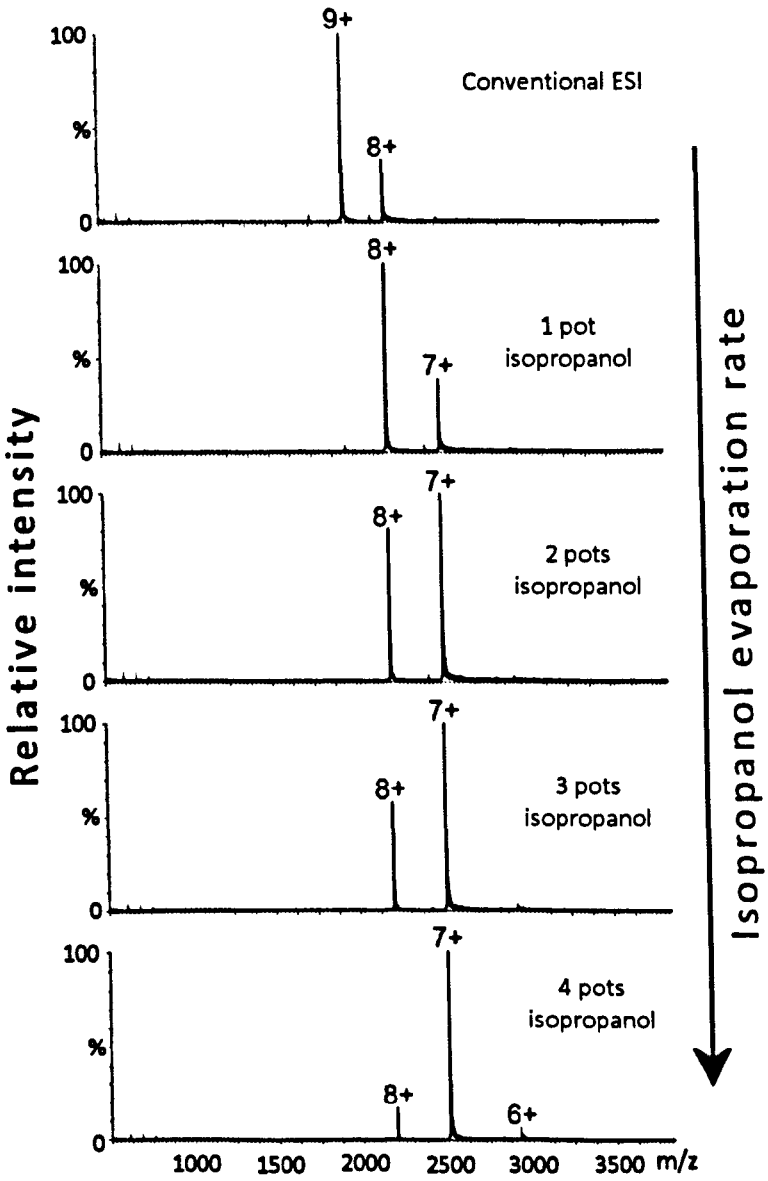

Figure 3.2.3 ESI mass spectra of 2 μM myoglobin sprayed from 25 mM ammonium acetate, under exposure to isopropanol vapour. Increasing degrees of charge reduction are observed upon introduction of each additional container to the source.

Apparently, the vapour pressure of isopropanol would remain constant regardless to quantity of liquid solvent present. However, the condensed solvent and its vapour are not in equilibrium due to the influence of the nebuliser gas (nitrogen) flow which constantly flushes the source. In addition to this experiment, the effect of volatility was also investigated by reducing the evaporation rate of a high volatile

solvent (acetonitrile). This was achieved by placing inside the ESI source a reservoir containing frozen acetonitrile and continuously acquiring data as the acetonitrile was progressively melting (Figure 3.2.4).

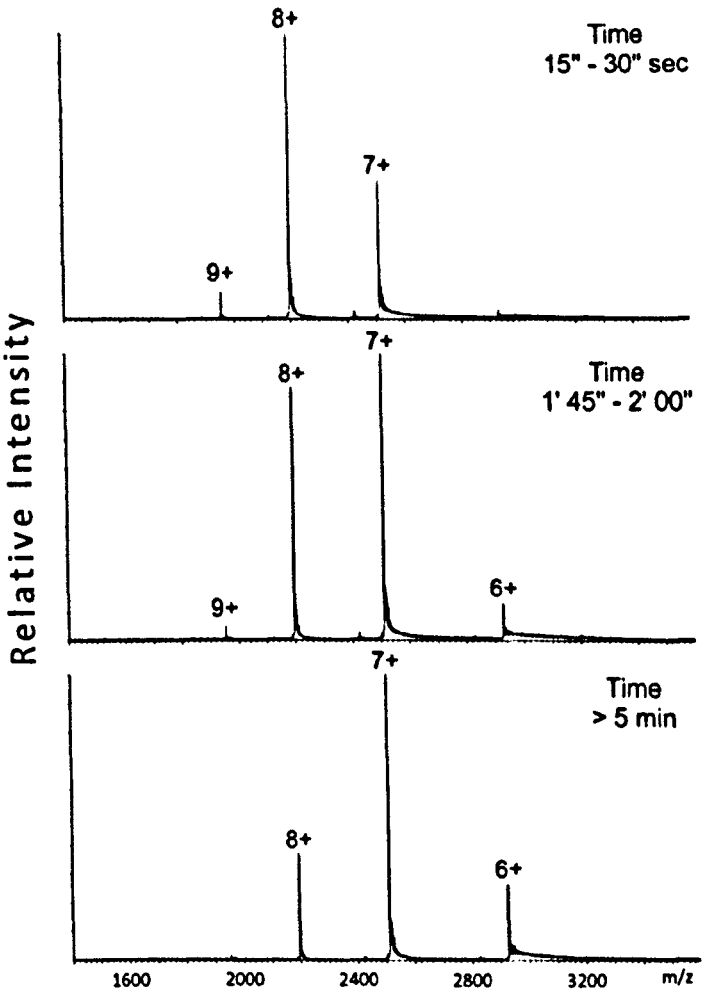

Figure 3.2.4 ESI mass spectra of 2 μM myoglobin sprayed from 25 mM ammonium acetate, under exposure to acetonitrile vapour.

It is notable that all solvents used in the above experiments, with the exception of triethylamine, exhibit lower gas-phase basicities than the desolvated myoglobin ions (~ 822 kJ·mol^{-1}) [148]. This suggests that proton transfer must occur at the level of charged droplets, where proton transfer from H_3O^+ to neutral solvent would be energetically favourable. This is supported by the fact that the ions generated in a

typical ESI process are believed to be largely solvated therefore proton competition must utilise neutral solvent vapour and charged water droplets.

The presence of alkali metal adducts in biomolecules has been proved problematic for ESI-MS. For example, it has been shown that alkali metal cations can destabilise the interaction between a protein and its ligand by lowering the activation barrier to dissociation [158]. In addition, there is a reduction in the signal-to-noise ratio for an adducted ion when compared with a purely protonated ion. Therefore, a method that reduces the adduction of alkali metal ions would be very useful. Figure 3.2.5 shows the nanoESI mass spectra of a myoglobin sprayed from 25 mM ammonium acetate obtained under laboratory atmosphere conditions and under exposure to acetonitrile vapour. Both spectra were acquired from the same sample sprayed from the same nano-tip emitter.

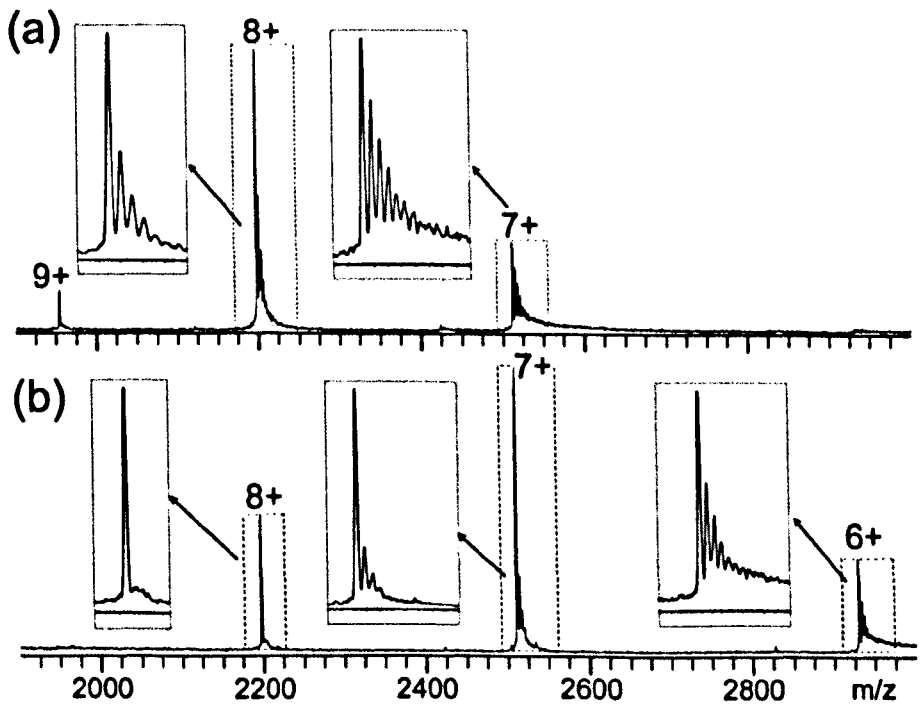

Figure 3.2.5 nanoESI of 2 μM myoglobin sprayed from 25 mM ammonium acetate solution under (a) open laboratory atmosphere and (b) exposure to acetonitrile vapour.

In both cases, it is clear that adduction is more pronounced for lower charge states. However, in case of charge reduction (Figure 3.2.5b), a reduction in adducts was also observed. By adding the intensities of all adducts across the charge states and expressed them as percentage of the summed protonated intensities, a decrease in total adduction, from 52 % to 34 % was determined. From the proposed a charge transfer mechanism at the droplet stage of the electrospray process, it seems plausible to suggest that acetonitrile favours the removal of alkali metal cations over protons, possibly via multiple coordination of the metal.

In order to test the feasibility of this straightforward charge reduction approach, which requires only the exposure of electrospray plume into solvent vapour, a series of examples where charge state is crucial, was selected from the literature. A recent study has shown that different dissociation pathways are achieved when different charge states are subjected to CID [142]. The study showed that CID of specific charge states (15+, 11+ and 9+) of the homotetrameric TTR complex yielded different products, result in asymmetric charge partitioning in case of the 15+ charge state and symmetric partitioning in case of 11+ charge state. The subunits derived from the dissociation of the former (15+) exhibited significant unfolding whereas those subunits generated by the latter (11+) retain near 'native-like' geometries. The charge states were formed by conventional nanoESI (charge states 12+ to 15+) and by the use of solution based additives, such as TEAA (in case of 11+) and TEAA with A118C6 (in case of 9+) [142]. Given that the most important information in a structural biology sense were derived from intermediate charge states that were created by charge reduction, we tested the applicability of the solvent (acetonitrile) vapour exposure approach to this system. Figure 3.2.6a and b shows the mass spectra of hTTR sprayed from 25 mM ammonium acetate under conventional nanoESI and in the presence of acetonitrile vapour.

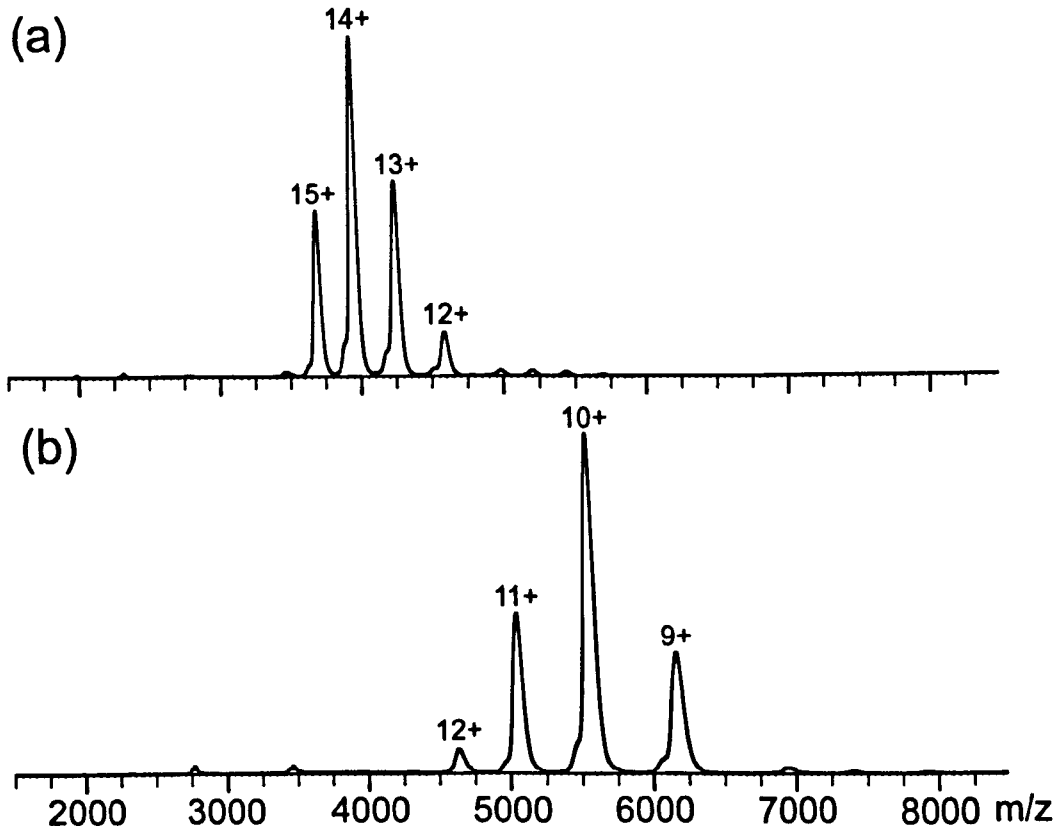

Figure 3.2.6 NanoESI spectra of hTTR (2.5 μM) sprayed from 25 mM ammonium acetate (a) under atmospheric conditions and (b) in the presence of acetonitrile vapour

It is notable that the degree of charge reduction obtained by solvent (acetonitrile) vapour exposure was between the levels obtained by the solution based additives, TEAA and TEAA + A118C6, respectively. Moreover, this method allowed access to both 11+ and 9+ charge states, which were proven to be the most important ones. [142]

A weak hydrophobic protein-protein system, the Ub•UQ1, was also used to further demonstrate useful biological applications of this method. The association between Ub and UQ1 is driven by hydrophobic interactions, which are significantly weaker in the absence of water. It has therefore been a notable challenge to maintain, within the desolvated environment of the mass spectrometer, complexes that are driven by these forces. Illustrated in Figure 3.2.7a, is the ESI mass spectrum of Ub and UQ1

sprayed from 25 mM ammonium acetate. The $(Ub+UQ1+7H^+)^{7+}$ ion is observed at 1896 m/z. Quadrupole isolation of this ion (Figure 3.2.7b) shows that it is readily dissociated into its components (Ub 4+ and UQ1 3+) without the elevated collision energy. Ion mobility measurements were applied to this complex to determine its CCS. Figure 3.2.7c shows the drift trace of this species, which is presented on a CCS axis. The dashed line represents the theoretical CCS (1457 $Å^2$) as calculated by a "hybrid" PA–TM (projection approximation, trajectory method) method (*see* Chapter 2) of the available NMR structure of the complex (PDB: 2JY6). As illustrated in Figure 3.2.7c, the experimentally measured CCS for the 7+ complex ion was 1703 $Å^2$. When measured in the presence of acetonitrile vapour, charge states of the complex were effectively reduced to 6+ and 5+ (Figure 3.2.7d). Additionally, no complex dissociation was observed post quadrupole isolation of the $(Ub+UQ1+6H^+)^{6+}$ as demonstrated in Figure 3.2.7e. Presumably, this is principally a result of lowering the kinetic energy transferred to the complex throughout the MS instrument and reducing perturbation of the complex by protonation. The compact nature of the complex was confirmed when analysing the resulting drift trace for this ion (Figure 3.2.7f), which was highly Gaussian and in good agreement with the theoretically calculated CCS, indicative of an ion that has not undergone gas–phase collisional activation and where there is little Coulombic repulsion.

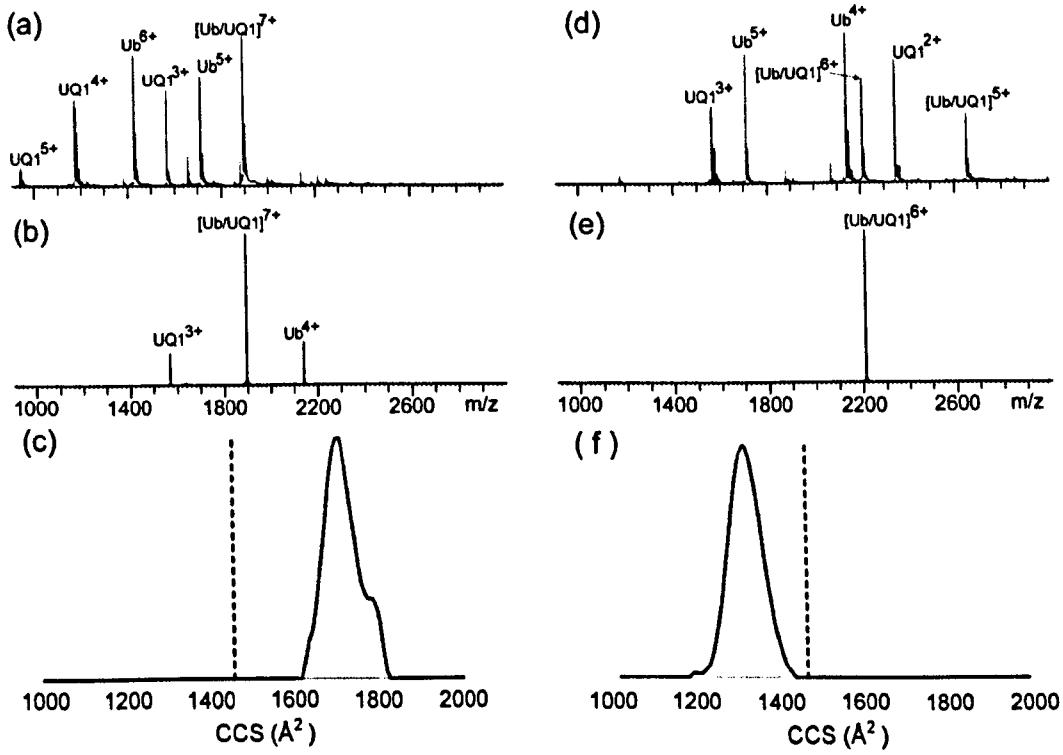

Figure 3.2.7 ESI mass spectra of Ub (4 μM) and UQ1 (16 μM) complex, sprayed from 25mM ammonium acetate solution under (a) atmosphere conditions and (d) exposure to acetonitrile vapour. Spectra of quadrupole isolated Ub•UQ1 complex charge states 7+ (b) and 6+ (e). Ion mobility drift time converted to a CCS axis, of the Ub•UQ1 complex charge states 7+ (c) and 6+ (f).

To further investigate whether exposure of the electrospray plume to acetonitrile vapour induces any conformational changes to gas-phase protein ions of a specific charge state, we have performed IM-MS analysis of gas-phase myoglobin ions generated under standard ESI process (25 mM ammonium acetate) and under the exposure of ESI to acetonitrile vapour. Illustrated in Figure 3.2.8 are the IM drift traces of the 8+ myoglobin ions obtained by conventional electrospray process (blue trace) and after exposure of the electrosprayed droplets to acetonitrile vapour (red trace). The latter shows a slightly narrower distribution of gas-phase conformers than the former. The difference is not significant though, and therefore, it can be concluded that solvent exposure has no effect on the mobility of the ions, indicating that the method does not adversely affect protein structure.

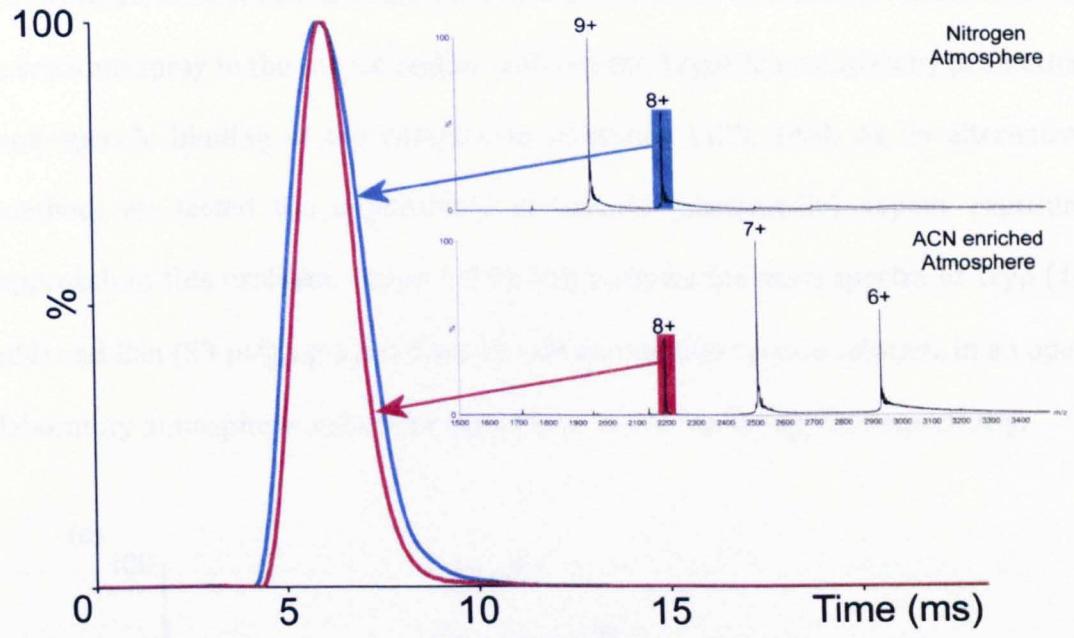

Figure 3.2.8 IM drift traces for the 8+ myoglobin ions obtained by standard ESI (blue trace) and under exposure to acetonitrile vapour (red trace).

Clearly, the aforementioned Ub•UQ1 protein–protein system demonstrates how lower charge states can be beneficial in reducing the perturbation of protein complexes during ionization in the mass spectrometer. Additional benefits of using a charge reduction method can be also seen in MS experiments designed to measure apparent solution based affinity constants (K_a) of protein–ligand interactions. As demonstrated by the example of Ub•UBD above, non–polar hydrophobic forces are greatly reduced in the absence of water. Therefore, preserving these interactions upon transition to the gas–phase is crucial for the measurement of a representative degree of binding. Several studies have successfully demonstrated the ability of ESI–MS to preserve such interactions [17, 133, 159-162], however, the determination of affinity constants for a variety of non–covalent complexes has proved problematic [154, 163]. For example, the complex between trypsin (Tryp) and its inhibitor benzamidine (Bzn) is destabilised in the gas–phase and it was proved to be extremely challenging to be studied using ESI–MS [154]. Two studies by Klassen and

co-workers, have shown that the use of imidazole either as a solution additive, or as a separate spray in the source region, stabilise the Tryp•Bzn complex by promoting non-specific binding of the complex to imidazole [133, 144]. As an alternative method, we tested the applicability of solvent (acetonitrile) vapour exposure approach to this problem. Figure 3.2.9a and b shows the mass spectra of Tryp (12 μM) and Bzn (53 μM), sprayed from 10 mM ammonium acetate solution, in an open laboratory atmosphere and under exposute to acetonitrile vapour, respectively.

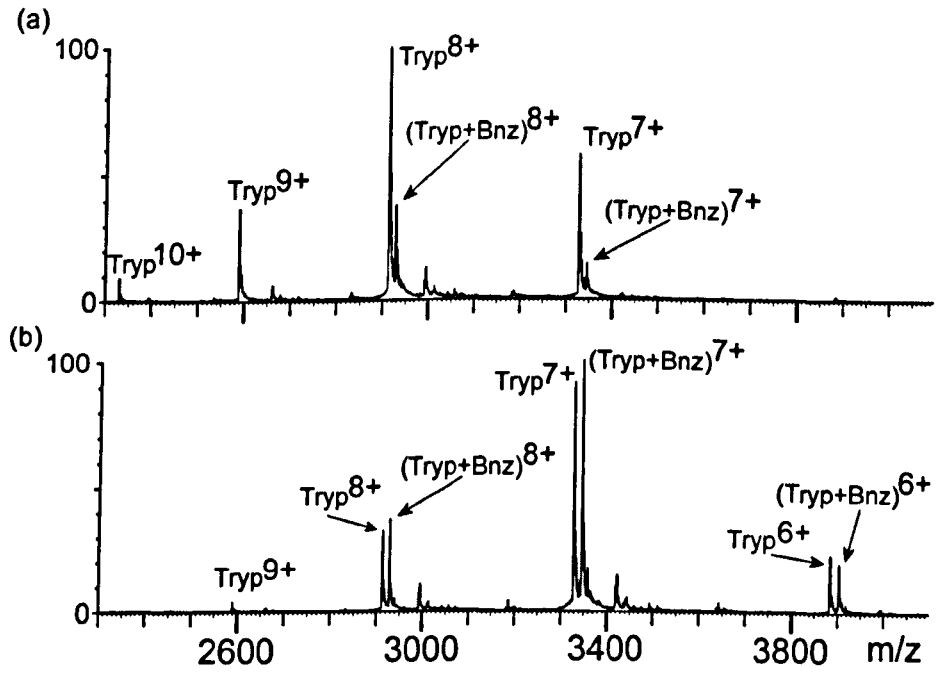

Figure 3.2.9 NanoESI spectra of 12 μM trypsin (Tryp) and 52 μM benzamidine (Bzn) sprayed from 10 mM ammonium acetate in an open laboratory atmosphere conditions (a) and under exposure to acetonitrile vapour (b).

In the case of conventional nanoESI (Figure 3.2.9a), the most abundant distribution corresponds to that of unbound trypsin $[Tryp + nH]^{n+}$ ions ranging in charge state between n=7–10. A small distribution for the $[Tryp–Bzn + nH]^{n+}$ complex at charge states n=7 and 8 is also detectable. The calculated K_a value (see Chapter 2) from this spectrum is 0.5×10^4 M^{-1}, which is significantly lower than the previously reported K_a value of 2.6×10^4 M^{-1} (taken from kinetic (K_i) measurement) [164] and of values

between 1.9×10^4 M^{-1}–2.1×10^4 M^{-1} determined by direct nanoESI-MS approach combined with imidazole [133, 144]. In contrast, the K_a determined from the spectrum illustrated in Figure 3.2.9b is 2.2×10^4 M^{-1}, which is in a good agreement with the literature values reported previously. Thus, the simple exposure of the electrospray plume to acetonitrile vapour is effectively capable of stabilise weak gas-phase protein-ligand interactions.

3.3 Conclusions

This chapter has shown that exposure of the electrospray plume to solvent vapours, and particularly to acetonitrile vapour, is a simple and effective method that can be used to decrease protein ion charge states and reduce cation-adduct formation. The fidelity of the method has been successfully tested in a number of MS experiments, which include examples of an intact protein, a protein-protein association and a protein-ligand complex. Moreover, the results of the charge reduction method that is described in this chapter were also compared with results obtained by other techniques. In all the cases, solvent exposure method was proven to effectively reduce charge states to a similar or even higher degree.

Lowering charge states reduces Coulombic repulsion-driven unfolding and dissociation events in the gas-phase, decreases amount of kinetic (hence internal) energy gained, and eventually assists the preservation of weak interactions upon their transfer to gas-phase. The applicability of solvent exposure method in studies of weak non-covalent interactions has been successfully demonstrated in the cases of [Tryp-Bzn] complex and [Ub-UQ1] complex.

As has been demonstrated, the degree of charge reduction is clearly dependant on, the gas-phase basicity (GB) and the volatility of the solvent. The fact that charge

state reduction is obtained using solvents of substantially lower GB values than the desolvated protein ions, lead us to the conclusion that the effect must occur between the charged droplets and solvent vapour while the protein is still solvated. The proposed droplet–solvent vapour competition mechanism it is also supported by the generally accepted belief that total desolvation is not achieved in the source region of a standard ESI source.

Furthermore, an earlier study by Fernadez de Mora [33] has provided a relationship between the mass of a spherical globular protein and the predicted maximum charge state, which is given by:

$$Z = 8\pi/e(\gamma\varepsilon_0 R^3)^{1/2}$$

in which, γ is the surface tension of the water droplet, ε_0 the electrical permittivity of vacuum, e the elementary charge and R the radius of the droplet. By assuming that the density of a protein is similar to that of water and that the radius of a protein is correlated to its molecular weight, the above equation can be rewritten as:

$$Z = 0.078\, M^{1/2}$$

in which M is the mass of the protein in Daltons [160].

From the above, it is clear that the highest value of charges that will be found on a spherical globular protein depend upon the solution parameters of the surface tension and the final droplet radius. Therefore, a droplet–solvent vapour process that would result in increased surface tension will consequently reduce the maximum charge state of a protein.

CHAPTER 4

PROBING AFFINITY & UBIQUITIN LINKAGE SELECTIVITY OF UBIQUITIN-BINDING DOMAINS

4.1 INTRODUCTION

It is well established that Ub interacts with UBDs through non-covalent associations which are driven by hydrophobic interactions. These interactions may promote covalent Ub attachment (ubiquitination) and direct the fate of ubiquitinated proteins leading to regulation of cellular processes [82]. Examples of these include interactions with the UBA domain of UQ1, a protein which acts as a presenilin regulator [115], and the UBA domains of hHR23A protein which mediates the delivery of substrates to the 26S proteasome [112] and the regulation of p53 [165], as well as nucleotide excision repair [166]. Moreover, associations between the vesicular trafficking protein Rabex-5 and Ub are mediated by a RUZ (Rabex-5 ubiquitin binding ZnF) domain which interacts with an Asp58-centred region and a MIU domain that binds the Ile44-centred patch on Ub [98]. The deubiquitinating (DUB) enzyme isopeptidase-T (Iso-T or USP5) carries out the dissociation of free poly-Ub chains into mono-Ub moieties. Since the interaction is mediated by a ZnF Ub-protease (UBP) domain, which recognizes the C-terminal Gly residue of Ub [106], it is believed that the ZnF UBP domain of IsoT (hereon refer to as IsoT-ZnF) has no preference for chain length or topology. The specific recognition of poly-Ub chain length and topology by UBDs is only now beginning to emerge. Recent studies have revealed that the UQ1-UBA domain does not possess any binding preference

for poly-Ub chain linkage [101, 102]. In contrast, the hHR23A-UBA domains are reported to show a clear selectivity for Lys48-linked over Lys63-linked poly-Ub chains [100, 101, 112, 167].

The intrinsic importance of UBDs has also been highlighted by their recent links to a variety of pathological conditions, including cancer and immunodeficiency [168]. In addition, mutations in UBDs are important in human diseases, including the skeletal disorder Paget's disease of the bone [169]. The importance of quantifying UBD binding affinities is exemplified by the Vps36 protein, which although it appears to bind Lys63-linked or linear Ub_2 equally well when using pull-down assays, fluorescence studies have shown that it preferentially binds to the former [170]. Methods that are currently employed to study Ub•UBD non-covalent associations include; nuclear magnetic resonance (NMR) [100, 102, 171, 172], surface plasmon resonance (SPR) [97, 167], isothermal titration calorimetry (ITC) [106] and fluorescence anisotropy (FA) [173]. NMR and SPR experiments have been used to probe the specificity of a number of UBDs for mono-Ub and poly-Ub chains [97, 100, 102, 167, 171, 172] and have contributed significantly to our understanding of the often weak non-covalent interactions of Ub. However, NMR and ITC require substantial quantities of protein, often at non-physiological concentrations, and are relatively low-throughput. Although SPR is a more sensitive and rapid method, it can suffer from artefacts associated with immobilization of one of the protein binding partners such as avidity effects. In addition, studies on complexes where the mass of poly-Ub•UBD non-covalent assembly exceeds the 40 kDa may be very challenging by NMR. Given these considerations, the development of a rapid and highly sensitive method for studying the affinity and specificity of UBDs would revolutionize the study of these crucial regulatory complexes.

Several studies have successfully demonstrated potential use of ESI-MS as a tool to probe non-covalent associations. These studies have also shown that the binding constants determined by ESI-MS experiments were found to be in a good agreement with those obtained by other biophysical methods, such as NMR, SPR and ITC [17, 133, 159-162]. Other studies, however, have concluded that the affinity constants for a variety of non-covalent complexes could not be determined by ESI-MS, or the values where significantly different from solution measurements [154, 163]. These effects have often been attributed to the instability of the complex in the gas phase due to the absence of stabilizing hydrophobic effects. Liu and Konermann [174], have suggested that the determination of the binding affinity for a protein-protein assembly by ESI-MS can be challenging due to potential differences in the behaviour of individual and complexed proteins in the vacuum of the MS. However, under carefully optimised instrumental conditions it is feasible to study protein-protein interactions quantitatively by ESI-MS [174]. The association between Ub and UBDs is driven by hydrophobic interactions, which are significantly weaker in the absence of water. It is therefore a considerable challenge to maintain, within the desolvated environment of the MS, complexes that are driven by these forces. This chapter describes the successful development of an ESI-MS approach for the quantitative study of the weak hydrophobic interactions seen in many Ub•UBD complexes. Principally, it shows that the ESI-MS method can report binding constants in good agreement with solution data obtained by other biophysical techniques and that the complexes observed arise due to specific interactions between binding surfaces. In addition, UBD preference for poly-Ub length and topology can be revealed. The applicability of ESI-MS in studies of Ub ternary complexes involving multi-site UBD interactions is also demonstrated.

4.2 Results and Discussion

Key to the success of this method is the ability of ESI-MS to preserve the Ub•UBD interactions upon transition to the gas-phase, hence allowing an accurate representation to the degree of binding to be measured. A series of previously studied Ub•UBDs complexes was selected in order to evaluate the potential use of MS as a tool for studying Ub•UBD interactions. Particularly, representative UBDs from two categories were chosen; *helical domains* including the single α-helix domain MIU and the three-helix bundles, UQ1-UBA domain and hHR23A-UBA2 domain; *ZnF domains* including the IsoT-ZnF, commonly referred as ZnF-UBP domain. Comparison of values measured by ESI-MS (Table 4.2.1) with those taken from the literature (Table 4.2.1, values in parenthesis) shows an excellent agreement, indicating that the ESI-MS method reported in this Chapter is suitable for quantifying these biologically important interactions.

Table 4.2.1 Apparent dissociation constants (K_d) values for UBD•(poly-)Ub interactions

	K_d (μM)[a]						
UBD	Ub	Lys48-Ub_2	Lys 63-Ub_2	Lys 11-Ub_2	Lys 27-Ub_2	Lys 48-Ub_4	Lys 63-Ub_4
UQ1-UBA	22±2 (20±5)[102]	15±2 (4±5)[102]	24 ± 2 (18±18)[102]	21±2	35±3	13±2 (1.2)[101]	15±2 (0.5)[101]
UBA2	200±14 (400±100)[100	18±2 (18±7)[100]	126±18 (210±100)[171	72±10	81±10	8±1 (7.7)[101]	>70[b] (28)[101]
MIU	36±4 (29±1)[97]	11±2	16±2	12±2	ND	ND	ND
IsoT-ZnF	2.3±0.2 (2.8±0.1)[106]	3.6±0.8	2.8±0.3	1.7±0.2	ND	ND	ND

[a] The K_d values reported here (mean ± SD) were averaged from values measured at different concentrations. Given in parenthesis the previously reported values obtained by NMR or SPR.

[b] Complex signal below the limit of detection, which equates to a K_d of 70 μM for this system using the available concentration of 0.5 μM.

ND, not determined

The apparent K_d values shown in Table 4.2.1 were determined from titration experiments where the concentration of Ub component was kept constant while the concentration of UBDs was varied. The resulting solutions were then subjected to ESI-MS analysis and the ratios (R) of the total signal intensities attributed to free and UBD-bound Ub ions, were recorded (*see* Chapter 2, equation 2.2.2). The apparent K_ds were then calculated using the equation 2.2.6 (*see* Chapter 2). An example of the calculation process is shown below (Table 4.2.2).

Table 4.2.2 Determination of the apparent K_d value of the Ub•UQ1-UBA complex. $[Ub]_0$ and $[UBD]_0$ are the initial concentrations of Ub and UBD components, respectively. $I(Ub^{n+})$ and $I((Ub•UBD)^{n+})$ are the signal intensity attributed to free and bound Ub ions, respectively. n+ is the observed charge state.

$[Ub]_0$ = 0.5 μM		$[UBD]_0$ = 1 μM	
n+	$I(Ub^{n+})$	n+	$I((Ub•UBD)^{n+})$
4	471	5	13
5	488	6	31
6	38		
∑n = 997		∑n = 44	
Ratio (R) = 22.7			
K_d = 22.2 μM			

$[Ub]_0$ = 0.5 μM		$[UBD]_0$ = 2 μM	
n+	$I(Ub^{n+})$	n+	$I((Ub•UBD)^{n+})$
4	459	5	27
5	533	6	74
6	49		
∑n = 1041		∑n = 101	
Ratio (R) = 10.3			
K_d = 20.2 μM			

$[Ub]_0$ = 0.5 μM		$[UBD]_0$ = 3 μM	
n+	$I(Ub^{n+})$	n+	$I((Ub•UBD)^{n+})$
4	477	5	46
5	528	6	115
6	47		
∑n = 1052		∑n = 161	
Ratio (R) = 6.5			
K_d = 19.2 μM			

$[Ub]_0$ = 0.5 μM		$[UBD]_0$ = 4 μM	
n+	$I(Ub^{n+})$	n+	$I((Ub•UBD)^{n+})$
4	453	5	48
5	515	6	132
6	41		
∑n = 1009		∑n = 180	
Ratio (R) = 5.6			
K_d = 22.0 μM			

$[Ub]_0$ = 0.5 μM		$[UBD]_0$ = 6 μM	
n+	$I(Ub^{n+})$	n+	$I((Ub•UBD)^{n+})$
4	456	5	75
5	521	6	195
6	48		
∑n = 1052		∑n = 161	
Ratio (R) = 22.3			
K_d = 22.3 μM			

$[Ub]_0$ = 0.5 μM		$[UBD]_0$ = 8 μM	
n+	$I(Ub^{n+})$	n+	$I((Ub•UBD)^{n+})$
4	445	5	85
5	502	6	219
6	47		
∑n = 994		∑n = 304	
Ratio (R) = 3.3			
K_d = 25.8 μM			

averaged K_d = 22 ± 2 μM

It is worth noting that multiple replicates (at least 3) of each titration sample were performed. For convenience, the example (Table 4.2.2) shows the results obtained from only one titration series. In addition, to minimize the time of calculations and calculation errors, a K_d calculator software has been developed (*see* Appendix).

4.2.1 Optimisation of ESI-MS conditions

It has been mentioned previously that the study of protein-protein interactions would be feasible under carefully optimised instrumental conditions. To do so, the relatively "strong" (see Table 1.2) Ub•UQ1-UBA complex (K_d = 20 ± 5 μM) [102] was chosen as a reference to optimise the instrumental parameters (*see* Chapter 2). Illustrated in Figure 4.2.1a is the ESI mass spectrum of the (Ub•UQ1-UBA) complex sprayed from 25 mM ammonium acetate. The 8+ and 7+ complex ions are observed at *m/z* 1659 and 1896, respectively. Quadrupole isolation of the $[Ub•UQ1\text{-}UBA+8H^+]^{8+}$ ion shows that it is readily dissociated into its components (Ub, 5+; UQ1-UBA, 3+) without elevated collision energy (Figure 4.2.2a). Presumably, this is principally a result of the relatively high kinetic (and hence internal) energy gained by the 8+ complex ion, and Coulombic repulsion between the binding partners. As a consequence the binding affinity determined from this spectrum (Figure 4.2.1a) was found to be 47 μM, which was more than two-fold lower compared to the previously reported literature values (K_d~20 μM). It has been previously discussed in Chapter 3, that lowering charge states reduces the amount of kinetic energy gained as well as decreases the Coulomb repulsion-driven unfolding and dissociation events in gas-phase; exposure of electrospray plume into acetonitrile vapour lead to charge reduction. Figure 4.2.1b shows the ESI spectrum of (Ub•UQ1-UBA) complex obtained in the presence of acetonitrile vapour. The charge states of the complex were effectively reduced to 6+ and 5+ at *m/z* 2612 and 2654, respectively. Additionally, no complex dissociation was observed post quadrupole isolation of the 6+ complex ion (Figure 4.2.2b). Under these conditions, Ub charge states are

distributed between 3+ (2856 *m/z*) and 6+ (1428 *m/z*), with the 4+ (2142 *m/z*) and 5+ (1714 *m/z*) ions the dominant peaks. Unbound domain is observed at 2351 *m/z* (2+) at 1568 *m/z* (3+) and at 1176 *m/z* (4+).

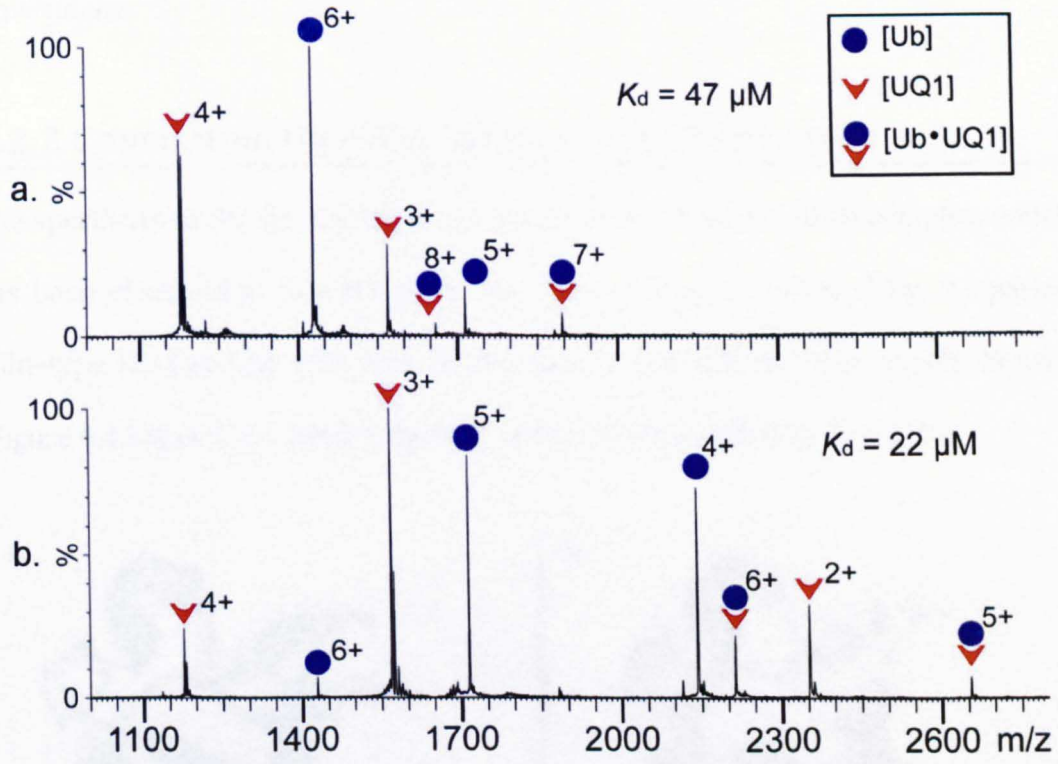

Figure 4.2.1 a) ESI mass spectra of Ub (0.5 µM) and UQ1–UBA (4 µM) complex, sprayed from 25mM ammonium acetate solution, b) ESI mass spectra of Ub (0.5 µM) and UQ1–UBA (4 µM) complex, sprayed from 25mM ammonium acetate solution in the presence of acetonitrile vapour.

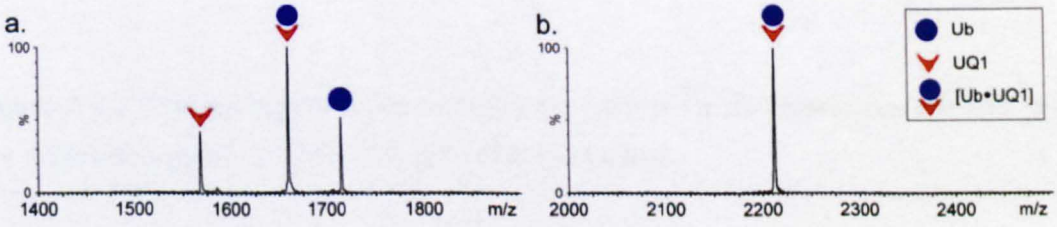

Figure 4.2.2 ESI mass spectra of quadrupole isolated Ub•UQ1–UBA complex charge states (a) 8+ and (b) 6+ of Ub (0.5 µM) and UQ1-UBA (4 µM) complex

It was observed that increasing the concentration of domain resulted in its dimerisation, which affects the determination of K_d and it must be considered in the K_d calculations. Therefore, to simplify calculations, we kept the concentration of the

domain below 6 μM, where negligible amount of dimer was formed. The mean apparent K_d value determined from these measurements was 22 ± 2 μM, which is in good agreement with 20 ± 5 μM from NMR [102] and 27 μM from SPR [101] experiments.

4.2.2 Confirming Ub•UBD Interaction Specificity

The specificity of the interaction and the formation of the Ub–UBD complex, which has been observed in this MS study was examined and confirmed by comparing wild-type Ub (wt-Ub) with two Ub mutants; a Leu8Ala/Ile44Ala double mutant (Figure 4.2.3a) and the deletion mutant Δ-Gly75/Gly76-Ub (Figure 4.2.3b).

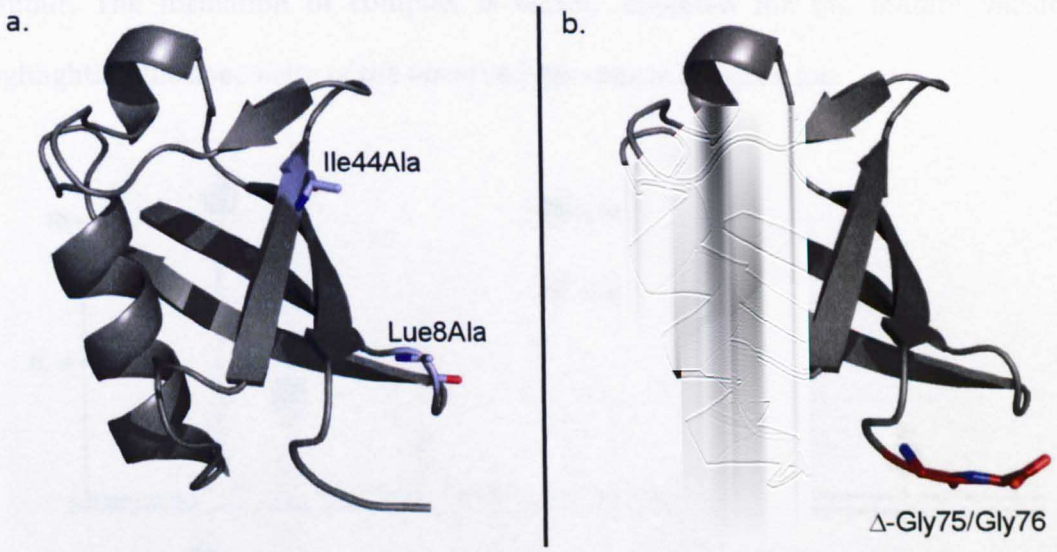

Figure 4.2.3 Cartoon representation of (a) the L8A/I44A Ub double mutant and (b) the deletion mutant Δ-G75/G76-Ub (PDB ID: 1UBQ)

4.2.2.1 Confirming specificity of helical domains

The Leu8Ala/Ile44Ala double mutant of Ub was used to test the specificity of the single α-helix domain MIU and the three-helix bundle UQ1-UBA, which are known to bind Ub *via* its Ile44-centred hydrophobic patch (Figure 4.2.4).

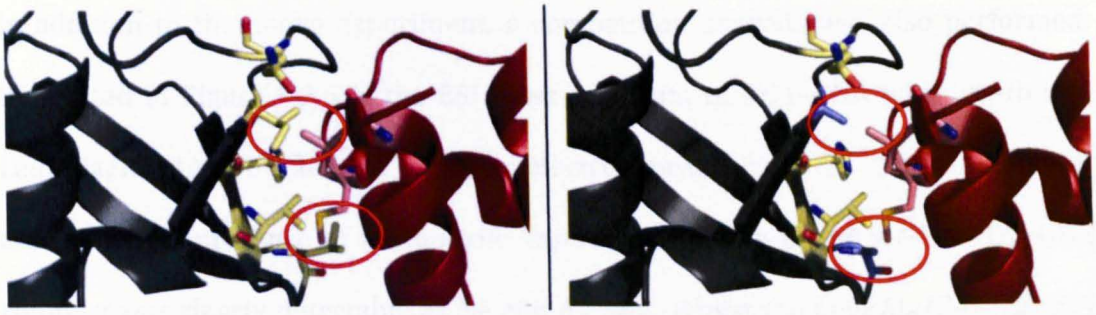

Figure 4.2.4 Cartoon representation of UQ1–UBA (red) complex with wt–Ub (left panel) and L8A/I44A Ub double mutant (right panel) (PDB ID: 2JY6)

Illustrated in Figure 4.2.5 is the ESI mass spectra obtained for the complex between UQ1 and either the wt–Ub or the Leu8Ala/Ile44Ala–Ub double mutant, electrosprayed from 25 mM ammonium acetate in the presence of acetonitrile vapour. The formation of complex is clearly depleted for the mutant variant highlighting the specificity of the observed gas–phase complex ion.

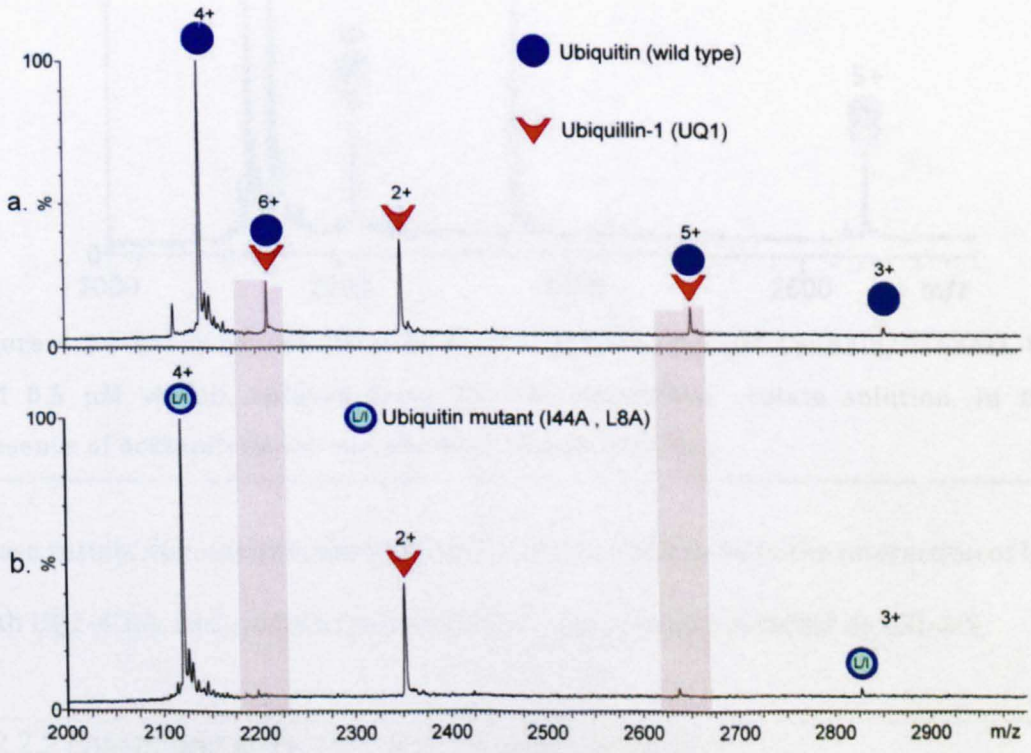

Figure 4.2.5 ESI mass spectrum of UQ1–UBA (2 μM) complex with a) wt–Ub (1 μM) and b) Leu8Ala/Ile44Ala (1 μM) double mutant, sprayed from 25mM ammonium acetate solution under acetonitrile vapour.

In addition to the above experiment, a competition analysis was also performed. Illustrated in Figure 4.2.6 is the ESI mass spectrum of UQ1–UBA with wt-Ub and Leu8Ala/Ile44Ala–Ub double mutant, electrosprayed from 25 mM ammonium acetate in the presence of acetonitrile vapour. Formation of the wt-Ub•UQ1–UBA complex was clearly detectable as 5+ and 6+ ions, whilst the Leu8Ala/Ile44Ala–Ub mutant complex with UQ1–UBA was barely detectable demonstrating the specificity of the interaction observed by ESI–MS method.

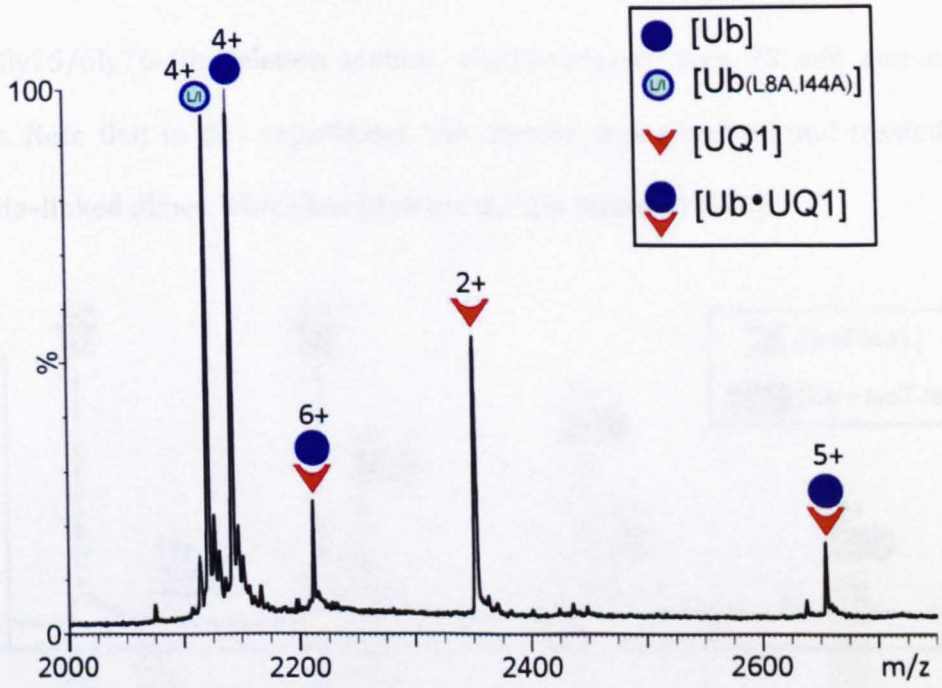

Figure 4.2.6 ESI mass spectrum of 4 μM UQ1–UBA, 0.5 μM Leu8Ala/Ile44Ala–Ub and 0.5 μM wt–Ub, sprayed from 25 mM ammonium acetate solution, in the presence of acetonitrile vapour, showing specific binding.

These results demonstrate the importance of Leu8 and Ile44 in the interaction of Ub with UQ1–UBA, and confirm the specificity of the complex detected by ESI–MS.

4.2.2.2 Confirming specificity of zinc finger domains

In contrast to the helical domains, the IsoT–ZnF domain interacts with Ub *via* the latter's C–terminal residues [106] (Figure 4.2.7). The Δ–Gly75/Gly76–Ub deletion mutant was used to test the specificity of this ZnF domain.

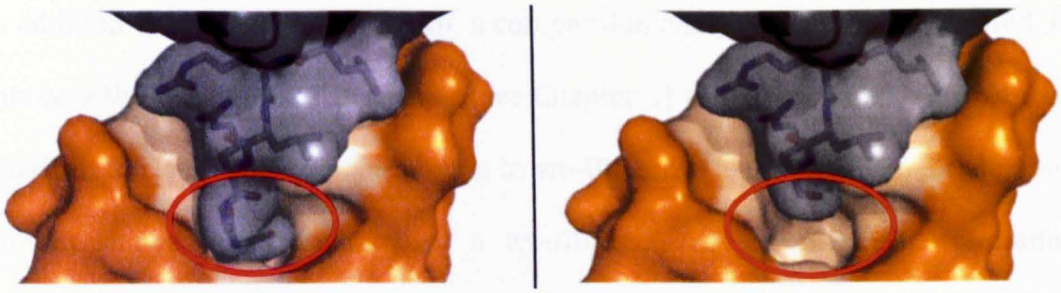

Figure 4.2.7 Cartoon representation of IsoT–ZnF (bright orange) complex with wt-Ub (left panel) and Δ–G75/G76–Ub mutant (right panel) (PDB ID: 2G45)

Figure 4.2.8 shows the ESI mass spectra of the IsoT–ZnF complex with a) wt–Ub and b) Δ–Gly75/Gly76–Ub deletion mutant, electrosprayed from 25 mM ammonium acetate. Note that in this experiment, the domain was observed and treated as a disulfide–linked dimer, which has been previously reported [106].

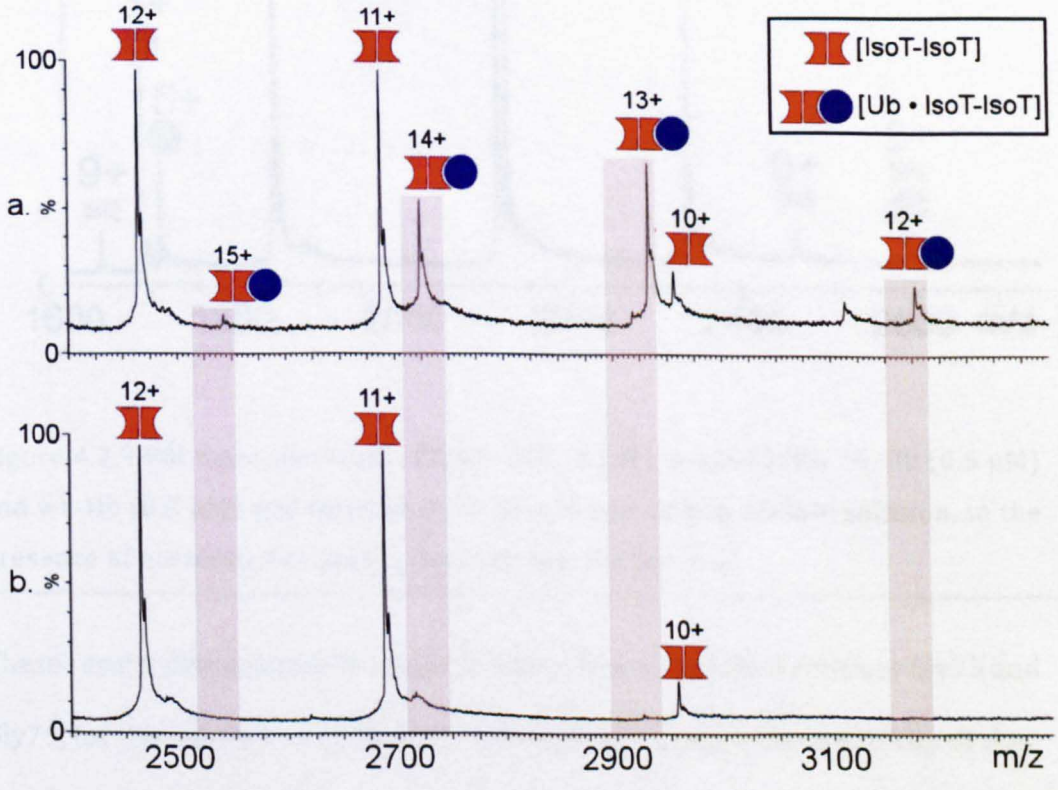

Figure 4.2.8 ESI mass spectrum of IsoT–ZnF (2 μM) complex with a) wt–Ub (1 μM) and b) Δ–Gly75/Gly76–Ub (1 μM) deletion mutant sprayed from 25mM ammonium acetate solution.

In addition to the above experiment, a competition analysis was also performed. In this case the reduced IsoT monomer (see Chapter 2) was used. Comparison of data obtained for IsoT–ZnF domain binding to wt–Ub and a Δ–Gly75/Gly76–Ub deletion mutant showed the formation of a wt–Ub•IsoT–ZnF complex. No association between Δ–Gly75/Gly76–Ub and the domain was observed (Figure 4.2.9).

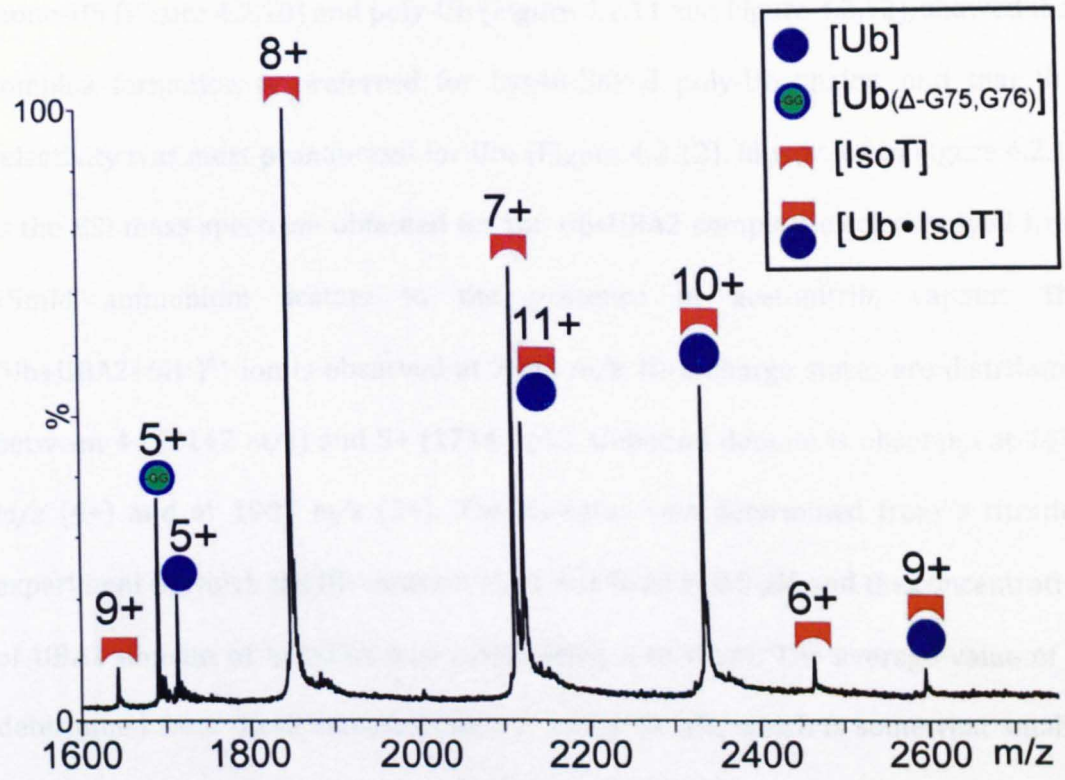

Figure 4.2.9 ESI mass spectrum of IsoT–ZnF (2 μM), Δ–Gly75/Gly76–Ub (0.5 μM) and wt–Ub (0.5 μM) and sprayed from 25 mM ammonium acetate solution, in the presence of acetonitrile vapour, showing specific binding.

These results demonstrate the requirement of the C–terminal residues Gly75 and Gly76, for the interaction of Ub with IsoT–ZnF, and confirm the specificity of the interaction observed by MS.

4.2.3 Specificity for poly-Ub chain topology

4.2.3.1 The case of the hHR23A–UBA2 domain

The UBA2 domain of hHR23A is known to demonstrate preferential binding to Lys48–linked poly-Ub over mono-Ub and Lys63–linked poly-Ub [100, 101, 112, 167]. Comparison of ESI–MS spectra obtained in this study for UBA2 complexes with mono-Ub (Figure 4.2.10) and poly-Ub (Figure 4.2.11 and Figure 4.2.12), showed that complex formation is preferred for Lys48-linked poly-Ub chains, and that this selectivity was most pronounced for Ub_4 (Figure 4.2.12). Illustrated in Figure 4.2.10 is the ESI mass spectrum obtained for the Ub•UBA2 complex, electrosprayed from 25mM ammonium acetate in the presence of acetonitrile vapour. The $(Ub+UBA2+6H^+)^{6+}$ ion is observed at 2382 *m/z*. Ub's charge states are distributed between 4+ (2142 *m/z*) and 5+ (1714 *m/z*). Unbound domain is observed at 1430 *m/z* (4+) and at 1907 *m/z* (3+). The K_d value was determined from a titration experiment in which the Ub concentration was fixed at 0.5 μM and the concentration of UBA2 domain of hHR23A was varied from 2 to 8 μM. The average value of K_d determined from these measurements is 200 ± 14 μM, which is somewhat smaller than the previously reported value 400 ± 100 μM [100].

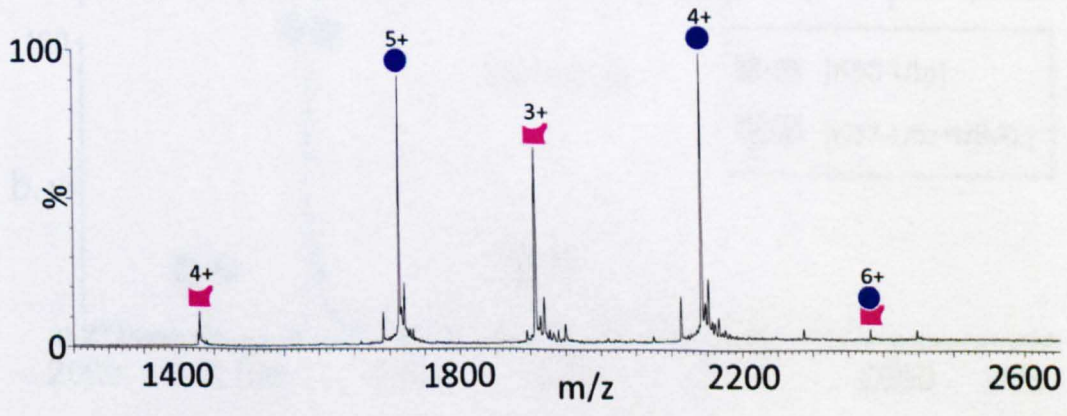

Figure 4.2.10 ESI mass spectrum of 0.5 μM Ub (blue) and 2 μM hHR23A–UBA2 (red), sprayed from 25mM ammonium acetate solution under acetonitrile vapour.

The ESI mass spectra obtained for UBA2 complex with Lys48– and Lys63–linked Ub_2, electrosprayed from 25mM ammonium acetate are shown in Figure 4.2.11. Likewise, Figure 4.2.12 shows the ESI mass spectra of UBA2 complex with Lys48– and Lys63–linked Ub_4. It is clear that formation of complex is preferred for Lys48-linked poly-Ub. ESI–MS apparent K_d values for UBA2 (Table 4.2.1) were found to be in good agreement with previously reported values obtained by NMR [100, 101, 171].

It is notable that charge reduction was not absolutely required to stabilize complexes between the UBA2 with Ub_2 and Ub_4 chains, as similar apparent K_ds were obtained with and without exposure to acetonitrile vapour. Charge reduction does, however, have the advantage of simplifying the spectrum of UBA2 and Ub_4 by preventing signal overlap.

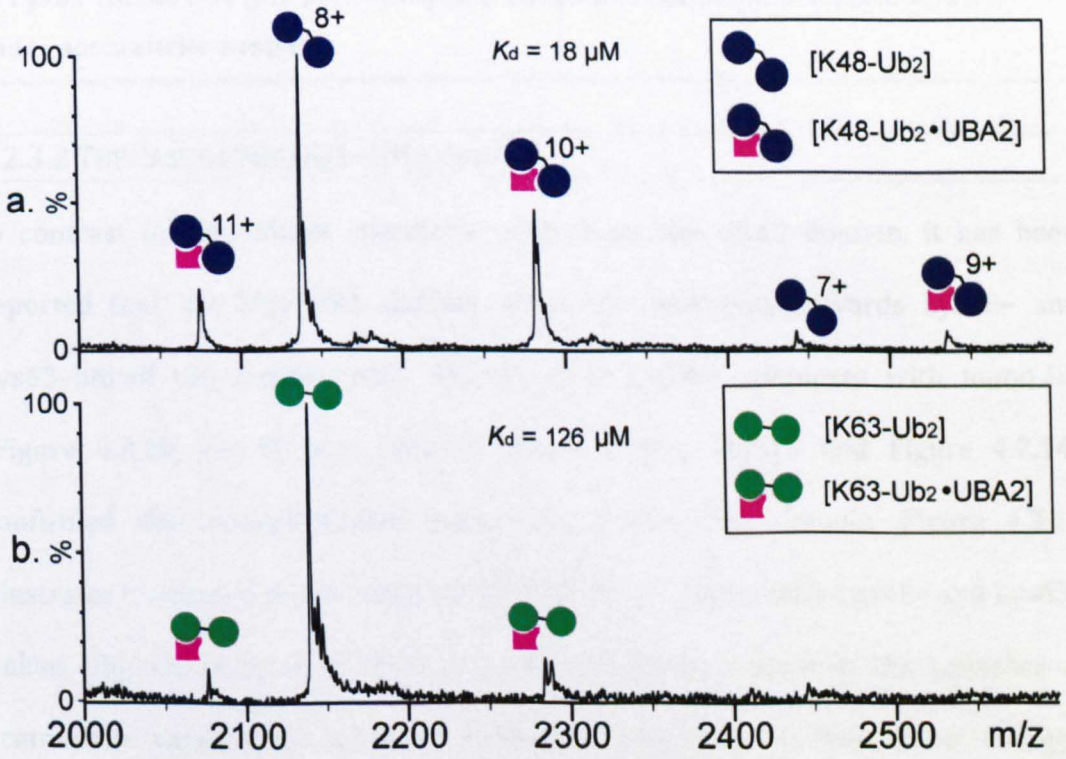

Figure 4.2.11 ESI mass spectra of UBA2 (4 μM) with: a) Lys48-linked Ub_2 (0.5 μM), b) Lys63-linked Ub_2 (0.5 μM), sprayed from 25 mM ammonium acetate solution.

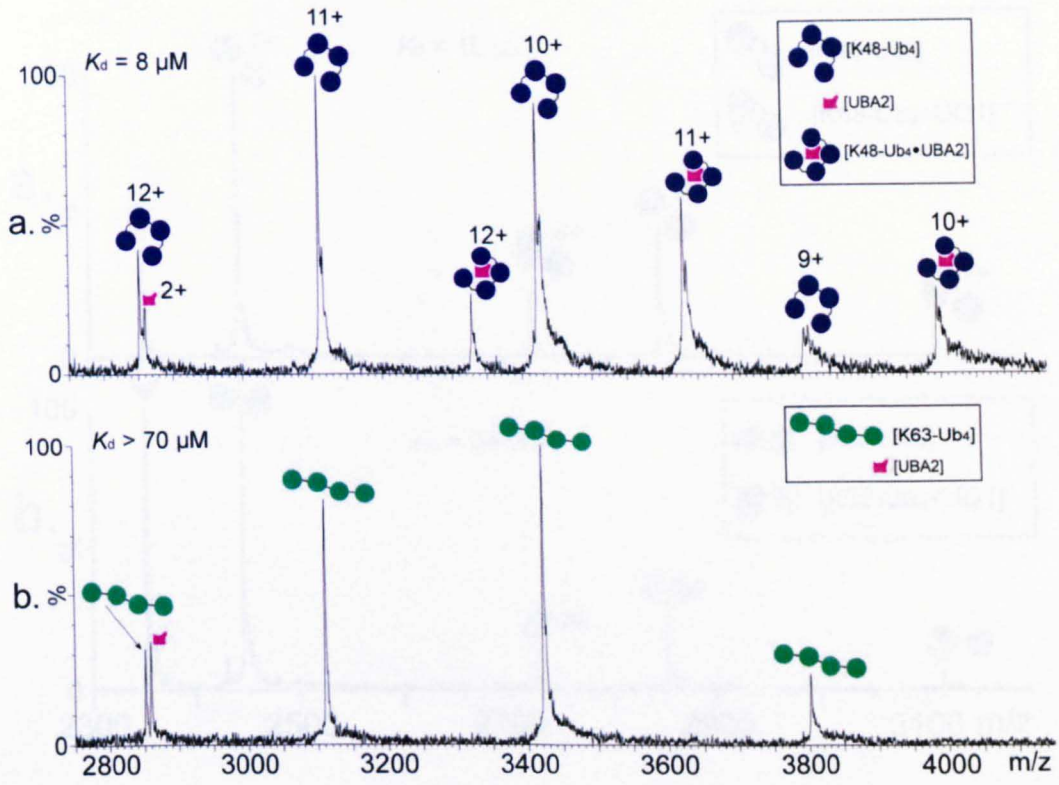

Figure 4.2.12 ESI mass spectra of UBA2 (4 μM) with: a) Lys48-linked Ub_4 (0.5 μM), b) Lys63-linked Ub_4 (0.5 μM), sprayed from 25 mM ammonium acetate solution under acetonitrile vapour

4.2.3.2 The case of the UQ1–UBA domain

In contrast to the linkage specificity evident for the UBA2 domain, it has been reported that the UQ1–UBA domain shows no selectivity towards Lys48– and Lys63–linked Ub_2 chains [102]. ESI–MS of UQ1–UBA complexes with mono-Ub (Figure 4.2.1b, see 0) and poly-Ub chains (Figure 4.2.13 and Figure 4.2.14) confirmed the aforementioned behaviour of UQ1–UBA domain. Figure 4.2.13 illustrates the mass spectra obtained for UQ1–UBA complex with Lys48– and Lys63–linked Ub_2, electrosprayed from 25 mM ammonium acetate in the presence of acetonitrile vapour. Formation of complex is observed for both chain linkages. Measured apparent K_ds for Lys48–linked Ub_2 (K_d = 15 ± 2 μM) and Lys63–linked Ub_2 (K_d = 24 ± 2 μM) were found to be similar in value and in good agreement with previously reported data (Table 4.2.1).

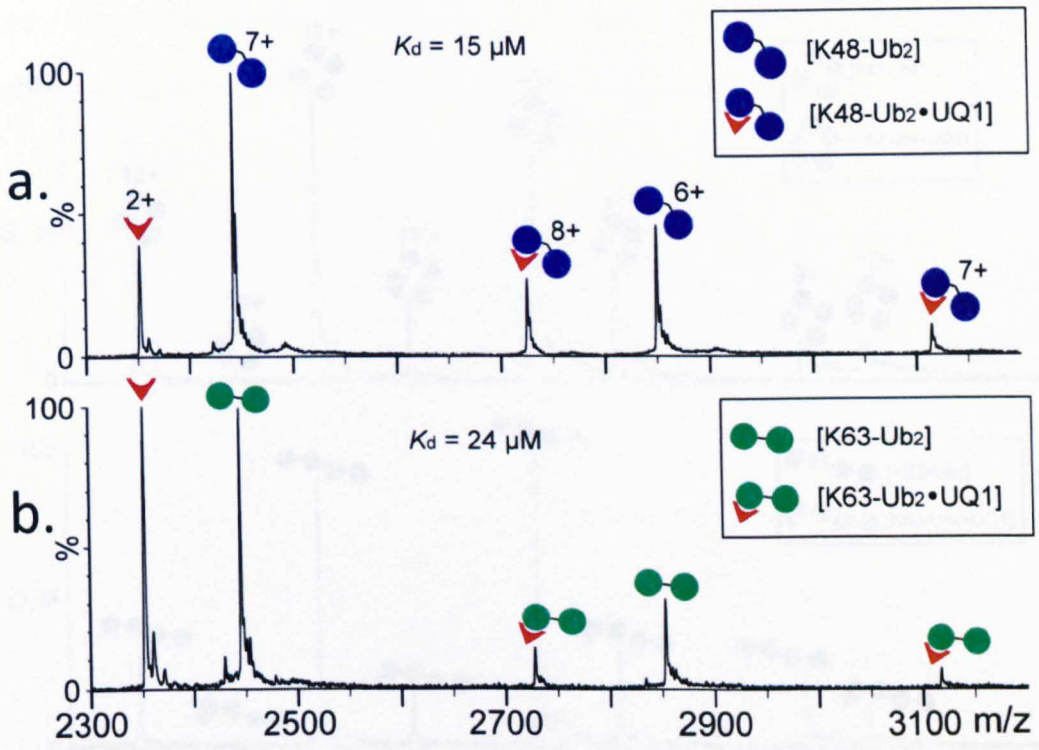

Figure 4.2.13 ESI mass spectra of 4 μM UQ1 with: a) Lys48–linked Ub_2 (0.5 μM) and b) Lys63–linked Ub_2 (0.5 μM), sprayed from 25 mM ammonium acetate solution under acetonitrile vapour.

Furthermore, the binding between UQ1–UBA with either Lys48– or Lys63–linked forms of Ub_4 was also determined to be in the 15 μM range (Figure 4.2.14). These data are consistent with the conclusions of a NMR study that suggested that intermolecular contacts between the UQ1–UBA and the individual Ubs in Lys48– and Lys63–linked Ub_2 chains, are essentially the same as with mono-Ub [102]. In contrast, a SPR study [101], showed that the UQ1–UBA interaction with Ub_4 moieties, is somewhat stronger than the values reported by the ESI–MS method (Table 4.2.1). The SPR experiments, however, were conducted on dimeric GST–(UQ1–UBA) fusions, and hence, artifactual chelate effects leading to apparently higher affinity with longer poly-Ub chains are a possible explanation. Indeed, this effect has previously been observed with GST-UBD fusion proteins [175].

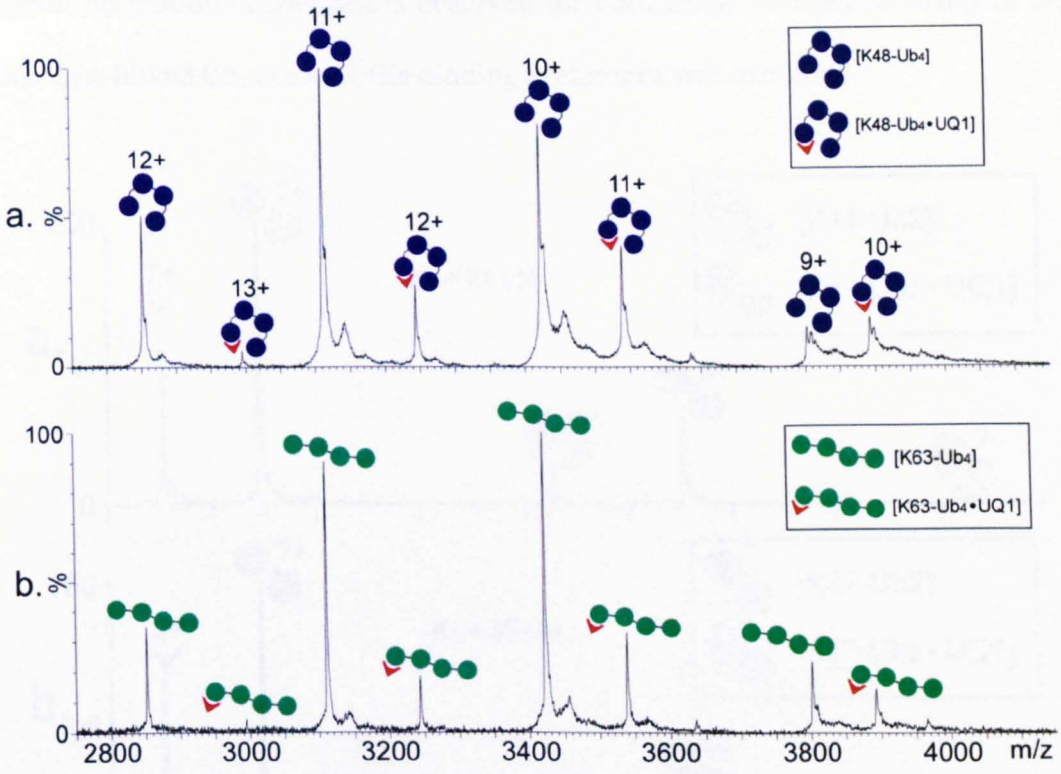

Figure 4.2.14 ESI mass spectra of 4 μM UQ1 with: a) Lys48–linked Ub_4 (0.5 μM) and b) Lys63–linked Ub_4 (0.5 μM), sprayed from 25 mM ammonium acetate solution under acetonitrile vapour.

4.2.4 Quantifying Ub–UBD binding affinity

4.2.4.1 Ubiquitin complexes with UQ1–UBA domain

The UQ1–UBA forms complexes with mono-Ub, Lys48– and Lys63–linked Ub_2 as well as Lys48– and Lys63–linked Ub_4 and have been examined in sections 0 and 4.2.3.2. with Apparent K_ds are shown in Table 4.2.1 and are compared with the previously reported values determined by other methods. Additionally to these measurements, the apparent K_ds of UQ1–UBA complexes with Lys11– and Lys27–linked Ub_2 were also determined (Table 4.2.1). Figure 4.2.15 illustrates the mass spectra obtained for UQ1–UBA complex with Lys11– and Lys27–linked Ub_2, electrosprayed from 25 mM ammonium acetate in the presence of acetonitrile

vapour. Formation of complex is observed for both chain linkages. Similarly to the other Lys–linked Ub_2 chains, little binding preference was exhibited.

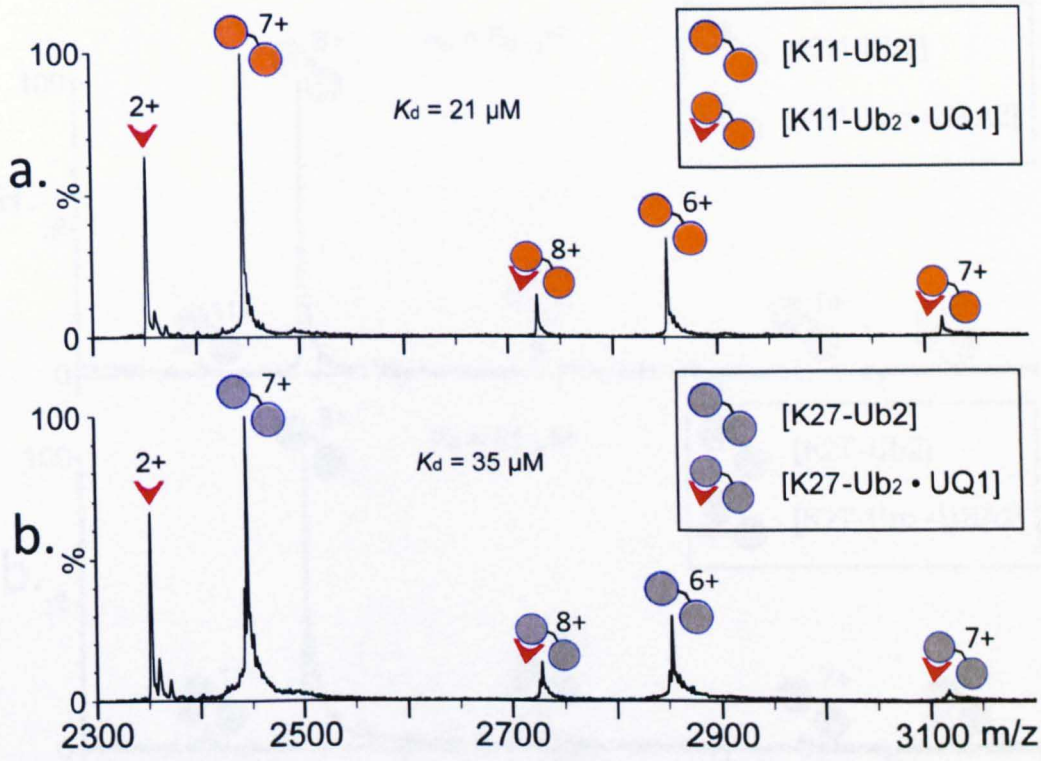

Figure 4.2.15 ESI mass spectra of 4 μM UQ1 with: a) Lys11–linked Ub_2 (0.5 μM) and b) Lys27–linked Ub_2 (0.5 μM), sprayed from 25 mM ammonium acetate solution under acetonitrile vapour.

4.2.4.2 Ubiquitin complexes with hHR23A–UBA2 domain

The UBA2 complexes with mono-Ub, Lys48– and Lys63–linked Ub_2 as well as Lys48– and Lys63–linked Ub_4 have been examined in section 4.2.3.1. The apparent K_ds are shown in Table 4.2.1 and are compared with the previously reported values determined by other methods. In addition to these values, new data for Lys11– and Lys27–Ub_2•UBA2 interactions were also determined (Table 4.2.1). Figure 4.2.16 illustrates the mass spectra obtained of UBA2 complex with Lys11– and Lys27–linked Ub_2, electrosprayed from 25 mM ammonium acetate. The measured apparent K_ds for these two linkage topologies are also significantly weaker than for the Lys48–Ub_2 linkage (Table 4.2.1), which confirms the preference of UBA2 domain

towards Lys48–linked poly-Ub chains and demonstrates the ability of ESI–MS method to probe selectivity of Ub•UBD interactions.

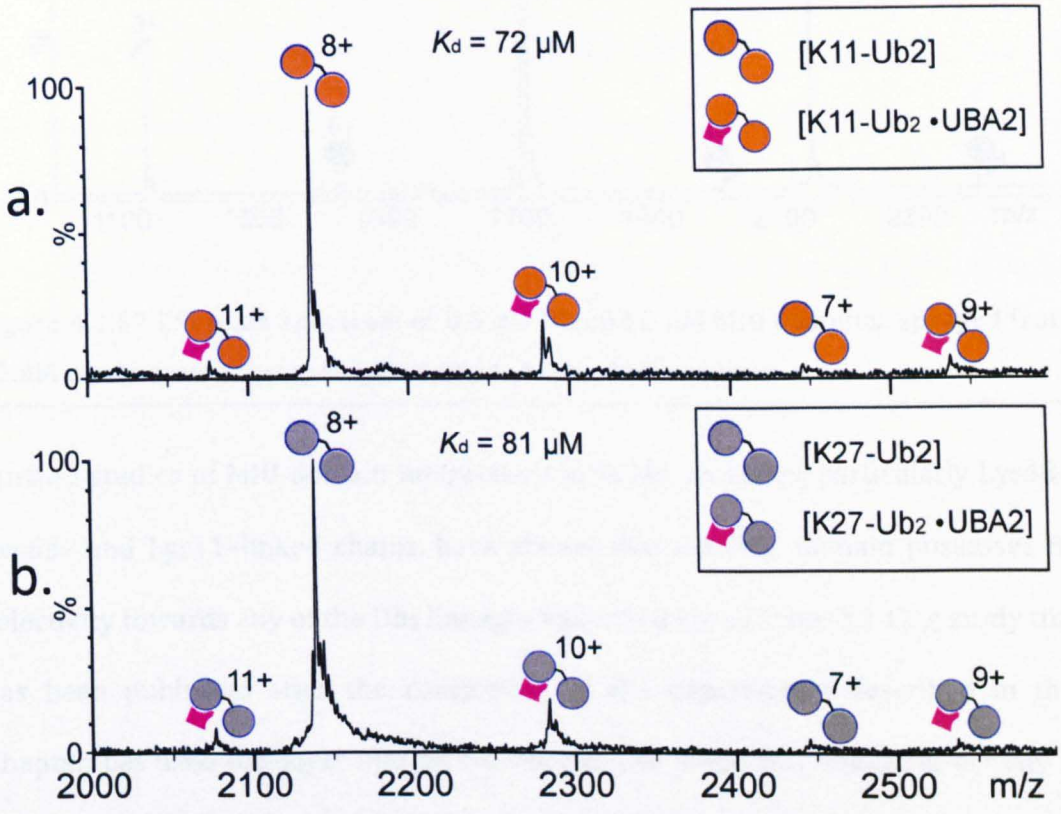

Figure 4.2.16 ESI mass spectra of UBA2 (4 µM) with: a) Lys11-linked Ub_2 (0.5 µM), b) Lys27-linked Ub_2 (0.5 µM), sprayed from 25mM ammonium acetate solution.

4.2.4.3 Ubiquitin complexes with MIU domain

MIU binds to the hydrophobic patch Ile44 on the β-sheet region of ubiquitin, with a K_d ~30 µM. Illustrated in Figure 4.2.17 is the mass spectrum obtained for the Ub•MIU complex, electrosprayed from 25 mM ammonium acetate in the presence of acetonitrile vapour. The $(Ub+MIU+6H^+)^{6+}$ and the $(Ub+MIU+5H^+)^{5+}$ ions are observed at 1996 m/z and 2395 m/z, respectively. Ub's charge states are distributed between 4+ (2142 *m/z*) 5+ (1714 m/z) and 6+ (1428 *m/z*). Unbound domain is observed at 1704 *m/z* (2+) and at 1136 *m/z* (3+). The apparent K_d value determined from these measurements was 36 ± 4 µM, which is in good agreement with previously reported values determined by SPR (Table 4.2.1).

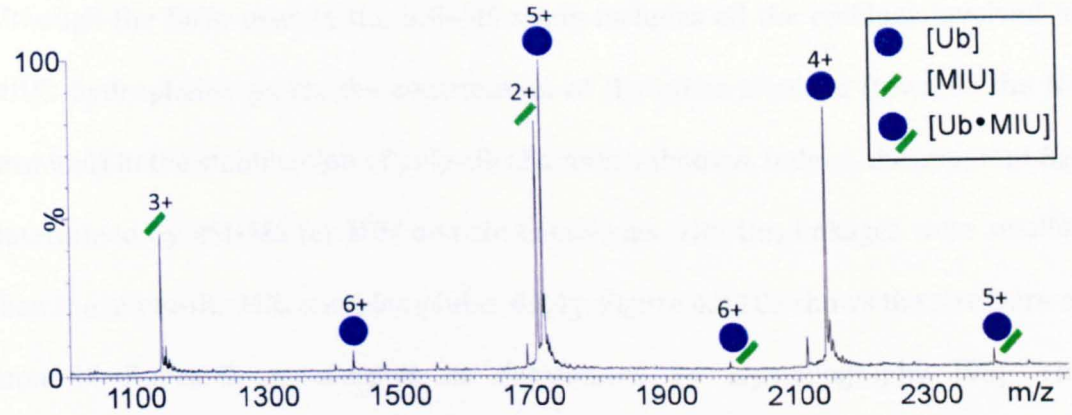

Figure 4.2.17 ESI mass spectrum of 0.5 μM Ub and 2 μM MIU complex, sprayed from 25mM ammonium acetate solution under acetonitrile vapour.

Further studies of MIU domain interactions with Ub_2 moieties, particularly Lys48–, Lys63– and Lys11–linked chains, have shown that the MIU domain possesses no selectivity towards any of the Ub_2 linkages examined here (Table 4.2.1). A study that has been published after the completion of the experiments described in this Chapter, has used bio–layer interferometry (BLI) to probe Ub_4 linkage selectivity of the tandem UBDs (MIU and A20–ZnF domains) of Rabex–5 [176]. The study has shown that MIU domain exhibits some selectivity for linear and Lys63–linked Ub_4 over Lys48–linked Ub_4. In addition, the binding affinities of MIU domain for Ub_4 chains (linear Ub_4, 0.28 ± 0.14 μM; Lys63–Ub_4, 1.0 ± 0.65 μM; Lys48–Ub_4, 3.1 ± 1.1 μM) were found to be somewhat higher than the determined values for the Ub_2 linkages (Table 4.2.1). Further to the different experimental setup between the two studies (BLI and ESI–MS), another difference that might be contributed to these discrepancies is the use of a longer domain in the case of the BLI study; in the BLI study, the Tyr25Ala/Tyr26Ala GST–Rabex–5_{9-73} double mutant was used to study interactions of MIU with Ub_4, in contrast to the thrombin cleaved Gly–Ser–Rabex–5_{48-75} that used in the case of ESI–MS method. It has been shown that Ub bind MIU domain *via* the latter's hydrophobic patch centred around Ala58 residue (involving Ile51, Trp55, Leu57, Ala58, Leu61 and Phe69 residues) [97].

Although the form used in the ESI–MS study includes all the residues involved in MIU's hydrophobic patch, the contribution of the other residues (towards the N-terminal) in the stabilization of poly-Ub chains is unknown. Indeed, the apparent K_ds determined by ESI–MS for MIU domain complexes with Ub_2 linkages were smaller than the mono-Ub•MIU complex (Table 4.2.1). Figure 4.2.18a shows the structure of mono-Ub•Rabex-5_{17-74} complex as determined by crystallography [98]. The structure of the Rabex-5_{17-74} (light blue) shown here, is a very good approximation of the Rabex-5 form used in the BLI study. In contrast, the Rabex-5 form used in the ESI–MS study is shown in Figure 4.2.18b. Comparison of the two Rabex-5 forms highlights the potential role of the additional residues, in the stabilisation of poly-Ub•MIU domain interactions.

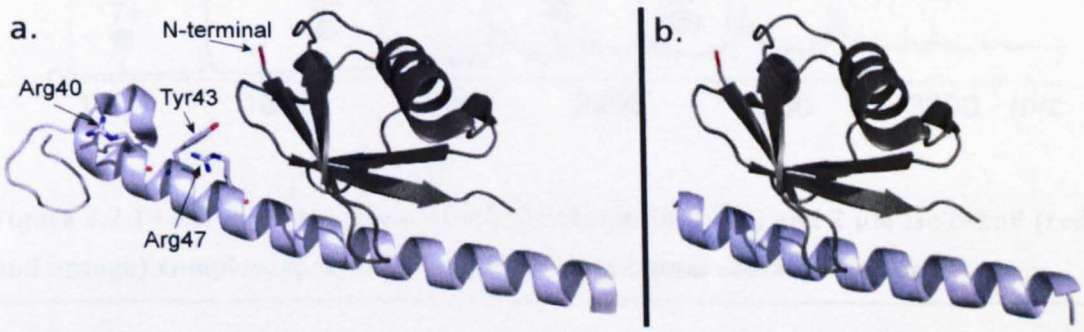

Figure 4.2.18 Cartoon representation of Ub (dark grey) complex with (a) Rabex-5_{17-74} and (b) MIU domain used in this study; Rabex-5_{48-74}, (PDB ID: 2C7M).

4.2.4.4 Ubiquitin complexes with IsoT–ZnF domain

The IsoT–ZnF domain demonstrates a very high Ub binding affinity with a K_d~3 μM [106]. Illustrated in Figure 4.2.19 is the mass spectrum obtained for the Ub•IsoT–ZnF complex, electrosprayed from 25 mM ammonium acetate. Note that in this experiment, the domain was observed and treated as a disulfide-linked dimer (2xIsoT), which has been previously reported [106]. The $(Ub+IsoT–ZnF+nH^+)^{n+}$ complex ions ranged in charge state between n=12–15. Additionally, a smaller

distribution of unbound dimer domain ions $(IsoT–ZnF+nH^+)^{n+}$ at charge states n=10–12 were observed. Ub's charge states are distributed between 5+ (1714 *m/z*), 6+ (1428 m/z) and 7+ (1224 *m/z*). The apparent K_d determined from these measurements is 2.5 ± 0.5 μM, which is in excellent agreement with 2.8 ± 0.1 μM determined from ITC measurements [106]. It has to be noted that the calculation of K_d was based on the assumption that both sides of the dimer can equally bind Ub and that only one form of complex is formed (only one Ub moiety bind to the dimer).

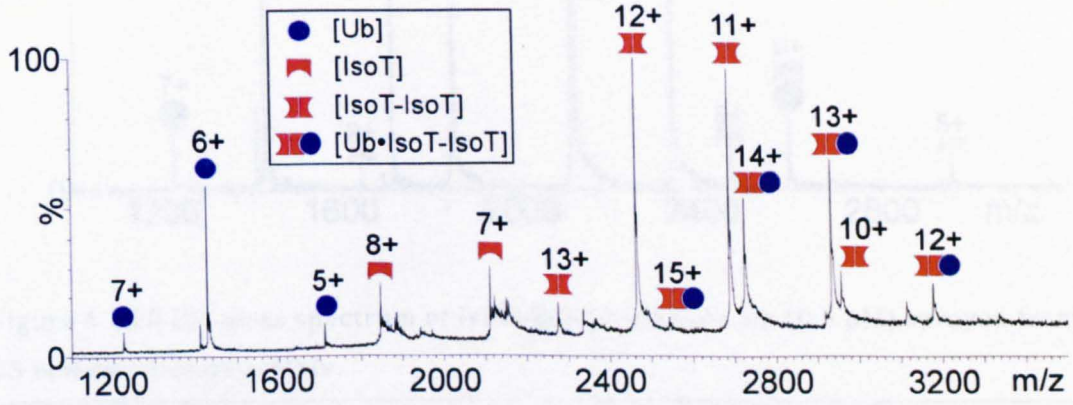

Figure 4.2.19 ESI mass spectrum of 0.5 μM ubiquitin (blue) and 2 μM IsoT–ZnF (red and orange) complex, sprayed from 25 mM ammonium acetate solution.

To test of the validity of this assumption, the IsoT–ZnF dimer, which is formed by a disulfide bond between the Cys195 residues of the monomeric species [106], was reduced to its monomer form by dithiothreitol (DTT) (*see* Chapter 2). Illustrated in Figure 4.2.20 is the ESI mass spectrum of the IsoT–ZnF domain complex with Ub, sprayed from 25 mM ammonium acetate. The $(Ub+IsoT–ZnF+nH^+)^{n+}$ complex ions are ranging in charge state between n=9–11. Additionally, a distribution of unbound $(IsoT–ZnF+nH^+)^{n+}$ ions at charge states n=5–9 is presented. Ub's charge states are distributed between 5+ (1714 *m/z*), 6+ (1428 m/z) and 7+ (1224 *m/z*).

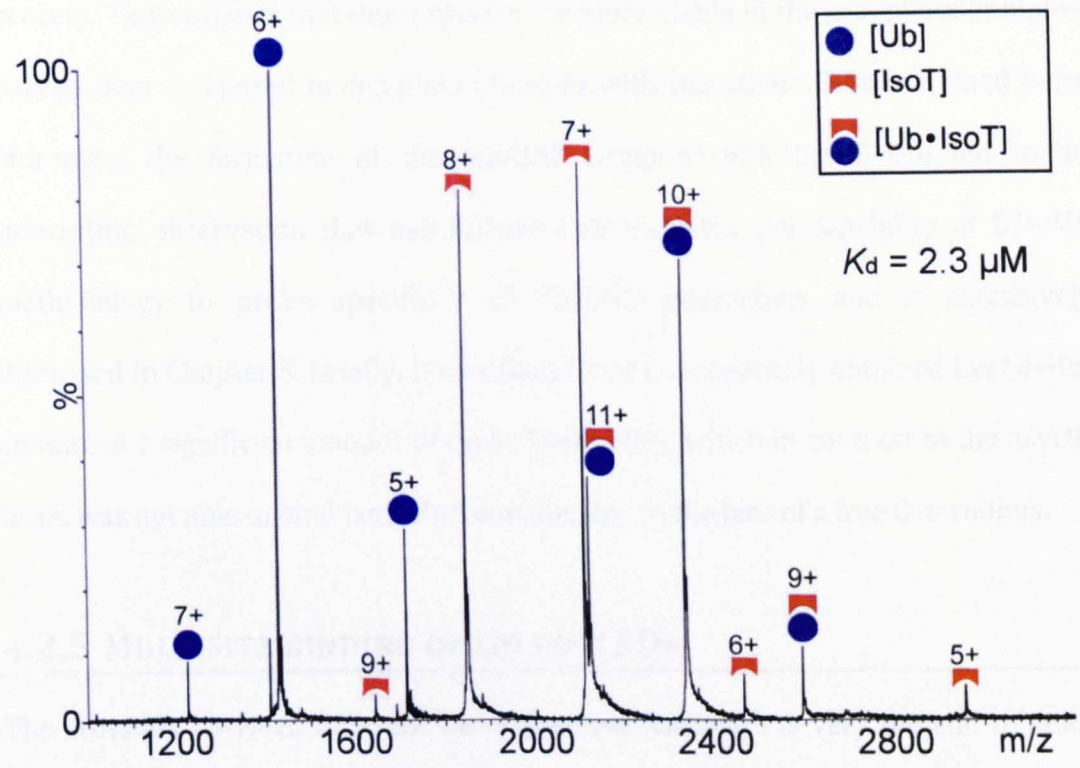

Figure 4.2.20 ESI mass spectrum of IsoT–ZnF (2 μM) and Ub (0.5 μM) sprayed from 25 mM ammonium acetate.

The binding affinity determined from these data (2.3 ± 0.5 μM), was found, again, to be in good agreement with the literature value (2.8 ± 0.5 μM) [106]. Furthermore, it supports the assumption been made before in the case where the dimer form of the IsoT–ZnF domain was used.

Further studies of IsoT–ZnF domain interactions with Ub_2 moieties, particularly Lys48–, Lys63– and Lys11–linked chains, have shown that the IsoT–ZnF possesses no selectivity towards any of the Ub_2 linkages and bind them with affinities very similar to that observed for mono-Ub (Table 4.2.1). Given that the IsoT–ZnF domain binds Ub *via* IsoT-ZnF's C–terminal residues (Gly75 and Gly76) and that unanchored poly-Ub chains have a free C–terminus, these results were expected. Interestingly, it was observed that the use of charge reduction on complexes of IsoT–ZnF resulted in almost identical K_d values compared to those obtained from conventional ESI

process. This suggests that these species are more stable in the gas-phase at higher charge state compared to complexes formed with the other UBDs examined here. Moreover, the formation of the Iso-ZnF complex with Lys48-Ub_2 led to an interesting observation that has further demonstrates the capability of ESI-MS methodology to probe specificity of Ub•UBD interaction, and is extensively discussed in Chapter 5. Briefly, it was found that commercially obtained Lys48-Ub_2 contained a significant amount of cyclic Lys48-Ub_2, which in contrast to the acyclic form, was not able to bind IsoT-ZnF domain, due to the lack of a free C-terminus.

4.2.5 Multisite binding of Ub to UBDs

The crosstalk between different Ub-dependent pathways is very difficult to study using currently available biophysical techniques. Therefore, a rapid and sensitive method that could probe such interactions is essential. Having established that ESI-MS methodology is able to detect specific interactions between Ub and a range of UBDs, it was postulated that it could be also employed to examine multiple domain interactions with different Ub site specificities. A recent study has assessed the probability of Ub-mediated ternary complex formation [177]. As it has been mentioned above, the UQ1-UBA and the IsoT-ZnF domains bind Ub via latter's Ile44 hydrophobic patch and Gly75/Gly76 C-terminus, respectively. Therefore, these domains should be able to form a ternary Ub•UQ1-UBA•IsoT-ZnF complex. ESI-MS of a mixture of the three components did, indeed, lead to a clearly detectable ternary complex (Figure 4.2.21), confirming that multiple domains can bind mono-Ub or poly-Ub simultaneously.

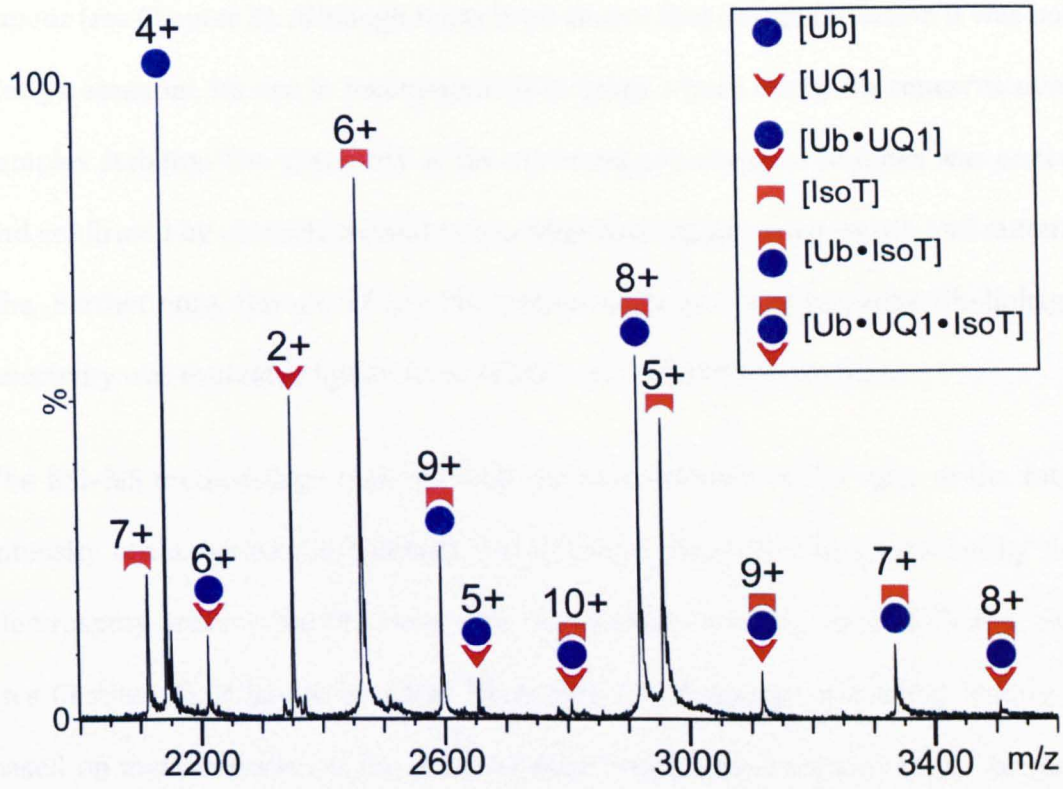

Figure 4.2.21 ESI mass spectrum of 0.5 μM mono-Ub with 4 μM UQ1–UBA and 2 μM IsoT–ZnF, in the presence of acetonitrile vapour, showing the presence of a Ub•UQ1–UBA•IsoT–ZnF ternary complex.

Additionally to the formation of the ternary complex, the binary complexes Ub•UQ1 and Ub•IsoT–ZnF were also observed. There was no evidence for the formation of any non specific complex between the two UBDs, UQ1–UBA and IsoT–ZnF. This, again, demonstrates the ability of ESI–MS methodology to detect specific interactions.

4.2.6 Fidelity of the MS method

A series of experiments has been conducted in order to test the fidelity of results derived from the ESI–MS methodology. Particularly, it has been demonstrated that the use of a charge reduction approach was essential, at least for some complexes, to minimize disruption of non-covalent complexes in the MS region (section 0). Lower charge states were obtained by exposure of the electrospray plume to acetonitrile

vapour (*see* Chapter 3). Although it has been shown that charge reduction it was not always essential, its use is recommended in cases where there are concerns over complex stability. The specificity of the observed non-covalent complex was tested and confirmed by competitive and non-competitive assays using wt-Ub and mutant Ubs. Furthermore, the use of ESI-MS methodology as a tool to probe Ub-linkage selectivity was evaluated by the cases of UQ1-UBA and UBA2 domains.

The ESI-MS methodology requires only the measurement of the ratio of the total intensity of the bound (complexed) and unbound (free) Ub ions generated by the electrospray process and the knowledge of the initial concentration of Ub and UBD (*see* Chapter 2). It has to be noted here, that determination of binding affinity is based on measurements of the solution equilibrium concentrations of the binding partners. ESI-MS, in contrast, measures the ion abundance, which is the result of the *conversion* of analyte species in solution into measurable ESI-MS signal. The relationship between signal intensity and solution-phase concentration is given by $\mathbf{I_A=\gamma_A[A]}$, where I_A and [A] are the signal intensity and the solution concentration of analyte A, and γ_A is the response factor, which reflects the extent of *conversion* as defined above. Therefore, the use of ESI-MS as a tool for binding affinity measurements requires the knowledge of the analytes response factors, particularly their ratio. Methods for determining ESI-MS response factors have been reported [178, 179], however, due to the complexity of these approaches, it is usually postulated that the ratio of the response factor is equal to 1 [180]. In cases of protein-ligand associations where the ligand is relatively small compared to the size of the protein, the assumption that free and bound protein ions have similar response factors is valid. However, formation of protein-protein complexes in solution can be associated with conformational changes that, may affect the response factors. It is also known that the effective hydrophobicity of a protein in

solution is linked to its ESI ionization efficiency which, in turn, is related to the response factor of the protein [181]. Therefore, if the free state of a protein is partially unfolded compared to the complex form, its effective hydrophobicity will be enhanced and as a consequence the ionization efficiency of the free protein will be increased, leading to discrepancies in the response factors of unbound and bound protein ions [174]. Interactions between Ub and UBDs will bury a small number of hydrophobic residues on both proteins, and therefore the ionization efficiency of the complex and the unbound Ub species it might be affected. Such a scenario would influence the response factors and possibly would drive off the response factors ratio from the ideal value of 1. To examine whether or not this case applies to the Ub•UBD complexes studied in this project, we applied a simple test. A study by Kaltashov and Mohimen, has shown that for natively folded proteins there is a linear relationship between ln(average ESI charge state) and ln(surface area, Å^2) with a slope of 0.69 ± 0.02 [182]. Using the logic developed by Liu and Konermann [174], significant departure from this relationship may indicate changes in ionization efficiency and hence response factors. These changes might be driven by the formation of protein–protein association that result in the exposure or burial of hydrophobic residues.

Plotting ln(average ESI charge state) versus ln(surface area, Å^2) for mono-Ub and the four complexes investigated in this study, resulted a straight line with a slope of 0.68 ± 0.01 (Figure 4.2.22), which is in excellent agreement with the value reported by Kaltashov and Mohimen [182]. Thus, we conclude that formation of Ub•UBD complexes is not linked with major conformational changes in the subunits, consistent with previously reported data from solution studies [102], and that burial of a relatively small number of hydrophobic residues does not appear to impact upon ionization properties of the complex compared to the unbound Ub.

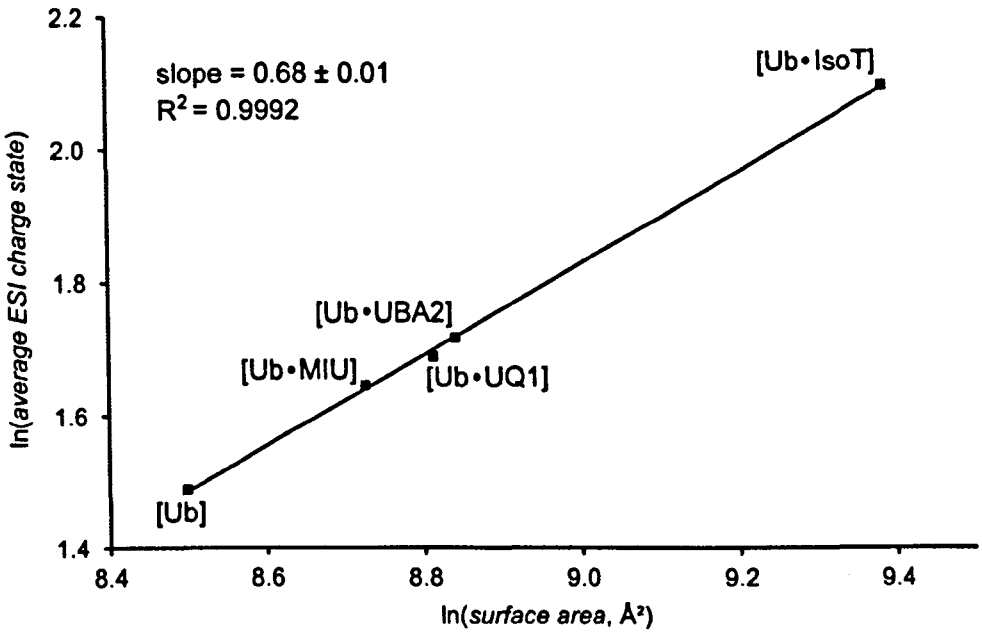

Figure 4.2.22 Plot of ln(average ESI charge state) versus ln(surface area, Å²). Solvent accessible surface areas were calculated for Ub, Ub•MIU and Ub•UQ1-UBA complexes from modified PDB files 1D3Z, 2C7M and 2JY6, respectively, using the program GetArea (http://curie.utmb.edu/getarea.html). The modified PDB structures were built by adding or subtracting amino acids, to/from the published structures, using PyMOL. Model structures for the Ub•UBA2 and Ub•IsoT-ZnF complexes were build from PDB files 1ZO6 and 2G45, respectively.

4.3 Conclusions

The ESI-MS approach described in this Chapter provides a new, rapid and highly sensitive tool for studying the affinity and specificity of Ub•UBD complexes. The key advantages of this method are the speed of analysis (in an optimized instrument the analysis can be completed within minutes), the low sample consumption (less than 50 µL of sample at micromolar concentration are required for a single measurement), sensitivity (weak and low abundance complexes can be detected without the need of saturation, as demonstrated in case of the UBA2 complex with Ub) and selectivity.

The method is based on titration experiments, where the concentration of the Ub component is fixed to 0.5 μM and the concentration of UBD varies from 1 to 8 μM. Although, the concentration of UBD could be increased, we have shown that the sensitivity of the method allows a very weak interaction between mono-Ub and UBA2 (K_d = 200 μM) by the addition of only 4 μM of the UBD. Moreover, in the cases of the UQ1-UBA and UBA2 domains we have also observed that increasing the domain concentration above 6 μM resulted in the formation of a significant amount of UBD homodimer, which may affect precise determination of K_d. Indeed, the ability to work at low micromolar range better reflects the physiological situation as the cellular concentration of Ub is estimated to be approximately 85 μM [183].

The experiments were performed on a commercially available IM-MS instrument (SYNAPT™ HDMS, Waters, UK). Although the determination of binding affinities by ESI-MS, does not require the ion mobility function, its use in our experiments has demonstrated some clear benefits. For example, in the case of Ub•UBA2, the unbound mono-Ub ion 3+, the unbound domain ion 2+ and the complex ion 5+, show *m/z* values of 2856 *m/z*, 2858 *m/z* and 2857*m/z*, respectively, which are almost impossible to discriminate in the mass spectrometer. The problem was overcome by the use of IM-MS, which has the additional ability to separate ions based on their mobility through a buffer gas, providing a second dimension for resolution of isobaric or near-isobaric species.

Perhaps the most compelling evidence for the applicability of this approach for studying Ub•UBD complexes is the excellent agreement achieved between ESI-MS affinity data and that of other biophysical methods. When tested against a series of previously studied Ub•UBD complexes the MS results were found to be in an excellent agreement with the K_d values that have been previously determined. In addition, we have provided new insights into binding affinities of previously

unstudied complexes. The methodology described shows great promises in probing biologically-relevant multivalent interactions with poly-Ub, for example to gain insights in to how UBDs of proteasome subunits, Rpn13-Pru and Rpn10-UIM, cooperate to function as a 'molecular ruler' effectively sensing the length of poly-Ub chains delivered to the proteasome [184, 185].

CHAPTER 5

TOP-DOWN PROTEOMICS TO CHARACTERIZE POLY-UB CHAINS AND CYCLIZATION OF LYS48-UB$_2$ *IN VITRO* AND *IN VIVO*

5.1 INTRODUCTION

The role of unanchored poly-Ub chains has only recently begun to be understood and linked to Ub-mediated processes. Piotrowski *et al.* have demonstrated that *in vitro* synthesised Lys48-poly-Ub chains could inhibit the proteasomal degradation of polyubiquitinated substrates [186]. In addition, it has been shown that degradation of the polyubiquitinated p53 by the 26S proteasome is affected by the accumulation of free chains in cells that is caused by IsoT knockdown [187]. The potential roles of unanchored Lys63-linked chains in activating kinases [188] and in signalling during innate immunity [189, 190], as well as the inhibition of the DUB enzyme, Ub carboxyl-terminal hydrolase isozyme L3 (UCH-L3) by Lys48-Ub$_2$ [191], have also been reported. Similarly to conjugated Ub chains, unanchored chains also exhibit linkage specificity and therefore, their study is equally important.

In addition to unanchored poly-Ub chains, *in vitro*-generated cyclic forms of Lys48-Ub$_2$, -Ub$_3$ and -Ub$_4$ have also been reported [192-194]. In each of these species, the normally free C-terminal Gly76 residue of the proximal Ub forms an additional isopeptide bond with the Lys48 of the distal Ub, which probably occurs due to the close spatial proximity of these residues in the compact conformations of Lys48-poly-Ub. Notably however, to date cyclic poly-Ub has not been identified *in vivo*.

The potential of MS-based, bottom-up proteomics to study ubiquitin modification has been previously demonstrated [195, 196]. This method has managed to detect all seven Lys-linkages in yeast [197] and HeLa cells [198], however, some important structure information is lost due to trypsin digestion. For instance, the bottom-up approach cannot discriminate homogeneous Lys-linked poly-Ub chains from forked chains [195]. Contrary, middle-down approaches have utilized partial digestion of poly-Ub chains under native conditions, allowing this way, mapping of the absolute topology of poly-Ub chains [199]. Moreover, absolute quantification (AQUA) approach for the analysis of linkage types has been employed to determine the percentage composition of poly-Ub linkages attached to individual proteins or mixtures [200, 201]. In contrast to bottom-up and middle-down methods which rely on tryptic digestion, top-down approach does not require the use of proteases. Although the potential of top-down proteomics to study ubiquitin modification has been demonstrated using poly-Ub chains generated *in vitro* [199], characterization of endogenous unanchored poly-Ub chains using such an approach has not yet been achieved.

This chapter describes the successful employment of top-down proteomics to reveal the topology of an unanchored poly-Ub chain (Lys48-Ub_2) that has been purified from tissue extracts using affinity chromatography methodologies based on the use of the ZnF domains, IsoT-ZnF and A20 ZnF (from the ZNF216 protein), which bind Ub by utilizing latter's free C-terminal or Asp58 residue, respectively. Furthermore, the presence of cyclic Ub_2 as the major component in a sample of commercial Lys48-Ub_2 (Boston Biochem, Cambridge, USA) as well as the isolation and characterization of endogenous cyclic Lys48-Ub_2 from rat skeletal muscle and cultured mammalian cells, are also reported in this chapter.

5.2 Results and Discussion

5.2.1 MS analysis of unanchored poly-Ub chains

The strategy used for A20 ZnF and IsoT-ZnF domain affinity chromatography is described elsewhere [118]. This section deals with the development of a MS top-down approach for the characterization of endogenous unanchored poly-Ub chains. The immobilised A20 ZnF domain captures a complex mixture of polyubiquitinated proteins from rat skeletal muscle extracts (Figure 5.2.1A) including a prominent Ub-immunoreactive band (Figure 5.2.1A, red arrow), which co-migrates with species of commercial unanchored Lys48- and Lys63-linked Ub_2 standards.

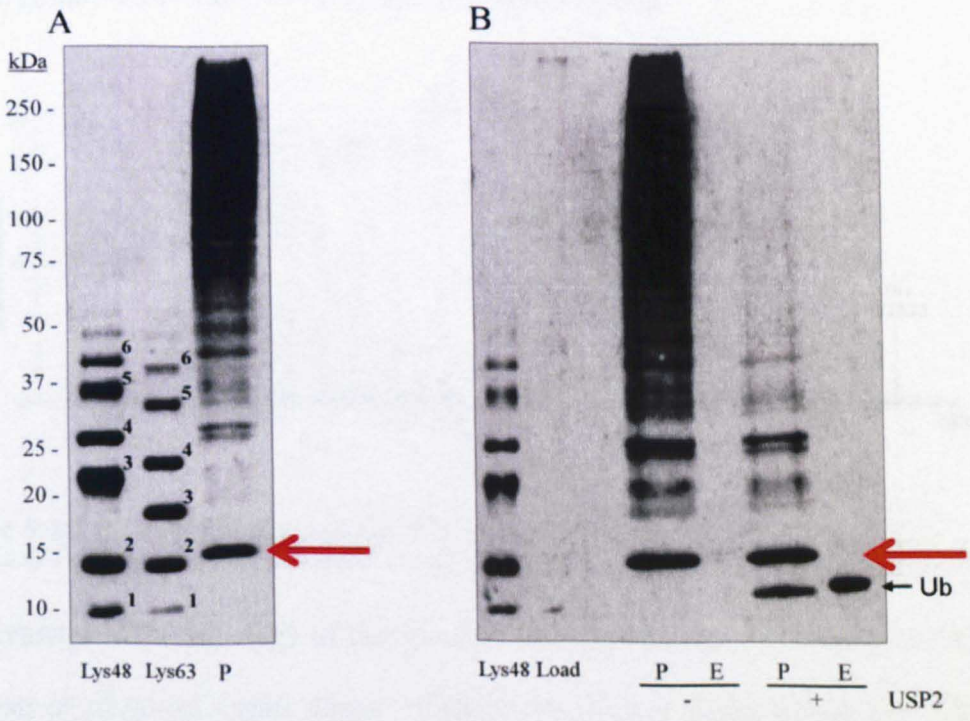

Figure 5.2.1 A) Anti-Ub Western blotting of purified polyubiquitinated proteins (P) from rat skeletal muscle captured by A20 ZnF domain. The high molecular weight smear is mainly attributed to ubiquitinated proteins. The arrow indicates a band that co-migrates with the Ub_2 standards. B) Incubation of beads with (+) or without (-) USP2 followed by anti-Ub Western blotting of the beads (P) or elution (E). Western blot assays were carried out by Dr. Joanna Strachan.

Further analysis showed that deubitination of the A20 ZnF domain-immobilised polyubiquitinated proteins by USP2 DUB, spared the Ub_2 (Figure 5.2.1B).

5.2.1.1 MS CHARACTERIZATION OF THE PURIFIED DI-UBIQUITIN

The purified proteins that remained attached to the beads after USP2 treatment, were eluted using formic acid (*see* Chapter 2) and were subjected to nanoLC-MS analysis for accurate mass determination. Figure 5.2.2 shows the mass spectrum obtained for the purified protein under denaturing conditions. The deconvoluted mass obtained from this spectrum (*m/z* 17102) was consistent with the mass of unmodified and unanchored intact Ub_2. Charge states from 10+ to 21+ are attributed to Ub_2 species whereas the presence of a small amount of mono-Ub is also observed at charge states 11+ (*m/z* 779.61) and 12+ (*m/z* 714.64).

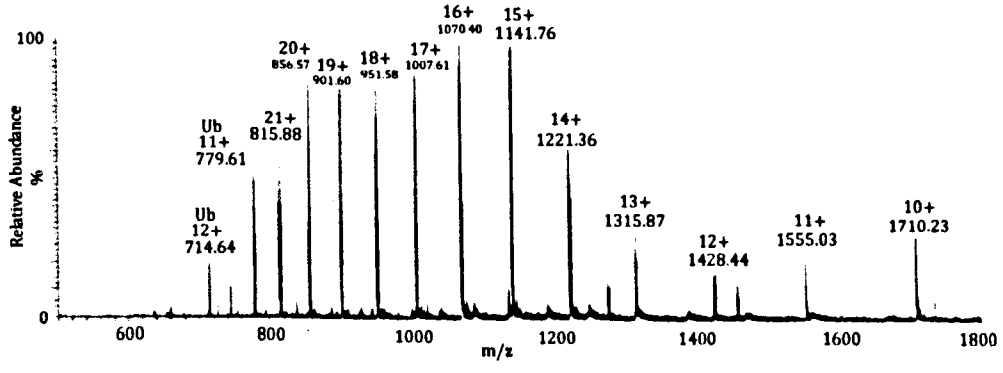

Figure 5.2.2 LC-ESI-MS spectrum of Ub_2 purified from rat skeletal muscle.

To investigate the topology of the purified Ub_2 species, we performed LC-MS/MS analysis of an in-gel tryptic digest (of the purified Ub_2 species) using both, CID and ECD fragmentation (Figure 5.2.3). This bottom-up approach is based on the generation of poly-Ub linkage specific GG-modified tryptic peptides, which contain a missed tryptic cleavage at the modified Lys site. For example, the ubiquitin tryptic peptide LIFAGKQLEDGR has an average mass of 1346.55 Da and contains only the Lys48 residue. In the case of a Lys48-linked poly-Ub chain, the di-Gly peptide will

remain attached to the Lys48 residue therefore it will increase the mass of the related ubiquitin tryptic peptide by 114.04 Da. The sequence of the GG-modified peptide, LIFAGK(GG)QLEDGR, can be revealed and hence verified by CID and ECD fragmentation, as demonstrated in the case of Lys48-Ub_2 (Figure 5.2.3).

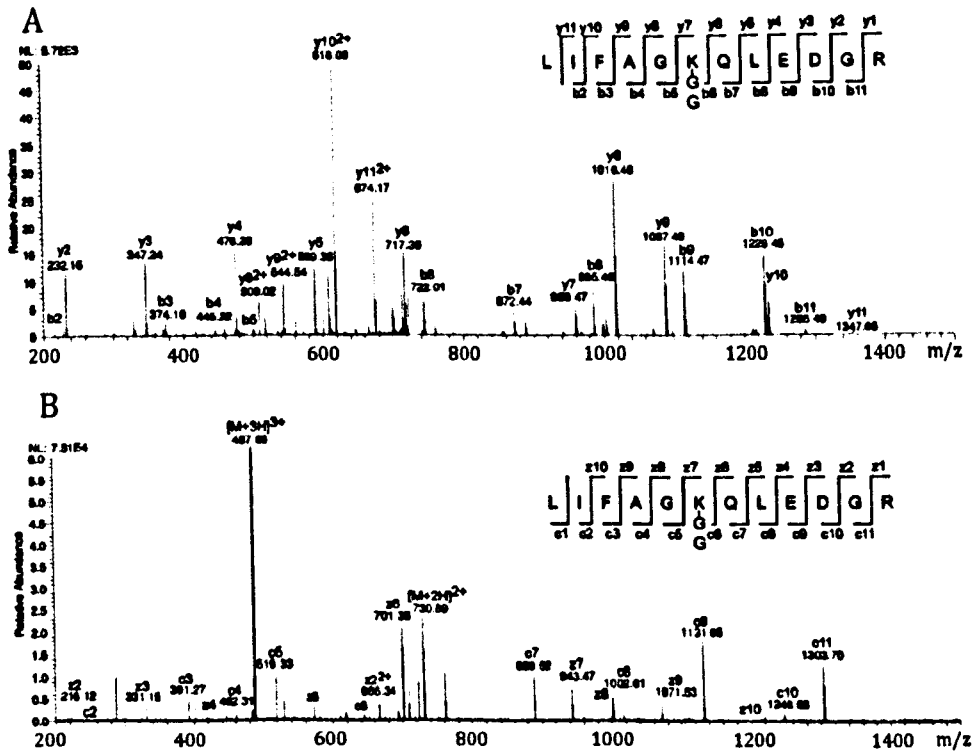

Figure 5.2.3 LC-ESI-MS/MS spectra of tryptic peptide 43-54 from Ub_2 purified from rat skeletal muscle resulting from (A) CID of the $[M+2H]^{2+}$ at *m/z* 731.0 and (B) ECD of the $[M+3H]^{3+}$ at *m/z* 487.7, clearly locating the linkage site to Lys48.

The bottom-up experiments suggested that the purified Ub_2 species observed in rat skeletal muscle sample was Lys48-linked.

To further investigate the presence of endogenous unanchored poly-Ub chains in the rat skeletal muscle samples, we also performed pull-down assays using the IsoT-ZnF domain. This UBD utilizes Ub's free C-terminal to bind, therefore exhibits specificity for unanchored poly-Ub chains whereas due to the binding mechanism it is unlikely to show any poly-Ub linkage specificity. Indeed, in chapter 4, it has been well demonstrated that IsoT-ZnF, binds mono-Ub and different linked Ub_2 chains

with similar affinity. Figure 5.2.4 illustrates the LC-MS/MS spectra obtained for the tryptic peptides derived from the gel-purified Ub_2, using ECD fragmentation. Signature peptides from both, Lys48-linked (1460.65 Da) and Lys11-linked (2402.68 Da) were detected (Figure 5.2.4).

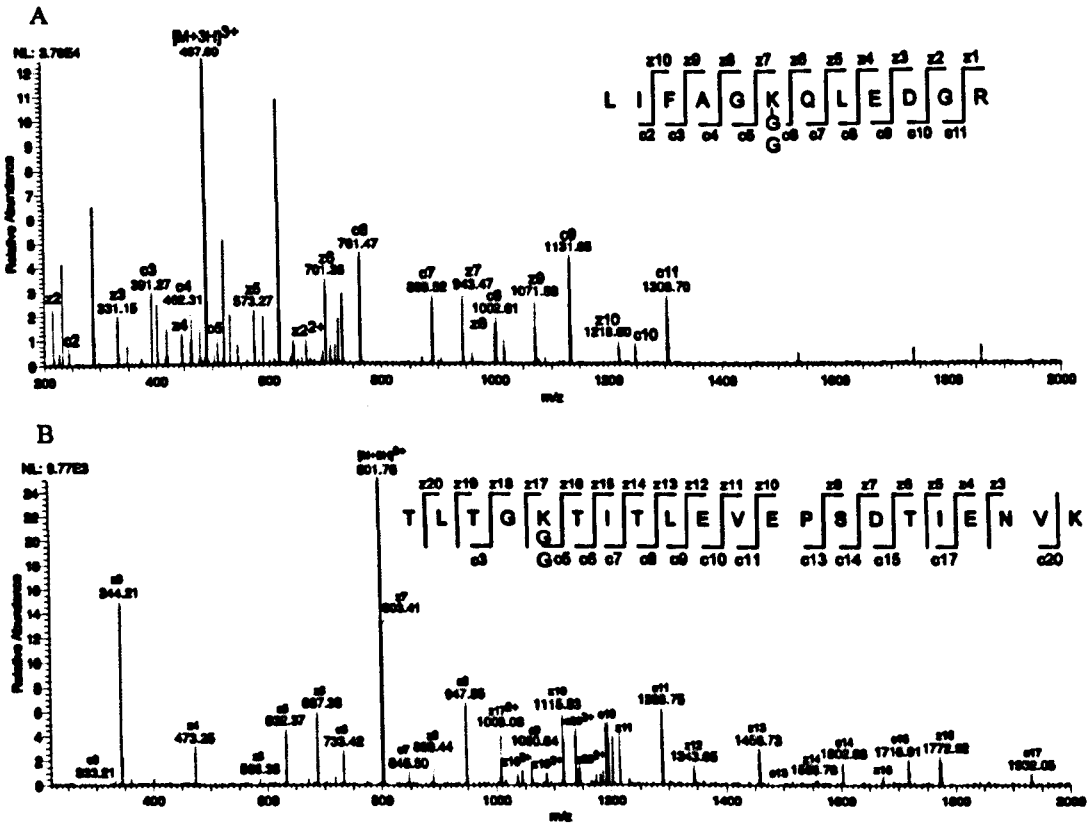

Figure 5.2.4 ECD MS/MS spectra of the tryptic peptides (A) 43-54 and (B) 7-27 derived from purified Ub_2 that was captured from rat skeletal muscle by IsoT-ZnF domain. These spectra suggest the presence of Lys48 (A) and Lys11 (B) linkages.

5.2.1.2 Top-down MS characterization of the Lys48-Ub_2

Top-down MS was performed to probe the structure of the sample and to ascertain linkage information. Illustrated in Figure 5.2.5 is the CID MS/MS spectrum of mono-Ub, resulting from low energy CID of the $[M+11H]^{11+}$ ion (*m/z* 779.2). Both, b and y ions were generated; b18 = *m/z* 2032.13, b39 = *m/z* 4307.30, b52 = *m/z* 5834.12 y24 = *m/z* 2725.50, y58 = *m/z* 6527.50 and y74 = *m/z* 8300.52 (Figure 5.2.5).

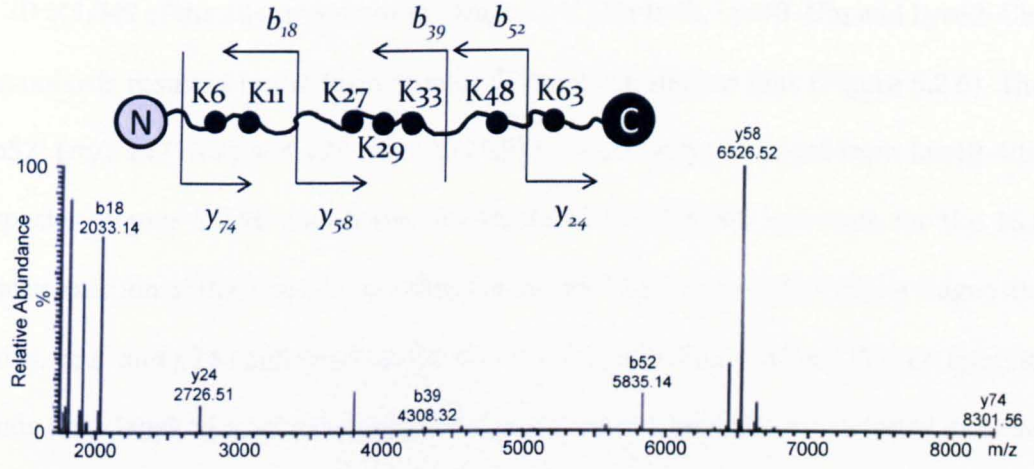

Figure 5.2.5 CID MS/MS deconvoluted spectrum obtained for the 11+ precursor ion (*m/z* 779.2) of mono-Ub demonstrating the major fragmentation patterns in the polypeptide chain. The top schematic shows the fragmentation sites of mono-Ub, resulting from low energy CID.

Based on the CID MS/MS results obtained for mono-Ub, a top–down approach should theoretically be able to distinguish between Lys6/11–, Lys27/29/33–, Lys48–, and Lys63–linked poly-Ub chains. In the particular case of Ub_2 species the differentiation could be based on the presence or absence of diagnostic ions produced by single fragmentation events (Table 5.2.1).

Table 5.2.1 Predicted *m/z* values of diagnostic b′ and y series ions produced by a single CID fragmentation of Ub_2 with the indicated Lys linkages.

b′	*m/z*	K6	K11	K27	K29	K33	K48	K63	y	*m/z*	K6	K11	K27	K29	K33	K48	K63
52	14377		+	+			+		24	2725		+	+			+	
39	12850		+						37	4252		+	+				
36	12541								40	4561		+					
18	10575		+						58	6527		+					
13	10004								63	7098		+					

Blue highlighted boxes indicate the predicted ions to be produced by fragmentation of a given Ub_2. Red highlighted boxes indicate the Ub_2 standards analysed in this study and the relevant detected diagnostic ions are indicated '+'. b′ ions represent the b ions derive from the fragmentation of the proximal Ub only i.e. the distal Ub remains intact.

CID MS/MS of the 15+ precursor ion (*m/z* 1141) for both, Lys48-Ub_2 and Lys63-Ub_2 standards resulted in the formation of diagnostic fragment ions (Figure 5.2.6). The b52′ (*m/z* 14375.7) and y24 (*m/z* 2726.5) ions are only produced from Lys48-Ub_2 species. Figure 5.2.6C shows the deconvoluted CID MS/MS spectrum for the 15+ precursor ion of the A20 ZnF-purified rat muscle Ub_2. The presence of the diagnostic ions, b52′ and y24 confirms that the Ub_2 is not Lys63-linked. Given that no specific ions associated with other non-Lys48 linkages were observed, is concluded that the purified Ub_2 species was Lys48-linked, which is consistent with the results obtained from the bottom-up experiments.

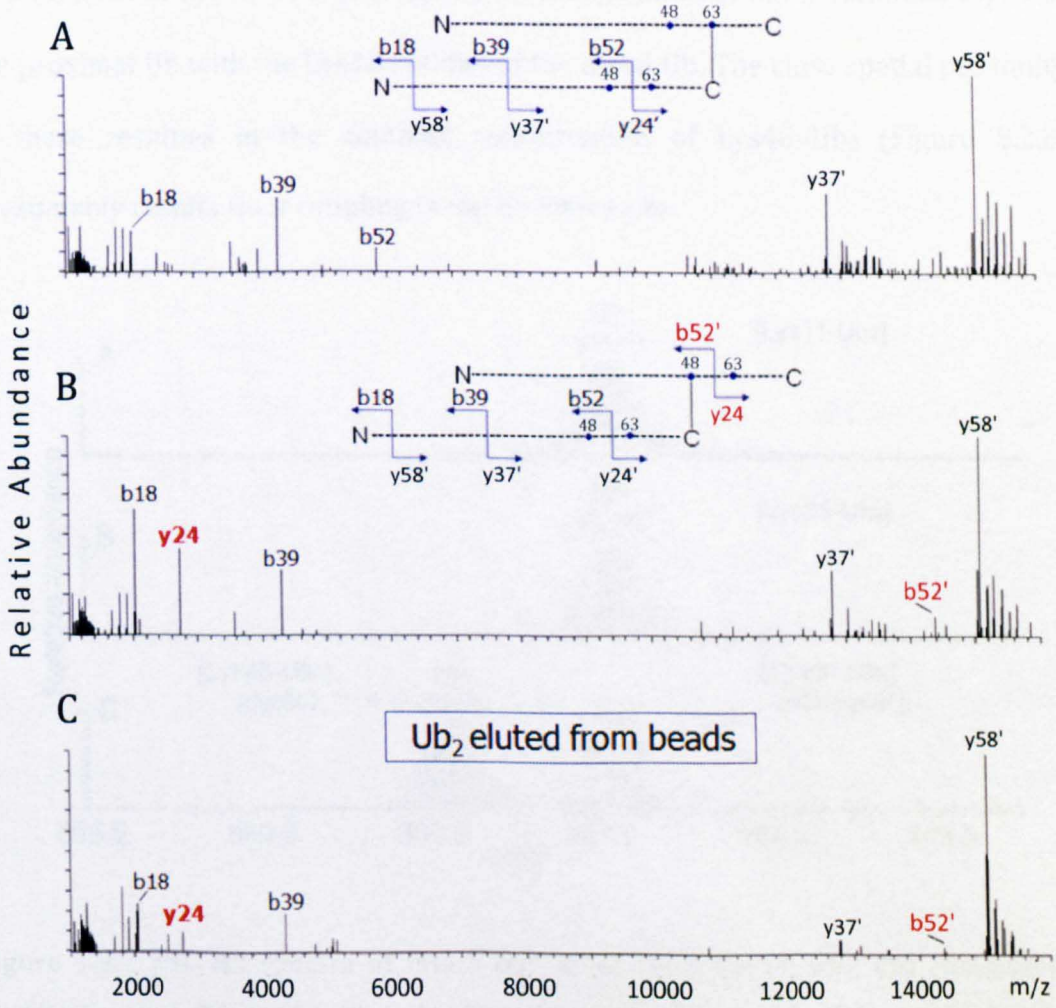

Figure 5.2.6 LC-MS/MS deconvoluted spectra obtained for the 15+ precursor ion (*m/z* 1141.8) for (A) commercial Lys63-Ub_2, (B) commercial Lys48-Ub_2 and (C) Ub_2 purified from rat skeletal muscle.

5.2.2 Cyclization of Lys48-Ub2

Illustrated in Figure 5.2.7 are the ESI-MS spectra obtained for commercial samples of *in vitro* generated native Lys11-, Lys63- and Lys48-Ub_2 (only the $[M+19H]^{19+}$ charge state is shown for clarity). In the cases of Lys11 and Lys63 linkages, a single charge distribution was obtained at *m/z* 901.60 (19+), corresponding to a molecular mass (M_r) of 17,111 Da. In contrast, for Lys48-Ub_2 species, two series were detected. Signals for 19+ ions occurred at *m/z* 901.60 (M_r 17,111 Da) and at *m/z* 900.65, which corresponds to M_r = 17,093 Da that is 18 Da lower than the mass of the full length polypeptide chain. The latter indicated dehydration, which is consistent with a cyclic form of Lys48-Ub2 that results from cyclisation of the C-terminus Gly76 of the proximal Ub with the Lys48 residue of the distal Ub. The close spatial proximity of these residues in the compact conformation of Lys48-Ub_2 (Figure 5.2.8) presumably results their coupling in the E2 active site.

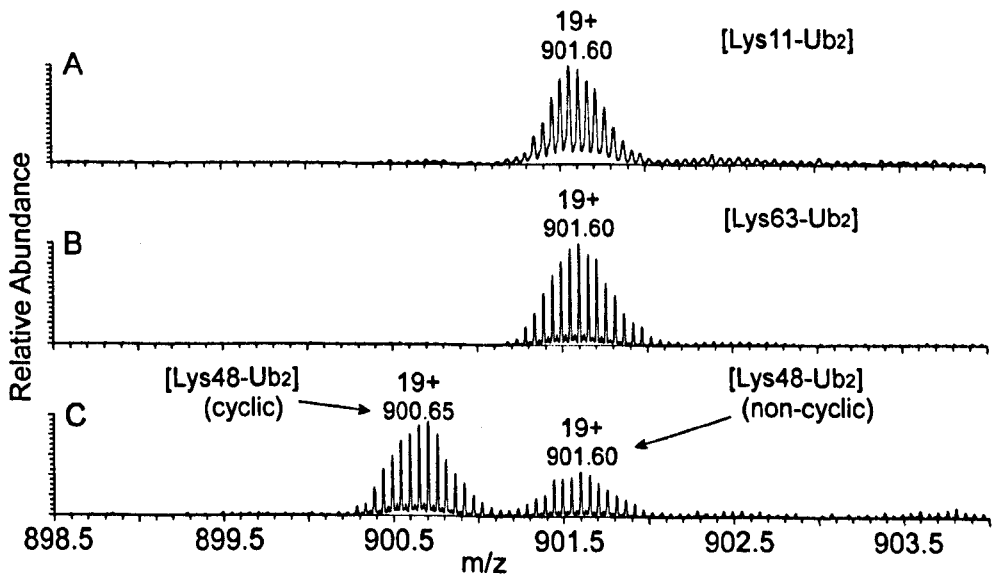

Figure 5.2.7 ESI-MS spectra of intact (A) commercial Lys11-Ub_2, (B) commercial Lys63-Ub_2 and (C) Lys48-Ub_2, showing the presence of cyclic Ub_2 in the Lys48-linked sample. Spectra were acquired under denaturing conditions. Only the $[M+19H]^{19+}$ ion is shown for clarity.

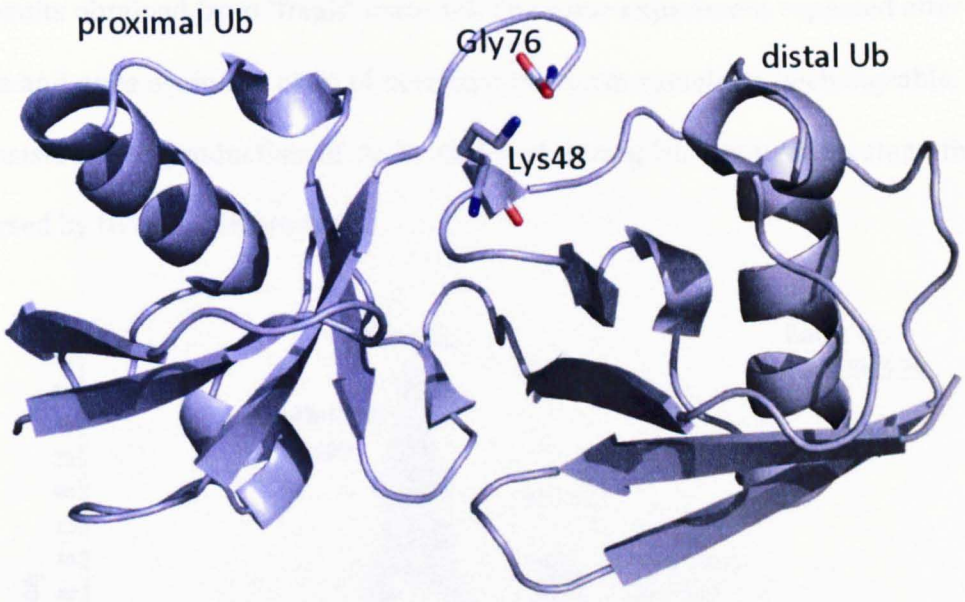

Figure 5.2.8 NMR structure of compact Lys48-Ub_2 (PDB ID: 2BGF) showing the close spatial proximity of Gly76 (proximal Ub) and Lys48 (distal Ub) residues.

Cyclic Lys48-Ub_3 has previously been reported as a product of *in vitro* ligation of Ub using E2-25K [193], which is the E2 enzyme used in the production of the commercial Lys48-Ub_2 analysed in this study. Cyclic Lys48-Ub_2 was found to be the major form (ca. 70 %) in the original batch of commercial native Lys48-Ub_2 (Lot # 3291529). It is worth to be noted that new batches of commercial Lys48-Ub_2 (Lot # 11515211) contain much less cyclic material (Figure 5.2.9) as a result of improved production procedures implemented after our initial observations (halting E2 catalysed polymerisation as soon cyclic Lys48-Ub_4 is observed). Additionally, the possibility of product (commercial Lys48-Ub_2) instability due to storage conditions (temperature and solution pH) was investigated. This was performed using the later batch of commercial Lys48-Ub_2 (Lot # 11515211) which was found to contain much less cyclic material than the older batch (Lot # 3291529). Two aliquots of the Lys48-Ub_2 material in a nearly native solution (25 mM ammonium acetate) and in a highly organic solution (50% acetonitrile, 0.1% formic acid), respectively, were stored in a fridge (~ 4 °C). Examination of these samples after a period of one week did not show any differences in the ratio of acyclic/cyclic form when compared with

the results obtained from "fresh" material. The same experiment repeated after two weeks and once again the ratio of acyclic/cyclic form remained unchangeable. This is consisted with production of cyclic material during Ub conjugation stage that is catalysed by the E2-25K enzyme.

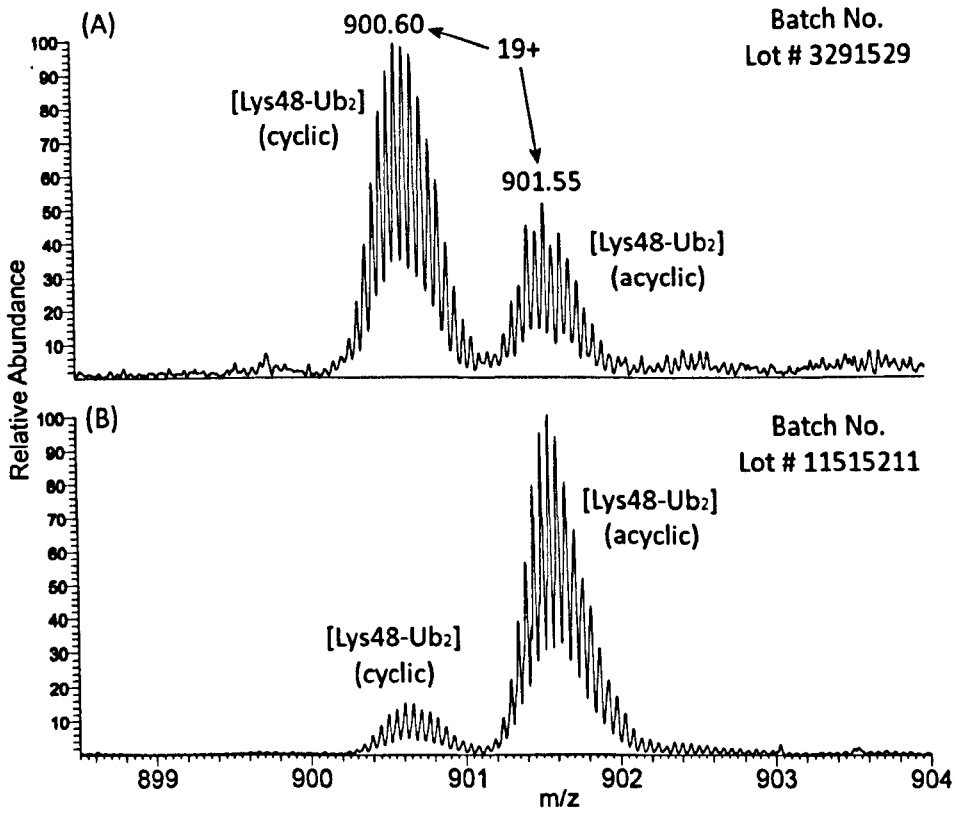

Figure 5.2.9 ESI-MS spectra of commercial native Lys48-Ub₂ from two different batches (A) Lot#3291529 and (B) Lot#11515211, showing the reduction of cyclic Lys48-Ub₂ in the new batches. Spectra were acquired under denaturing conditions. Only the 19+ ion is shown for clarity.

Given that cyclic Lys48-Ub₂ will not possess a free C-terminal Gly76 residue which is required for recognition by the IsoT-ZnF [106] it was postulated that the cyclic form would not bind to this UBD. Figure 5.2.10 shows the interacting regions of IsoT-ZnF (bright orange) and bound Ub (green) as determined by X-ray crystallography (PDB ID: 2G45) [106]. The C-terminus of Ub can clearly be seen to occupy the binding pocket of the IsoT-ZnF domain. When the NMR-derived compact structure of Lys48-Ub₂ (Figure 5.2.10, cyan, PDB ID: 2BGF) [202] is aligned it

demonstrates that the close intra-molecular association of Gly76 and Lys48 between the two Ubs should prevent interaction between cyclic Lys48-Ub_2 and the IsoT-ZnF.

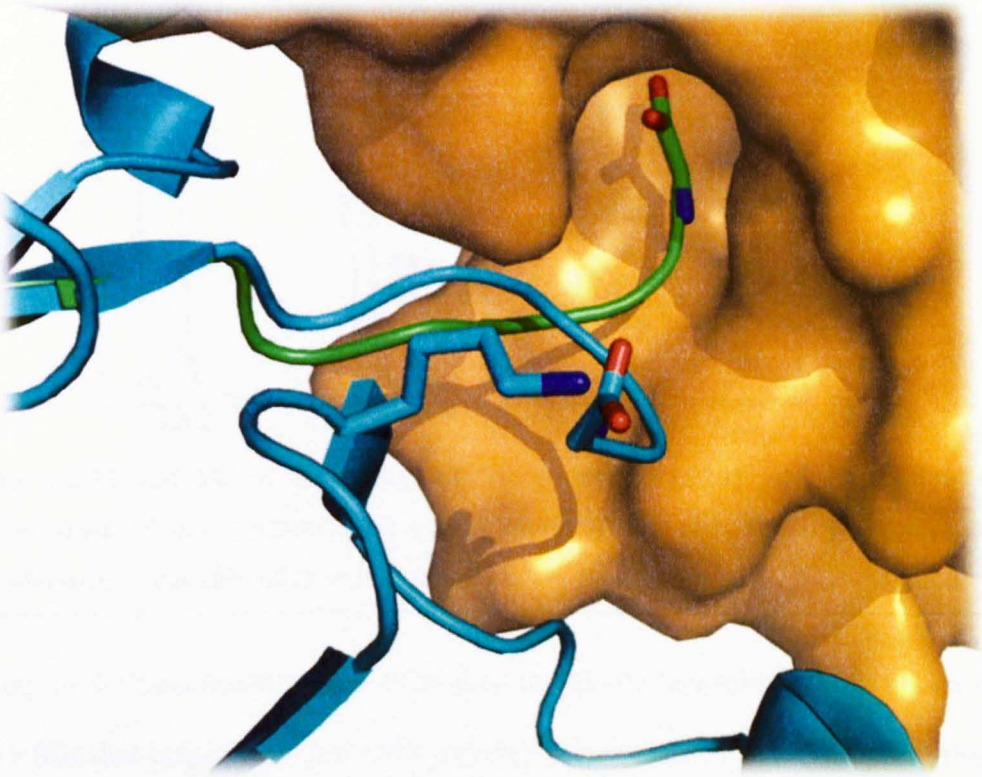

Figure 5.2.10 Overlaid structures of mono-Ub (green) complexed to the IsoT-ZnF domain (bright orange surface) (PDB ID: 2G45) and compact Lys48-Ub_2 (cyan) (PDB ID: 2BGF). The C-terminal Gly76 of mono-Ub binds deep pocket within IsoT-ZnF. This is prevented by a second isopeptide bond between Gly76 (proximal Ub) and Lys48 (distal Ub) in cyclic Lys48-Ub_2. The figure prepared using PyMOL.

To investigate this hypothesis, purified IsoT-ZnF was mixed with commercial Lys48-Ub_2 (Lot # 3291529) and the resulting non-covalent complex analysed by ESI-MS under carefully optimised conditions (*see* Chapters 2 and 4). Examination of the resulting spectrum showed that only the acyclic form of Lys48-Ub_2 was able to associate with IsoT-ZnF domain as expected. Contrary, the more abundant cyclic Lys48-Ub_2 did not interact with the IsoT-ZnF domain, which confirmed the initial prediction (Figure 5.2.11).

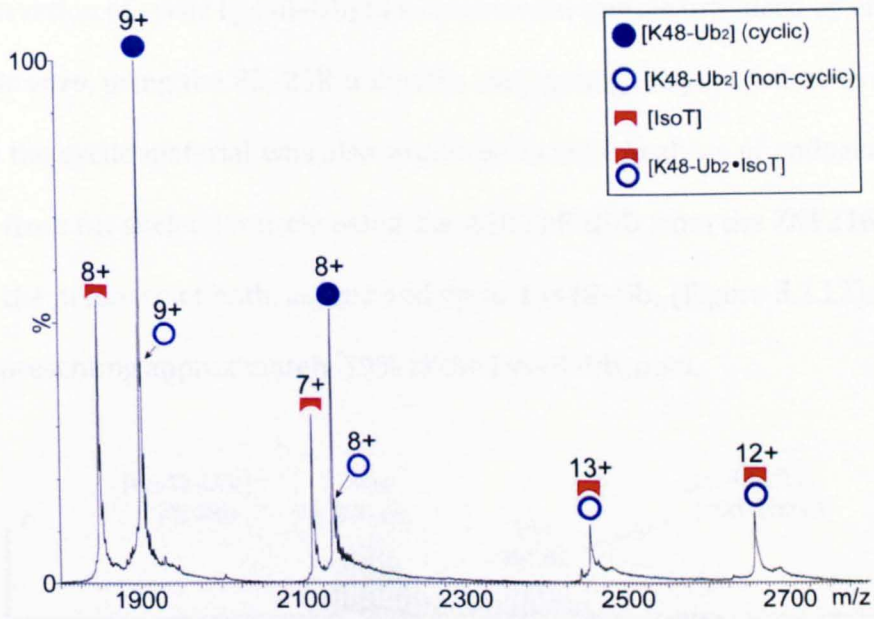

Figure 5.2.11 ESI-MS of 1 μM Lys48-Ub₂ (Lot#3291529) and 2 μM IsoT-ZnF sprayed from 25 mM ammonium acetate, showing that only the acyclic population of Lys48-Ub₂ is capable of forming complex.

In chapter 4 I demonstrated the capability of ESI-MS in probing interactions of Ub with UBDs that target both, the Ile44-centred hydrophobic patch (including the UBA domains, UBA2-hHR23A, UQ1-UBA and MIU) and the free C-terminus of Ub (IsoT-ZnF). In this chapter we have shown that cyclic Lys48-Ub₂ cannot bind IsoT-ZnF due to the absence of a free C-terminal Gly76 residue from the former. Considering these observations it was reasonable to question the behaviour of the aforementioned UBA domains against cyclic Lys48-Ub₂. Interestingly, calculations of the apparent K_ds based on either cyclic or acyclic Lys48-Ub₂ made no significant difference to the values (Table 5.2.2), which is consistent with the utilisation of Ub's Ile44-centred hydrophobic patch rather than its free C-terminal.

Table 5.2.2 Apparent K_d values for domains binding to cyclic and acyclic Lys48-Ub₂

UBD	K_d (μM)	
	acyclic Lys48-Ub₂	cyclic Lys48-Ub₂
UQ1-UBA	15 ± 2	15 ± 2
UBA2	15 ± 2	21 ± 2
MIU	9 ± 1	14 ± 2
IsoT-ZnF	3.6 ± 0.8	Not observed

The observation of cyclic Lys48-Ub_2 in a commercial sample produced by enzymatic ligation *in vitro*, using the E2-25K ubiquitin conjugating enzyme, led us to consider whether the cyclic material was also produced *in vivo*. Analysis of endogenous Ub_2 purified from rat skeletal muscle using the A20 ZnF UBD from the ZNF216 protein, showed the presence of both, acyclic and cyclic Lys48-Ub_2 (Figure 5.2.12), with the latter representing approximately 30% of the Lys48-Ub_2 pool.

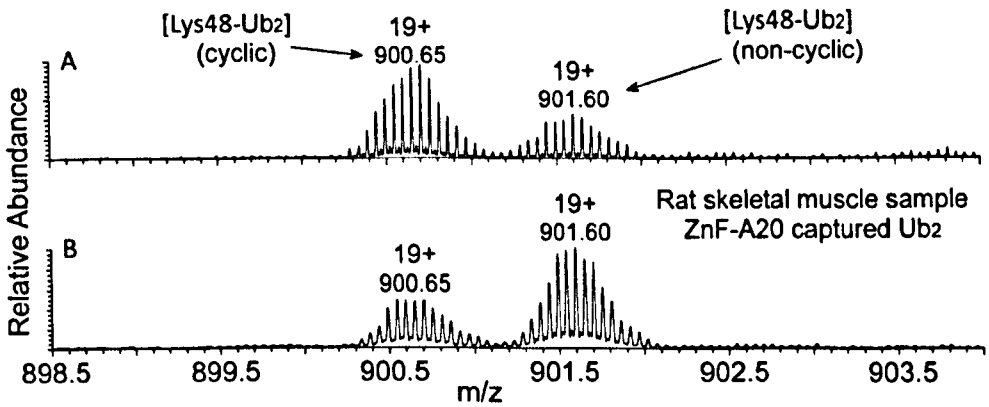

Figure 5.2.12 ESI-MS of intact (A) commercial Lys48-Ub_2 and (B) Ub_2 purified from rat skeletal muscle using A20 ZnF, showing the presence of cyclic Lys48-Ub_2. Spectra were acquired under denaturing conditions. Only the 19+ is shown for clarity.

It has been shown in section 5.2.1 that the purified endogenous rat muscle Ub_2 pulled-down by A20 ZnF domain, was predominately Lys48-linked. In addition, the use of a top-down approach for Lys linkage characterization of Ub_2 species was also demonstrated. MS/MS analysis of the isolated 17+ precursor ion (*m/z* 1006.5-1007.5) of each Ub_2 commercial standard resulted to the formation of b and y ions. Figure 5.2.13A-B shows the y58 14+ (*m/z* 1078.02; y ions in this case derived from the fragmentation of the distal Ub while proximal Ub remains intact) ion derived from Lys11- and Lys63-Ub_2, respectively, whereas Figure 5.2.13C shows the relevant spectra obtained in the case of Lys48-Ub_2. The latter contains an additional peak at *m/z* 1076.73, which corresponded to the y58 14+ cyclic structure found only in the Lys48-Ub_2 standard.

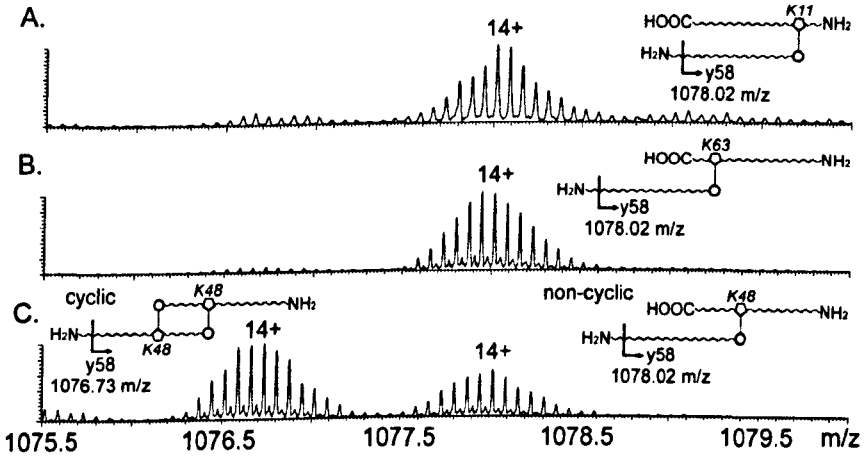

Figure 5.2.13 ESI-MS/MS spectra if the 17+ precursor ions of (A) commercial Lys11-Ub_2, (B) commercial Lys63-Ub_2 and (C) commercial Lys48-Ub_2, showing the fragment ion y58 14+. A cyclic Lys48-Ub_2 is observed at *m/z* 1076.73

Using ESI-MS, we have shown that IsoT-ZnF domain cannot bind *in vitro* generated cyclic Lys48-Ub_2 (Figure 5.2.11). Given that we have identified cyclic Lys48-Ub_2 in samples of rat skeletal muscle (Figure 5.2.12) we postulated that IsoT-ZnF domain will be incapable of pulling-down endogenous cyclic material. Figure 5.2.14 shows the y58 14+ fragment ion generated from 17+ precursor ion of, commercial Lys48-Ub2, A20 ZnF captured Ub_2 and IsoT-ZnF captured Ub_2, respectively.

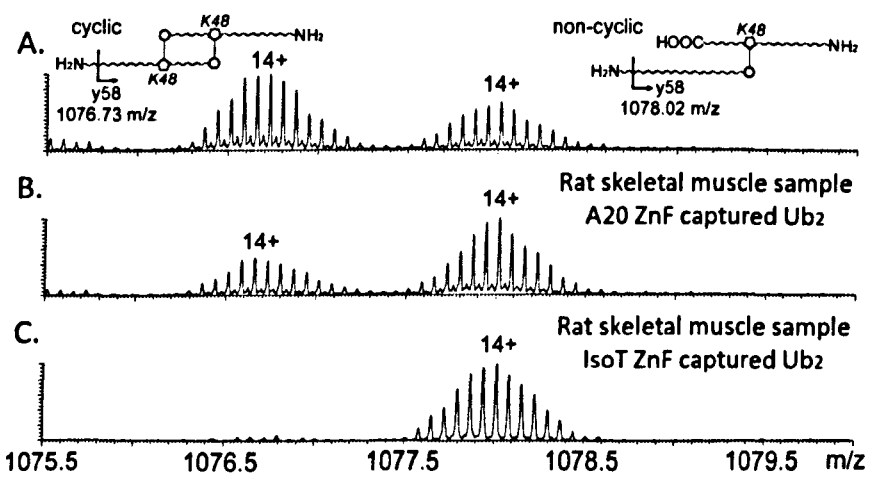

Figure 5.2.14 ESI-MS/MS spectra if the 17+ precursor ions of (A) commercial Lys48-Ub_2 and (B-C) Ub_2 isolated from rat skeletal muscle using the A20 ZnF and the IsoT-ZnF, respectively. The y58′ 14+ fragment ion exhibits a cyclic form in (A) and (B). The IsoT-ZnF domain is unable to capture cyclic Lys48-Ub_2 effectively.

Further investigation using A20 ZnF domain pull-downs from cultured HEK293T cells also showed the presence of cyclic Lys48-Ub₂ (Figure 5.2.15).

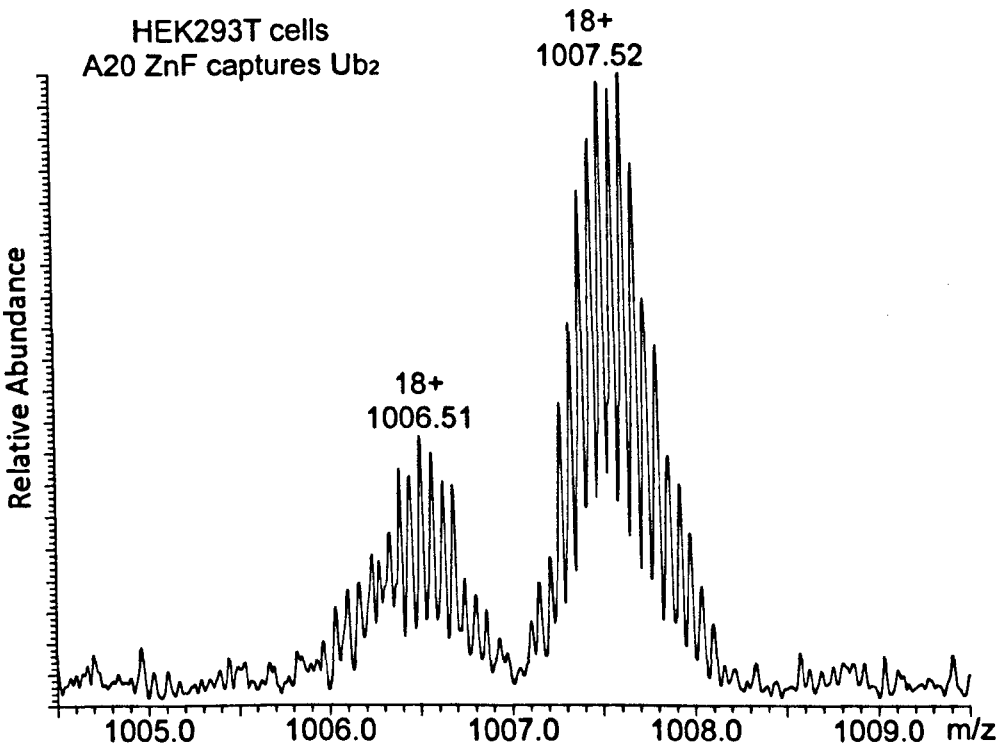

Figure 5.2.15 ESI-MS of Ub_2 pulled-down from HEK293T cells using the A20 ZnF domain, showing the presence of cyclic Lys48-Ub_2. Spectrum was acquired under denaturing conditions. Only the 18+ ion is shown for clarity.

From the above experiments it is clear that endogenous cyclic Lys48-Ub_2 is formed *in vivo* and it is not an artefact of *in vitro* production. In addition, given the relative abundance of Ub_2 that we have noted *in vivo* and the care taken to avoid adventitious proteolysis or Ub conjugation during the purification protocol, the scenario of artificial cyclisation seems unlikely. It has to be noted here, that bottom-up MS approach would fail to discriminate cyclic from acyclic Lys48-Ub_2, since both forms will generate the same tryptic peptide, LIFAGK(GG)QLEDGR (even thought the cyclic material will appear as two equivalents of this peptide) which serves as the fingerprint of Lys48-linked poly-Ub chains.

5.3 CONCLUSIONS

This chapter has demonstrated the potential use of top-down protein MS to study and characterize poly-Ub species derived from an *in vivo* source. Such a method, which avoids the use of proteases that destroy poly-Ub connectivity, could probe absolute poly-Ub chain topology. Using top-down proteomics and combining both, CID and ECD fragmentation techniques, we have managed to reveal the linkage type of Ub_2 purified from rat skeletal muscle using either A20 ZnF domain or IsoT-ZnF domain; linkage identified to be Lys48. The results were confirmed by bottom-up approaches; the sequence of the characteristic tryptic peptide, LIFAGK(GG)QLEDGR, was verified by ECD MS/MS. Although analysis of longer poly-Ub chains by this method is far more challenging, here we have provided the first proof of concept that top-down MS in combination with other techniques can be used to probe the connectivity of poly-Ub chains.

The presence of cyclic Lys48-Ub_2 as the major component of a commercial native Lys48-Ub_2, generated using E2-25K, was also reported. Contrary, ESI-MS analyses of other linkage types (Lys11-, Lys27- and Lys63-) showed that these linkages were consisted exclusively from acyclic Ub_2. It is noteworthy to mention that cyclic Lys48-Ub_2 is absent in material available from Enzo, a supplier that uses modified [186] (as opposed to wild type sequence) Ub to generate poly-Ub *in vitro*. We have also demonstrated the incapability of IsoT-ZnF domain to bind cyclic Lys48-Ub_2 due to the lack of a free C-terminus from the latter.

Furthermore, and possibly more importantly, a cyclic Lys48-Ub_2 species has been identified in A20 ZnF pull-downs from muscle tissue and cultured mammalian cells. Contrary, cyclic form was absent from endogenous material pulled-down using the IsoT-ZnF domain, which is consistent with the need of a free C-terminus. Combined

these results with the results obtained from the analyses of *in vitro* generated poly-Ubs, it is clear that cyclization occurs only in cases of Lys48-linked poly-Ub chains. This suggests that E2-25K may play a major role in the cyclization of Lys48-linked poly-Ub chains. Treatment of the A20 ZnF purified poly-Ubs with USP2 DUB, in order to remove longer unanchored poly-Ub chains, did not show any effect upon recovery levels of cyclic Lys48-Ub_2. Indeed, cyclization of poly-Ub chains and hence lack of a free C-terminus, it is likely to induce to some extent at least, resistance to DUB activity. Indeed, *in vitro* generated cyclic poly-Ub is known to be resistant to many DUBs, however, it has been reported that red blood cell extract contains an activity able to open and disassemble the cyclic chain [193]. Therefore, cyclic poly-Ub is unlikely to represent a dead-end product *in vivo*.

In summary, cyclic poly-Ub could represent a structurally unique form of unanchored poly-Ub, with perhaps related functional properties, but with the ability to be protected from disassembly by free chain disassembling DUBs such as IsoT.

CHAPTER 6

PROBING CONFORMATIONAL CHANGES ON THE STRUCTURE OF THREE-HELIX BUNDLE PROTEINS BY TWIMS

6.1 INTRODUCTION

TWIMS-MS has been successfully utilised to study the conformation and stoichiometry of proteins and protein assemblies [64, 66-70]. This success relies upon the ability of ESI to generate gas-phase ions, with low internal energies, directly from native aqueous solutions. Further to IM approaches, charge state analysis has also been utilised to study mixed populations of gas-phase protein conformers. A study by Kaltashov and Abzalimov has shown that the mean charge of each discrete distribution of ions, produced by ESI, correlates with the exposed protein surface area of that population [203]. Positively charged protein ions are usually generated by adduction of H^+, a phenomenon known as protonation. However, charged ions can also form with other adducting species, particularly with the alkali metal cations Na^+ and K^+, and the ammonium ion (NH_4^+). Typically, the extent of metal or ammonium adduction is highest on lower charge states. This can be attributed to their lower kinetic energy, and hence internal energy, leading to less efficient collisional cleaning [204]. Contrary to dissociation of alkali metal cations, which is often accompanied with a loss of charge, ammonium adducts are removed as neutral ammonia molecules. The presence of alkali metal adducts in biomolecules has been associated with a series of effects. For example, it has been shown that the

presence of alkali metal cations in a protein–ligand system can lower the activation barrier to dissociation leading to the destabilization of the complex [158]. In contrast, it has been demonstrated that metal adducts can stabilize gas-phase protein structure via formation of additional interactions [205, 206]. It was shown that the alkali metal adducted gas-phase ions exhibited lower CCS and hence more compact conformations, compared to their protonated counterparts.

This chapter reports the unusual effects of ammonium and alkali metal ion adducts upon the conformation of the three-helix bundle proteins UQ1-UBA and hHR23A-UBA2. We demonstrate that the presence of cations, particularly Na^+ and NH_4^+, in these proteins, provokes dramatic conformational changes to their gas-phase structures, whereas the purely protonated species exhibit compact structures. We also show that the CCS values of the latter are in good agreement with results obtained from molecular dynamics simulations. Moreover, we demonstrate that the adduction of multiple sodium cations can stabilize compact gas-phase conformations.

6.2 Results and Discussion

Ammonium acetate solutions are often used at millimolar concentrations for "native-like" ESI-MS studies. This can mainly be attributed to its useful property of generating very clean mass spectra of protonated proteins in the gas-phase. It can prevent alkali metal adduction by promoting ion pair reaction between the ammonium ion and acidic functional groups of the protein. Removal of the ion paired acetate and ammonium ions, is entropically favourable and their facile dissociation (15 kcal mol^{-1} for acetic acid and 11 kcal mol^{-1} for ammonia), which is accompanied by a proton transfer reaction, makes ammonium acetate an ideal

buffer for 'native-like' ESI [207]. Figure 6.2.1A shows the ESI mass spectrum of UQ1-UBA domain sprayed from 25 mM ammonium acetate solution. Contrary to a typical positive ESI mass spectra, where protonated peaks are commonly accompanied by trace amounts of adducts (usually Na^+, K^+ and NH_4^+) here we observed very high levels of ammonium adduction. A graphical representation of the extent of adduction by charge state (Figure 6.2.1B) revealed an interesting trend.

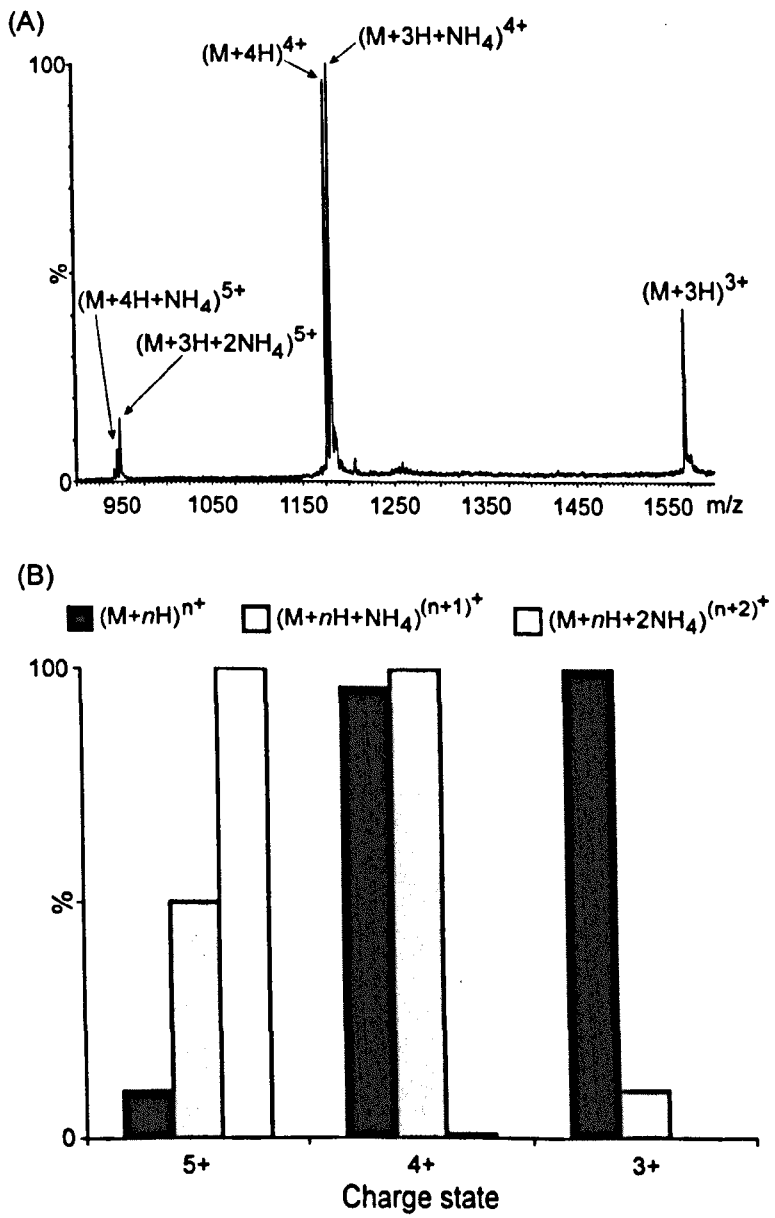

Figure 6.2.1 The charge state distribution of protonated and ammonium adducted ions (A) ESI mass spectrum of UQ1-UBA domain sprayed form 25 mM ammonium acetate and (B) graphical representation of the relative intensity of protonated and ammonium adducted ions at each charge state

The purely protonated ions and their mono- and di-ammonium adducted equivalents formed three distinct CSDs. In contrast to our experience of all other proteins sprayed from similar neutral solutions, where adduction (usually Na^+, K^+ and NH_4^+) is more prominent on the ions of lowest charge state, here the highest charge states were found to be more adducted. It is worth noting that the degree of ammonium adduction rarely reaches the levels observed here. Indeed, the ESI mass spectra of bradykinin, melittin and Ub, acquired under identical conditions, for the purpose of TWIMS calibration (*see* Chapter 2), showed almost no NH_4^+ adduction (< 10 %).

As previously mentioned the CSD of gas-phase protein ions is related to protein's exposed surface area in solution [203]. Considering that relationship, it can be postulated that ammonium adducted species derive by preferential adduction of ammonium ions on a distinct population of UQ1-UBA species that adopt extended conformations (and hence increased exposed surface area). Alternatively, it could be proposed that the process of adduct formation induces limited protein unfolding during the ESI process. A potential source of a UQ1-UBA species with increased surface area is a permanently misfolded/partially denatured protein population in solution. Hypothetically, such putative forms could be resolved by gel filtration. Therefore, a sample of UQ1-UBA protein was subjected to gel filtration on a PD10 column (*see* Chapter 2). Fractions collected through the elution profile of the protein from the column were subjected to analysis by ESI-MS. No significant differences in CSDs of the protonated or adducted ions were observed, suggesting that no permanently unfolded population of UQ1-UBA existed in solution. However, these results cannot exclude the possibility of rapidly interconverting conformers of UQ1-UBA, which would immediately re-equilibrate upon separation. NMR studies, however, do not support the presence of such equilibrium in solution [102].

To further investigate these interesting observations, we sought to examine the UQ1–UBA protein by ESI–TWIMS–MS. Figure 6.2.2 illustrates the ion mobility drift traces of the +3 (blue trace) and +4 (red trace) charge states obtained from the UQ1–UBA sprayed from 25 mM ammonium acetate. Traces represent the combined signal for protonated and mono-adducted ions for each charge state. In contrast to the +3 charge state which maintained a relatively narrow Gaussian distribution of conformers (the additional distribution on the left is due to background noise), the +4 charge state showed both, compact and unfolded distributions around 706 $Å^2$ and 980 $Å^2$, respectively.

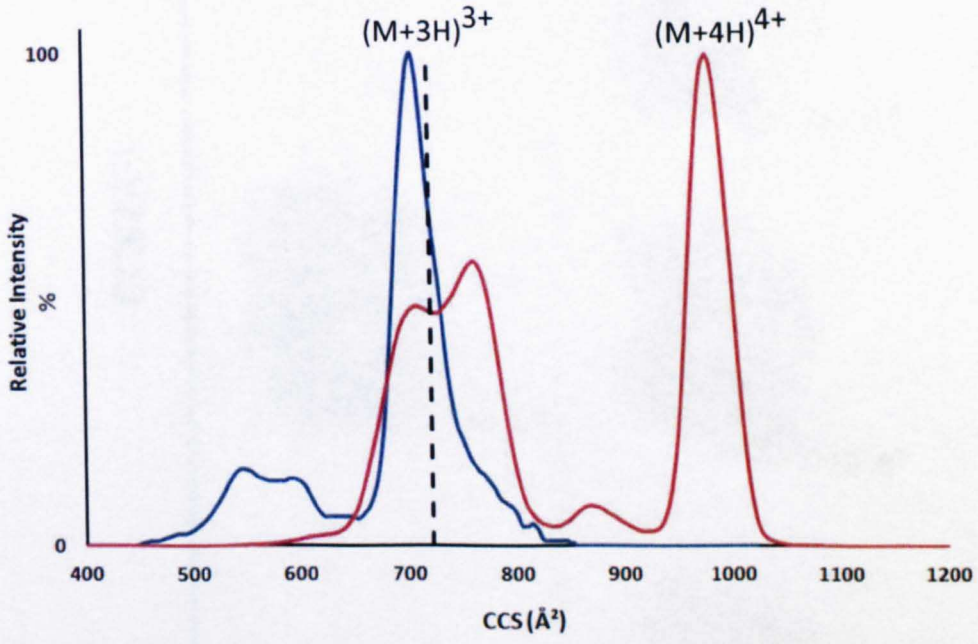

Figure 6.2.2 Ion mobility drift traces obtained for the +3 and +4 charge states of the UQ1–UBA protein sprayed from 25 mM ammonium acetate solutions.

When we examined the ESI spectra that resulted from the two distinct populations of the +4 charge state, an interesting phenomenon was revealed; the population of compact conformers was largely consisted of purely protonated species ($[M+4H]^{4+}$) while the more open structures where a mixture of adducted species, mainly $[M+3H+NH_4]^{4+}$ and a lower amount of protonated ions.

The experimentally determined CCS value of the compact conformers (706 Å^2) was compared with theoretical CCS values calculated from the NMR solution structure of UQ1–UBA protein (PDB ID: 2JY5) and from modelled structures generated by MD simulations performed at 300 K (Figure 6.2.3).

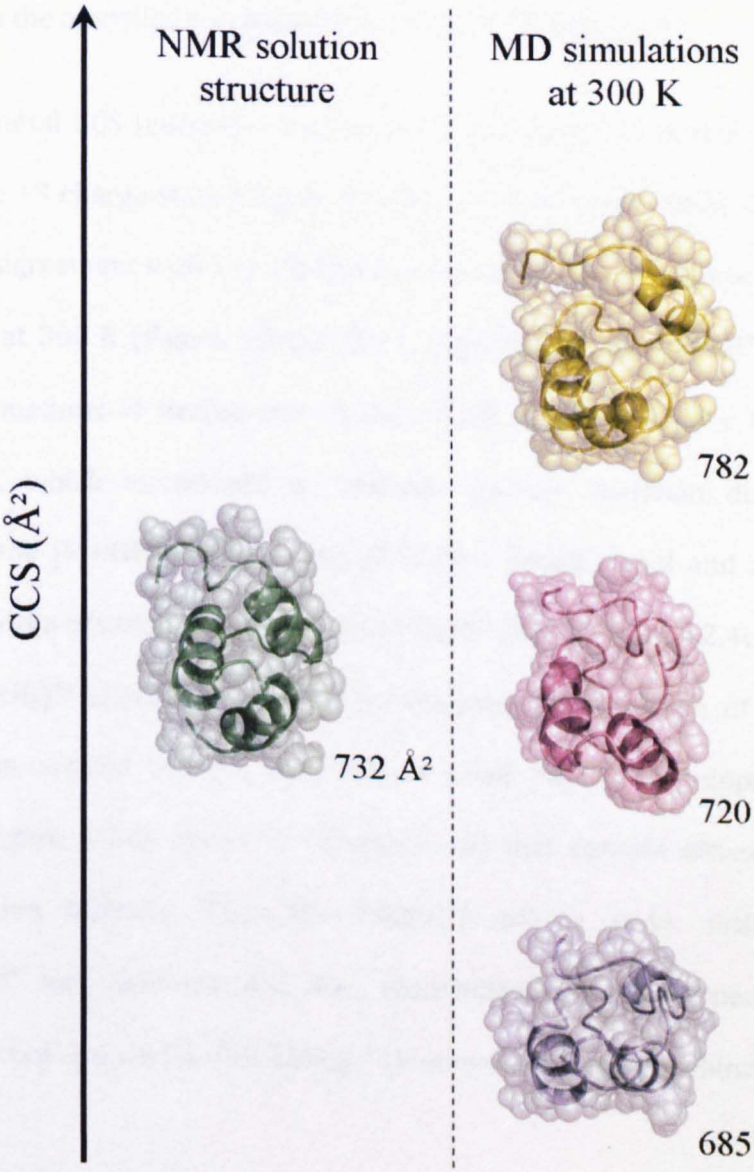

Figure 6.2.3 A comparison of the theoretical CCS values of the NMR solution structure of UQ1–UBA domain (PDB ID: 2JY5) and of structures derived by MD simulations at 300 K. Only the most compact (635 Å^2), the most open (782 Å^2) and the most frequently occurred (720 Å^2) MD structures are shown

To further investigate the intriguing behaviour of the UQ1–UBA gas-phase ions (both, protonated and adducted) as discussed above (Figure 6.2.2), experimentally derived IM drift traces of purely protonated (black, solid trace), singly ammonium ion adducted (red, dashed trace) and doubly ammonium ion adducted (blue, dotted trace) species were compared with the theoretical distribution of the conformers resulted from the modelled +3 charge state at 300 K (Figure 6.2.4).

The experimental CCS (corresponding to the peak maximum in the mobility drift trace) for the +3 charge state (Figure 6.2.4b) was determined to be 706 $Å^2$ which was in good agreement with the TM theoretical value (720 $Å^2$) of the modelled +3 charge state at 300 K (Figure 6.2.4a). This suggests that the $[M+3H^+]^{3+}$ ions may adopt conformations of similar size to the folded structure. Unlike the $[M+3H]^{3+}$ charge state, which maintained a relatively narrow Gaussian distribution of conformers, the $[M+4H]^{4+}$ charge state showed a broad signal and an additional small distribution of unfolded conformers around 980 $Å^2$ (Figure 6.2.4c). In contrast, the $[M+3H+NH_4]^{4+}$ species (Figure 6.2.4c) adopted a distribution of mainly open conformations, around 985 $Å^2$, with only a small population adopting compact structures. Figure 6.2.4d shows +5 charged ions that contain either one or two ammonium ion adducts. The $[M+4H+NH_4]^{5+}$ charge state, rather like the $[M+3H+NH_4]^{4+}$ ion, demonstrated two distributions of conformers, while the doubly-adducted species $[M+3H+2NH_4]^{5+}$ (Figure 6.2.4d) did not show any compact forms.

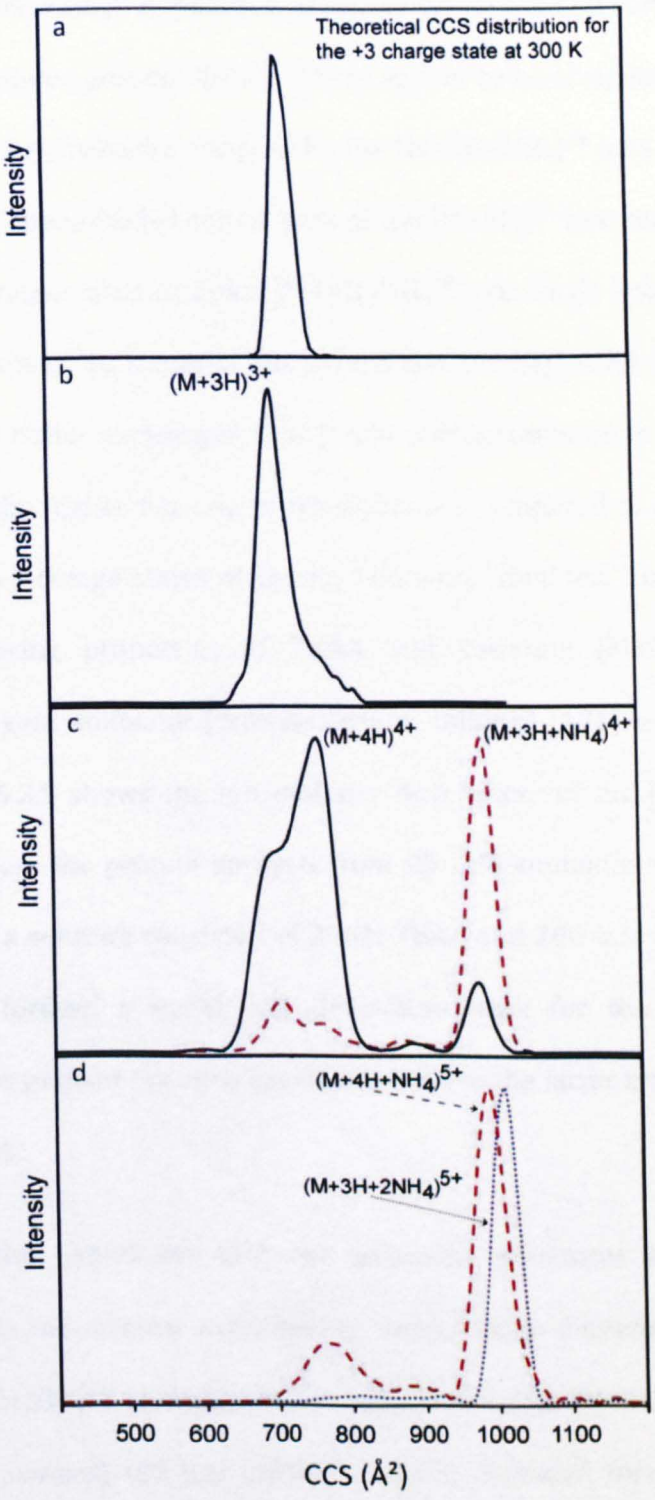

Figure 6.2.4 Ion mobility drift traces obtained for UQ1–UBA showing (a) modelled +3 charge state at 300 K, (b) +3 protonated charge state, (c) +4 charge state, protonated (*black, solid trace*) and slightly ammonium ion adducted (*red, dashed trace*) and (d) +5 charge state, singly ammonium ion adducted (*red, dashed trace*) and double ammonium ion adducted (*blue, dotted trace*)

As mentioned above, a small population of purely protonated $[M+4H]^{4+}$ ions exhibit extended conformations around 980 $Å^2$. These appear to be of similar size (in terms of CCS) to that of the structures adopted by the $[M+3H+NH_4]^{4+}$ ions (Figure 6.2.4c). We suspected that the unfolded conformers of the $[M+4H]^{4+}$ ions may have derived from the fragile ammoniated complex $[M+3H+NH_4]^{4+}$, via facile loss of ammonia in the mass spectrometer. To examine this hypothesis, the UQ1–UBA domain solution was desalted and buffer exchanged into 2 mM triethylammonium acetate (TEAA) solution. Due to the higher basicity of triethylamine compared to ammonia [208], only the +2 and +3 charge states of the protein were obtained. To counterbalance the charge reducing properties of TEAA and generate $[M+4H]^{4+}$ ions, the superchargingg agent sulfolane (tetramethylene sulfone) [131] was added to the solution. Figure 6.2.5 shows the ion mobility drift traces of the $[M+4H]^{4+}$ charge state obtained from the protein sprayed from 25 mM ammonium acetate (Figure 6.2.5a) and from a solution consisted of 2 mM TEAA and 200 mM sulfolane (Figure 6.2.5b). In the former, a small, but detectable peak for the more extended conformation was present (as seen previously) but in the latter trace this peak was essentially absent.

This supports the hypothesis that the extended structures obtained for the $[M+4H]^{4+}$ ions, in the original experiments, were due to dissociation of ammonia from the $[M+3H+NH_4]^{4+}$ complex. We conclude that the $[M+4H]^{4+}$ ions (formed during the ESI process) did not exhibit a highly extended form, but that these extended conformations were only produced from the ammonium adduct. The fact that open conformers were observed even after quadrupole isolation of the $[M+4H]^{4+}$ charge state (1176 *m/z*), suggests that the loss of ammonia possibly occur as early as the transfer region of the mass spectrometer; between the source and the quadrupole. Interestingly, the $[M+3H+NH_4]^{4+}$ complex showed both open and

compact forms, in contrast to the $[M+4H]^{4+}$ ion (formed directly during ESI) which adapted relatively compact conformations. This mixed population suggests that the site of ammonium adduction might be important for determining protein conformation.

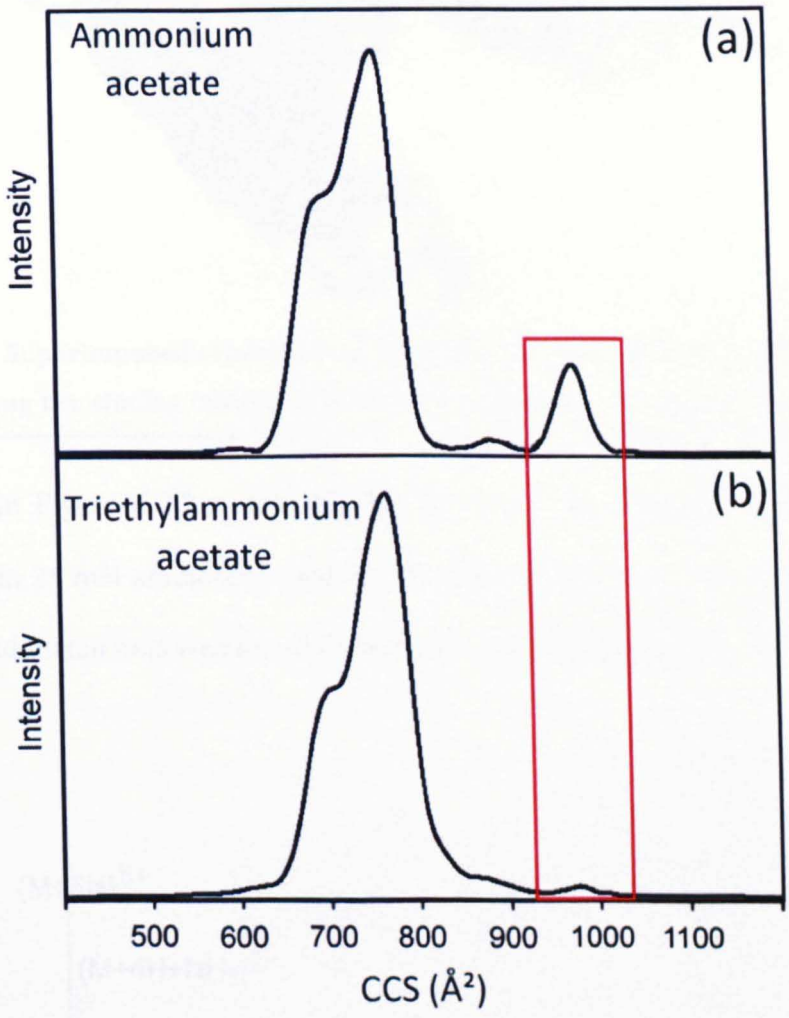

Figure 6.2.5 IM drift traces obtained for the $[M+4H]^{4+}$ ions of the UQ1–UBA protein, sprayed from (a) 25 mM ammonium acetate and (b) solution consist of 2 mM TEAA and 200 mM sulfolane, showing the absence of extended conformers in the absence of ammonium ions

---

The hHR23A–UBA2 domain has been chosen as a second example of a triple–helix bundle protein due to the fact that it exhibit solution structures that are similar to UQ1–UBA domain (Figure 6.2.6).

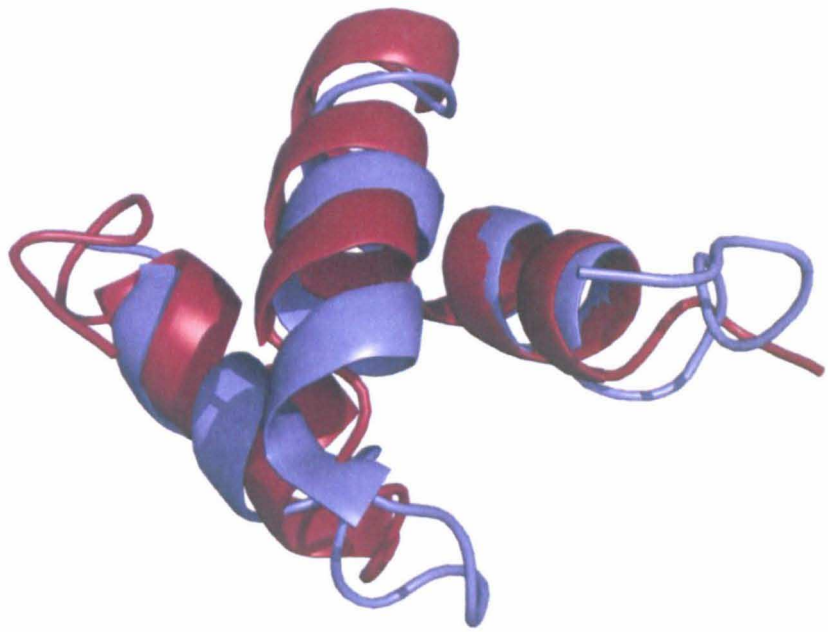

Figure 6.2.6 Superimposed structures of the hHR23A–UBA2 (blue) and UQ1–UBA (red), showing the similar folding of these two three-helix bundle proteins

Illustrated in Figure 6.2.7 is the ESI–MS spectra of the hHR23A–UBA2 protein, sprayed from 25 mM ammonium acetate solution. Similar to the UQ1–UBA domain, the CSD of adducted ions was found to be highest at higher charge states.

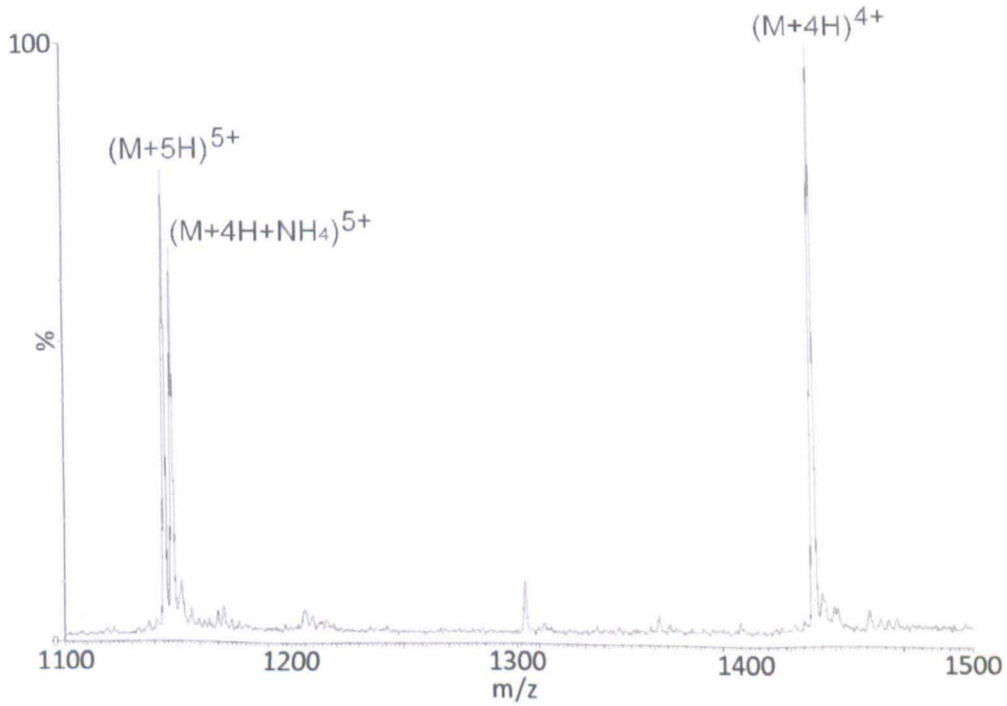

Figure 6.2.7 ESI mass spectrum of hHR23A–UBA2 (2 mM) sprayed from 25 mM ammonium acetate, showing highest ammonium adduction at higher charge states

Figure 6.2.8 shows a comparison of theoretically and experimentally derived IM drift traces obtained for the hHR23A-UBA protein. IM drift traces of purely protonated (solid trace) and singly ammonium ion adducted (dashed trace) species obtained for hHR23A-UBA2 domain sprayed from 25 mM ammonium acetate, while theoretical distribution of the conformers resulted from the modelled +4 charge state at 300 K. The $[M+4H+NH_4]^{5+}$ ions adopted more extended conformations than their solely protonated counterparts, which showed two distributions of conformers, both close and open, around 827 $Å^2$ and 965 $Å^2$, respectively (Figure 6.2.8c). The appearance of the two populations of protonated conformers can be explained by analogy with the case of UQ1-UBA i.e. the extended structures of purely protonated ions are the product of facile dissociation of ammonia from the related ammonium adducted species. The comparable CCS values of the $[M+4H+NH_4]^{5+}$ (940 $Å^2$) and open form of $[M+5H]^{5+}$ (965 $Å^2$) support this assumption. Furthermore, MD simulations on the +4 charged modelled structure at 300 K generated structures which demonstrated a narrow CCS distribution concentrated around 825 $Å^2$ (Figure 6.2.8a). The compact structures obtained for the $[M+5H]^{5+}$ ions (Figure 6.2.8c, solid trace) were found to exhibit conformations of similar size to the +4 modelled structures. In contrast, the $[M+4H]^{4+}$ ions showed CCS around 782 $Å^2$ that was slightly smaller (~5 %) compared to the compact conformers (825 $Å^2$). This may be attributed to side chains collapse in gas-phase which is a phenomenon that has been described previously [59].

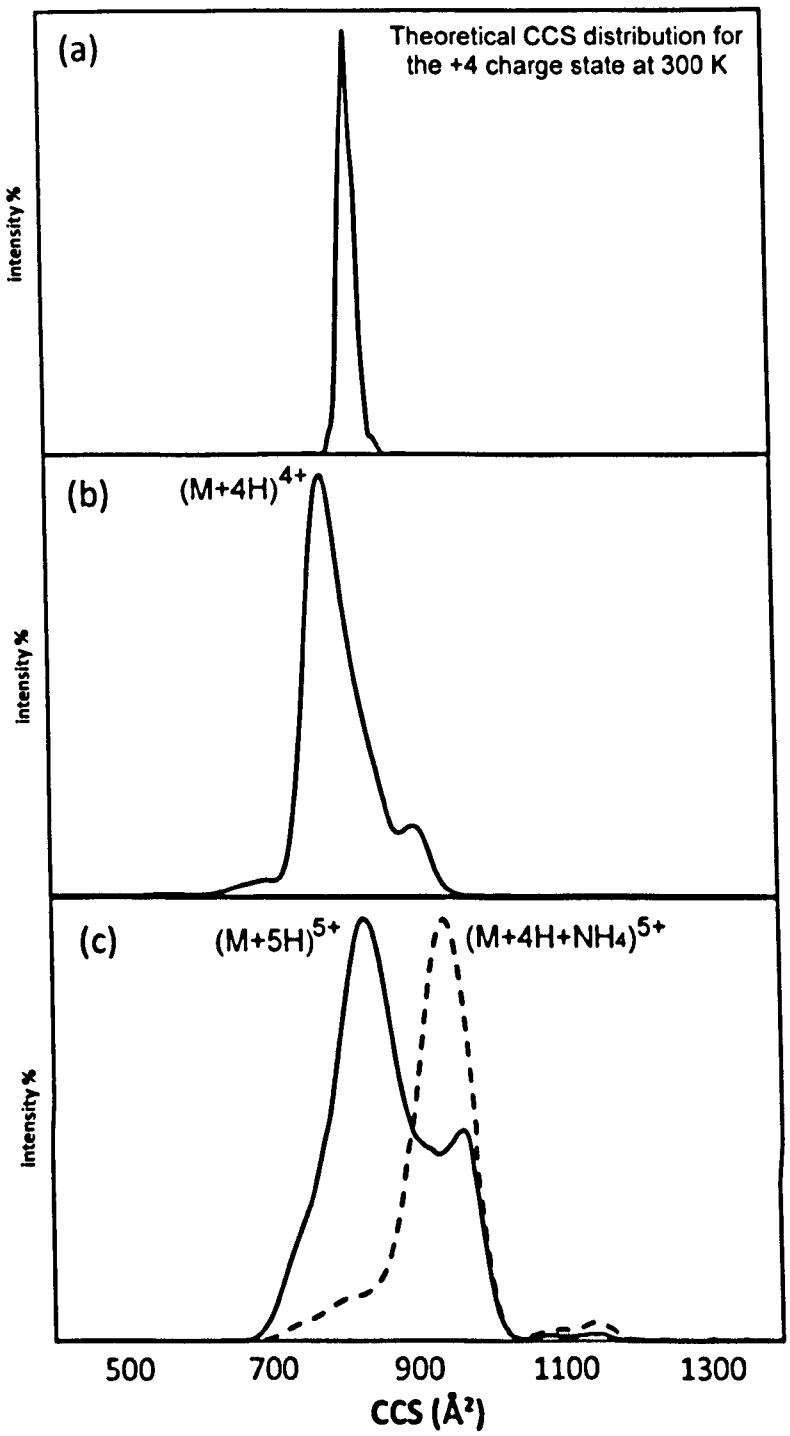

Figure 6.2.8 IM drift traces obtained for hHR23A-UBA2 showing (a) modelled +4 charge state at 300 K, (b) +4 protonated charge state and (c) +5 charge state, protonated (solid trace) and singly ammonium ion adducted (dashed trace)

In both cases investigated above, it has been shown that the presence of ammonium adducts was accompanied by conformational changes. But, how can the adduction of ammonium ion (or of another cation) induce structural rearrangements?

Protein gas-phase ions are stabilised by salt bridges and hydrogen bonds, which are the main forces that can preserve compact, folded protein conformations shortly after desolvation [209]. However, with increasing charge in combination with the absence of solvent, Coulomb repulsion becomes significant and overcomes the stabilizing intramolecular interactions. The result is the adoption of extended conformation by the protein in the gas-phase in order to counterbalance the repulsion forces [53]. An interesting study by Breuker and McLafferty [59] has shown that a protein in the gas-phase may re-fold to a structure where the charge sites are coordinated by other residues within the protein structure. According to the authors, such structure rearrangements depend on the charge state of the protein ion, and timescale of measurement. Therefore, both the number and site of the charges in the gas-phase ion influence the conformation. Another factor that may play an important role is the nature of the attached charge carrier, which could be a proton or another cation (e.g. Na^+ or NH_4^+). Generally, H^+ is attached to a basic site by forming one or two bonds. In contrast, alkali metal cation attachment, often requires the availability of several (generally up to six) coordinating electron pairs in its surroundings (known as charge solvation) [210]. The ammonium ion, on the other hand, has the ability to form multiple hydrogen bonds (N···H···O) [211]. Moreover, the large size of the ammonium cation possibly will also influence the gas-phase structure of proteins.

It is clear that disruption of salt bridges will induce a degree of unfolding and that the severity of this effect will depend on the site of adduction. The dramatic change in the conformation of, in particular, the UQ1-UBA protein can be attributed to disruption of salt bridges. The Arg546-Glu563 salt bridge has been identified as a potential candidate for this effect. The two residues are located on the opposing faced helices α1 and α2, respectively (Figure 6.2.9) and are likely to stabilize the

global protein fold in gas-phase. Ammonium cation attachment at this site may break the salt bridge by cation displacement of the Glu563 side chain, leading to perturbation of the protein native fold. Moreover, the presence of a small compact population of the $[M+3H+NH_4]^{4+}$ can be related to the attachment of NH_4^+ to other residues, an event which does not induce unfolding. In the case of the $[M+3H+2NH_4]^{5+}$ it is postulated that at least one of the two ammonium ions is adducted to Arg546 and thus only unfolded structures were obtained for this ion.

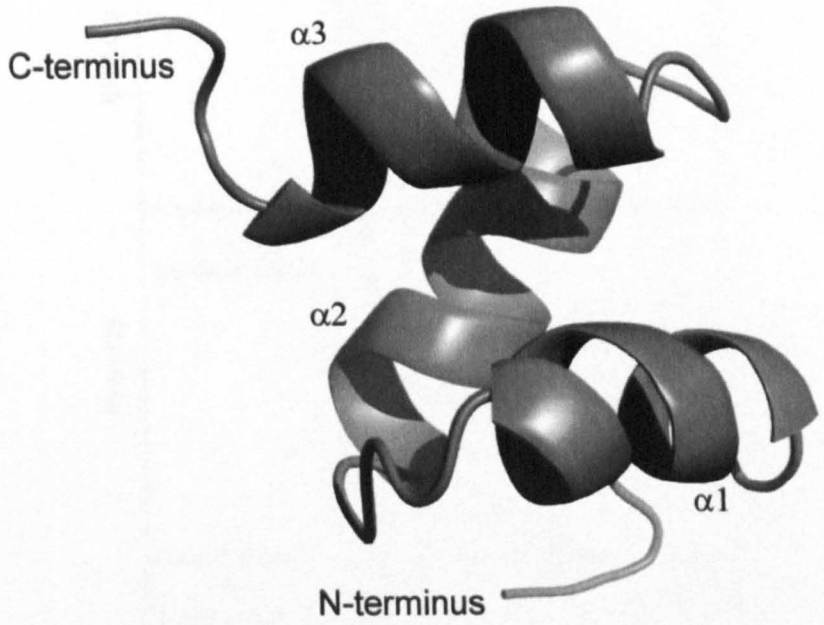

Figure 6.2.9 A cartoon representation of the 3D structure of the UQ1-UBA domain as determined by NMR (PDB ID: 2JY5)

The effects of multisodium adduction upon the conformation of UQ1-UBA domain were also investigated. Figure 6.2.10b-d illustrates the obtained IM drift traces for the quadruply charged ions of M+*n*Na species, where n = 4-6, sprayed from 2 mM sodium acetate. Figure 6.2.10a shows the IM drift traces of the $[M+4H]^{4+}$ and $[M+3H+Na]^{4+}$ charge states sprayed from 2 mM TEAA solution. Comparison of the monosodiated with the multisodiated species reveals that, whilst a single Na^+ ion is destabilising to UQ1-UBA structure, the attachment of additional sodium cations stabilizes the protein's compact gas-phase structure.

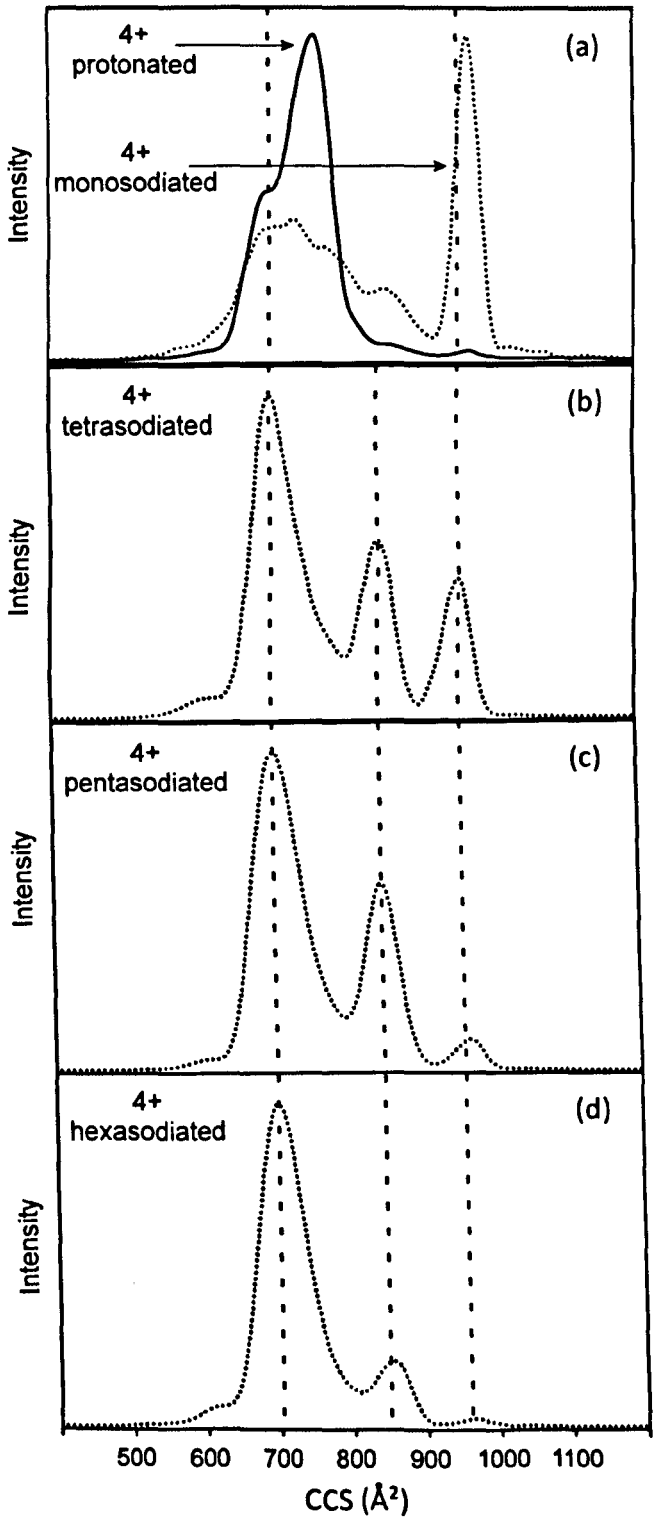

Figure 6.2.10 IM drift traces obtained for the +4 charge state of the UQ1-UBA domain showing (a) Purely protonated and monosodiated species, (b) tetrasodiated, (c) pentasodiated and (d) hexasodiated species. The dashed lines are included to guide to the eye.

Indeed, the stabilization of the protein structure in gas-phase, which here is monitored by the depletion of the signal related to open conformations, scales with the number of sodium cations.

The formation of multisodiated adducts can be rationalised by: a) replacement of H^+ by Na^+ and b) ion pairing of Na^+ with the negatively charged acidic residues [207]. Stabilization of the gas-phase structure of the doubly charged bradykinin ion, has been attributed to the ability of Na^+ to establish interactions with functional groups on the peptide backbone [205]. In the case of UQ1-UBA protein, whilst monosodium adduction destabilises the compact structure, multisodiation lead to more compact forms. This may be attributed to formation of additional salt bridges (between Na^+ and polypeptide functionality) that stabilize the gas-phase structure.

6.3 Conclusions

The effects of cation adduction upon the conformation of the three-helix bundle proteins, UQ1-UBA and hHR23A-UBA, have been demonstrated in this chapter. Unusually high levels of ammonium adduction have been observed when these proteins sprayed from 25 mM ammonium acetate solution. Intriguingly, these levels became highest for higher charge states. It has to be pointed out that ammonium or metal ion adduction is not always associated with increased CSD of protein ions. Indeed, such adducts are normally most abundant on lower charge states. Furthermore, the possibility of a permanent misfolded/partially denatured protein population in solution was investigated, but our results did not support this hypothesis.

We have also employed ESI-TWIMS-MS approaches to study the aforementioned proteins. It has been demonstrated that ammonium cation adduction is associated

with extended conformations of the examined proteins, especially in the case of UQ1-UBA domain. It has also been shown that even within the same protein charge state, ammonium complexes give rise to more extended species than their purely protonated counterparts. It has been suggested that destabilization of the gas-phase structure of UQ1-UBA may be attributed to the disruption of a salt bridge formed between the Arg546 and Glu563, by ammonium cation attachment at the latter's side chain.

The effects of sodium adduction upon the structure of UQ1-UBA have also been examined. Monosodium adduction led to similar to those caused by ammonium adduction. In contrast, it has been shown that the attachment of multiple sodium cations, stabilized the gas-phase conformation. Indeed, it has been demonstrated that the stabilization effect, scales with the number of sodium cations.

CHAPTER 7

THE INHIBITION OF Ub•IsoT-ZnF INTERACTION BY SYNTHETIC PEPTIDES

7.1 INTRODUCTION

The majority of intracellular proteins are degraded by the Ub–proteasome pathway. Such regulatory mechanisms are crucial to maintain normal cellular homeostasis. The Ub–proteasome pathway is mediated by proteasome holoenzyme, Ub ligases and DUB enzymes [76]. Non-lysosomal proteolysis relies on the ability of Ub to label substrates for protein degradation by proteasome. Previous studies have linked the pathogenesis of various human diseases with deregulation of the Ub–proteasome pathway [212, 213]. Inhibition of this regulation mechanism, either at the level of proteasome, ubiquitination or DUB enzymes, provides new targets for the development of novel therapeutic strategies. Indeed, bortezomib, a boronic acid dipeptide [214], is the first proteasome inhibitor that has been approved for the treatment of multiple myeloma patients. A crystal structure of the yeast 20S proteasome in complex with bortezomib has shown that the latter blocks the activity of the proteolytically active threonine (Thr21) residue; the boron atom of bortezomib is covalently attached to the nucleophilic oxygen lone pair of Thr21 [215].

Further to proteasome inhibitors, more recent studies have been focused on the discovery and development of inhibitors of the ubiquitination cycle (via inhibition of E1 and E3 enzymes) and of DUB enzymes, which have recently been linked to

several human diseases [216]. A recent study has reported the inhibition of the DUB enzyme USP7 (ubiquitin-specific protease 7) by the small molecule P5091 (2-acetyl-4-nitro-5-(2,3-dicloro-phenylsulfanyl)-thiophene) [217]. USP7 stabilizes MDM2 (murine double minute oncogene) levels, which consequently mediates p53 ubiquitination and thus its proteasomal degradation. The study also has suggested that P5091 inhibits USP7 activity without blocking proteasome function directly. This inhibition approach, according to the authors, is less likely to trigger off-target activities and associated toxicities.

IsoT, also known as USP5, belongs to the group of DUB enzymes that disassemble unanchored poly-Ub chains and thereby recycling free Ub [218, 219]. More importantly, the deubiquitination procedure prevents accumulation of unanchored poly-Ub chains which can inhibit the proteasome [218, 220]. The recognition of free poly-Ub chains by IsoT is mediated by a ZnF UBP domain which requires the C-terminus of Ub for binding [106]. It has also been reported that modification or deletion of Ub's C-terminal residue, Gly76, reduces the rate of deubiquitination [221]. It can be assumed that a decrease in deubiquitination rate will result in accumulation of Ub moieties, which in turn may inhibit the proteasome. Therefore, disruption of the IsoT•poly-Ub complex may result in indirect inhibition of the proteasome by accumulated free poly-Ub chains. The crystal structure of the IsoT-ZnF•mono-Ub interaction showed that the C-terminal residues of Ub (from Leu71 to Gly76) form a rigid tail that penetrates deeply into the hydrophobic pocket of the IsoT-ZnF domain [106]. Blockage of that pocket, therefore, will disrupt the complex and consequently deubiquitination rate. The tail formed by Ub's C-terminus residues adopts the ideal stereochemistry to fit into the hydrophobic pocket of IsoT-ZnF domain. Therefore, a potential inhibitor has to exhibit a structure of similar stereochemistry.

The ability of ESI–MS to probe binding affinities of Ub•UBD interactions has been demonstrated in chapter 4. This chapter describes the synthesis of small peptides (based on Ub's C–terminal peptide, LRLRGG) and the use of ESI–MS to investigate their potential inhibitory activity against the Ub•IsoT–ZnF interaction.

7.2 Results and Discussion

7.2.1 Peptide synthesis and purification

The peptides were synthesised using the Fmoc SPPS protocol described in chapter 2, and purified by preparative LC chromatography. Table 7.2.1 gives the peptides synthesised here, as well as the obtained quantity of each purified material.

Table 7.2.1 Hexapeptides synthesised using Fmoc SPPS approach, showing their primary structure and the final purified quantity obtained for each peptide.

Peptide	MW *(Da)*	Weight *(mg)*
LRLRGG	670.8	1.1
KRFRGG	719.8	1.4
LRLAGG	585.7	9.1
LALRGG	585.7	5.4
FRLRGG	704.8	2.1
LRFRGG	704.8	2.9
KLRRGG	685.8	5.1
HRLRGG	694.8	0.7
FALRGG	619.7	2.9
LRLRGV	712.9	1.2

Figure 7.2.1 illustrates the ESI–MS spectra of LRLRGG peptide, obtained before and after purification, sprayed from denaturing solution (50% methanol, 1% acetic acid).

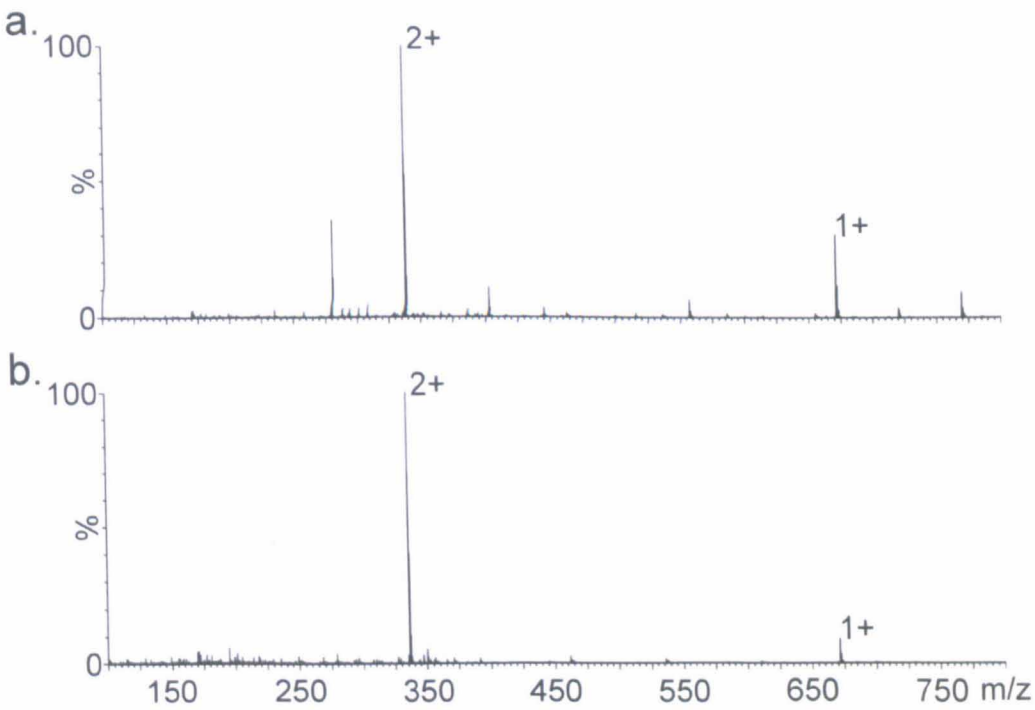

Figure 7.2.1 ESI mass spectra of LRLRGG (4 μM) peptide a) prior HPLC purification and b) after HPLC purification, sprayed from 50:50 MeCN:H_2O, 0.1% Acetic acid.

Illustrated in Figure 7.2.2 is the HPLC separation chromatograph obtained for the LRLRGG peptide.

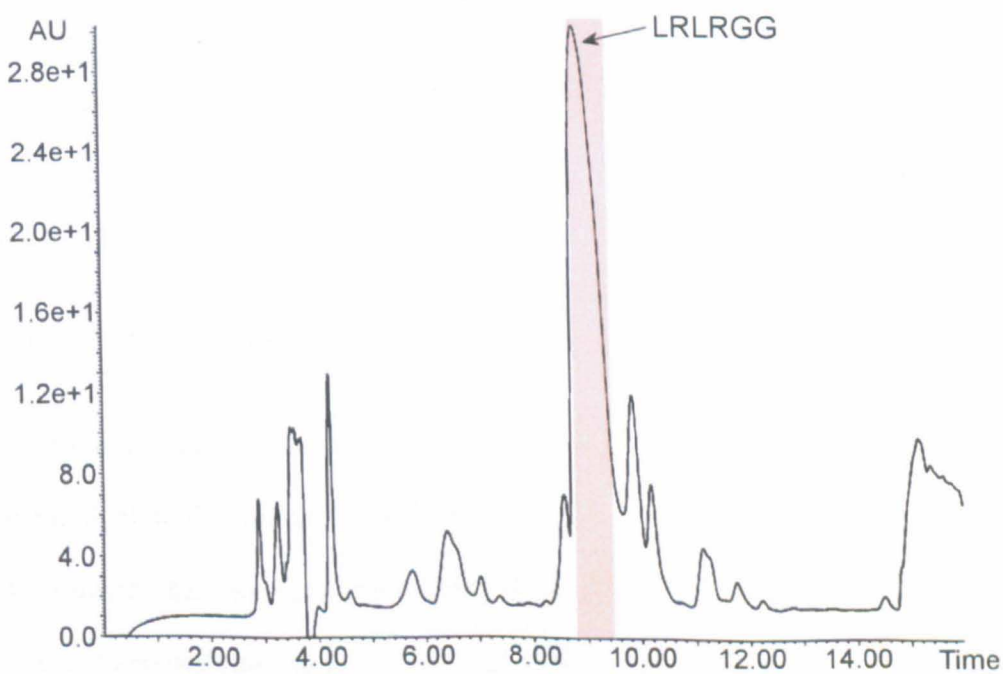

Figure 7.2.2 HPLC separation chromatograph for LRLRGG peptide. Red highlighted is the collected HPLC fraction.

Similar purification profiles were obtained for all the peptides synthesised in this study, and the purity of each peptide was confirmed by ESI–MS.

7.2.2 Inhibition of Ub•IsoT–ZnF complex

The ability of ESI–MS to probe the specificity and selectivity of Ub•UBD complexes, has been demonstrated in chapter 4. The specificity of the IsoT–ZnF complex with Ub was also examined and confirmed using the deletion mutant Δ–Gly75/Gly76–Ub. As previously discussed, Ub's C–terminal amino acids, Leu71 to Gly76, form a rigid tail that binds to the hydrophobic pocked of the IsoT–ZnF domain (Figure 7.2.3).

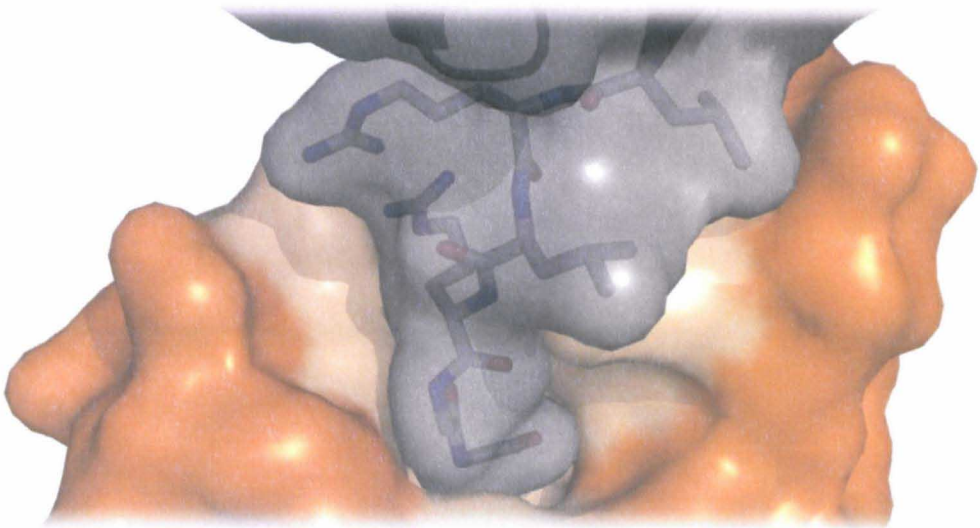

Figure 7.2.3 Crystal structure of mono-Ub (grey surface) complexed to the IsoT–ZnF domain (bright orange surface) (PDB ID: 2G45), showing the rigid tail formed of Ub penetrating into hydrophobic pocket of the domain.

We postulated that the chemically synthesised peptide, LRLRGG which mimics Ub's C–terminal, should bind the IsoT–ZnF domain with relatively high affinity. Figure 7.2.4a show the ESI mass spectrum of LRLRGG and IsoT–ZnF domain obtained in the presence of acetonitrile vapour. The 7+, 6+ and 5+ complex ions are observed at *m/z* 2208, 2576 and 3091, respectively. The K_d value determined from this spectrum was found to be 5.8 μM, which was somewhat higher than the value determined for the

Ub•IsoT–ZnF complex (K_d~2.3 μM). This can potentially be attributed to additional interactions that may be present in the Ub•IsoT–ZnF complex, which could stabilize the complex more effectively in solution and in the gas–phase. To examine the specificity of the (LRLRGG•IsoT–ZnF) complex, we used the LRLRGV peptide as a negative control. In contrast to the LRLRGG peptide, the increased steric bulk of the C-terminal Val residue was predicted to prevent access of the LRLRGV peptide to the hydrophobic pocket of the ZnF domain. Indeed, LRLRGV peptide did not form detectable complex with the IsoT–ZnF domain (Figure 7.2.4b). This result is consistent with the crucial role of Ub's C–terminal Gly76 residue.

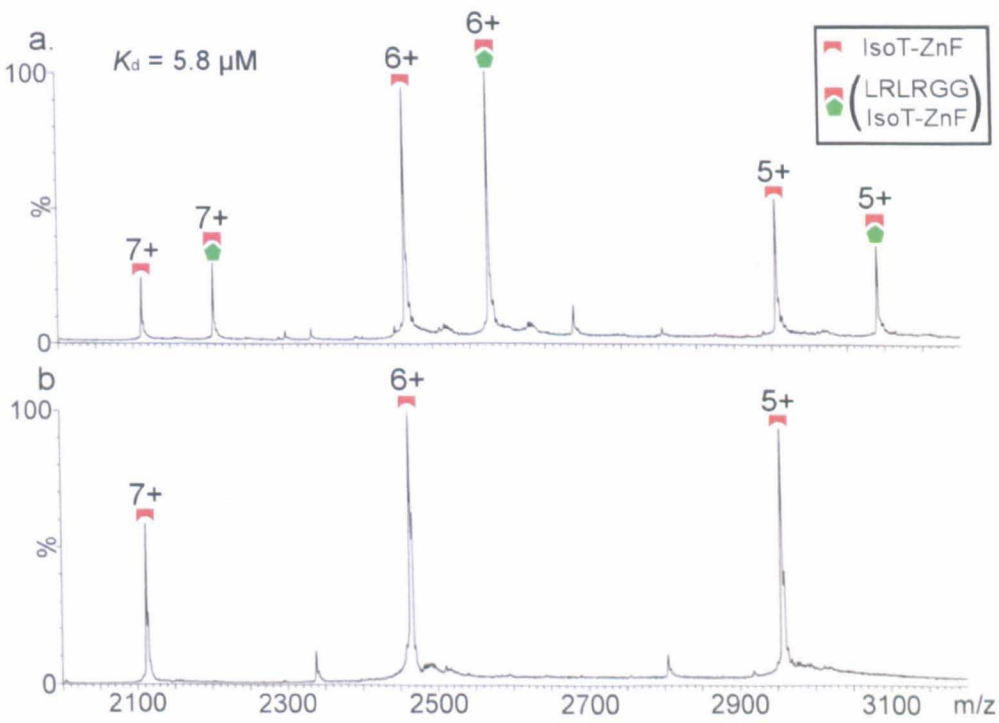

Figure 7.2.4 ESI–MS spectra of IsoT–ZnF (4 μM) complex with a) LRLRGG peptide (7.5 μM) and b) LRLRGV peptide (7.5 μM), sprayed from 25 mM ammonium acetate solution in the presence of acetonitrile vapour

Having confirmed the specificity of the complex formed between IsoT–ZnF domain and the LRLRGG peptide, and given the importance of the Gly residue in this peptide, we went on to synthesise eight peptides in which the C–terminal dipeptide –GG was

kept unmodified. The apparent binding affinity (K_d) values of each (peptide•IsoT–ZnF) are given in Table 7.2.2.

Table 7.2.2 Apparent binding constant (K_d) values for (peptide•IsoT–ZnF) complex

Peptide	K_d (μM)
LRLRGG	5.8
LRFRGG	7.6
FRLRGG	7.7
KRLRGG	9.5
HRLRGG	12
KRFRGG	17
FALRGG	34
LALRGG	42
LRLAGG	43
LRLRGV	Not Detected

The determined binding affinities (Table 7.2.2) suggest an important role for the Arg residues in the (peptide•IsoT–ZnF) interaction. For example, when the distal and proximal Arg residues were systematically replaced by Ala (LALRGG and LRLAGG), the K_d values were found to be 42 μM and 43 μM, respectively, which were than seven–fold lower compared to the value determined for the LRLRGG peptide (5.8 μM). The simultaneous substitution of Arg for Ala and of Leu for Phe (FALRGG) resulted in higher binding affinity value (34 μM) than the case of a single substitution of Arg for Ala. However, this was significantly lower than the value obtained for the wt–like peptide. In addition, the KRFRGG peptide bound to the IsoT–ZnF domain with a K_d value of 17 μM. In contrast, the single exchange of Leu with Phe (LRFRGG and FRLRGG) did not appear to have significant influence on the binding interaction (K_ds = 7.6 μM and 7.7 μM, respectively). Finally, replacement of N–terminus Leu with either Lys or His, produced peptides that bind domain with apparent K_d values of 9.5 μM and 12 μM, respectively.

The inhibitory activity of the synthesised peptides upon the Ub•IsoT–ZnF complex was also investigated. Illustrated in Figure 7.2.5aFigure 4.2.6 is the ESI mass spectrum of IsoT–ZnF with Ub sprayed from 25 mM ammonium acetate. Formation of the Ub•IsoT–ZnF complex was observed at *m/z* 2335 (10+) and 2123 (11+). Figure 7.2.5b shows the ESI mass spectra of IsoT–ZnF with Ub and LRLRGG peptide, sprayed from 25 mM ammonium acetate solution. Additionally to the Ub•IsoT–ZnF complex, the LRLRGG•IsoT–ZnF complex was also observed at *m/z 2208 (7+), 1932* (8+) and 1717 (9+). In the presence of the LRLRGG peptide the determined apparent binding affinity of the Ub•IsoT–ZnF complex was found to be lower (K_d = 3.4 μM) compared to 2.4 μM obtained previously, both in chapter 4 and in the literature [106].

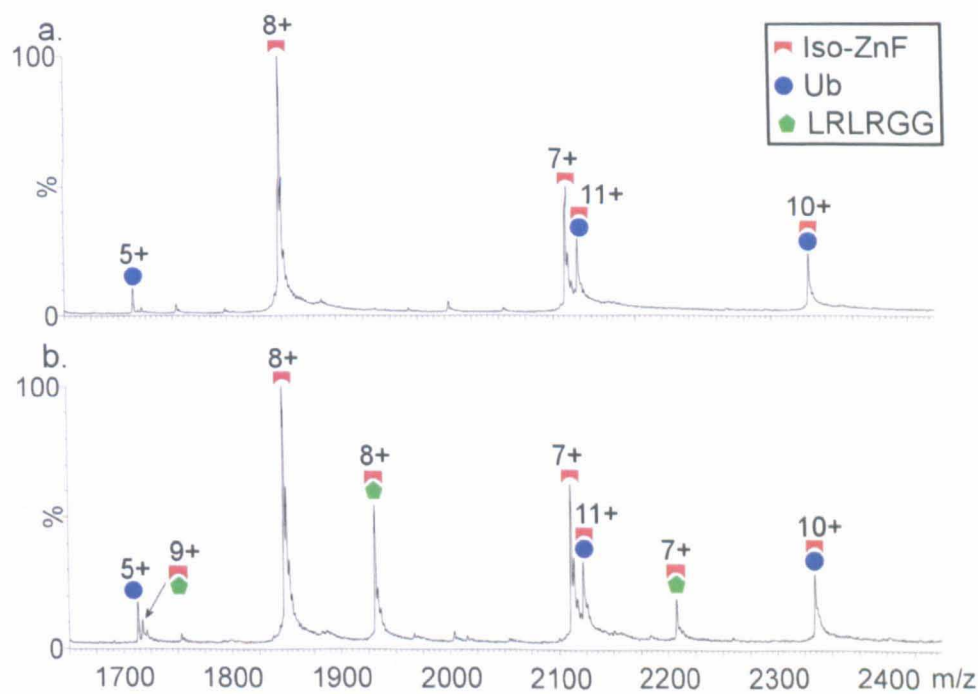

Figure 7.2.5 ESI–MS spectra of 2 μM IsoT–ZnF with a) 0.5 μM Ub and b) 0.5 μM Ub and 5 μM LRLRGG peptide, sprayed from 25 mM ammonium acetate solution

The effects of peptide (LRLRGG) concentration upon the Ub•IsoT–ZnF interaction, were also investigated. To do this, the concentration of the complex's components (Ub and Iso–ZnF) was kept constant whilst the concentration of the peptide was

varied from 2 to 10 μM. Similarly, the effects of the following synthesised hexapeptides were also examined: LRFRGG, FRLRGG and KRLRGG. The results obtained for each peptide are given in Table 7.2.3. Figure 7.2.6, illustrates the effects of peptide concentration upon the binding affinity of the complex.

Table 7.2.3 Apparent binding constant (K_d) values for (Ub•IsoT–ZnF) complex in the presence of peptide inhibitors.

Peptide	K_d (μM)					
	Peptide concentration (μM)					
	0	2	4	6	8	10
LRLRGG	2.4	3.4	3.5	3.5	3.7	4.3
FRLRGG	2.4	3.6	3.6	3.8	4.0	4.2
LRFRGG	2.4	3.5	3.7	4.0	4.4	4.8
KRLRGG	2.4	3.8	3.9	4.4	3.7	4.0

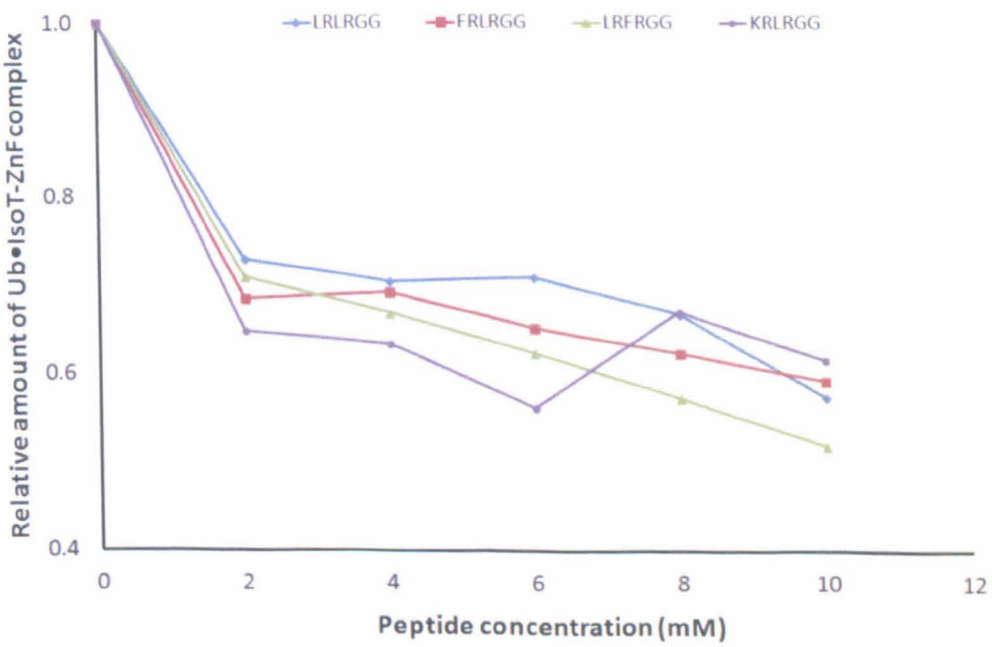

Figure 7.2.6 Diagram showing the inhibitory activity of synthetic peptides against the Ub•IsoT–ZnF complex; at 0 μM peptide concentration the relative amount of complex is 1.0

All the four peptides used here (Table 7.2.3) have demonstrated inhibitory activity against the Ub•IsoT-ZnF complex, albeit not very effectively (EC_{50} > 10 μM in all cases). Substitution of Leu residue with Phe had a somewhat improved effect on the inhibitory activity of the peptides, FRLRGG and LRFRGG (especially the latter's) compared to that achieved by the wt-peptide, LRLRGG.

7.3 Conclusions

This chapter has described the chemical synthesis of hexapeptides by Fmoc SPPS approach. The peptides have been designed as alternatives to Ub's C-terminal hexapeptide, LRLRGG. The employment of ESI-MS to study the inhibitory activity of each peptide against the Ub•IsoT-ZnF complex, has been also demonstrated. The obtained data have confirmed again the crucial role of the C-terminal Gly residue, as the LRLRGV peptide was the only peptide of the total ten synthesised here that did not bind IsoT-ZnF. It has also been demonstrated that substitution of Arg by either Ala or Phe residues significantly decreased the binding affinity of the relevant peptide to the IsoT-ZnF domain. Although the peptides reported in this chapter, did not inhibit Ub•IsoT-ZnF complex very effectively (EC_{50} > 10 μM), the data obtained here, is a proof of principle that ESI-MS can be used to screen, very efficiently, potential inhibitors of protein-protein interactions.

REFERENCES

1. Thomson, J.J., *Rays of Positive Electricity and Their Application to Chemical Analysis.* Longmans Green, London, 1913.

2. Squires, G., *Francis Aston and the mass spectrograph.* J. Chem. Soc., Dalton Trans., 1998(23): p. 3893-3900.

3. Edmond, d.H. and S. Vincent, in *Mass Spectrometry: Principles and Applications*2007, John Wiley & Sons, Ltd: England.

4. Beckey, H.D., *Principles of Field Ionization and Field Desorption in Mass Spectrometry*1977, Oxford: Pargamon Press.

5. Barber, M., R.S. Bordoli, R.D. Sedgwick, and A.N. Tyler, *Fast atom bombardment of solids (FAB) - A new ion source for mass spectrometry.* J. Chem. Soc., Chem. Commun., 1981(7): p. 325-327.

6. Aberth, W., K.M. Straub, and A.L. Burlingame, *Secondary ion mass spectrometry with cesium ion primary beam and liquid target matrix for analysis of biorganic compounds.* Anal. Chem., 1982. **54**(12): p. 2029-2034.

7. Tanaka, K., H. Waki, Y. Ido, S. Akita, Y. Yoshida, T. Yoshida, and T. Matsuo, *Protein and polymer analyses up to m/z 100 000 by laser ionization time-of-flight mass spectrometry.* Rapid Commun. Mass Spectrom., 1988. **2**(8): p. 151-153.

8. Karas, M. and F. Hillenkamp, *Laser desorption ionization of proteins with molecular masses exceeding 10000 Daltons.* Anal. Chem., 1988. **60**(20): p. 2299-2301.

9. Posthumus, M.A., P.G. Kistemaker, H.L.C. Meuzelaar, and M.C. Tennoeverdebrauw, *Laser desorption mass spectrometry of polar non-volatile bio-organic molecules.* Anal. Chem., 1978. **50**(7): p. 985-991.

10. Knochenmuss, R., *A quantitative model of ultraviolet matrix-assisted laser desorption/ionization.* J. Mass Spectrom., 2002. **37**(8): p. 867-877.

11. Karas, M. and R. Kruger, *Ion formation in MALDI: The cluster ionization mechanism.* Chem. Rev., 2003. **103**(2): p. 427-439.

12. Zenobi, R. and R. Knochenmuss, *Ion formation in MALDI mass spectrometry.* Mass Spectrom. Rev., 1998. **17**(5): p. 337-366.

13. Knochenmuss, R. and R. Zenobi, *MALDI ionization: The role of in-plume processes.* Chem. Rev., 2003. **103**(2): p. 441-452.

14. Dreisewerd, K., *The desorption process in MALDI.* Chem. Rev., 2003. **103**(2): p. 395-425.

15. McKay, A.R., B.T. Ruotolo, L.L. Ilag, and C.V. Robinson, *Mass measurements of increased accuracy resolve heterogeneous populations of intact ribosomes.* J. Am. Chem. Soc., 2006. **128**(35): p. 11433-11442.

16. Robinson, V.C. and F. Sobott, *Understanding protein interactions and their representation in the gas phase of the mass spectrometer,* in *Principles of Mass Spectrometry Applied to Biomolecules,* J. Laskin and C. Lifshitz, Editors. 2006, Wiley: New Jersey. p. 147-237.

17. Loo, J.A., B. Berhane, C.S. Kaddis, K.M. Wooding, Y.M. Xie, S.L. Kaufman, and I.V. Chernushevich, *Electrospray ionization mass spectrometry and ion mobility analysis of the 20S proteasome complex.* J. Am. Soc. Mass Spectrom., 2005. **16**(7): p. 998-1008.

18. Rayleigh, *On the equilibrium of liquid conducting masses charged with electricity.* Philos. Mag., 1882. **14**(87): p. 184-186.

19. Zeleny, J., *On the conditions of instability of electrified drops, with applications to the electrical discharge from liquid points.* Proc. Cambridge Philos. Soc., 1916. **18**: p. 71-83.

20. Zeleny, J., *Instability of Electrified Liquid Surfaces.* Phys. Rev., 1917. **10**(1): p. 1-6.

21. Dole, M., L.L. Mack, R.L. Hines, R.C. Mobley, L.D. Ferguson, and M.B. Alice, *Molecular Beams of Macroions.* J. Chem. Phys., 1968. **49**(5): p. 2240-2249.

22. Fenn, J.B., M. Mann, C.K. Meng, S.F. Wong, and C.M. Whitehouse, *Electrospray Ionization for Mass-Spectrometry of Large Biomolecules.* Science, 1989. **246**(4926): p. 64-71.

23. Fenn, J.B., *Electrospray wings for molecular elephants (Nobel lecture).* Angew. Chem., Int. Ed., 2003. **42**(33): p. 3871-3894.

24. Taylor, G., *Disintegration of Water Drops in an Electric Field.* Proc. R. Soc. London, A, 1964. **280**(1382): p. 383-397.

25. Kebarle, P., *A brief overview of the present status of the mechanisms involved in electrospray mass spectrometry.* J. Mass Spectrom., 2000. **35**(7): p. 804-817.

26. Gomez, A. and K.Q. Tang, *Charge and Fission of Droplets in Electrostatic Sprays.* Phys. Fluids, 1994. **6**(1): p. 404-414.

27. Kebarle, P. and M. Peschke, *On the mechanisms by which the charged droplets produced by electrospray lead to gas phase ions.* Anal. Chim. Acta, 2000. **406**(1): p. 11-35.

28. Iribarne, J.V. and B.A. Thomson, *Evaporation of small ions from charged droplets.* J. Chem. Phys., 1976. **64**(6): p. 2287-2294.

29. Thomson, B.A. and J.V. Iribarne, *Field induced ion evaporation from liquid surfaces at atmospheric pressure.* J. Chem. Phys., 1979. **71**(11): p. 4451-4463.

30. Nguyen, S. and J.B. Fenn, *Gas-phase ions of solute species from charged droplets of solutions.* Proc. Natl. Acad. Sci. USA., 2007. **104**(4): p. 1111-1117.

31. Gamero-Castano, M. and J.F. de la Mora, *Direct measurement of ion evaporation kinetics from electrified liquid surfaces.* J. Chem. Phys., 2000. **113**(2): p. 815-832.

32. Winger, B.E., K.J. Lightwahl, R.R.O. Loo, H.R. Udseth, and R.D. Smith, *Observation and implications of high mass-to-charge ratio ions from electrospray-ionization mass spectrometry.* J. Am. Soc. Mass Spectrom., 1993. 4(7): p. 536-545.

33. de la Mora, J.F., *Electrospray ionization of large multiply charged species proceeds via Dole's charged residue mechanism.* Anal. Chim. Acta, 2000. **406**(1): p. 93-104.

34. Konermann, L., E. Ahadi, A.D. Rodriguez, and S. Vahidi, *Unraveling the Mechanism of Electrospray Ionization.* Anal. Chem., 2013. **85**(1): p. 2-9.

35. Paul, W. and H. Steinwedel, *Ein neues Massenspektrometer ohne Magnetfeld.* Zeitschrift für Naturforschung A, 1953. **8**(7): p. 448-450.

36. Douglas, D.J., A.J. Frank, and D.M. Mao, *Linear ion traps in mass spectrometry.* Mass Spectrom. Rev., 2005. **24**(1): p. 1-29.

37. Wolff, M.M. and W.E. Stephens, *A Pulsed Mass Spectrometer with Time Dispersion.* Rev. Sci. Instrum., 1953. **24**(8): p. 616-617.

38. Cameron, A.E. and D.F. Eggers, *An ion velocitron.* Rev. Sci. Instrum., 1948. **19**(9): p. 605-607.

39. Wiley, W.C. and I.H. McLaren, *Time-of-flight mass spectrometer with improved resolution.* Rev. Sci. Instrum., 1955. **26**(12): p. 1150-1157.

40. Wiley, W.C., *Bendix Time-of-Flight Mass Spectrometer.* Science, 1956. **124**(3226): p. 817-820.

41. Önnerfjord, P., J. Nilsson, L. Wallman, T. Laurell, and G. Marko-Varga, *Picoliter Sample Preparation in MALDI-TOF MS Using a Micromachined Silicon Flow-Through Dispenser.* Anal. Chem., 1998. **70**(22): p. 4755-4760.

42. Alikhanov, S.G., *A new impulse technique for ion mass measurements.* Soviet Physics Jetp-Ussr, 1957. **4**(3): p. 452-453.

43. Mamyrin, B.A., V.I. Karataev, D.V. Shmikk, and V.A. Zagulin, *The mass-reflectron, a new nonmagnetic time-of-flight mass spectrometer with high resolution.* TrAC, Trends in Anal. Chem., 1973. **37**: p. 45-48.

44. Marshall, A.G. *Fourier transform ion cyclotron resonance mass spectrometry.* in *11th International Conference on Fourier Transform Spectroscopy (ICOFTS 11).* 1997. Athens, Ga.

45. Schmid, D.G., F. von der Mulbe, B. Fleckenstein, T. Weinschenk, and G. Jung, *Broadband detection electrospray ionization fourier transform ion cyclotron resonance mass spectrometry to reveal enzymatically and chemically induced deamidation reactions within peptides.* Anal. Chem., 2001. **73**(24): p. 6008-6013.

46. Bruins, A.P., *Mass spectrometry with ion sources operating at atmospheric pressure.* Mass Spectrom. Rev., 1991. **10**(1): p. 53-77.

47. McLuckey, S.A., *Principles of collisional activation in analytical mass spectrometry.* J. Am. Soc. Mass Spectrom., 1992. **3**(6): p. 599-614.

48. Kanu, A.B., P. Dwivedi, M. Tam, L. Matz, and H.H. Hill, *Ion mobility-mass spectrometry.* J. Mass Spectrom., 2008. **43**(1): p. 1-22.

49. Dwivedi, P., C. Wu, L.M. Matz, B.H. Clowers, W.F. Siems, and H.H. Hill, *Gas-phase chiral separations by ion mobility spectrometry.* Anal. Chem., 2006. **78**(24): p. 8200-8206.

50. Tao, L., J.R. McLean, J.A. McLean, and D.H. Russell, *A collision cross-section database of singly-charged peptide ions.* J. Am. Soc. Mass Spectrom., 2007. **18**(7): p. 1232-1238.

51. Clemmer, D.E., R.R. Hudgins, and M.F. Jarrold, *Naked protein conformations - Cytochrome-c in the gas-phase.* J. Am. Chem. Soc., 1995. **117**(40): p. 10141-10142.

52. Wyttenbach, T., G. vonHelden, and M.T. Bowers, *Gas-phase conformation of biological molecules: Bradykinin.* J. Am. Chem. Soc., 1996. **118**(35): p. 8355-8364.

53. Clemmer, D.E. and M.F. Jarrold, *Ion mobility measurements and their applications to clusters and biomolecules.* J. Mass Spectrom., 1997. **32**(6): p. 577-592.

54. Wyttenbach, T. and M. Bowers, *Gas-Phase Conformations: The Ion Mobility/Ion Chromatography Method,* in *Modern Mass Spectrometry,* C. Schalley, Editor 2003, Springer Berlin Heidelberg. p. 207-232.

55. McLean, J.A., B.T. Ruotolo, K.J. Gillig, and D.H. Russell, *Ion mobility-mass spectrometry: a new paradigm for proteomics.* Int. J. Mass Spectrom., 2005. **240**(3): p. 301-315.

56. Barran, P.E., N.C. Polfer, D.J. Campopiano, D.J. Clarke, P.R.R. Langridge-Smith, R.J. Langley, J.R.W. Govan, A. Maxwell, J.R. Dorin, R.P. Millar, and M.T. Bowers, *Is it biologically relevant to measure the structures of small peptides in the gas-phase?* Int. J. Mass Spectrom., 2005. **240**(3): p. 273-284.

57. Ruotolo, B.T., J.L.P. Benesch, A.M. Sandercock, S.J. Hyung, and C.V. Robinson, *Ion mobility-mass spectrometry analysis of large protein complexes.* Nat. Protoc., 2008. **3**(7): p. 1139-1152.

58. Benesch, J.L.P., J.A. Aquilina, B.T. Ruotolo, F. Sobott, and C.V. Robinson, *Tandem mass spectrometry reveals the quaternary organization of macromolecular assemblies.* Chem. Biol., 2006. **13**(6): p. 597-605.

59. Breuker, K. and F.W. McLafferty, *Stepwise evolution of protein native structure with electrospray into the gas phase, 10(-12) to 10(2) S.* Proc. Natl. Acad. Sci. USA., 2008. **105**(47): p. 18145-18152.

60. Mason, E.A. and E.W. McDaniel, *Transport properties of ions in gases*1988, New York: Wiley.

61. Hoaglund, C.S., S.J. Valentine, and D.E. Clemmer, *An ion trap interface for ESI-ion mobility experiments.* Anal. Chem., 1997. **69**(20): p. 4156-4161.

62. Giles, K., S.D. Pringle, K.R. Worthington, D. Little, J.L. Wildgoose, and R.H. Bateman, *Applications of a travelling wave-based radio-frequencyonly stacked ring ion guide.* Rapid Commun. Mass Spectrom., 2004. **18**(20): p. 2401-2414.

63. Pringle, S.D., K. Giles, J.L. Wildgoose, J.P. Williams, S.E. Slade, K. Thalassinos, R.H. Bateman, M.T. Bowers, and J.H. Scrivens, *An investigation of the mobility separation of some peptide and protein ions using a new hybrid quadrupole/travelling wave IMS/oa-ToF instrument.* Int. J. Mass Spectrom., 2007. **261**(1): p. 1-12.

64. Duijn, E.V., A. Barendregt, S. Synowsky, C. Versluis, and A.J.R. Heck, *Chaperonin Complexes Monitored by Ion Mobility Mass Spectrometry.* J. Am. Chem. Soc., 2009. **131**(4): p. 1452-1459.

65. Smith, D.P., T.W. Knapman, I. Campuzano, R.W. Malham, J.T. Berryman, S.E. Radford, and A.E. Ashcroft, *Deciphering drift time measurements from travelling wave ion mobility spectrometry-mass spectrometry studies.* Eur. J. Mass Spectrom., 2009. **15**(2): p. 113-130.

66. Smith, D.P., S.E. Radford, and A.E. Ashcroft, *Elongated oligomers in beta(2)-microglobulin amyloid assembly revealed by ion mobility spectrometry-mass spectrometry.* Proc. Natl. Acad. Sci. USA., 2010. **107**(15): p. 6794-6798.

67. Hilton, G.R., K. Thalassinos, M. Grabenauer, N. Sanghera, S.E. Slade, T. Wyttenbach, P.J. Robinson, T.J.T. Pinheiro, M.T. Bowers, and J.H. Scrivens, *Structural Analysis of Prion Proteins by Means of Drift Cell and Traveling Wave Ion Mobility Mass Spectrometry.* J. Am. Soc. Mass Spectrom., 2010. **21**(5): p. 845-854.

68. Wyttenbach, T., M. Grabenauer, K. Thalassinos, J.H. Scrivens, and M.T. Bowers, *The Effect of Calcium Ions and Peptide Ligands on the Relative Stabilities of the Calmodulin Dumbbell and Compact Structures.* J. Phys. Chem. B, 2010. **114**(1): p. 437-447.

69. Ruotolo, B.T., K. Giles, I. Campuzano, A.M. Sandercock, R.H. Bateman, and C.V. Robinson, *Evidence for macromolecular protein rings in the absence of bulk water.* Science, 2005. **310**(5754): p. 1658-1661.

70. Jenner, M., J. Ellis, W.C. Huang, E.L. Raven, G.C.K. Roberts, and N.J. Oldham, *Detection of a Protein Conformational Equilibrium by Electrospray Ionisation-Ion Mobility-Mass Spectrometry.* Angew. Chem., Int. Ed., 2011. **50**(36): p. 8291-8294.

71. Bleiholder, C., N.F. Dupuis, T. Wyttenbach, and M.T. Bowers, *Ion mobility-mass spectrometry reveals a conformational conversion from random assembly to beta-sheet in amyloid fibril formation.* Nat. Chem., 2011. **3**(2): p. 172-177.

72. De Cecco, M., E.S. Seo, D.J. Clarke, B.J. McCullough, K. Taylor, D. Macmillan, J.R. Dorin, D.J. Campopiano, and P.E. Barran, *Conformational Preferences of Linear beta-Defensins Are Revealed by Ion Mobility-Mass Spectrometry.* J. Phys. Chem. B, 2010. **114**(6): p. 2312-2318.

73. Scarff, C.A., K. Thalassinos, G.R. Hilton, and J.H. Scrivens, *Travelling wave ion mobility mass spectrometry studies of protein structure: biological significance and comparison with X-ray crystallography and nuclear magnetic resonance spectroscopy measurements.* Rapid Commun. Mass Spectrom., 2008. **22**(20): p. 3297-3304.

74. Mesleh, M.F., J.M. Hunter, A.A. Shvartsburg, G.C. Schatz, and M.F. Jarrold, *Structural information from ion mobility measurements: Effects of the long-range potential.* J. Phys. Chem., 1996. **100**(40): p. 16082-16086.

75. Shvartsburg, A.A. and M.F. Jarrold, *An exact hard-spheres scattering model for the mobilities of polyatomic ions.* Chem. Phys. Lett., 1996. **261**(1-2): p. 86-91.

76. Hershko, A. and A. Ciechanover, *The ubiquitin system.* Annu. Rev. Biochem., 1998. **67**: p. 425-479.

77. Ikeda, F. and I. Dikic, *Atypical ubiquitin chains: new molecular signals - 'Protein modifications: Beyond the usual suspects' review series.* EMBO Rep., 2008. **9**(6): p. 536-542.

78. Elsasser, S. and D. Finley, *Delivery of ubiquitinated substrates to protein-unfolding machines.* Nat. Cell Biol., 2005. **7**(8): p. 742-749.

79. Staub, O. and D. Rotin, *Role of ubiquitylation in cellular membrane transport.* Physiol. Rev., 2006. **86**(2): p. 669-707.

80. Huang, T.T. and A.D. D'Andrea, *Regulation of DNA repair by ubiquitylation.* Nat. Rev. Mol. Cell Biol., 2006. **7**(5): p. 323-334.

81. Raiborg, C., K.G. Bache, D.J. Gillooly, I.H. Madshush, E. Stang, and H. Stenmark, *Hrs sorts ubiquitinated proteins into clathrin-coated microdomains of early endosomes.* Nat. Cell Biol., 2002. **4**(5): p. 394-398.

82. Hurley, J.H., S. Lee, and G. Prag, *Ubiquitin-binding domains.* Biochem. J., 2006. **399**: p. 361-372.

83. Ciechanover, A. and R. Ben-Saadon, *N-terminal ubiquitination: more protein substrates join in.* Trends Cell Biol., 2004. **14**(3): p. 103-106.

84. Ravid, T. and M. Hochstrasser, *Autoregulation of an E2 enzyme by ubiquitin-chain assembly on its catalytic residue.* Nat. Cell Biol., 2007. **9**(4): p. 422-427.

85. Wang, X.L., R.A. Herr, W.J. Chua, L. Lybarger, E. Wiertz, and T.H. Hansen, *Ubiquitination of serine, threonine, or lysine residues on the cytoplasmic tail can induce ERAD of MHC-I by viral E3 ligase mK3.* J. Cell Biol., 2007. **177**(4): p. 613-624.

86. Chau, V., J.W. Tobias, A. Bachmair, D. Marriott, D.J. Ecker, D.K. Gonda, and A. Varshavsky, *A multiubiquitin chain is confined to specific lysise in a targeted short-lived protein.* Science, 1989. **243**(4898): p. 1576-1583.

87. Cook, W.J., L.C. Jeffrey, M. Carson, Z.J. Chen, and C.M. Pickart, *Structure of a diubiquitin conjugate and a model for interaction with ubiquitin conjugating enzyme (E2).* J. Biol. Chem., 1992. **267**(23): p. 16467-16471.

88. Sun, L.J. and Z.J. Chen, *The novel functions of ubiquitination in signaling.* Curr. Opin. Cell Biol., 2004. **16**(2): p. 119-126.

89. Hicke, L. and R. Dunn, *Regulation of membrane protein transport by ubiquitin and ubiquitin-binding proteins.* Annu. Rev. Cell Dev. Biol., 2003. **19**: p. 141-172.

90. Spence, J., R.R. Gali, G. Dittmar, F. Sherman, M. Karin, and D. Finley, *Cell cycle-regulated modification of the ribosome by a variant multiubiquitin chain.* Cell, 2000. **102**(1): p. 67-76.

91. Komander, D., *The emerging complexity of protein ubiquitination.* Biochem. Soc. Trans., 2009. **37**: p. 937-953.

92. Wu-Baer, F., K. Lagrazon, W. Yuan, and R. Baer, *The BRCA1/BARD1 heterodimer assembles polyubiquitin chains through an unconventional*

linkage involving lysine residue K6 of ubiquitin. J. Biol. Chem., 2003. **278**(37): p. 34743-34746.

93. Morris, J.R. and E. Solomon, *BRCA1 : BARD1 induces the formation of conjugated ubiquitin structures, dependent on K6 of ubiquitin, in cells during DNA replication and repair.* Hum. Mol. Genet., 2004. **13**(8): p. 807-817.

94. Pickart, C.M., *Mechanisms underlying ubiquitination.* Annu. Rev. Biochem., 2001. **70**: p. 503-533.

95. Bhoj, V.G. and Z.J. Chen, *Ubiquitylation in innate and adaptive immunity.* Nature, 2009. **458**(7237): p. 430-437.

96. Hicke, L., H.L. Schubert, and C.P. Hill, *Ubiquitin-binding domains.* Nat. Rev. Mol. Cell Biol., 2005. **6**(8): p. 610-621.

97. Lee, S., Y.C. Tsai, R. Mattera, W.J. Smith, M.S. Kostelansky, A.M. Weissman, J.S. Bonifacino, and J.H. Hurley, *Structural basis for ubiquitin recognition and autoubiquitination by Rabex-5.* Nat. Struct. Mol. Biol., 2006. **13**(3): p. 264-271.

98. Penengo, L., M. Mapelli, A.G. Murachelli, S. Confalonieri, L. Magri, A. Musacchio, P.P. Di Fiore, S. Polo, and T.R. Schneider, *Crystal structure of the ubiquitin binding domains of rabex-5 reveals two modes of interaction with ubiquitin.* Cell, 2006. **124**(6): p. 1183-1195.

99. Hirano, S., M. Kawasaki, H. Ura, R. Kato, C. Raiborg, H. Stenmark, and S. Wakatsuki, *Double-sided ubiquitin binding of Hrs-UIM in endosomal protein sorting.* Nat. Struct. Mol. Biol., 2006. **13**(3): p. 272-277.

100. Varadan, R., M. Assfalg, S. Raasi, C. Pickart, and D. Fushman, *Structural determinants for selective recognition of a lys48-linked polyubiquitin chain by a UBA domain.* Mol. Cell, 2005. **18**(6): p. 687-698.

101. Raasi, S., R. Varadan, D. Fushman, and C.M. Pickart, *Diverse polyubiquitin interaction properties of ubiquitin-associated domains.* Nat. Struct. Mol. Biol., 2005. **12**(8): p. 708-714.

102. Zhang, D., S. Raasi, and D. Fushman, *Affinity makes the difference: Nonselective interaction of the UBA domain of ubiquilin-1 with monomeric ubiquitin and polyubiquitin chains.* J. Mol. Biol., 2008. **377**(1): p. 162-180.

103. Sundquist, W.I., H.L. Schubert, B.N. Kelly, G.C. Hill, J.M. Holton, and C.P. Hill, *Ubiquitin recognition by the human TSG101 protein.* Mol. Cell, 2004. **13**(6): p. 783-789.

104. Brzovic, P.S., A. Lissounov, D.E. Christensen, D.W. Hoyt, and R.E. Klevit, *A UbcH5/ubiquitin noncovalent complex is required for processive BRCA1-directed ubiquitination.* Mol. Cell, 2006. **21**(6): p. 873-880.

105. Alam, S.L., J. Sun, M. Payne, B.D. Welch, B.K. Blake, D.R. Davis, H.H. Meyer, S.D. Emr, and W.I. Sundquist, *Ubiquitin interactions of NZF zinc fingers.* EMBO J., 2004. **23**(7): p. 1411-1421.

106. Reyes-Turcu, F.E., J.R. Horton, J.E. Mullally, A. Heroux, X.D. Cheng, and K.D. Wilkinson, *The ubiquitin binding domain ZnFUBP recognizes the C-terminal diglycine motif of unanchored ubiquitin.* Cell, 2006. **124**(6): p. 1197-1208.

107. Wang, Q., A.M. Goh, P.M. Howley, and K.J. Walters, *Ubiquitin Recognition by the DNA Repair Protein hHR23a.* Biochemistry, 2003. **42**(46): p. 13529-13535.

108. Deveraux, Q., V. Ustrell, C. Pickart, and M. Rechsteiner, *A 26-S protease subunit that binds ubiquitin conjugates.* J. Biol. Chem., 1994. **269**(10): p. 7059-7061.

109. Fisher, R.D., B. Wang, S.L. Alam, D.S. Higginson, H. Robinson, W.I. Sundquist, and C.P. Hill, *Structure and ubiquitin binding of the ubiquitin-interacting motif.* J. Biol. Chem., 2003. **278**(31): p. 28976-28984.

110. Hofmann, K. and P. Bucher, *The UBA domain: A sequence motif present in multiple enzyme classes of the ubiquitination pathway.* Trends Biochem. Sci., 1996. **21**(5): p. 172-173.

111. Wilkinson, C.R.M., M. Seeger, R. Hartmann-Petersen, M. Stone, M. Wallace, C. Semple, and C. Gordon, *Proteins containing the UBA domain are able to bind to multi-ubiquitin chains.* Nat. Cell Biol., 2001. **3**(10): p. 939-943.

112. Raasi, S. and C.M. Pickart, *Rad23 ubiquitin-associated domains (UBA) inhibit 26 S proteasome-catalyzed proteolysis by sequestering lysine 48-linked polyubiquitin chains.* J. Biol. Chem., 2003. **278**(11): p. 8951-8959.

113. Mueller, T.D. and J. Feigon, *Solution structures of UBA domains reveal a conserved hydrophobic surface for protein-protein interactions.* J. Mol. Biol., 2002. **319**(5): p. 1243-1255.

114. Mah, A.L., G. Perry, M.A. Smith, and M.J. Monteiro, *Identification of ubiquilin, a novel presenilin interactor that increases presenilin protein accumulation.* J. Cell Biol., 2000. **151**(4): p. 847-862.

115. Massey, L.K., A.L. Mah, D.L. Ford, J. Miller, J. Liang, H. Doong, and M.J. Monteiro, *Overexpression of ubiquilin decreases ubiquitination and degradation of presenilin proteins.* J. Alzheimers Dis., 2004. **6**(1): p. 79-92.

116. Dikic, I., S. Wakatsuki, and K.J. Walters, *Ubiquitin-binding domains - from structures to functions.* Nat. Rev. Mol. Cell Biol., 2009. **10**(10): p. 659-671.

117. VanDemark, A.P., R.M. Hofmann, C. Tsui, C.M. Pickart, and C. Wolberger, *Molecular insights into polyubiquitin chain assembly: Crystal structure of the Mms2/Ubc13 heterodimer.* Cell, 2001. **105**(6): p. 711-720.

118. Strachan, J., L. Roach, K. Sokratous, D. Tooth, J. Long, T.P. Garner, M.S. Searle, N.J. Oldham, and R. Layfield, *Insights into the Molecular Composition of Endogenous Unanchored Polyubiquitin Chains.* J. Proteome Res., 2012. **11**(3): p. 1969-1980.

119. Counterman, A.E., S.J. Valentine, C.A. Srebalus, S.C. Henderson, C.S. Hoaglund, and D.E. Clemmer, *High-order structure and dissociation of gaseous peptide aggregates that are hidden in mass spectra.* J. Am. Soc. Mass Spectrom., 1998. **9**(8): p. 743-759.

120. Salbo, R., M.F. Bush, H. Naver, I. Campuzano, C.V. Robinson, I. Pettersson, T.J.D. Jorgensen, and K.F. Haselmann, *Traveling-wave ion mobility mass spectrometry of protein complexes: accurate calibrated collision cross-sections of human insulin oligomers.* Rapid Commun. Mass Spectrom., 2012. **26**(10): p. 1181-1193.

121. Williams, J.P., J.A. Lough, I. Campuzano, K. Richardson, and P.J. Sadler, *Use of ion mobility mass spectrometry and a collision cross-section algorithm to study an organometallic ruthenium anticancer complex and its adducts with a DNA oligonucleotide.* Rapid Commun. Mass Spectrom., 2009. **23**(22): p. 3563-3569.

122. Davis, I.W., A. Leaver-Fay, V.B. Chen, J.N. Block, G.J. Kapral, X. Wang, L.W. Murray, W.B. Arendall, J. Snoeyink, J.S. Richardson, and D.C. Richardson, *MolProbity: all-atom contacts and structure validation for proteins and nucleic acids.* Nucleic Acids Res., 2007. **35**: p. W375-W383.

123. Chen, V.B., W.B. Arendall, J.J. Headd, D.A. Keedy, R.M. Immormino, G.J. Kapral, L.W. Murray, J.S. Richardson, and D.C. Richardson, *MolProbity: all-atom structure validation for macromolecular crystallography.* Acta Crystallogr. D Biol. Crystallogr., 2010. **66**: p. 12-21.

124. Bertini, I., D.A. Case, L. Ferella, A. Giachetti, and A. Rosato, *A Grid-enabled web portal for NMR structure refinement with AMBER.* Bioinformatics, 2011. **27**(17): p. 2384-2390.

125. Case, D.A., T.E. Cheatham, T. Darden, H. Gohlke, R. Luo, K.M. Merz, A. Onufriev, C. Simmerling, B. Wang, and R.J. Woods, *The Amber biomolecular simulation programs.* J. Comput. Chem., 2005. **26**(16): p. 1668-1688.

126. Benesch, J.L.P. and B.T. Ruotolo, *Mass spectrometry: come of age for structural and dynamical biology.* Curr. Opin. Struct. Biol., 2011. **21**(5): p. 641-649.

127. Merrifield, R.B., *Solid phase peptide synthesis. I. The synthesis of a tetrapeptide.* J. Am. Chem. Soc., 1963. **85**(14): p. 2149-2154.

128. Iavarone, A.T. and E.R. Williams, *Mechanism of Charging and Supercharging Molecules in Electrospray Ionization.* J. Am. Chem. Soc., 2003. **125**(8): p. 2319-2327.

129. Iavarone, A.T., J.C. Jurchen, and E.R. Williams, *Supercharged Protein and Peptide Ions Formed by Electrospray Ionization.* Anal. Chem., 2001. **73**(7): p. 1455-1460.

130. Lomeli, S.H., S. Yin, R.R.O. Loo, and J.A. Loo, *Increasing: Charge While Preserving Noncovalent Protein Complexes for ESI-MS.* J. Am. Soc. Mass Spectrom., 2009. **20**(4): p. 593-596.

131. Lomeli, S.H., I.X. Peng, S. Yin, R.R.O. Loo, and J.A. Loo, *New Reagents for Increasing ESI Multiple Charging of Proteins and Protein Complexes.* J. Am. Soc. Mass Spectrom., 2010. **21**(1): p. 127-131.

132. Scalf, M., M.S. Westphall, J. Krause, S.L. Kaufman, and L.M. Smith, *Controlling charge states of large ions.* Science, 1999. **283**(5399): p. 194-197.

133. Bagal, D., E.N. Kitova, L. Liu, A. El-Hawiet, P.D. Schnier, and J.S. Klassen, *Gas Phase Stabilization of Noncovalent Protein Complexes Formed by Electrospray Ionization.* Anal. Chem., 2009. **81**(18): p. 7801-7806.

134. Zubarev, R.A., N.L. Kelleher, and F.W. McLafferty, *Electron Capture Dissociation of Multiply Charged Protein Cations. A Nonergodic Process.* J. Am. Chem. Soc., 1998. **120**(13): p. 3265-3266.

135. Xie, Y., J. Zhang, S. Yin, and J.A. Loo, *Top-Down ESI-ECD-FT-ICR Mass Spectrometry Localizes Noncovalent Protein-Ligand Binding Sites.* J. Am. Chem. Soc., 2006. **128**(45): p. 14432-14433.

136. Sterling, H., M. Daly, G. Feld, K. Thoren, A. Kintzer, B. Krantz, and E. Williams, *Effects of supercharging reagents on noncovalent complex structure in electrospray ionization from aqueous solutions.* J. Am. Soc. Mass Spectrom., 2010. **21**(10): p. 1762-1774.

137. Kharlamova, A., B.M. Prentice, T.Y. Huang, and S.A. McLuckey, *Electrospray Droplet Exposure to Gaseous Acids for the Manipulation of Protein Charge State Distributions.* Anal. Chem., 2010. **82**(17): p. 7422-7429.

138. Shelimov, K.B., D.E. Clemmer, R.R. Hudgins, and M.F. Jarrold, *Protein structure in vacuo: Gas-phase confirmations of BPTI and cytochrome c.* J. Am. Chem. Soc., 1997. **119**(9): p. 2240-2248.

139. Baumketner, A., S.L. Bernstein, T. Wyttenbach, G. Bitan, D.B. Teplow, M.T. Bowers, and J.-E. Shea, *Amyloid β-protein monomer structure: A computational and experimental study.* Protein Sci., 2006. **15**(3): p. 420-428.

140. Lemaire, D., G. Marie, L. Serani, and O. Laprevote, *Stabilization of gas-phase noncovalent macromolecular complexes in electrospray mass spectrometry using aqueous triethylammonium bicarbonate buffer.* Anal. Chem., 2001. **73**(8): p. 1699-1706.

141. Halgand, F. and O. Laprevote, *Mean charge state and charge state distribution of proteins as structural probes. An electrospray ionisation mass spectrometry study of lysozyme and ribonuclease A.* Eur. J. Mass Spectrom., 2001. **7**(6): p. 433-439.

142. Pagel, K., S.J. Hyung, B.T. Ruotolo, and C.V. Robinson, *Alternate Dissociation Pathways Identified in Charge-Reduced Protein Complex Ions.* Anal. Chem., 2010. **82**(12): p. 5363-5372.

143. Catalina, M.I., R.H.H. van den Heuvel, E. van Duijn, and A.J.R. Heck, *Decharging of Globular Proteins and Protein Complexes in Electrospray.* Chem. Eur. J., 2005. **11**(3): p. 960-968.

144. Sun, J.X., E.N. Kitova, and J.S. Klassen, *Method for stabilizing protein-ligand complexes in nanoelectrospray ionization mass spectrometry.* Anal. Chem., 2007. **79**(2): p. 416-425.

145. Sun, N., N. Soya, E.N. Kitova, and J.S. Klassen, *Nonspecific Interactions Between Proteins and Charged Biomolecules in Electrospray Ionization Mass Spectrometry.* J. Am. Soc. Mass Spectrom., 2010. **21**(3): p. 472-481.

146. Winger, B.E., K.J. Lightwahl, and R.D. Smith, *Gas-phase proton-transfer reactions involving multiply charged cytochrome-C ions and water under thermal conditions.* J. Am. Soc. Mass Spectrom., 1992. **3**(6): p. 624-630.

147. Takats, Z., J.M. Wiseman, B. Gologan, and R.G. Cooks, *Electrosonic spray ionization. A gentle technique for generating folded proteins and protein complexes in the gas phase and for studying ion - Molecule reactions at atmospheric pressure.* Anal. Chem., 2004. **76**(14): p. 4050-4058.

148. Touboul, D., M.C. Jecklin, and R. Zenobi, *Rapid and Precise Measurements of Gas-Phase Basicity of Peptides and Proteins at Atmospheric Pressure by*

Electrosonic Spray Ionization-Mass Spectrometry. J. Phys. Chem. B, 2007. **111**(40): p. 11629-11631.

149. Touboul, D., M.C. Jecklin, and R. Zenobi, *Investigation of deprotonation reactions on globular and denatured proteins at atmospheric pressure by ESSI-MS.* J. Am. Soc. Mass Spectrom., 2008. **19**(4): p. 455-466.

150. Loo, R.R.O., H.R. Udseth, and R.D. Smith, *Evidence of charge inversion in the reaction of singly charged anions with multiply charged macroions.* J. Phys. Chem., 1991. **95**(17): p. 6412-6415.

151. Ogorzalek Loo, R.R., H.R. Udseth, and R.D. Smith, *A new approach for the study of gas-phase ion-ion reactions using electrospray ionization.* J. Am. Soc. Mass Spectrom., 1992. **3**(7): p. 695-705.

152. Zhao, Q., M.W. Soyk, G.M. Schieffer, K. Fuhrer, M.M. Gonin, R.S. Houk, and E.R. Badman, *An Ion Trap-Ion Mobility-Time of Flight Mass Spectrometer with Three Ion Sources for Ion/Ion Reactions.* J. Am. Soc. Mass Spectrom., 2009. **20**(8): p. 1549-1561.

153. Zhao, Q., G.M. Schieffer, M.W. Soyk, T.J. Anderson, R.S. Houk, and E.R. Badman, *Effects of Ion/Ion Proton Transfer Reactions on Conformation of Gas-Phase Cytochrome c Ions.* J. Am. Soc. Mass Spectrom., 2010. **21**(7): p. 1208-1217.

154. Clark, S.M. and L. Konermann, *Determination of ligand-protein dissociation constants by electrospray mass spectrometry-based diffusion measurements.* Anal. Chem., 2004. **76**(23): p. 7077-7083.

155. Jecklin, M.C., D. Touboul, C. Bovet, A. Wortmann, and R. Zenobi, *Which electrospray-based ionization method best reflects protein-ligand interactions found in solution? A comparison of ESI, nanoESI, and ESSI for the determination of dissociation constants with mass spectrometry.* J. Am. Soc. Mass Spectrom., 2008. **19**(8): p. 1237-1237.

156. Benkestock, K., G. Sundqvist, P.-O. Edlund, and J. Roeraade, *Influence of droplet size, capillary–cone distance and selected instrumental parameters for*

the analysis of noncovalent protein–ligand complexes by nano-electrospray ionization mass spectrometry. J. Mass Spectrom., 2004. **39**(9): p. 1059-1067.

157. Hunter, E.P.L. and S.G. Lias, *Evaluated gas phase basicities and proton affinities of molecules: An update.* J. Phys. Chem. Ref. Data, 1998. **27**(3): p. 413-656.

158. Hopper, J.T.S. and N.J. Oldham, *Alkali Metal Cation-Induced Destabilization of Gas-Phase Protein-Ligand Complexes: Consequences and Prevention.* Anal. Chem., 2011. **83**(19): p. 7472-7479.

159. Daniel, J.M., S.D. Friess, S. Rajagopalan, S. Wendt, and R. Zenobi, *Quantitative determination of noncovalent binding interactions using soft ionization mass spectrometry.* Int. J. Mass Spectrom., 2002. **216**(1): p. 1-27.

160. Heck, A.J.R. and R.H.H. van den Heuvel, *Investigation of intact protein complexes by mass spectrometry.* Mass Spectrom. Rev., 2004. **23**(5): p. 368-389.

161. Liu, L., D. Bagal, E.N. Kitova, P.D. Schnier, and J.S. Klassen, *Hydrophobic Protein-Ligand Interactions Preserved in the Gas Phase.* J. Am. Chem. Soc., 2009. **131**(44): p. 15980-15981.

162. Loo, J.A., P.F. Hu, P. McConnell, W.T. Mueller, T.K. Sawyer, and V. Thanabal, *A study of Src SH2 domain protein-phosphopeptide binding interactions by electrospray ionization mass spectrometry.* J. Am. Soc. Mass Spectrom., 1997. **8**(3): p. 234-243.

163. Robinson, C.V., E.W. Chung, B.B. Kragelund, J. Knudsen, R.T. Aplin, F.M. Poulsen, and C.M. Dobson, *Probing the nature of noncovalent interactions by mass spectrometry. A study of protein-CoA ligand binding and assembly.* J. Am. Chem. Soc., 1996. **118**(36): p. 8646-8653.

164. Rauh, D., G. Klebe, J. Sturzebecher, and M.T. Stubbs, *ZZ made EZ: Influence of inhibitor configuration on enzyme selectivity.* J. Mol. Biol., 2003. **330**(4): p. 761-770.

165. Brignone, C., K.E. Bradley, A.F. Kisselev, and S.R. Grossman, *A post-ubiquitination role for MDM2 and hHR23A in the p53 degradation pathway.* Oncogene, 2004. **23**(23): p. 4121-4129.

166. Walters, K.J., P.J. Lech, A.M. Goh, Q.H. Wang, and P.M. Howley, *DNA-repair protein hHR23a alters its protein structure upon binding proteasomal subunit S5a.* Proc. Natl. Acad. Sci. USA., 2003. **100**(22): p. 12694-12699.

167. Raasi, S., I. Orlov, K.G. Fleming, and C.M. Pickart, *Binding of polyubiquitin chains to ubiquitin-associated (UBA) domains of HHR23A.* J. Mol. Biol., 2004. **341**(5): p. 1367-1379.

168. Hoeller, D. and I. Dikic, *Targeting the ubiquitin system in cancer therapy.* Nature, 2009. **458**(7237): p. 438-444.

169. Garner, T.P., J. Long, R. Layfield, and M.S. Searle, *Impact of p62/SQSTM1 UBA Domain Mutations Linked to Paget's Disease of Bone on Ubiquitin Recognition.* Biochemistry, 2011. **50**(21): p. 4665-4674.

170. Trempe, J.-F., *Reading the ubiquitin postal code.* Curr. Opin. Struct. Biol., 2011. **21**(6): p. 792-801.

171. Varadan, R., M. Assfalg, A. Haririnia, S. Raasi, C. Pickart, and D. Fushman, *Solution conformation of Lys(63)-linked di-ubiquitin chain provides clues to functional diversity of polyubiquitin signaling.* J. Biol. Chem., 2004. **279**(8): p. 7055-7063.

172. Long, J., T.P. Garner, M.J. Pandya, C.J. Craven, P. Chen, B. Shaw, M.P. Williamson, R. Layfield, and M.S. Searle, *Dimerisation of the UBA Domain of p62 Inhibits Ubiquitin Binding and Regulates NF-kappa B Signalling.* J. Mol. Biol., 2010. **396**(1): p. 178-194.

173. Kulathu, Y., M. Akutsu, A. Bremm, K. Hofmann, and D. Komander, *Two-sided ubiquitin binding explains specificity of the TAB2 NZF domain.* Nat. Struct. Mol. Biol., 2009. **16**(12): p. 1328-1330.

174. Liu, J.J. and L. Konermann, *Protein-Protein Binding Affinities in Solution Determined by Electrospray Mass Spectrometry.* J. Am. Soc. Mass Spectrom., 2011. **22**(3): p. 408-417.

175. Sims, J.J., A. Haririnia, B.C. Dickinson, D. Fushman, and R.E. Cohen, *Avid interactions underlie the Lys63-linked polyubiquitin binding specificities observed for UBA domains.* Nat. Struct. Mol. Biol., 2009. **16**(8): p. 883-889.

176. Shin, D., S.Y. Lee, S. Han, S. Ren, S. Kim, Y. Aikawa, and S. Lee, *Differential polyubiquitin recognition by tandem ubiquitin binding domains of Rabex-5.* Biochem. Biophys. Res. Commun., 2012. **423**(4): p. 757-762.

177. Garner, T.P., J. Strachan, E.C. Shedden, J.E. Long, J.R. Cavey, B. Shaw, R. Layfield, and M.S. Searle, *Independent Interactions of Ubiquitin-Binding Domains in a Ubiquitin-Mediated Ternary Complex.* Biochemistry, 2011. **50**(42): p. 9076-9087.

178. Gabelica, V., F. Rosu, and E. De Pauw, *A Simple Method to Determine Electrospray Response Factors of Noncovalent Complexes.* Anal. Chem., 2009. **81**(16): p. 6708-6715.

179. Wilcox, J.M., D.L. Rempel, and M.L. Gross, *Method of measuring oligonucleotide-metal affinities: Interactions of the thrombin binding aptamer with K+ and Sr2+.* Anal. Chem., 2008. **80**(7): p. 2365-2371.

180. Sun, J., E.N. Kitova, N. Sun, and J.S. Klassen, *Method for identifying nonspecific protein-protein interactions in nanoelectrospray ionization mass Spectrometry.* Anal. Chem., 2007. **79**(21): p. 8301-8311.

181. Kuprowski, M.C. and L. Konermann, *Signal response of coexisting protein conformers in electrospray mass spectrometry.* Anal. Chem., 2007. **79**(6): p. 2499-2506.

182. Kaltashov, I.A. and A. Mohimen, *Estimates of protein surface areas in solution by electrospray ionization mass spectrometry.* Anal. Chem., 2005. **77**(16): p. 5370-5379.

183. Kaiser, S.E., B.E. Riley, T.A. Shaler, R.S. Trevino, C.H. Becker, H. Schulman, and R.R. Kopito, *Protein standard absolute quantification (PSAQ) method for the measurement of cellular ubiquitin pools.* Nat Meth, 2011. **8**(8): p. 691-696.

184. Zhang, N.X., Q.H. Wang, A. Ehlinger, L. Randles, J.W. Lary, Y. Kang, A. Haririnia, A.J. Storaska, J.L. Cole, D. Fushman, and K.J. Walters, *Structure of*

the S5a:K48-Linked Diubiquitin Complex and Its Interactions with Rpn13. Mol. Cell, 2009. **35**(3): p. 280-290.

185. Chen, X., B.H. Lee, D. Finley, and K.J. Walters, *Structure of Proteasome Ubiquitin Receptor hRpn13 and Its Activation by the Scaffolding Protein hRpn2.* Mol. Cell, 2010. **38**(3): p. 404-415.

186. Piotrowski, J., R. Beal, L. Hoffman, K.D. Wilkinson, R.E. Cohen, and C.M. Pickart, *Inhibition of the 26 S proteasome by polyubiquitin chains synthesized to have defined lengths.* J. Biol. Chem., 1997. **272**(38): p. 23712-23721.

187. Dayal, S., A. Sparks, J. Jacob, N. Allende-Vega, D.P. Lane, and M.K. Saville, *Suppression of the Deubiquitinating Enzyme USP5 Causes the Accumulation of Unanchored Polyubiquitin and the Activation of p53.* J. Biol. Chem., 2009. **284**(8): p. 5030-5041.

188. Xia, Z.P., L.J. Sun, X. Chen, G. Pineda, X.M. Jiang, A. Adhikari, W.W. Zeng, and Z.J. Chen, *Direct activation of protein kinases by unanchored polyubiquitin chains.* Nature, 2009. **461**(7260): p. 114-119.

189. Pertel, T., S. Hausmann, D. Morger, S. Zuger, J. Guerra, J. Lascano, C. Reinhard, F.A. Santoni, P.D. Uchil, L. Chatel, A. Bisiaux, M.L. Albert, C. Strambio-De-Castillia, W. Mothes, M. Pizzato, M.G. Grutter, and J. Luban, *TRIM5 is an innate immune sensor for the retrovirus capsid lattice.* Nature, 2011. **472**(7343): p. 361-365.

190. Zeng, W., L. Sun, X. Jiang, X. Chen, F. Hou, A. Adhikari, M. Xu, and Z.J. Chen, *Reconstitution of the RIG-I pathway reveals a signaling role of unanchored polyubiquitin chains in innate immunity.* Cell. **141**(2): p. 315-30.

191. Setsuie, R., M. Sakurai, Y. Sakaguchi, and K. Wada, *Ubiquitin dimers control the hydrolase activity of UCH-L3.* Neurochem. Int., 2009. **54**(5-6): p. 314-321.

192. Hirano, T., O. Serve, M. Yagi-Utsumi, E. Takemoto, T. Hiromoto, T. Satoh, T. Mizushima, and K. Kato, *Conformational Dynamics of Wild-type Lys-48-linked Diubiquitin in Solution.* J. Biol. Chem., 2011. **286**(43): p. 37496-502.

193. Yao, T.T. and R.E. Cohen, *Cyclization of polyubiquitin by the E2-25K ubiquitin conjugating enzyme.* J. Biol. Chem., 2000. **275**(47): p. 36862-36868.

194. Satoh, T., E. Sakata, S. Yamamoto, Y. Yamaguchi, A. Sumiyoshi, S. Wakatsuki, and K. Kato, *Crystal structure of cyclic Lys48-linked tetraubiquitin.* Biochem. Biophys. Res. Commun., 2010. **400**(3): p. 329-333.

195. Peng, J., *Evaluation of proteomic strategies for analyzing ubiquitinated proteins.* Bmb Reports, 2008. **41**(3): p. 177-183.

196. Sobott, F., S.J. Watt, J. Smith, M.J. Edelmann, H.B. Kramer, and B.M. Kessler, *Comparison of CID Versus ETD Based MS/MS Fragmentation for the Analysis of Protein Ubiquitination.* J. Am. Soc. Mass Spectrom., 2009. **20**(9): p. 1652-1659.

197. Peng, J.M., D. Schwartz, J.E. Elias, C.C. Thoreen, D.M. Cheng, G. Marsischky, J. Roelofs, D. Finley, and S.P. Gygi, *A proteomics approach to understanding protein ubiquitination.* Nat. Biotechnol., 2003. **21**(8): p. 921-926.

198. Meierhofer, D., X. Wang, L. Huang, and P. Kaiser, *Quantitative analysis of global ubiquitination in HeLa cells by mass spectrometry.* J. Proteome Res., 2008. **7**(10): p. 4566-4576.

199. Xu, P. and J.M. Peng, *Characterization of polyubiquitin chain structure by middle-down mass spectrometry.* Anal. Chem., 2008. **80**(9): p. 3438-3444.

200. Kirkpatrick, D.S., N.A. Hathaway, J. Hanna, S. Elsasser, J. Rush, D. Finley, R.W. King, and S.P. Gygi, *Quantitative analysis of in vitro ubiquitinated cyclin B1 reveals complex chain topology.* Nat. Cell Biol., 2006. **8**(7): p. 700-710.

201. Ziv, I., Y. Matiuhin, D.S. Kirkpatrick, Z. Erpapazoglou, S. Leon, M. Pantazopoulou, W. Kim, S.P. Gygi, R. Haguenauer-Tsapis, N. Reis, M.H. Glickman, and O. Kleifeld, *A Perturbed Ubiquitin Landscape Distinguishes Between Ubiquitin in Trafficking and in Proteolysis.* Mol. Cell. Proteomics, 2011. **10**(5).

202. van Dijk, A.D.J., D. Fushman, and A. Bonvin, *Various strategies of using residual dipolar couplings in NMR-driven protein docking: Application to Lys48-linked Di-ubiquitin and validation against N-15-relaxation data.* Proteins: Struct., Funct., Bioinf., 2005. **60**(3): p. 367-381.

203. Kaltashov, I.A. and R.R. Abzalimov, *Do ionic charges in ESI MS provide useful information on macromolecular structure?* J. Am. Soc. Mass Spectrom., 2008. **19**(9): p. 1239-1246.

204. Benesch, J.L.P., *Collisional Activation of Protein Complexes: Picking Up the Pieces.* J. Am. Soc. Mass Spectrom., 2009. **20**(3): p. 341-348.

205. Wu, C., J. Klasmeier, and H.H. Hill, *Atmospheric pressure ion mobility spectrometry of protonated and sodiated peptides.* Rapid Commun. Mass Spectrom., 1999. **13**(12): p. 1138-1142.

206. Rozman, M. and S.J. Gaskell, *Non-covalent interactions of alkali metal cations with singly charged tryptic peptides.* J. Mass Spectrom., 2010. **45**(12): p. 1409-1415.

207. Verkerk, U.H. and P. Kebarle, *Ion-ion and ion-molecule reactions at the surface of proteins produced by nanospray. Information on the number of acidic residues and control of the number of ionized acidic and basic residues.* J. Am. Soc. Mass Spectrom., 2005. **16**(8): p. 1325-1341.

208. Julian, R.R. and J.L. Beauchamp, *The unusually high proton affinity of aza-18-crown-6 ether: Implications for the molecular recognition of lysine in peptides by lariat crown ethers.* J. Am. Soc. Mass Spectrom., 2002. **13**(5): p. 493-498.

209. Steinberg, M.Z., R. Elber, F.W. McLafferty, R.B. Gerber, and K. Breuker, *Early Structural Evolution of Native Cytochrome c after Solvent Removal.* Chembiochem, 2008. 9(15): p. 2417-2423.

210. Wyttenbach, T., J.E. Bushnell, and M.T. Bowers, *Salt Bridge Structures in the Absence of Solvent? The Case for the Oligoglycines.* J. Am. Chem. Soc., 1998. **120**(20): p. 5098-5103.

211. Felitsyn, N., M. Peschke, and P. Kebarle, *Origin and number of charges observed on multiply-protonated native proteins produced by ESI.* Int. J. Mass Spectrom., 2002. **219**(1): p. 39-62.

212. Adams, J., *The proteasome: A suitable antineoplastic target.* Nat. Rev. Cancer, 2004. 4(5): p. 349-360.

213. Hoeller, D., C.M. Hecker, and I. Dikic, *Ubiquitin and ubiquitin-like proteins in cancer pathogenesis.* Nat. Rev. Cancer, 2006. **6**(10): p. 776-788.

214. Richardson, P.G., B. Barlogie, J. Berenson, S. Singhal, S. Jagannath, D. Irwin, S.V. Rajkumar, G. Srkalovic, M. Alsina, R. Alexanian, D. Siegel, R.Z. Orlowski, D. Kuter, S.A. Limentani, S. Lee, T. Hideshima, D.L. Esseltine, M. Kauffman, J. Adams, D.P. Schenkein, and K.C. Anderson, *A phase 2 study of bortezomib in relapsed, refractory myeloma.* N. Engl. J. Med., 2003. **348**(26): p. 2609-2617.

215. Groll, M., C.R. Berkers, H.L. Ploegh, and H. Ovaa, *Crystal structure of the boronic acid-based proteasome inhibitor bortezomib in complex with the yeast 20S proteasome.* Structure, 2006. **14**(3): p. 451-456.

216. Nicholson, B., J.G. Marblestone, T.R. Butt, and M.R. Mattern, *Deubiquitinating enzymes as novel anticancer targets.* Future Oncol., 2007. **3**(2): p. 191-199.

217. Chauhan, D., Z. Tian, B. Nicholson, K.G.S. Kumar, B. Zhou, R. Carrasco, J.L. McDermott, C.A. Leach, M. Fulcinniti, M.P. Kodrasov, J. Weinstock, W.D. Kingsbury, T. Hideshima, P.K. Shah, S. Minvielle, M. Altun, B.M. Kessler, R. Orlowski, P. Richardson, N. Munshi, and K.C. Anderson, *A Small Molecule Inhibitor of Ubiquitin-Specific Protease-7 Induces Apoptosis in Multiple Myeloma Cells and Overcomes Bortezomib Resistance.* Cancer Cell, 2012. **22**(3): p. 345-358.

218. Amerik, A.Y., S. Swaminathan, B.A. Krantz, K.D. Wilkinson, and M. Hochstrasser, *In vivo disassembly of free polyubiquitin chains by yeast Ubp14 modulates rates of protein degradation by the proteasome.* EMBO J., 1997. **16**(16): p. 4826-4838.

219. Lindsey, D.F., A. Amerik, W.J. Deery, J.D. Bishop, M. Hochstrasser, and R.H. Gomer, *A deubiquitinating enzyme that disassembles free polyubiquitin chains is required for development but not growth in Dictyostelium.* J. Biol. Chem., 1998. **273**(44): p. 29178-29187.

220. Lam, Y.A., C.M. Pickart, A. Alban, M. Landon, C. Jamieson, R. Ramage, R.J. Mayer, and R. Layfield, *Inhibition of the ubiquitin-proteasome system in Alzheimer's disease.* Proc. Natl. Acad. Sci. USA., 2000. **97**(18): p. 9902-9906.

221. Wilkinson, K.D., V.L. Tashayev, L.B. Oconnor, C.N. Larsen, E. Kasperek, and C.M. Pickart, *Metabolism of the polyubiquitin signal - Structure, mechanism, and role of Isopeptidase-T.* Biochemistry, 1995. **34**(44): p. 14535-14546.

APPENDIX

The figure below shows the Windows form application designed using the Microsoft Visual Studio 2010 (.NET framework 4.0). The calculator is available on request (kleitos.sokratous@gmail.com).

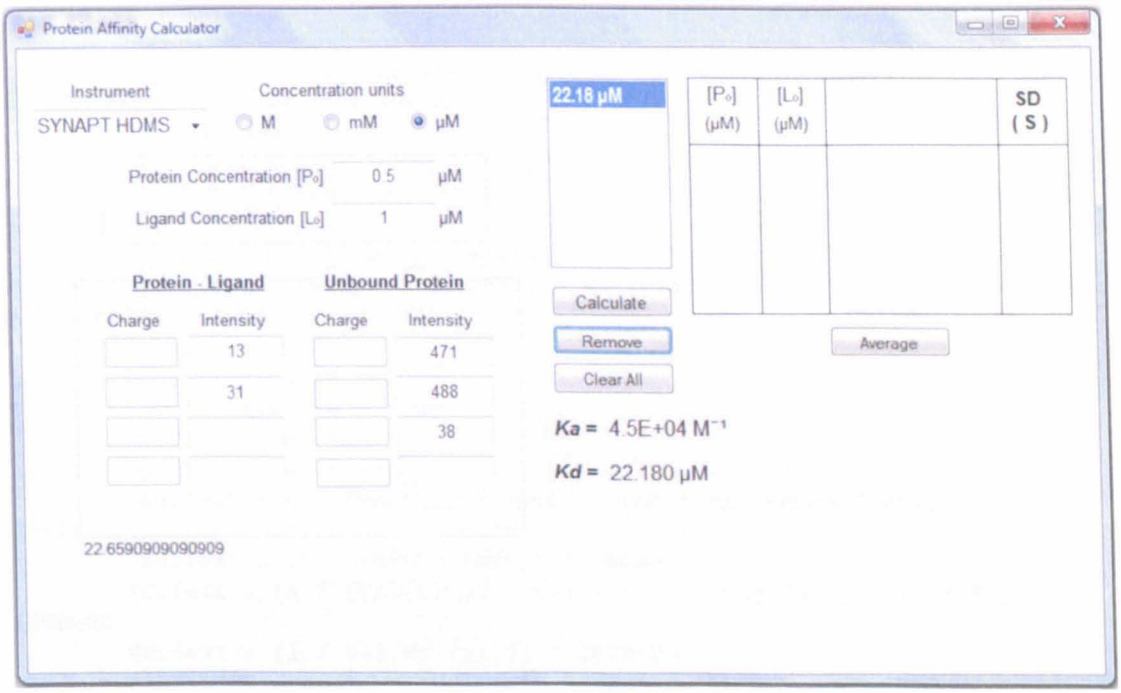

The source code of the calculator is given below.

```
Public Class Kd_Cal

    Dim scientific As String

    Private Sub Form1_Load(ByVal sender As System.Object, ByVal e As
System.EventArgs) Handles MyBase.Load
        PLch1.Enabled = False
        PLch2.Enabled = False
        PLch3.Enabled = False
        PLch4.Enabled = False
        UPch1.Enabled = False
        UPch2.Enabled = False
        UPch3.Enabled = False
        UPch4.Enabled = False

        Label12.Visible = False
        Label13.Visible = False
        Label15.Visible = False
        Label17.Visible = False
```

```
        Label19.Visible = False

        Avg.Visible = False
        StDev.Visible = False
        StdError.Visible = False
        Ka.Visible = False
        Kd.Visible = False
        PrCon.Visible = False
        LiCon.Visible = False

        Lconc.Enabled = False
        Pconc.Enabled = False


    End Sub
    Private Sub KdCal_Click(ByVal sender As System.Object, ByVal e As
System.EventArgs) Handles KdCal.Click
        Dim R As Double
        'R = (Val(PLint1.Text) + Val(PLint2.Text) + Val(PLint3.Text) +
Val(PLint4.Text)) / (Val(UPint1.Text) + Val(UPint2.Text) + Val(UPint3.Text)
+ Val(UPint4.Text))
        R = (Val(UPint1.Text) + Val(UPint2.Text) + Val(UPint3.Text) +
Val(UPint4.Text)) / (Val(PLint1.Text) + Val(PLint2.Text) + Val(PLint3.Text)
+ Val(PLint4.Text))
        Ratio.Text = R
        Label12.Visible = True
        Label13.Visible = True
        Ka.Visible = True
        Kd.Visible = True
        'Ka.Text = R / (Val(LiCon.Text) - ((R * Val(PrCon.Text)) / (1 +
R)))
        'Kd.Text = (1 / Val(Ka.Text)) * 1000000
        Kd.Text = (R * (Val(LiCon.Text) - (Val(PrCon.Text) / (1 + R)))) *
1000000
        Ka.Text = (1 / Val(Kd.Text)) * 1000000
        Ka.Text = Format(Val(Ka.Text), "G2") & " M ⁻¹"

        Kd.Text = Format(Val(Kd.Text), "F3") & " µM"
        Dim Kds As String = Val(Kd.Text)
        ListBoxKd.Items.Add(Kds & " µM")


    End Sub

    Private Sub Pconc_Click(ByVal sender As Object, ByVal e As
System.EventArgs) Handles Pconc.Click
        If RadioButton1.Checked = True Then
            PrCon.Text = Val(Pconc.Text)
        ElseIf RadioButton2.Checked = True Then
            PrCon.Text = Val(Pconc.Text) / 1000
        ElseIf RadioButton3.Checked = True Then
            PrCon.Text = Val(Pconc.Text) / 1000000
        End If
    End Sub

    Private Sub Pconc_KeyPress(ByVal sender As Object, ByVal e As
System.Windows.Forms.KeyPressEventArgs) Handles Pconc.KeyPress

        If Not Asc(e.KeyChar) = 8 AndAlso Not Asc(e.KeyChar) = 46 AndAlso
Not Asc(e.KeyChar) = 13 AndAlso Not IsNumeric(e.KeyChar) Then
            MessageBox.Show("Please enter numbers only")
```

```
            e.Handled = True
        End If
    End Sub

    Private Sub Lconc_Click(ByVal sender As Object, ByVal e As
System.EventArgs) Handles Lconc.Click

        If RadioButton1.Checked = True Then
            LiCon.Text = Val(Lconc.Text)
        ElseIf RadioButton2.Checked = True Then
            LiCon.Text = Val(Lconc.Text) / 1000
        ElseIf RadioButton3.Checked = True Then
            LiCon.Text = Val(Lconc.Text) / 1000000
        End If
    End Sub

    Private Sub Lconc_KeyPress(ByVal sender As Object, ByVal e As
System.Windows.Forms.KeyPressEventArgs) Handles Lconc.KeyPress

        If Not Asc(e.KeyChar) = 8 AndAlso Not Asc(e.KeyChar) = 46 AndAlso
Not Asc(e.KeyChar) = 13 AndAlso Not IsNumeric(e.KeyChar) Then
            MessageBox.Show("Please enter numbers only")
            e.Handled = True
        End If

    End Sub

    Private Sub RadioButton1_CheckedChanged(ByVal sender As System.Object,
ByVal e As System.EventArgs) Handles RadioButton1.CheckedChanged
        Label4.Text = "M"
        Label5.Text = "M"
        PrCon.Text = Val(Pconc.Text)
        LiCon.Text = Val(Lconc.Text)
        LabelPunit.Text = "(M)"
        LabelLunit.Text = "(M)"
        Lconc.Enabled = True
        Pconc.Enabled = True
    End Sub

    Private Sub RadioButton2_CheckedChanged(ByVal sender As System.Object,
ByVal e As System.EventArgs) Handles RadioButton2.CheckedChanged
        Label4.Text = "mM"
        Label5.Text = "mM"
        PrCon.Text = Val(Pconc.Text) / 1000
        LiCon.Text = Val(Lconc.Text) / 1000
        LabelPunit.Text = "(mM)"
        LabelLunit.Text = "(mM)"
        Lconc.Enabled = True
        Pconc.Enabled = True

    End Sub

    Private Sub RadioButton3_CheckedChanged(ByVal sender As System.Object,
ByVal e As System.EventArgs) Handles RadioButton3.CheckedChanged
        Label4.Text = "µM"
        Label5.Text = "µM"
        PrCon.Text = Val(Pconc.Text) / 1000000
        LiCon.Text = Val(Lconc.Text) / 1000000
        LabelPunit.Text = "(µM)"
        LabelLunit.Text = "(µM)"
        Lconc.Enabled = True
```

```
        Pconc.Enabled = True
    End Sub

    Private Sub Pconc_TextChanged(ByVal sender As System.Object, ByVal e As
System.EventArgs) Handles Pconc.TextChanged
        If RadioButton1.Checked = True Then
            PrCon.Text = Val(Pconc.Text)
        ElseIf RadioButton2.Checked = True Then
            PrCon.Text = Val(Pconc.Text) / 1000
        ElseIf RadioButton3.Checked = True Then
            PrCon.Text = Val(Pconc.Text) / 1000000
        End If

    End Sub

    Private Sub Lconc_TextChanged(ByVal sender As System.Object, ByVal e As
System.EventArgs) Handles Lconc.TextChanged
        If RadioButton1.Checked = True Then
            LiCon.Text = Val(Lconc.Text)
        ElseIf RadioButton2.Checked = True Then
            LiCon.Text = Val(Lconc.Text) / 1000
        ElseIf RadioButton3.Checked = True Then
            LiCon.Text = Val(Lconc.Text) / 1000000
        End If
    End Sub

    Private Sub ButtonAvg_Click(ByVal sender As System.Object, ByVal e As
System.EventArgs) Handles ButtonAvg.Click

        Dim i As Integer
        Dim m As Double
        Dim squares As Double
        Dim mean As Double
        Dim SampleSize As Double
        Dim SampleSize1 As Double

        Label15.Visible = True
        Label17.Visible = True
        Label19.Visible = True

        Avg.Visible = True
        StDev.Visible = True
        StdError.Visible = True

        For i = 0 To ListBoxKd.Items.Count - 1
            m = m + Val(ListBoxKd.Items(i))
        Next

        mean = (m / ListBoxKd.Items.Count)
        SampleSize = 1 / (Val(ListBoxKd.Items.Count) - 1)

        Avg.Text = Format(mean, "F2")

        For i = 0 To ListBoxKd.Items.Count - 1
            squares = squares + ((Val(ListBoxKd.Items.Item(i)) - mean) ^ 2)
        Next

        StDev.Text = Format(((squares * SampleSize) ^ 0.5), "F3")
```

```
        StdError.Text = Format((Val(StDev.Text) / ((ListBoxKd.Items.Count)
^ 0.5)), "F4")

        ListBoxP.Items.Add(Pconc.Text)
        ListBoxL.Items.Add(Lconc.Text)
        ListBoxSD.Items.Add(StDev.Text)
        ListBoxAvg.Items.Add(Avg.Text & " ± " & Format((Val(StdError.Text)
* 1.96), "F2") & " µM")
        ListBoxKd.Items.Clear()
        Ka.Text = 0
        Kd.Text = 0

    End Sub

    Private Sub Reset_Click(ByVal sender As System.Object, ByVal e As
System.EventArgs) Handles Reset.Click
        ListBoxKd.Items.Clear()
        Ka.Text = 0
        Kd.Text = 0

    End Sub

    Private Sub Remove_Click(ByVal sender As System.Object, ByVal e As
System.EventArgs) Handles Remove.Click
        ListBoxKd.Items.Remove(ListBoxKd.SelectedItem)

    End Sub

    Private Sub ListBox4_SelectedIndexChanged(ByVal sender As
System.Object, ByVal e As System.EventArgs) Handles
ListBoxAvg.SelectedIndexChanged

    End Sub

    Private Sub ListBoxKd_SelectedIndexChanged(ByVal sender As
System.Object, ByVal e As System.EventArgs) Handles
ListBoxKd.SelectedIndexChanged

    End Sub
End Class
```